Spectroscopic Investigation of Ultrafast Photo-physical Processes in Chalcogenide Based Two-Dimensional (2D) Materials

Tanmay Goswami

A thesis submitted for the partial fulfillment of
the degree of Doctor of Philosophy

Institute of Nano Science and Technology

Knowledge city, Sector 81, SAS Nagar, Manauli PO, Mohali 140306, Punjab, India

Indian Institute of Science Education and Research Mohali

Knowledge city, Sector 81, SAS Nagar, Manauli PO, Mohali 140306, Punjab, India

March 2023

Dedication

To my family and

all my friends who crossed my path in this journey

Declaration

The work presented in this thesis has been carried out by me under the guidance of Prof. Hirendra N. Ghosh and Prof. Deepa Ghosh at the Institute of Nano Science and Technology, Mohali. This work has not been submitted in part or in full for a degree, a diploma, or a fellowship to any other university or institute. Whenever contributions of others are involved, every effort is made to indicate this clearly, with due acknowledgement of collaborative research and discussions. This thesis is a bona fide record of original work done by me and all sources listed within have been detailed in the bibliography.

Tanmay Goswami

In my capacity as the supervisor of the candidate's thesis work, I certify that the above statements by the candidate are true to the best of my knowledge.

Prof. Hirendra N. Ghosh   Prof. Deepa Ghosh

(Co-Supervisor)   (Supervisor)

Acknowledgements

The Ph. D term in INST is a life changing experience for me. I have never imagined that I could ever bag the highest educational degree in my field. It came to reality because of many extraordinary human beings I came across throughout my carrier. I came to INST as a simple student of science and it transformed me into a researcher. Here, I would like to thank all those people who became a bridge for my hurdles and stood behind me. I am eternally grateful to all of you for being there with me. Thank you all.

First and foremost, it is my duty to acknowledge my co-supervisor, **Prof. Hirendra N. Ghosh** for his support, advice, and guidance throughout my entire Ph. D tenure. I sincerely appreciate him for giving me complete freedom to work on whatever topic I was interested to work on. I am grateful to him for his continuous support and motivation, which helped me immensely to complete this journey of Ph. D. His constant reassurance, and mental support in the difficult phase and valuable suggestions boosted my confidence at every step of my research work. He exposed me to many different areas and enriched my expertise as a spectroscopist. Apart from science, he made me aware of the current scenario of the world science and enlightened me with many important life lessons. He gave me space to fly and was always there whenever I needed him. I could never expect to find a better guide (or colleague) than him in my carrier. I take this opportunity to express my heartfelt gratitude to Prof. Ghosh for being my Ph.D. supervisor**.**

I want thank my supervisor **Prof. Deepa Ghosh** for her continuous support and guidance in the final year of my Ph. D tenure. She always backed us and gave complete assurance when Ghosh sir was not in INST.

Now, I am going to discuss about few very important people of my life, without whom I could have never completed my Ph. D journey. First of all, there are two people, the most important persons of my Ph. D life, **Anirbanda** and **Taniyadi**. They were the continuous support systems for me at the most difficult phase of my Ph. D life. I want to thank you both from the bottom of my heart. You are the best brother and sister anyone could ever ask for. Next, I want to thank my lab mate **Gurpreet.** She is the very first friend of mine in INST. Since the first day I met her on the way to Ghosh sir's office, we were inseparable. She is the finest human being I ever met in my life. Witnessing her unimaginable dedication to her family, friends and science daily made me a better person. **Sourav** is another such a friend; you can always rely on. He will knock the door at

your worst and will cheer you up. He is indeed a friend in need. We have spent uncountable nights speaking to each other, sharing our thoughts on cinema, culture, politics, cricket, history etc. He has helped me in rearranging my life at the latter stage of my Ph. D journey. Now, I want to thank two of my most favorite persons, **Ayushi,** and **Himanshu,** without whom I could have never survived the INST new campus. They are the best juniors anyone could ever think of. Starting from the morning breakfast to evening snacks, they were the constants for me. Since the very first day **Himanshu** joined our group, he was associated with all my research projects. I cannot imagine of completing all those projects without his continuous support. He has helped me in every way, be it synthesis, characterization or even paper writing. Later, **Ayushi** and **Himanshu** took over all the lab responsibilities as well, which was a great help for me. I want to thank both of them for always being there.

Now, I will acknowledge all those people who were associated with my Ph. D journey, from the very beginning. It all started with my M. Sc project in 2016 with **Dr. Arup Gayen** in **Jadavpur University**. I joined this amazing university at 2011 as a chemistry student and it changed my life completely. It gave me the most important lessons of my life and made me a better human being. During my project with Arup sir, I discovered the researcher in me. This project made me realize that I can pursue research as a career. During this period, **Sayantanidi** and **Kamaleshda** helped me immensely. I want to thank **Prof. Subhas Chandra Bhattacharya and Prof. Ashok K. Ganguli** as well, because of whom I came to know about INST Mohali. I would also like to express my gratitude towards my PG mates in my B. Sc and M. Sc times, **Nayanda, Sagarada, Debasis, Shanuda, Pronabda, Sadik** for being supportive and fun. I want to thank my university friends who still got my back, **Mohana, Saileswar, Subhasish, Anurag, Shantanu, Subarna, Rapti, Supriyo** and **Writha**. I also want to acknowledge my school friends, **Debasis, Sourav, Pabitra, Rajat, Ramu, Kartik, Saikat, Chandan, Manoj, Kaushik, Priyajit,** and **Partha.** We do not meet very often, but I get the exact same vibe from all these friends whenever we see each other.

I joined INST in August 2017 as a Ph. D student. Initially, it was very difficult for me as I came from the east to the north of India, which is completely different in culture. But then I met few amazing people who brushed off this division and made me realize that people are the same wherever you go. In my lab, there were **Soumenda, Radha Manohar Aperu sir, Souravda, Jayantada,** who were too good to be seniors. They taught me the lab culture and every basic thing of research to me. With **Souravda,** I learned the basics of transient data fitting and analysis. I want

Abstract

Since the discovery of monolayer graphene in 2004, there have been growing interest on two dimensional (2D) layered materials, motivated by their outstanding optical, electrical, and mechanical properties. These materials are blessed with many unique characteristics like, high charge carrier mobility, large surface area, strong light-matter interactions, tunable electronic band structure, large quasiparticle binding energy etc. The evolution of these layered entities has revolutionized the condensed matter opto-electronic field, owing to their potential in many exquisite applications like lasers, light emitting diodes (LED), photodetectors, displays, optical sensors, as well as in energy harvesting devices. The efficiencies of these optical devices would be primarily dependent on the material itself. Following the absorption of an electromagnetic radiation, the material gets excited and follow many radiative and non-radiative pathways to relax back to the ground state. So, in order to utilize the material better in an optical device, we need to study those excited state photophysical processes inside the material. These processes are ultrafast in nature and to monitor them we need a technique which can probe very short time scale processes. Transient absorption spectroscopy (TAS) is one such technique; it can study ultrashort processes occurring in picosecond (ps), femtosecond (fs) or even attosecond (as) time scales. In my thesis work, we have employed Femtosecond Transient Absorption Spectroscopy (FTAS) to study the excited state charge carrier dynamics in different 2D metal chalcogenides and their doped or heterostructured counterparts.

The first work deals with the formation and relaxation dynamics of exciton and trionic features in CVD (Chemical vapour deposition) synthesized monolayer MoS_2 flakes. Steady state photoluminescence (PL) measurements confirmed the presence of Characteristic A and B exciton of MoS_2, as well as negatively charged A^- trion in the system. Large exciton and trion binding energy made it possible, to observe these features even at room temperature. From the FTAS measurements, the exciton and trion formation time was calculated to be ~ 0.5 ps and ~ 1.2 ps, respectively. Subsequently, these quasiparticles decay with exciton-exciton annihilation or auger recombination processes. Further, we drop-casted Au nanoparticles (NPs) on top of monolayer MoS_2 in order to fabricate a metal-semiconductor (Au-MoS_2) heterojunction, where Au NPs act as a sink of electrons. With the illumination of pump, photoexcited electrons migrate from MoS_2 to Au with ~ 0.6 ps time scale, dissociating both the exciton and trions. In the next work, we have

studied four different excitonic features in a few layer WS_2. The WS_2 nanosheets were synthesized using liquid exfoliation technique, which were having 5-6 layers. Steady state absorption spectroscopy and FTAS study revealed the formation of A, B, C and D excitons in this layered material, irrespective of the excitation energy. Among which, A, B originate at the K/K' region and C, D form at the Λ-Γ region of the electronic band structure. This decides their formation and relaxation dynamics and influence the optical properties of this material. C, D excitons decay in a much slower manner than that of A, B, mainly because of Pauli blocking effect at the K valley and subsequent Λ-Γ indirect recombination channel. This slower decay of high energy excitons provides us a unique opportunity to extract these hot charge carriers for the betterment of an opto-electronic device. My next project is based on a ternary chalcogenide system, Cu_2MoS_4 (CMS), which showed great potential towards photovoltaic as well as photocatalytic applications lately. However, optical properties of this material are almost unexplored. Raman spectroscopy unveils the presence of very strong electron-phonon (e-ph) coupling in this material. The PL spectrum is comprised of two broad peaks, originated from the radiative recombinations associated with the band edge and near band edge trap states, respectively. In FTAS, we probed the band edge excitons and found that they are strongly influenced by both the trap mediated recombination and the Auger recombination. The saturation density of the material lies in the range of 5.3 ± 0.7 x 10^{14} photons/cm^2, beyond which Auger like processes dominate. The e-ph coupling strength reaches maximum at around 100K, which was emphasized in faster decay dynamics of the CMS exciton in this temperature region. The band gap as well becomes larger as we approach lower temperatures. This detailed spectroscopic investigation would be helpful in implementing CMS like ternary chalcogenides in diverse photonic applications. Finally, we have employed FTAS in studying two modified 2D systems, a CdS/MoS_2 heterojunction and non-metal doped $ZnIn_2S_4$ (ZIS) nanosheets. CdS/MoS_2 is a unique heterojunction, where 1D CdS nanorods are in close contact with 2D MoS_2 sheets. Here, MoS_2 works as a hot electron extractor. Upon photoexcitation, CdS hot charge carriers preferentially move towards the MoS_2 region. The hot carrier transfer rate was found to be much higher than the band edge transfer. This high probability of hot carrier transfer is a great sign for any opto-electronic device. In the other system, thin ZIS nanosheets are separately doped with 'O' and 'N' and their H_2 evolution efficiencies were correlated with the modulated charge carrier dynamics. The doped nanosheets proved to be better photocatalysts, owing to their modified energy band structure and enhanced charge carrier separation. FTAS

unveiled that, the H_2 evolution reaction in ZIS takes place in the near band edge trap states, not in the conduction band. This study will help in comprehending the H_2 evolution process and designing more photocatalytic materials like ZIS. In summary, we have explored the intrinsic photo-physical behaviours in some very important metal chalcogenide systems, which will be beneficiary in the study of these kind of materials and would guide the growing field of two-dimensional optical devices.

Table of contents

List of Figures

List of Tables

List of Abbreviations

1D	One-Dimensional
2D	Two-Dimensional
3D	Three-dimensional
AFM	Atomic force microscopy
AFM	Atomic force microscopy
AR	Auger recombination
as	Attosecond
Au NP	Gold nanoparticle
BE	Binding energy
BP	Black phosphorous
CB	Conduction band
CBM	Conduction band minima
CdS	Cadmium Sulfide
CHA	Concentric Hemispherical Analyser
CMOS	Complementary metal-oxide semiconductor
CMS	Cu_2MoS_4
CNT	Carbon nanotubes
CPA	Chirped pulse amplification

CVD	Chemical vapour deposition
DFG	Difference frequency generation
DIB	Defect induced bleach
DMF	N, N-dimethyl formamide
DMSO	Di-Methyl Sulphoxide
DOS	Density of states
DPSS	Diode pumped solid-state
DRS	Diffuse reflectance spectroscopy
EDS	Energy dispersive X-ray Spectroscopy
EEA	Exciton-exciton annihilation
ehp	Electron-hole pair
EM	Electron microscope
EN	Ethylenediamine
ESA	Excited state absorption
fs	Femtosecond
FTAS	Femtosecond transient absorption spectroscopy
FWHM	Full width half maxima
GSB	Ground state bleach
GVD	Group velocity dispersion

HCE	Hot carrier extraction
HEP	higher energy photon
ICDD	International Centre for Diffraction Data
IRF	Instrument response function
JCPDS	Joint Committee on Powder Diffraction Standards
JDOS	Joint density of state
KE	Kinetic energy
LED	Light emitting diode
LEP	Lower energy photon
LO	Longitudinal optical
LPE	Liquid phase exfoliation
MEG	Multi exciton generation
MoS$_2$	Molybdenum disulfide
NIR	Near-Infrared
nm	Nanometre
NMP	N-Methyl-2-Pyrrolidone
NR	Nanorod
ns	nanosecond
NZIS	O-doped ZnIn$_2$S$_4$

OPA	Optical parametric Amplifier
OZIS	O-doped $ZnIn_2S_4$
PIA	Photoinduced absorption
PL	Photoluminescence
PMT	Photomultiplier tube
ps	Picosecond
PSPD	Position sensitive photo-diode
PVD	Physical vapor deposition
PVP	polyvinyl pyrrolidine
PXRD	Powder X-ray diffraction
QD	Quantum dot
S	Sulphur
SAED	Selected area electron diffraction
SDG	Synchronisation and Delay Generator
SE	Stimulated emission
SEM	Scanning Electron Microscopy
SFG	Sum frequency generation
SFI	Sum frequency idler
SHG	Second harmonic generation

SPM	Self-phase modulation
STM	Scanning Tunnelling Microscopy
SVD	Singular value decomposition
SX	Surface Explorer
TA	Transient absorption
TAA	Thioacetamide
TAS	Transient absorption spectroscopy
TCSPC	Time Correlated Single Photon Counting
TEM	Transmission electron microscopy
TMC	Transition metal chalcogenides
TMDC	Transition metal dichalcogenides
TMO	Transition metal oxides
TRPL	Time resolved photoluminescence
UV	Ultra-violet
VB	Valance band
VBM	Valence band maxima
Vis	Visible
WLC	White light continuum
WLG	White light generation

WS$_2$	Tungsten disulfide
XPS	X-ray photoelectron spectroscopy
XRD	X-ray diffraction
YAG	Yttrium Aluminum Garnet
ZIS	Zinc Indium Sulphide
μs	microsecond

List of Symbols

a	Radius
a_B	Bohr radius
m	mass
k_B	Boltzmann constant
ω	Frequency
T	Absolute temperature
E	Energy
ΔG	Free energy change
λ	Wavelength
τ	Time component
ε	Dielectric constant
θ	Angle
φ	Work function
μ	Reduced mass
η	Refractive index
A	Absorption
c	Speed of light

<u>Chapter 1</u>

Introduction

The journey of two-dimensional (2D) materials started with the discovery of monolayer graphene sheets in 2004.[1] Since then, numerous 2D materials are being formulated and synthesized, motivated by their outstanding optical, electrical, and mechanical properties.[2–13] Thin 2D materials possess extremely high charge carrier mobility,[9,14] large specific surface area,[15] strong light-matter interactions,[9] tunable electronic band structure,[16] large quasiparticle binding energy[17] etc. The evolution of these layered entities has revolutionized the condensed matter opto-electronic field, owing to their potential in many exquisite applications like lasers, light emitting diodes (LED), photodetectors, displays, optical sensors, as well as in energy harvesting devices.[2,10,12,18–23] The efficiencies of these optical devices would be primarily dependent on the material itself. Following the absorption of an electromagnetic radiation, the material gets excited and follow many radiative and non-radiative pathways to relax back to the ground state. So, in order to utilize the material better in an optical device, we need to study those excited state photophysical processes inside the material.[24] These processes are ultrafast in nature and to monitor them we need a technique which can probe very short time scale processes. Transient absorption spectroscopy (TAS) is one such technique; it can study ultrashort processes occurring in picosecond (ps), femtosecond (fs) or even attosecond (as) time scales. In this thesis, we have employed Femtosecond Transient Absorption Spectroscopy (FTAS) to study excited state charge carrier dynamics in different 2D metal chalcogenides and their doped or heterostructured counterparts. We have also established direct correlation between the efficiency a real optical application and the excited state charge carrier behaviour in few cases, which again proved the efficacy of the FTAS instrument.

In this chapter, we will give a brief introduction about the electronic and optical properties of 2D metal chalcogenides, along with the discussion on the prospect of FTAS measurements in the implementation of these materials in real opto-electronic devices.

1.1. The journey of 2D chalcogenide materials

Layered materials were there for the last few decades around us. But, the true potential of these architectures was first realised when Novoselov and Geim exfoliated graphene nanoflakes in 2004, simply by peeling out flakes using a scotch tape.[1] This started a new area of research named as '2D materials.' Monolayer graphene is blessed with extremely high charge carrier mobility ($\sim 10^5$ cm^2 V^{-1} s^{-1}) even at room temperature.[25] Along with that, these materials possess large surface to volume ratio,[15] very high mechanical strength and stability,[7] lower scattering of charge carriers,[26] high thermal conductivity[6] etc., which are ideal for any opto-

electronic or energy storage device. But unfortunately, these were not enough. Graphene lacks a critical property to be used in an electronic device; it lacks a band gap. The conduction band (CB) and valence band (VB) touches in a particular point (Dirac point) and graphene act as a semimetal.[27,28] This leads to very low ON/Off ratio and extremely high stand-by power loss in a graphene-based device.[29] Chemical doping, functionalization or electrical gating might open a band gap in graphene, but these affect the charge carrier mobility.[30–33] Henceforth, the scientific community started looking for graphene like layered materials with semiconducting properties. This created a revolution in the 2D materials field. Several 2D structures were discovered and developed, including transition metal dichalcogenides (TMDC), transition metal chalcogenides (TMC), transition metal oxides (TMO), boron nitrides, black phosphorous (BP) etc.[34–41] Like graphene, these materials have layered structures; these layers are bonded with weak van der Waal's interactions and can be separated out very easily to form monolayer or few layer entities. In my thesis, we have mainly focussed on TMDC and TMC materials. Though the charge carrier mobility of these is not as high as graphene, they possess many extraordinary properties like, tunable band gap in the visible range, high absorption coefficient in the visible range for monolayer and few layer case, strong light-matter interactions, large quasiparticle binding energy, strong photoluminescence in monolayer, strong spin-orbit coupling, valley polarization etc.[17,42–50] These electronic and optical properties are layer dependent and easily tunable with the modulation of layer numbers. These chalcogen based 2D semiconductors are aspired to replace silicon from the electronics industry.

1.2. Quantum confinement effect

Quantum confinement is basically a spatial confinement of electron, hole or electron-hole pair wave functions in one, two or three dimensions inside a material,[51] thereby inducing extraordinary electrical, optical, and mechanical properties in the system. It can be achieved by reducing the particle size in nanometre (nm) range, exact size varies in material to material. As we lower the particle size, the confinement becomes stronger and the energy levels become more discrete in nature (**Figure 1.1**). Confinement effect divides the materials in three different groups,

(i) Quantum well (2D) – Confinement in only one direction,

(ii) Quantum wire (1D) – Confinement in two direction, and

(iii) Quantum dot (0D) – Confinement in all three directions.

These low dimensional materials act as a bridge between the bulk systems around us and the basic molecular entities inside those systems.
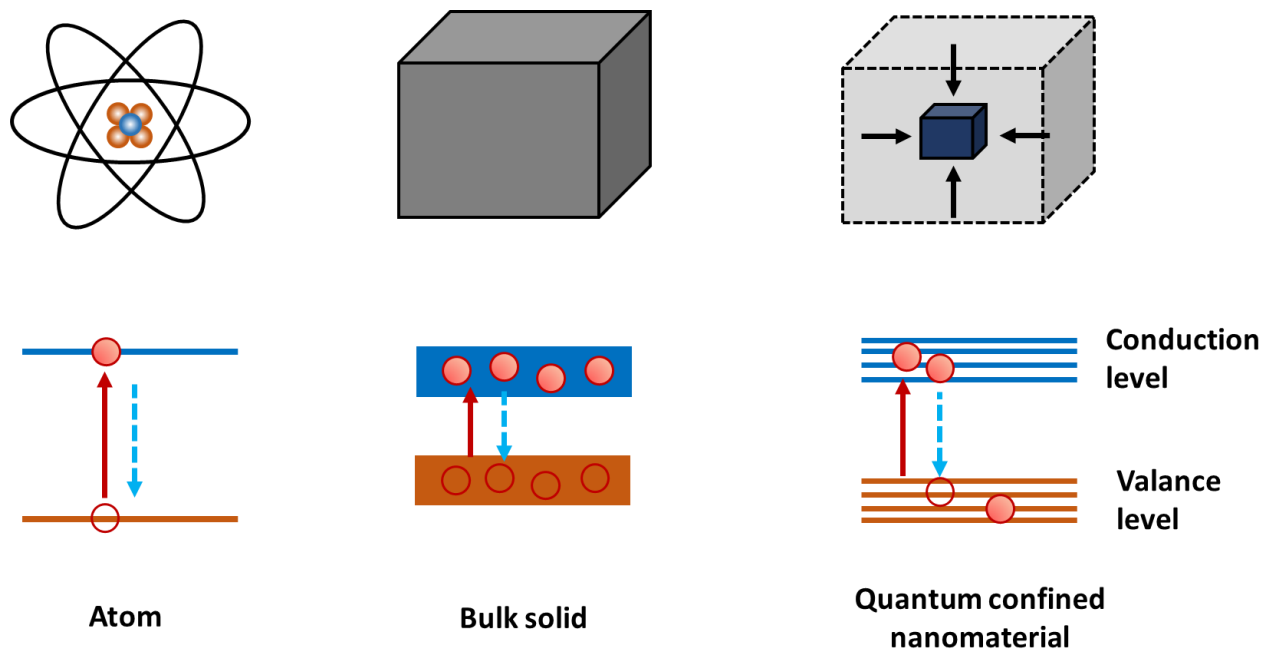
Figure 1.1: Quantum confinement effect and resultant energy band structure of a nanomaterial, as compared to an atom and a bulk material.

Now, we will try to understand the origin of quantum confinement effect in a material.

1.2.1. Particle in a sphere model

To comprehend, the effect of confinement, quantum dots (QDs) are our best model, where charge carriers are bond in all three directions. The quantum phenomena inside a QD can be realised through a particle-in-a-sphere model.[52–54]

If a particle having mass 'm', is bound inside a spherical potential wall of radius 'a', where potential energy of the particle v (r) follows the following condition,

$$V\ (r) = 0 \text{ for } r < a \text{ and}$$
$$V\ (r) = \infty \text{ for } r > a;$$

then the particle wave function resulted in,

$$\varphi\ (r, \theta, \varphi) = C \frac{j_l\ (k_{n,l}\ r)\ Y_l^m\ (\theta, \varphi)}{r}$$

Here, C is the normalization constant, $j_l\ (k_{n,l}, r)$ is the spherical Bessel function of lth order and $Y_l^m\ (\theta, \varphi)$ is the spherical harmonics function.

From this, the particle energy can be deduced into,

$$E_{n,l} = \frac{\hbar^2 \cdot k_{n,l}^2}{2m} = \frac{\hbar^2 \cdot \alpha_{n,l}^2}{2ma^2}$$

So, energy of the particle is inversely proportional to its mass (**m**) and the square of the sphere radius ($\boldsymbol{\alpha^2}$).

Here, the eigen functions have atomic like properties and noted using different quantum numbers (n, l, m). As the particle potential energy is zero inside the sphere, this energy refers only to the kinetic energy of free electrons.

Now, the drawback of this model is that, it has not considered any perturbation, assuming an empty sphere. This not a real scenario. In a real semiconductor lattice, there are several atoms, resulting in several particles. So, we need to modify this energy equation. We will now apply an Effective mass approximation theory.

1.2.2. Effective mass approximation (EMA) theory

In EMA, the VB and CB of a bulk semiconductor are approximated as parabolic isotopic bands. From the Bloch's theorem, the electron wave function in this bulk semiconductor can be expressed as,

$$\psi_{nk} (r) = u_{nk}(r) \cdot \exp(ik.r)$$

Here, $\boldsymbol{u_{nk}(r)}$ is the lattice periodicity function, n is the band index (c for CB and v for VB) and k represents the wave vector. By plotting energy '**E**' vs '**k**', we will get energy level diagram of this electron.

Now, the energies of CB and VB can be written as,

$$E \text{ (CB)} = E_k^c = \frac{\hbar^2 \cdot k^2}{2m_{eff}^c} + E_g$$

$$E \text{ (VB)} = E_k^v = -\frac{\hbar^2 \cdot k^2}{2m_{eff}^v}$$

Here, $\boldsymbol{E_g}$ is the band gap of this semiconductor, which is defined by the energy difference between VB maxima and CB minima. $\boldsymbol{m_{eff}^c}$ and $\boldsymbol{m_{eff}^v}$ are the free particle effective mass in CB and VB. The particles are considered to be free here, ignoring the crystal periodicity.

This equation is true for a bulk material only. To be considered for single particles like electron, hole or an electron-hole pair this model is modified using envelope function approximation. According to this theory, the single particle wave function can be written as,

$$\boldsymbol{\Psi}_{sp} (r) = \sum_i^k c_{nk} \, u_{nk}(r) \exp(ik.r)$$

where, $\boldsymbol{c_{nk}}$ represents the expansion coefficient, satisfying the boundary conditions of the sphere.

Now, if we consider the weak dependence of the $u_{nk}(r)$ parameter on the wave vector 'k', this equation will be simplified into,

$$\Psi_{sp}(r) = u_{n0}(r) \sum_k c_{nk} \exp(ik.r) = u_{nk}(r) f_{sp}(r)$$

Here, $f_{sp}(r)$ is called the single particle function and can be determined as,

$$f_{sp}(r) = \sum_k c_{nk} \exp(ik.r)$$

So, now the bulk equation is converted into a single particle equation. The electron-hole pair wave function will be the combination of electron wave function and the hole wave function. The energy of this electron-hole pair (ehp) can be expressed as,

$$E_{ehp} = E_g + \hbar^2 \left(\frac{k^2}{2m_{eff}^c} + \frac{k^2}{2m_{eff}^v} \right)$$

$$= E_g + \frac{\hbar^2}{2a^2} \left(\frac{\alpha^2}{2m_{eff}^c} + \frac{\alpha^2}{2m_{eff}^v} \right)$$

This is the energy of an electron-hole pair in a confined structure. The second term in the equation represents the confinement energy.

When an ehp is formed, an intense columbic interaction works between electron and hole, which try to break this pair. Considering this columbic interaction, the energy equation can be written as,

$$E_{ehp} = E_g + \frac{\hbar^2}{2a^2} \left(\frac{\alpha^2}{2m_{eff}^c} + \frac{\alpha^2}{2m_{eff}^v} \right) - \frac{1.8e^2}{\varepsilon a}$$

where, ε is the dielectric constant.

This is the final equation of electron-hole pair energy in the EMA model. It depends on three terms, band gap of the material, confinement energy and the coulombic interaction. As we decrease the particle size the confinement energy term becomes more dominant, stabilising the electron-hole pair.

The band gap of the QD nanocrystal can be written as,

$$E_g(QD) = E_g + \frac{\hbar^2 \Pi^2}{2m_{eh} a^2} \left(\frac{\alpha^2}{2m_{eff}^c} + \frac{\alpha^2}{2m_{eff}^v} \right) - \frac{1.8e^2}{\varepsilon a}$$

Here, m_{eh} represents the reduced mass of the electron-hole pair,

$$m_{eh} = \frac{m_{eff}(e). \ m_{eff}(h)}{m_{eff}(e) + m_{eff}(h)}$$

So, EMA model successfully explains the discreteness of energy levels and increment of band gap with reduced particle size. It also reasons with the stable electron-hole pair formation in the nanocrystals.

1.2.3. Density of states (DOS) in different type of quantum confinement

DOS is a very important factor for a material; it decides the transitions within the energy bands, thereby influencing the absorption and PL spectra of the system. It is defined as the number of energy states present in an energy level.

For a bulk **3D** semiconducting material, DOS can be expressed as,

$$g(E)^{3D} = \frac{\sqrt{2Em^3}}{\Pi^2 \hbar^3}$$

So, in case of bulk, DOS is proportional to the square root of the particle energy 'E' and represents as a continuous curve.

DOS **2D** materials do not depend on the energy,

$$g(E)^{2D} = \frac{m}{\Pi \hbar^2}$$

In **1D** case, DOS decreases with the increment of energy,

$$g(E)^{1D} = \frac{m}{\Pi \hbar} \cdot \sqrt{\frac{2m}{E}}$$

For 0D materials, extensive confinement in all three directions results in discrete energy states.
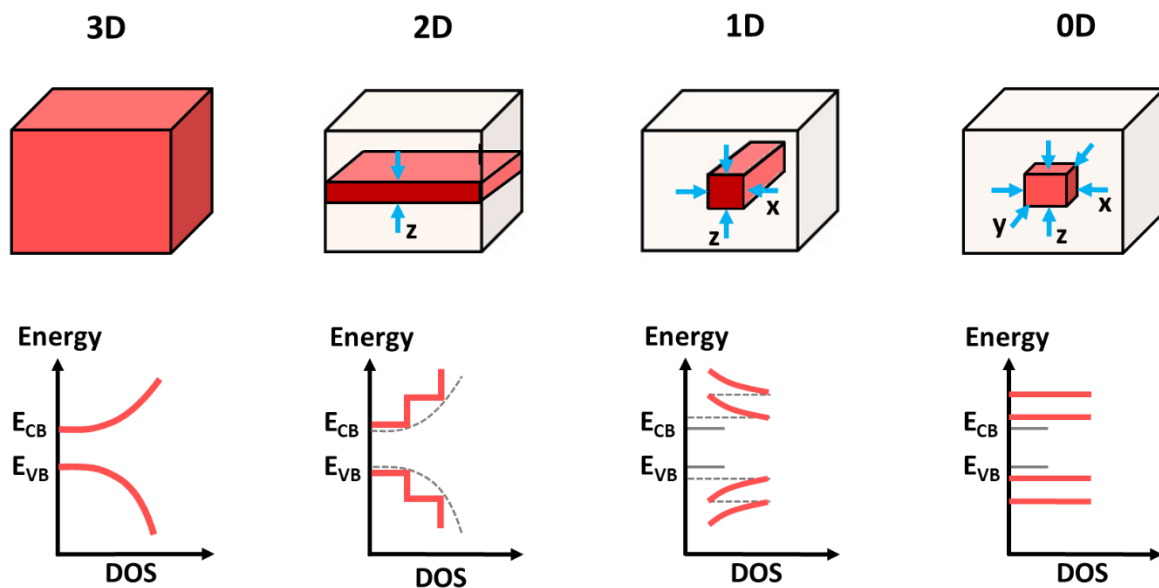
Figure 1.2: Schematic illustration of different quantum confinement in nanomaterials and corresponding DOS functions with energy.

1.2.4. Exciton formation

An exciton is a combination of negative electron and positive hole in the CB and VB of a semiconductor. It is a quasiparticle. The net charge of this system is zero and it moves freely within the system. The idea of an exciton was first given by Y. Frenkel in 1931.[55]

When a semiconducting system absorbs a photon higher than its electronic band gap, an electron and a hole generated in its CB and VB respectively. These electron and hole come together to form a pair named exciton. The stability of this pair rides on the repulsive coulombic interaction between the excited electron in CB and the ground state electrons in the VB. Attractive force within the electron-hole pair and repulsive interactions work simultaneously on this pair and the exciton possess a lower energy than an unbound pair electron and hole. There are mainly two types of excitons,[56]

Frenkel exciton – For materials of low dielectric constant, the electron and hole experience very strong coulombic interaction. These excitons are small in size and possess very strong binding energy (0.1-1 eV). Frenkel excitons are observed in molecular systems, alkali halides, transition metal compounds with empty d-shells etc.

Wannier- Mott exciton – For materials of large dielectric constant, the coulombic interaction between electron and hole decreases due to strong electric field screening, resulting in Wannier- Mott excitons. These excitons are large in size and possess low binding energy (~ 0.01 eV). These excitons are observed in small band gap semiconducting materials.

1.2.5. Exciton Bohr radius and quantum confinement regime

The exciton Bohr radius is the spatial separation between the electron and hole inside the quasiparticle. It is characteristic to a particular semiconducting material. The quantum size effect influences the properties of a material only when the particle size is equal or less than the Bohr radius. Bohr radius (a_B) is expressed as,[57]

$$a_B = \varepsilon \cdot \left(\frac{m}{m_{eh}}\right) \cdot a_H,$$

where, ε is the dielectric constant of the semiconductor medium, m is the rest mass of electron, m_{eh} is the reduced mass of the electron-hole pair and a_H presents the Bohr radius of a Hydrogen atom, which is around 0.05 nm.

For a low dimensional nanomaterial, this exciton Bohr radius is different for electron (a_e), hole (a_h), and the exciton (a_{ex}). These values decide the intensity of quantum confinement in a nanoparticle (particle radius 'r').

There are three different confinement regime,[58]

(i) **Strong confinement: $r < a_e$, a_h, a_{ex}.** Here both electron and hole are confined inside the potential energy barrier of the nanoparticle.

(ii) **Moderate confinement:** $a_e < r < a_h, a_{ex}$ or $a_h < r < a_e, a_{ex}$. Either electron or hole is confined here. One of these charge carriers is strongly confined, not the other.

(iii) **Weak confinement:** $a_e, a_h < r < a_{ex}$. Here only exciton is confined.

1.3. Exciton and charge carrier dynamics

Illuminating a nanomaterial with an electromagnetic radiation of sufficient photon energy, leads to the formation of excited electron and holes in the high energy states of CB and VB. These charge carriers relax to the band edge and form excitons, as discussed earlier. The stability of these excitons would depend on the material and the charge carrier population. These charge carriers would return to their ground state, either being individual carriers or being electron-hole pair (exciton), depending upon the stability and lifetime of those excitons. In general, the photo-physical processes involved in the relaxation and recombination of excited charge carriers in a low dimensional material are, thermalization, hot carrier relaxation, exciton formation, charge carrier trapping, Auger recombination, bi-exciton and trion formation etc. These processes decide the merit of the material in its usability in an opto-electronic device.
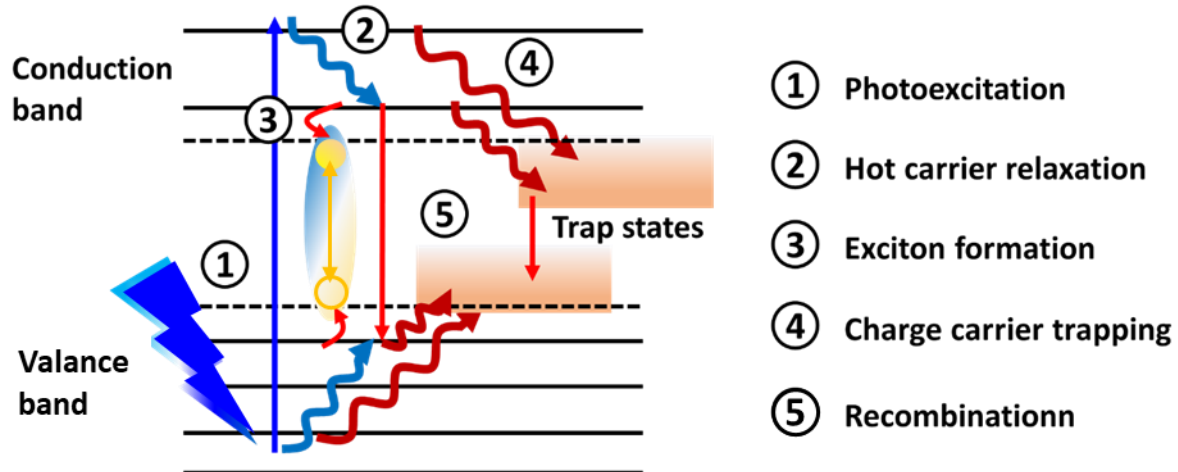
Figure 1.3: Different photo-physical processes in a semiconducting system, following absorption of an electromagnetic radiation.

1.3.1. Thermalization and hot carrier relaxation or cooling

When a quantum material is excited with higher energy photons than its electronic band gap, a non-thermal gaussian distribution electron and holes are created in the higher energy states of CB and VB.[59] These charge carriers interact among each other (carrier- carrier scattering) to

produce a thermal distribution (same temperature for all carriers). This process is named as thermalization.[60] It follows non-Markovian quantum kinetics and the carriers now enjoy a Fermi-Dirac distribution. Since the dielectric screening is very low in thin 2D materials, this carrier-carrier scattering phenomenon occurs at extremely fast time scale (10- 20 fs). The carrier temperature of these thermalized carriers is still higher than the lattice temperature and can be termed as hot carriers. Following that, these hot charge carriers relax down to the band edge states, via relaxation or cooling process. Subsequently the carrier temperatures are decreased and comparable to the lattice temperature now. This cooling process is associated with the emissions of hot phonons. In a few layer MoS_2 system, this cooling process was found to be occurring at ~ 500 fs time scale.[60] These time scales found in thermalization and cooling of 2D TMDC materials are much lower than conventional 2D architectures like GaAs[61] or similar QD systems, which indicates greater probability of carrier-carrier scattering and carrier-phonon scattering in mono and few layer TMDC.
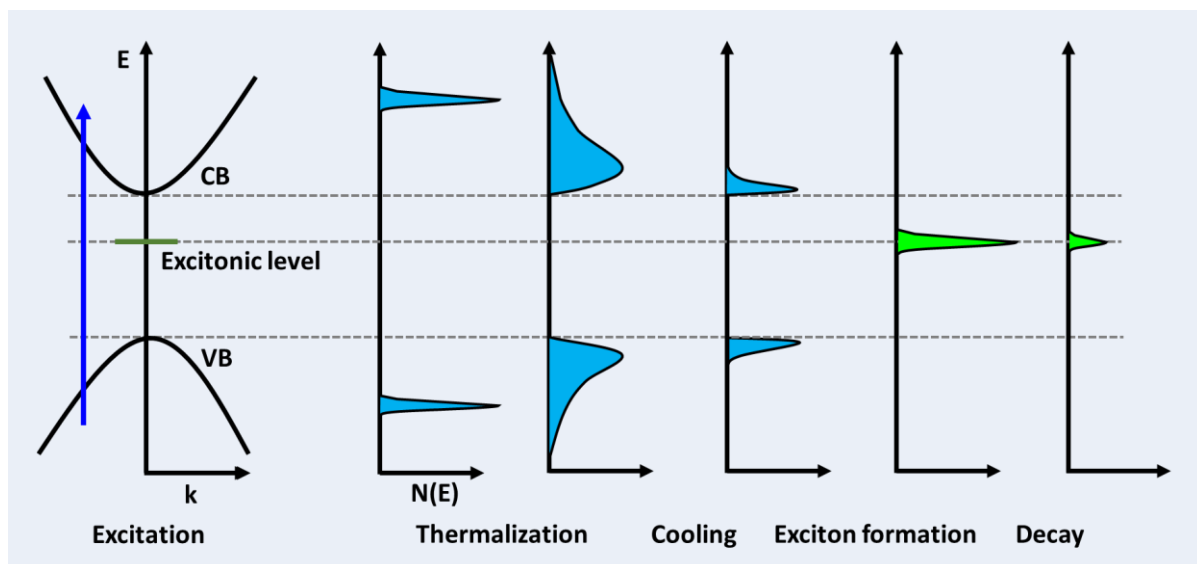
Figure 1.4: Evolution of charge carrier distribution following a high energy interband photoexcitation.

Phonon-bottleneck effect- In the cooling process the hot carriers relax into the band edge via transferring excess energy to the phonons. When the confinement is very strong, the energy difference between intraband states (Both in CB and VB, depending upon the effective mass of electron and hole, respectively) becomes so large that relaxation cannot proceed in emitting one phonon. Multi-phonon emission is observed in such cases, which is a very slow process. This slow down the hot carrier relaxation and this phenomenon is called phonon bottleneck

effect. If we consider that, the hot carrier relaxation is dominated by the Fröhlich interaction between charge carrier and longitudinal optical (LO) phonons, the charge carrier relaxation time can be written as,

$$\tau = \frac{1}{\omega_{LO}} \cdot \frac{\Delta E}{k_B T}$$

where, ω_{LO} is the frequency of the LO phonon, ΔE is the energy spacing in the intraband states and $k_B T$ represents thermal energy (Where, k_B is Boltzmann constant and T is absolute temperature). With the increment in the intraband energy spacing, the relaxation time increases.
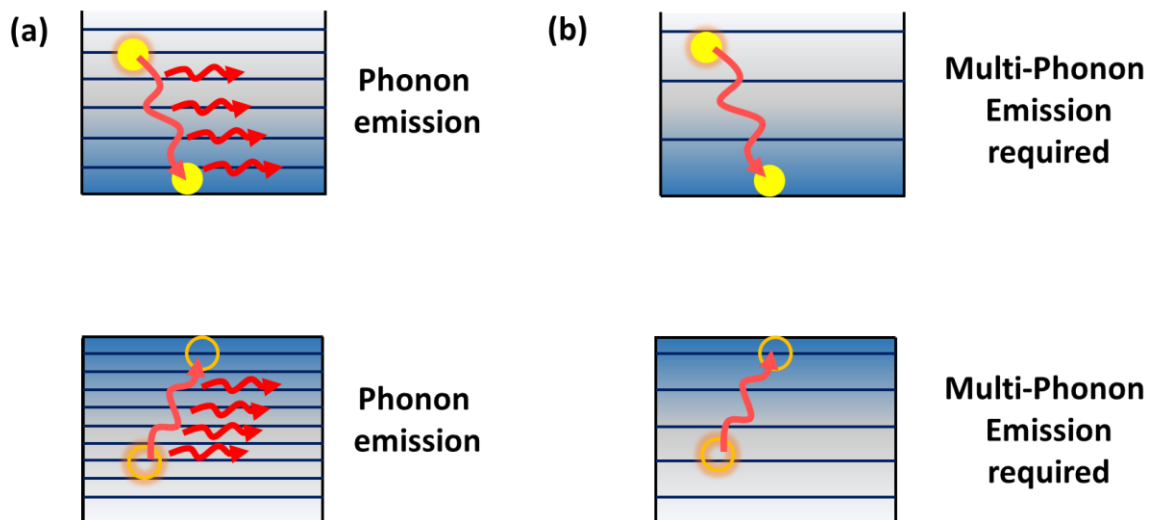
Figure 1.5: Hot exciton relaxation **(a)** without phono bottleneck, and **(b)** with phono bottleneck.

1.3.2. Exciton formation

As the hot charge carriers arrive at the band edges of the CB and VB, they feel strong coulombic attraction towards each other and form excitons. Usually, this exciton formation takes place in a very rapid manner and it is very difficult to differentiate cooling process and the exciton formation phenomenon. But atomically thin 2D TMDC materials are different. They possess exceptionally strong coulombic interaction between those electron-hole pairs and have very large exciton binding energy (Few hundreds of meV) even at room temperature.[62,63] As a result, the exciton formation process can be separately observed in the transient decay dynamics. The exciton formation time was found to be 0.3- 0.5 ps in monolayer MoS_2, WS_2, $MoSe_2$ and WSe_2.[59]

These excitons decay via formation of unpaired electron and holes or as an exciton itself, depending upon the material and conditions. The recombination could be either radiative or

non-radiative or both. Non-radiative processes are usually rate-determining step for the recombination of excited charge carriers in a condensed matter and they occur at very short time scale, which can only be monitored through a high resolution TAS technique. Here, we are going to discuss few such non-radiative processes.

1.3.2.1. Exciton-exciton annihilation (EEA) and Auger recombination (AR)

Exciton-exciton annihilation (EEA) and auger recombination (AR) works on the same principle. In case of EEA, two exciton interacts among each other, where one exciton recombines and transfer its energy to the other. This extra energy ionizes this exciton into separated electron and holes. The ionization energy comes from the exciton binding energy and later it is divided between those electron and holes, which are further excited into the higher energy states of CB and VB respectively.[64,65] EEA take place in high exciton density and in materials where exciton-exciton interaction is very high, like organic molecules,[66] Carbon nanotubes (CNT),[67] TMDC[64] etc.
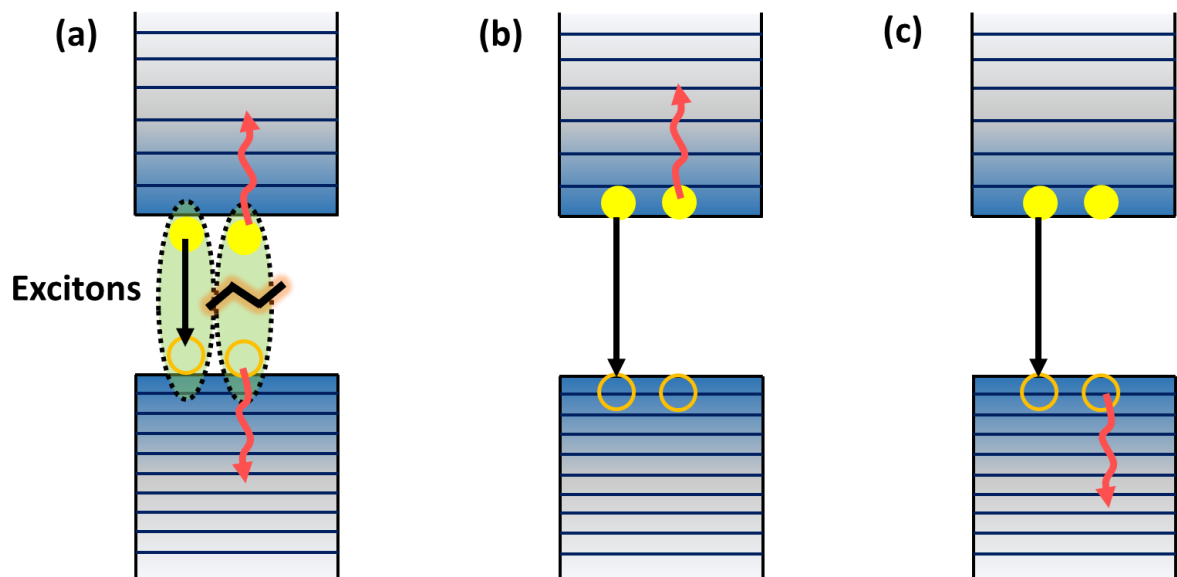
Figure 1.6: (a) Exciton-exciton annihilation process, **(b)** Auger recombination with electron heating and **(c)** Auger recombination with hole heating.

On the other hand, AR takes place when a photoexcited electron and hole recombines to transfer its energy to another carrier (either electron or hole), which further excites to the high energy states.[68–70] Also, when a hot carrier relaxes to the band edge, it can transfer its electron to a ground state electron or hole to be excited further. This auger mediated energy transfer leads to fast relaxation of hot charge carriers, diminishing the phonon bottleneck effect.[71,72] In

small nanoparticles, electron and holes are strongly coupled among each other (substantial overlap of electron and hole wave function). This helps in easy transfer of hot electron relaxation energy to the hole, which is excited further. AR process is also favoured in high charge carrier concentrations.

1.3.2.2. Recombination via charge carrier trapping

Defects play very important role in nanomaterials. As we decrease down the particle size, surface to volume ratio increases and more atoms are exposed to the atmosphere (It is more pronounced in 2D materials). This enhances defects in the system and results in shallow and/or deep trap states in the energy band structure of the material. These trap centres act as a sink for the photoexcited charge carriers. This trapping process is a non-radiative phenomenon and it has a negative effect on the radiative lifetime and quantum yield of the material. Charge trapping is usually very fast process and it can accelerate the hot carrier cooling and the subsequent recombination processes. Usually, when a system possesses inter band gap trap states, the photoexcited electron and holes first get trapped in the trap states and then recombine with each other. Once trapped, these charge carriers get decoupled and follow very slow recombination process.
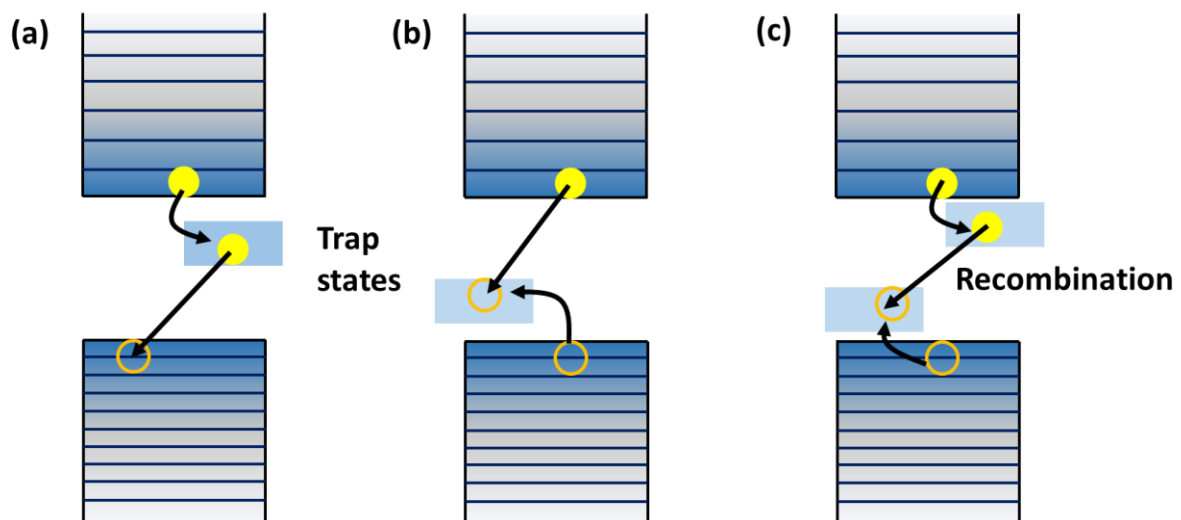
Figure 1.7: Different trapping mediated recombination processes: **(a)** electron trapping, **(b)** hole trapping and **(c)** both electron and hole trapping.

1.3.3. Bi-exciton and trion formation

When the photoexcitation energy is much higher (at least two times) than the band gap of the material, the relaxation energy released by the electron might produce another exciton,

resulting in bi-exciton.[73,74] This auger mediated process is known as impact ionization or multi exciton generation (MEG) process. MEG is usually observed in low band gap materials like, PbS, PbSe etc. and it is extremely beneficial in improving the efficiency of solar cell like applications.[75,76]

Trions are formed when, two electron and one hole (negative trion), or one electron and two holes (positive trion) binds together to form a three-particle quasiparticle system.[77,78] They are either formed from an exciton or from the dissociation of a bi-exciton. Both bi-exciton and trions usually decay through auger process.[79,80]
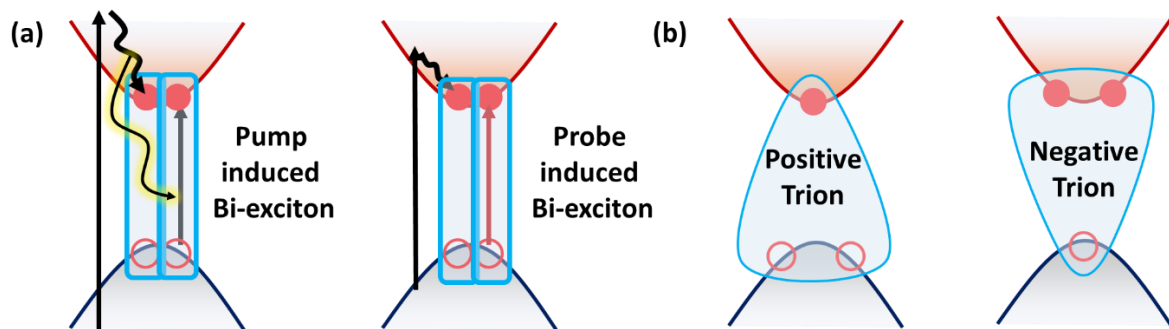
Figure 1.8: Different bi-exciton and trion formation processes: **(a)** Pump and probe induced bi-exciton, and **(b)** Positive and negative trion formation.

1.4. External tuning of the material properties

Sometimes pristine material system is not enough for an opto-electronic device to be efficient. The intrinsic properties of this material need to be improved, and it can be done via appropriate external manipulations, like doping, size modulation, surface passivation, heterojunction formation etc. In my thesis, we have used doping and heterojunction formation for the modulation of the opto-electronic properties of 2D chalcogenides.

1.4.1. Doping

Doping is an efficient strategy to modify the energy band structure and correspondingly improve the optical and electrical properties of a semiconducting material.[81] This technique not only improves the existing properties of the material, it can induce new functionality in the system depending upon the type of dopant, doping concentration, interaction between the host material and the dopants etc.[82] 2D materials are highly susceptible to doping due to their layered structures and high concentration of exposed surface area. There have been several instances where metal and non-metal elements are doped in a 2D material in order to improve their

efficiency in an optical application.[83–86] In my thesis also, we have doped 'O' and 'N' elements in $ZnIn_2S_4$ (ZIS) nanosheets and observed an enhanced photocatalytic activity.[87] While doping, the CB and VB of ZIS were uplifted, which facilitates the reduction probability of proton (producing H_2). Also, the concentration and lifetime of the charge carriers were highly improved in the doped systems, which proved to be beneficial for the photocatalytic efficiency.

1.4.2. Heterojunction formation

An efficient material to be used in an opto-electronic device should be empowered with many unique properties, like effective absorption of electromagnetic radiation, high charge carrier lifetime, complimentary energy band structure, optimum concentration of trap states, smooth diffusion of charge carriers etc.[88] So, it is always difficult to find a material with all these properties. Fabrication of a heterojunction can solve this problem.[24] There are many different types of semiconductor heterojunctions are reported corresponding to 2D materials, like 2D/0D, 2D/1D, 2D/2D, 2D/3D etc.[89–94] Metal-semiconductors are also fabricated and used in many photovoltaic and photocatalytic applications.[95,96] In my thesis work, we have synthesized a 2D/1D composite where CdS nanorods were in contact with the MoS_2 sheets.[97] We observed highly efficient hot electron migration from CdS to MoS_2. We have also fabricated a MoS_2-Au heterojunction, where photoexcited electrons from MoS_2 were instantaneously transferred to Au.[98]

1.5. Electron transfer theory

Electron transfer is a simple chemical reaction, where the charge moves from one spatial region to another inside a material or within two materials. The theory of this process was first explained by R. A Marcus in 1956.[99] Since then, there have many modifications and adjustments associated with this theory according to the conditions.[100] Here, we are going discuss only the basics of Marcus model for electron transfer. To describe this model a displaced harmonic oscillator approximation can be used, where a weakly coupled donor-acceptor complex (Reactant, D-A) is transformed into charge separated complex (Product, D^+-A^-) via transition state complexes (D---A).

This reaction is guided through a nuclear coordinate. In solution, a solvent coordinate is considered, where the solvent reorganizes itself to stabilize the extra positive and negative charges on donor and acceptor cites (**Figure 1.9**). The respective potential energy surface of reactant and product are shown in **figure 1.10**.
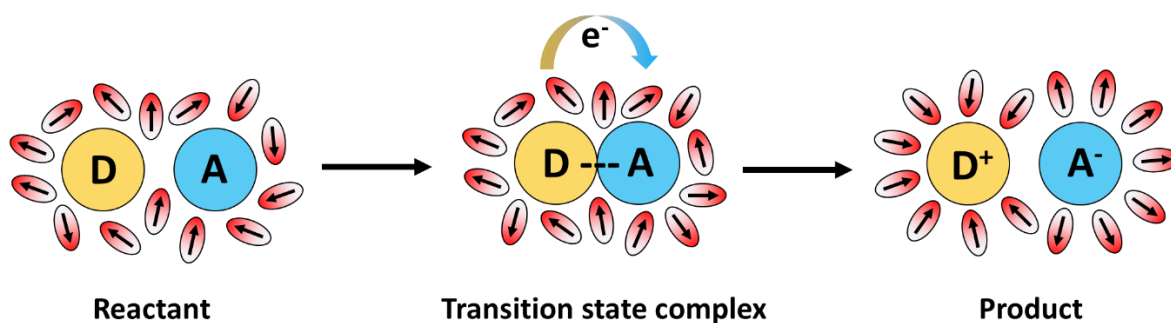
Figure 1.9: Outer sphere electron transfer between a donor and an acceptor, in a solution.

According to the semiclassical model of Marcus, the electron transfer rate is given by,[101]

$$k_{ET} = \mathrm{k}\frac{k_B T}{h}\exp\left(-\frac{\Delta G_{ET}^{\#}}{k_B T}\right)$$

where, the Arrhenius activation energy function can be expressed as,

$$\Delta G_{ET}^{\#} = \frac{-\left(\lambda + \Delta G_{ET}^0\right)^2}{4\lambda}$$

Here, $\mathbf{k}$ is the adiabaticity parameter, $\boldsymbol{k_B}$ is the Boltzmann constant, $\mathbf{T}$ is the absolute temperature, $\mathbf{h}$ is the plank constant, $\boldsymbol{\lambda}$ is the solvent reorganisation energy, $\boldsymbol{\Delta G_{ET}^0}$ is the Gibbs free energy change between reactant and product (Driving force of this reaction).
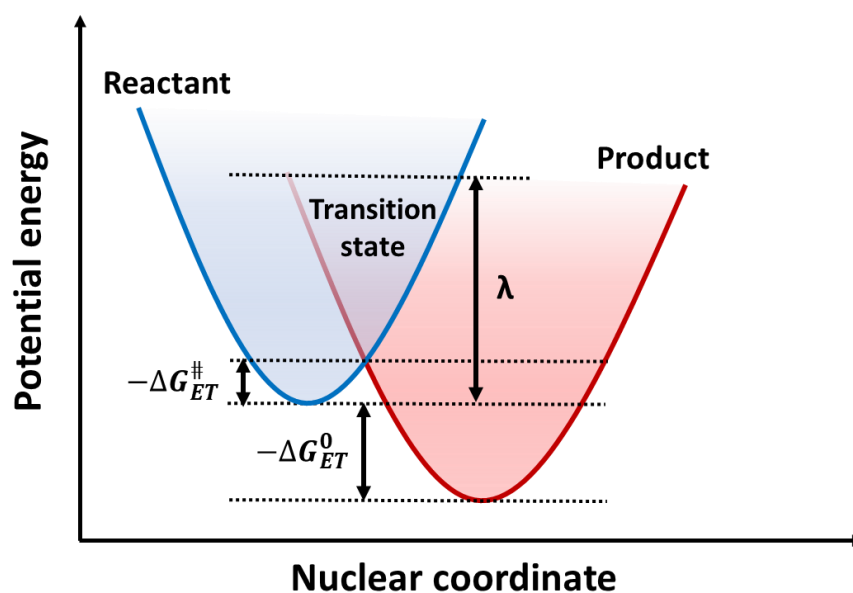
Figure 1.10: Potential energy vs. nuclear coordinate plot for an electron transfer reaction between a donor and an acceptor, where the reactant is donor-acceptor complex and the product is the charge separated complex.
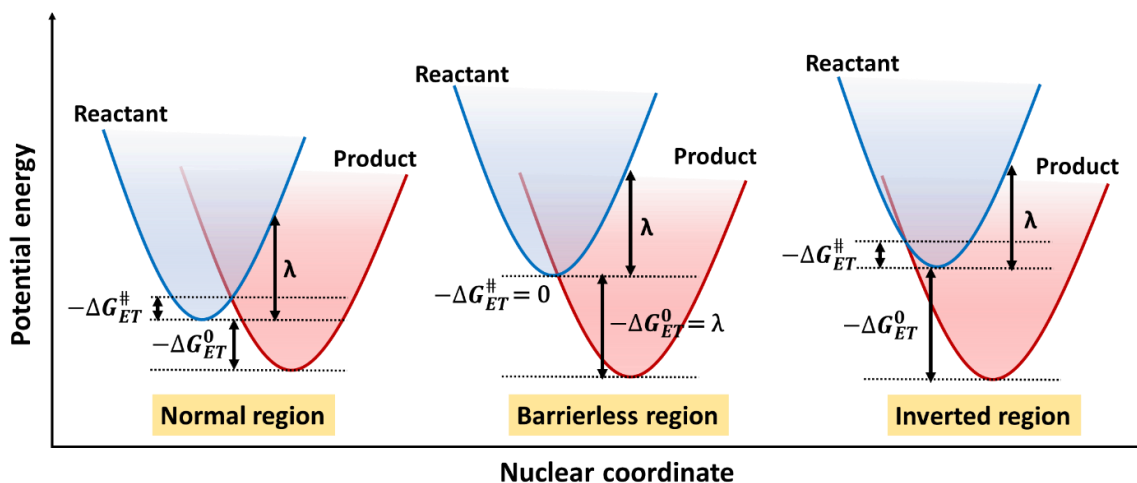
Figure 1.11: Plot of potential energy vs. nuclear coordinate for three different Marcus regions.

Based on the values of ΔG_{ET}^0 and λ, three regions can be recognized in a non-adiabatic scenario[101]:

(i) Normal region: $-\Delta G_{ET}^0 < \lambda$; Electron transfer rate increases with the increment of $-\Delta G_{ET}^0$.

(ii) Barrierless region: $-\Delta G_{ET}^0 = \lambda$; Electron transfer activation energy ΔG_{ET}^0 is zero here.

(iii) Inverted region: $-\Delta G_{ET}^0 > \lambda$; Electron transfer rate decreases with the increment of $-\Delta G_{ET}^0$.
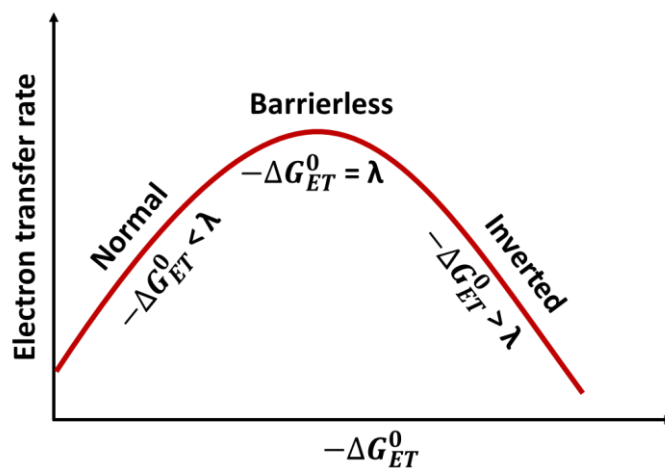
Figure 1.12: Dependence of electron transfer rate on the Gibbs free energy change of a reaction.

In adiabatic scenario, Marcus-Hush equation in utilized in place of simple Marcus equation,

$$k_{ET} = \frac{2\Pi}{\hbar} \left| H_{DA}^2 \right| \frac{1}{\sqrt{4\lambda k_B T}} \exp \frac{\left(\lambda + \Delta G_{ET}^0\right)^2}{4\lambda k_B T}$$

Here, H_{DA} is the electronic coupling of the donor and acceptor wave functions. This H_{DA} value decides whether the reaction will be adiabatic ($|H_{DA}| >> k_BT$) or non-adiabatic ($|H_{DA}| < k_BT$).

1.6. Thesis overview

In the present thesis, we have studied different 2D metal chalcogenide systems with the help of TAS, in order to investigate the intrinsic photophysical characteristics in these materials. We have further extended our study on the modulated charge carrier behaviour of these 2D materials, while being doped with novel elements or in contact with a metal or some other semiconductor. For the preparation of these materials many different synthetic approaches were adopted, like chemical vapour deposition (CVD), liquid exfoliation, solvothermal method, hot injection etc. These synthesized materials were characterized using many different techniques, like X-ray diffraction (XRD), Raman spectroscopy and X-ray photoelectron spectroscopy (XPS), used in case-to-case basis. Transmission electron microscopy (TEM) and High-resolution TEM (HRTEM) were employed to realise the morphology of these materials, and for establishing the existence of any intimate contact between two systems in a hetero-composite. Atomic force microscopy (AFM) helped in determining the thickness of these 2D architectures. The ground state optical behaviour of these materials was explored using steady state absorption and photoluminescence (PL) spectroscopy. Finally, detailed exploration of ultrafast photophysical processes were monitored through TAS. The first chapter gives the glimpses of these works discussing the background and possibilities of these materials, as well as TAS technique. In the second chapter, we have discussed synthesis and instrumental techniques in detail.

The third chapter is consisted with the formation and relaxation dynamics of exciton and trionic features in CVD synthesized monolayer MoS_2 flakes, at room temperature. Steady state PL measurements confirmed the presence of Characteristic A and B exciton of MoS_2, as well as negatively charged A^- trion in the system. Large exciton and trion binding energy made it possible, to observe these features even at room temperature. From the FTAS measurements, the exciton and trion formation time was calculated to be ~ 0.5 ps and ~ 1.2 ps, respectively. Subsequently, these quasiparticles decay with exciton-exciton annihilation or auger recombination processes. Further, we drop-casted Au nanoparticles (NPs) on top of monolater MoS_2 in order to fabricate a metal-semiconductor (Au-MoS_2) heterojunction. Au NPs act as a sink of electrons, as the Au fermi level reside way below the MoS_2 conduction band level.

In the fourth chapter, we have discussed the study of four different non-hydrogenic excitonic features in few layer WS_2. The WS_2 nanosheets were synthesized using liquid exfoliation technique, which were having 5-6 layers. Steady state absorption spectroscopy and FTAS study revealed the formation of A, B, C and D excitons in this layered material, irrespective of the excitation energy. Among which, A, B originate at the K/K' region and C, D form at the Λ-Γ region of the electronic band structure. This decides their formation and relaxation dynamics and influence the optical properties of this material. C, D excitons decay in a much slower manner than that of A, B, mainly because of Pauli blocking effect at the K valley and Subsequent Λ-Γ indirect recombination channel. This slower decay of high energy excitons provides us a unique opportunity to extract these hot charge carriers for the betterment of an opto-electronic device.

The fifth chapter is based on a ternary chalcogenide system, Cu_2MoS_4 (CMS), which showed great potential towards photovoltaic as well as photocatalytic applications lately. However, optical properties of this material are almost unexplored. Raman spectroscopy unveils the presence of very strong electron-phonon (e-ph) coupling in this material. The PL spectrum is comprised of two broad peaks, origination from the radiative recombinations from the band edge and near band edge trap states, respectively. In FTAS, we probed the band edge excitons and found that they are strongly influenced by both the trap mediated recombination and the Auger recombination. The saturation density of the material lies in the range of $5.3 \pm 0.7 \times 10^{14}$ photons/cm^2, beyond which Auger process predominates. The e-ph coupling strength reaches maximum at around 100K, which was emphasized in faster decay dynamics of the CMS exciton in this temperature region. The band gap as well jumps as we approach lower temperature. This detailed spectroscopic investigation would be helpful in implementing CMS like ternary chalcogenides in diverse photonic applications.

Finally, in the sixth and seventh chapter, we have employed FTAS in studying two modified 2D systems, a CdS/MoS_2 heterojunction and non-metal doped ZIS nanosheets. CdS/MoS_2 is a unique heterojunction, where 1D CdS nanorods are in close contact with 2D MoS_2 sheets. Here, MoS_2 works as a hot electron extractor. Upon photoexcitation, CdS hot charge carriers preferentially move toward the MoS_2 region. The hot carrier transfer rate was found to be much higher than the band edge transfer. This superiority of hot carrier transfer is a great sign for an opto-electronic device. In the other system, thin ZIS nanosheets are separately doped with 'O' and 'N' and their H_2 evolution efficiencies were correlated with the modulated charge carrier

dynamics. The doped nanosheets proved to be better photocatalysts, owing their modified energy band structure and enhanced charge carrier separation. FTAS unveiled that, the H_2 evolution reaction in ZIS takes place in the near band edge trap states, not in the conduction band. This study will help in understanding the H_2 evolution process and designing more photocatalytic materials like ZIS.

In the last chapter we have added a summarized discussion of all these studies with a detailed future perspective.

1.7. References

(1)   Novoselov, K. S.; Geim, A. K.; Morozov, S. V; Jiang, D.; Zhang, Y.; Dubonos, S. V; Grigorieva, I. V; Firsov, A. A. Electric Field Effect in Atomically Thin Carbon Films. *Science* **2004**, *306* (5696), 666–669.

(2)   Bonaccorso, F.; Sun, Z.; Hasan, T.; Ferrari, A. C. Graphene Photonics and Optoelectronics. *Nat Photonics* **2010**, *4* (9), 611-622.

(3)   Mayorov, A. S.; Gorbachev, R. V; Morozov, S. V; Britnell, L.; Jalil, R.; Ponomarenko, L. A.; Blake, P.; Novoselov, K. S.; Watanabe, K.; Taniguchi, T.; et al. Micrometer-Scale Ballistic Transport in Encapsulated Graphene at Room Temperature. *Nano Lett* **2011**, *11* (6), 2396-2399.

(4)   Huang, W.; Hu, L.; Tang, Y.; Xie, Z.; Zhang, H. Recent Advances in Functional 2D MXene-Based Nanostructures for Next-Generation Devices. *Adv Funct Mater* **2020**, *30* (49), 2005223.

(5)   Wei, Y.; Zhang, P.; Soomro, R. A.; Zhu, Q.; Xu, B. Advances in the Synthesis of 2D MXenes. *Adv Mater* **2021**, *33* (39), 2103148.

(6)   Balandin, A. A.; Ghosh, S.; Bao, W.; Calizo, I.; Teweldebrhan, D.; Miao, F.; Lau, C. N. Superior Thermal Conductivity of Single-Layer Graphene. *Nano Lett* **2008**, *8* (3), 902-907.

(7)   Papageorgiou, D. G.; Kinloch, I. A.; Young, R. J. Mechanical Properties of Graphene and Graphene-Based Nanocomposites. *Prog Mater Sci* **2017**, *90*, 75-127.

(8)   Jie, W.; Yang, Z.; Bai, G.; Hao, J. Luminescence in 2D Materials and van Der Waals Heterostructures. *Adv Opt Mater* **2018**, *6* (10), 1701296.

(9)   Mak, K. F.; Shan, J. Photonics and Optoelectronics of 2D Semiconductor Transition Metal Dichalcogenides. *Nat Photonics* **2016**, *10* (4), 216-226.

(10)   Tan, C.; Cao, X.; Wu, X.-J.; He, Q.; Yang, J.; Zhang, X.; Chen, J.; Zhao, W.; Han, S.; Nam, G.-H.; et al. Recent Advances in Ultrathin Two-Dimensional Nanomaterials. *Chem Rev* **2017**, *117* (9), 6225-6331.

(11)   Lv, R.; Robinson, J. A.; Schaak, R. E.; Sun, D.; Sun, Y.; Mallouk, T. E.; Terrones, M. Transition Metal Dichalcogenides and Beyond: Synthesis, Properties, and Applications of Single- and Few-Layer Nanosheets. *Acc Chem Res* **2015**, *48* (1), 56-64.

(12)   Mao, N.; Zhang, S.; Wu, J.; Tian, H.; Wu, J.; Xu, H.; Peng, H.; Tong, L.; Zhang, J. Investigation of Black Phosphorus as a Nano-Optical Polarization Element by Polarized Raman Spectroscopy. *Nano Res* **2018**, *11* (6), 3154-3163.

(13)   Zhang, J. L.; Han, C.; Hu, Z.; Wang, L.; Liu, L.; Wee, A. T. S.; Chen, W. 2D Phosphorene: Epitaxial Growth and Interface Engineering for Electronic Devices. *Adv Mater* **2018**, *30* (47), 1802207.

(14)   Wang, Q. H.; Kalantar-Zadeh, K.; Kis, A.; Coleman, J. N.; Strano, M. S. Electronics and Optoelectronics of Two-Dimensional Transition Metal Dichalcogenides. *Nat Nanotechnol* **2012**, *7* (11), 699- 712.

(15)   Zhang, H. Ultrathin Two-Dimensional Nanomaterials. *ACS Nano* **2015**, *9* (10), 9451-9469.

(16)   Chaves, A.; Azadani, J. G.; Alsalman, H.; da Costa, D. R.; Frisenda, R.; Chaves, A. J.; Song, S. H.; Kim, Y. D.; He, D.; Zhou, J.; et al. Bandgap Engineering of Two-Dimensional Semiconductor Materials. *npj 2D Mater Appl* **2020**, *4* (1), 29.

(17)   Mak, K. F.; He, K.; Lee, C.; Lee, G. H.; Hone, J.; Heinz, T. F.; Shan, J. Tightly Bound Trions in Monolayer MoS_2. *Nat Mater* **2013**, *12* (3), 207-211.

(18)   Kajale, S. N.; Yadav, S.; Cai, Y.; Joy, B.; Sarkar, D. 2D Material Based Field Effect Transistors and Nanoelectromechanical Systems for Sensing Applications. *iScience* **2021**, *24* (12), 103513.

(19)   Subbanna, B. B.; Choudhary, K.; Singh, S.; Kumar, S. 2D Material-Based Optical Sensors: A Review. *ISSS J Micro Smart Syst* **2022**, *11* (1), 169–177.

(20)   Kim, K. S.; Zhao, Y.; Jang, H.; Lee, S. Y.; Kim, J. M.; Kim, K. S.; Ahn, J.-H.; Kim, P.; Choi, J.-Y.; Hong, B. H. Large-Scale Pattern Growth of Graphene Films for Stretchable Transparent Electrodes. *Nature* **2009**, *457* (7230), 706-710.

(21)   Zhu, Y.; Murali, S.; Cai, W.; Li, X.; Suk, J. W.; Potts, J. R.; Ruoff, R. S. Graphene and Graphene Oxide: Synthesis, Properties, and Applications. *Adv Mater* **2010**, *22* (35), 3906-3924.

(22)   Ma, C.; Wang, C.; Gao, B.; Adams, J.; Wu, G.; Zhang, H. Recent Progress in Ultrafast Lasers Based on 2D Materials as a Saturable Absorber. *Appl Phys Rev* **2019**, *6* (4), 41304.

(23)   Wang, G.; Zhang, Y.; You, C.; Liu, B.; Yang, Y.; Li, H.; Cui, A.; Liu, D.; Yan, H. Two Dimensional Materials Based Photodetectors. *Infrared Phys Technol* **2018**, *88*, 149-173.

(24)   Goswami, T.; Bhatt, H.; Yadav, D. K.; Ghosh, H. N. Atomically Thin 2D Photocatalysts for Boosted H_2 Production from the Perspective of Transient Absorption Spectroscopy. *Phys Chem Chem Phys* **2022**, *24* (32), 19121-19143.

(25)   Novoselov, K. S.; Geim, A. K.; Morozov, S. V; Jiang, D.; Katsnelson, M. I.; Grigorieva, I. V; Dubonos, S. V; Firsov, A. A. Two-Dimensional Gas of Massless Dirac Fermions in Graphene. *Nature* **2005**, *438* (7065), 197-200.

(26)   Wang, F.; Wang, Z.; Wang, Q.; Wang, F.; Yin, L.; Xu, K.; Huang, Y.; He, J. Synthesis, Properties and Applications of 2D Non-Graphene Materials. *Nanotechnology* **2015**, *26* (29), 292001.

(27)   Lu, G.; Yu, K.; Wen, Z.; Chen, J. Semiconducting Graphene: Converting Graphene from Semimetal to Semiconductor. *Nanoscale* **2013**, *5* (4), 1353-1368.

(28)   Zhan, D.; Yan, J.; Lai, L.; Ni, Z.; Liu, L.; Shen, Z. Engineering the Electronic Structure of Graphene. *Adv Mater* **2012**, *24* (30), 4055-4069.

(29)   Xia, F.; Farmer, D. B.; Lin, Y.; Avouris, P. Graphene Field-Effect Transistors with High On/Off Current Ratio and Large Transport Band Gap at Room Temperature. *Nano Lett* **2010**, *10* (2), 715-718.

(30)   Zhang, S. J.; Lin, S. S.; Li, X. Q.; Liu, X. Y.; Wu, H. A.; Xu, W. L.; Wang, P.; Wu, Z. Q.; Zhong, H. K.; Xu, Z. J. Opening the Band Gap of Graphene through Silicon Doping

for the Improved Performance of Graphene/GaAs Heterojunction Solar Cells. *Nanoscale* **2016**, *8* (1), 226-232.

(31)   Balog, R.; Jørgensen, B.; Nilsson, L.; Andersen, M.; Rienks, E.; Bianchi, M.; Fanetti, M.; Lægsgaard, E.; Baraldi, A.; Lizzit, S.; et al. Bandgap Opening in Graphene Induced by Patterned Hydrogen Adsorption. *Nat Mater* **2010**, *9* (4), 315-319.

(32)   Han, M. Y.; Özyilmaz, B.; Zhang, Y.; Kim, P. Energy Band-Gap Engineering of Graphene Nanoribbons. *Phys Rev Lett* **2007**, *98* (20), 206805.

(33)   Zhang, Y.; Tang, T.-T.; Girit, C.; Hao, Z.; Martin, M. C.; Zettl, A.; Crommie, M. F.; Shen, Y. R.; Wang, F. Direct Observation of a Widely Tunable Bandgap in Bilayer Graphene. *Nature* **2009**, *459* (7248), 820-823.

(34)   Hu, C.-X.; Shin, Y.; Read, O.; Casiraghi, C. Dispersant-Assisted Liquid-Phase Exfoliation of 2D Materials beyond Graphene. *Nanoscale* **2021**, *13* (2), 460-484.

(35)   Geng, D.; Yang, H. Y. Recent Advances in Growth of Novel 2D Materials: Beyond Graphene and Transition Metal Dichalcogenides. *Adv Mater* **2018**, *30* (45), 1800865.

(36)   Bhimanapati, G. R.; Lin, Z.; Meunier, V.; Jung, Y.; Cha, J.; Das, S.; Xiao, D.; Son, Y.; Strano, M. S.; Cooper, V. R.; et al. Recent Advances in Two-Dimensional Materials beyond Graphene. *ACS Nano* **2015**, *9* (12), 11509-11539.

(37)   Gupta, A.; Sakthivel, T.; Seal, S. Recent Development in 2D Materials beyond Graphene. *Prog Mater Sci* **2015**, *73*, 44-126.

(38)   Li, J.; Guo, C.; Li, C. M. Recent Advances of Two-Dimensional (2D) MXenes and Phosphorene for High-Performance Rechargeable Batteries. *ChemSusChem* **2020**, *13* (6), 1047-1070.

(39)   Zhang, M.; Biesold, G. M.; Lin, Z. A Multifunctional 2D Black Phosphorene-Based Platform for Improved Photovoltaics. *Chem Soc Rev* **2021**, *50* (23), 13346-13371.

(40)   Ren, J.; Innocenzi, P. 2D Boron Nitride Heterostructures: Recent Advances and Future Challenges. *Small Struct* **2021**, *2* (11), 2100068.

(41)   Yang, T.; Song, T. T.; Callsen, M.; Zhou, J.; Chai, J. W.; Feng, Y. P.; Wang, S. J.; Yang, M. Atomically Thin 2D Transition Metal Oxides: Structural Reconstruction, Interaction with Substrates, and Potential Applications. *Adv Mater Interfaces* **2019**, *6* (1), 1801160.

(42)   Alidoust, N.; Bian, G.; Xu, S.-Y.; Sankar, R.; Neupane, M.; Liu, C.; Belopolski, I.; Qu, D.-X.; Denlinger, J. D.; Chou, F.-C.; et al. Observation of Monolayer Valence Band Spin-Orbit Effect and Induced Quantum Well States in MoX2. *Nat Commun* **2014**, *5* (1), 4673.

(43)   Splendiani, A.; Sun, L.; Zhang, Y.; Li, T.; Kim, J.; Chim, C.-Y.; Galli, G.; Wang, F. Emerging Photoluminescence in Monolayer MoS_2. *Nano Lett* **2010**, *10* (4), 1271-1275.

(44)   Bellus, M. Z.; Ceballos, F.; Chiu, H.-Y.; Zhao, H. Tightly Bound Trions in Transition Metal Dichalcogenide Heterostructures. *ACS Nano* **2015**, *9* (6), 6459-6464.

(45)   Xiao, J.; Zhao, M.; Wang, Y.; Zhang, X. Excitons in Atomically Thin 2D Semiconductors and Their Applications. *Nanophotonics* **2017**, *6* (6), 1309-1328.

(46)   Al-Ani, I. A. M.; As'ham, K.; Klochan, O.; Hattori, H. T.; Huang, L.; Miroshnichenko, A. E. Recent Advances on Strong Light-Matter Coupling in Atomically Thin TMDC Semiconductor Materials. *J Opt* **2022**, *24* (5), 53001.

(47)   Huang, L.; Krasnok, A.; Alú, A.; Yu, Y.; Neshev, D.; Miroshnichenko, A. E. Enhanced Light–Matter Interaction in Two-Dimensional Transition Metal Dichalcogenides. *Reports Prog Phys* **2022**, *85* (4), 46401.

(48)   Hanbicki, A. T.; Kioseoglou, G.; Currie, M.; Hellberg, C. S.; McCreary, K. M.; Friedman, A. L.; Jonker, B. T. Anomalous Temperature-Dependent Spin-Valley Polarization in Monolayer WS_2. *Sci Rep* **2016**, *6* (1), 18885.

(49)   Nayak, P. K.; Lin, F.-C.; Yeh, C.-H.; Huang, J.-S.; Chiu, P.-W. Robust Room Temperature Valley Polarization in Monolayer and Bilayer WS_2. *Nanoscale* **2016**, *8* (11), 6035-6042.

(50)   Li, W.-F.; Fang, C.; van Huis, M. A. Strong Spin-Orbit Splitting and Magnetism of Point Defect States in Monolayer WS_2. *Phys Rev B* **2016**, *94* (19), 195425.

(51)   Ramalingam, G.; Kathirgamanathan, P.; Ravi, G.; Elangovan, T.; kumar, B. A.; Manivannan, N.; Kasinathan, K. Quantum Confinement Effect of 2D Nanomaterials; Divsar, F., Ed.; IntechOpen: Rijeka, 2020; p Ch. 2.

(52)   Brus, L. E. Electron–Electron and Electron-hole Interactions in Small Semiconductor Crystallites: The Size Dependence of the Lowest Excited Electronic State. *J Chem Phys*

1984, *80* (9), 4403-4409.

(53)   Billaud, B.; Truong, T. T. Quantum Properties of Spherical Semiconductor Quantum Dots. *arXiv Mesoscale Nanoscale Phys* **2012**.

(54)   Savina, M. R.; Lohr, L. L.; Francis, A. H. A Particle-on-a-Sphere Model for C_{60}. *Chem Phys Lett* **1993**, *205* (2), 200-206.

(55)   Frenkel, J. On the Transformation of Light into Heat in Solids. I. *Phys Rev* **1931**, *37* (1), 17-44.

(56)   Acharya, S.; Pashov, D.; Rudenko, A. N.; Rösner, M.; Schilfgaarde, M. van; Katsnelson, M. I. Real- and Momentum-Space Description of the Excitons in Bulk and Monolayer Chromium Tri-Halides. *npj 2D Mater Appl* **2022**, *6* (1), 33.

(57)   Norris, D. J.; Bawendi, M. G. Measurement and Assignment of the Size-Dependent Optical Spectrum in CdSe Quantum Dots. *Phys Rev B* **1996**, *53* (24), 16338-16346.

(58)   Efros, A. L.; Rosen, M. The Electronic Structure of Semiconductor Nanocrystals. *Annu Rev Mater Sci* **2000**, *30* (1), 475-521.

(59)   Ceballos, F.; Cui, Q.; Bellus, M. Z.; Zhao, H. Exciton Formation in Monolayer Transition Metal Dichalcogenides. *Nanoscale* **2016**, *8* (22), 11681-11688.

(60)   Nie, Z.; Long, R.; Sun, L.; Huang, C.-C.; Zhang, J.; Xiong, Q.; Hewak, D. W.; Shen, Z.; Prezhdo, O. V; Loh, Z.-H. Ultrafast Carrier Thermalization and Cooling Dynamics in Few-Layer MoS2. *ACS Nano* **2014**, *8* (10), 10931-10940.

(61)   Ceballos, F.; Zhao, H. Ultrafast Laser Spectroscopy of Two-Dimensional Materials Beyond Graphene. *Adv Funct Mater* **2017**, *27* (19), 1604509.

(62)   Chernikov, A.; Berkelbach, T. C.; Hill, H. M.; Rigosi, A.; Li, Y.; Aslan, B.; Reichman, D. R.; Hybertsen, M. S.; Heinz, T. F. Exciton Binding Energy and Nonhydrogenic Rydberg Series in Monolayer WS$_2$. *Phys Rev Lett* **2014**, *113* (7), 76802.

(63)   Ye, Z.; Cao, T.; O'Brien, K.; Zhu, H.; Yin, X.; Wang, Y.; Louie, S. G.; Zhang, X. Probing Excitonic Dark States in Single-Layer Tungsten Disulphide. *Nature* **2014**, *513* (7517), 214-218.

(64)   Sun, D.; Rao, Y.; Reider, G. A.; Chen, G.; You, Y.; Brézin, L.; Harutyunyan, A. R.;

Heinz, T. F. Observation of Rapid Exciton–Exciton Annihilation in Monolayer Molybdenum Disulfide. *Nano Lett* **2014**, *14* (10), 5625-5629.

(65) Linardy, E.; Yadav, D.; Vella, D.; Verzhbitskiy, I. A.; Watanabe, K.; Taniguchi, T.; Pauly, F.; Trushin, M.; Eda, G. Harnessing Exciton–Exciton Annihilation in Two-Dimensional Semiconductors. *Nano Lett* **2020**, *20* (3), 1647-1653.

(66) McGehee, M. D.; Heeger, A. J. Semiconducting (Conjugated) Polymers as Materials for Solid-State Lasers. *Adv Mater* **2000**, *12* (22), 1655-1668.

(67) Lüer, L.; Hoseinkhani, S.; Polli, D.; Crochet, J.; Hertel, T.; Lanzani, G. Size and Mobility of Excitons in (6, 5) Carbon Nanotubes. *Nat Phys* **2009**, *5* (1), 54-58.

(68) Yuan, L.; Huang, L. Exciton Dynamics and Annihilation in WS_2 2D Semiconductors. *Nanoscale* **2015**, *7* (16), 7402-7408.

(69) Pietryga, J. M.; Park, Y.-S.; Lim, J.; Fidler, A. F.; Bae, W. K.; Brovelli, S.; Klimov, V. I. Spectroscopic and Device Aspects of Nanocrystal Quantum Dots. *Chem Rev* **2016**, *116* (18), 10513-10622.

(70) Poellmann, C.; Steinleitner, P.; Leierseder, U.; Nagler, P.; Plechinger, G.; Porer, M.; Bratschitsch, R.; Schüller, C.; Korn, T.; Huber, R. Resonant Internal Quantum Transitions and Femtosecond Radiative Decay of Excitons in Monolayer WSe_2. *Nat Mater* **2015**, *14* (9), 889-893.

(71) Kambhampati, P. Hot Exciton Relaxation Dynamics in Semiconductor Quantum Dots: Radiationless Transitions on the Nanoscale. *J Phys Chem C* **2011**, *115* (45), 22089-22109.

(72) Narvaez, G. A.; Bester, G.; Zunger, A. Carrier Relaxation Mechanisms in Self-Assembled (In, Ga) As / GaAs Quantum Dots: Efficient P to S Auger Relaxation of Electrons. *Phys Rev B* **2006**, *74* (7), 75403.

(73) Klimov, V. I. Spectral and Dynamical Properties of Multiexcitons in Semiconductor Nanocrystals. *Annu Rev Phys Chem* **2007**, *58* (1), 635-673.

(74) Rabouw, F. T.; de Mello Donega, C. Excited-State Dynamics in Colloidal Semiconductor Nanocrystals. *Top Curr Chem* **2016**, *374* (5), 58.

(75) Sambur, J. B.; Novet, T.; Parkinson, B. A. Multiple Exciton Collection in a Sensitized

Photovoltaic System. *Science* **2010**, *330* (6000), 63-66.

(76) Ellingson, R. J.; Beard, M. C.; Johnson, J. C.; Yu, P.; Micic, O. I.; Nozik, A. J.; Shabaev, A.; Efros, A. L. Highly Efficient Multiple Exciton Generation in Colloidal PbSe and PbS Quantum Dots. *Nano Lett* **2005**, *5* (5), 865-871.

(77) Chowdhury, T.; Paul, D.; Nechiyil, D.; M A, G.; Watanabe, K.; Taniguchi, T.; Kumar, G. V. P.; Rahman, A. Modulation of Trion and Exciton Formation in Monolayer WS_2 by Dielectric and Substrate Engineering. *2D Mater* **2021**, *8* (4), 45032.

(78) Singh, A.; Moody, G.; Tran, K.; Scott, M. E.; Overbeck, V.; Berghäuser, G.; Schaibley, J.; Seifert, E. J.; Pleskot, D.; Gabor, N. M.; et al. Trion Formation Dynamics in Monolayer Transition Metal Dichalcogenides. *Phys Rev B* **2016**, *93* (4), 41401.

(79) Klimov, V. I.; Mikhailovsky, A. A.; McBranch, D. W.; Leatherdale, C. A.; Bawendi, M. G. Quantization of Multiparticle Auger Rates in Semiconductor Quantum Dots. *Science* **2000**, *287* (5455), 1011-1013.

(80) Park, Y.-S.; Bae, W. K.; Pietryga, J. M.; Klimov, V. I. Auger Recombination of Biexcitons and Negative and Positive Trions in Individual Quantum Dots. *ACS Nano* **2014**, *8* (7), 7288-7296.

(81) Di, J.; Xiong, J.; Li, H.; Liu, Z. Ultrathin 2D Photocatalysts: Electronic-Structure Tailoring, Hybridization, and Applications. *Adv Mater* **2018**, *30* (1), 1704548.

(82) Lei, F.; Zhang, L.; Sun, Y.; Liang, L.; Liu, K.; Xu, J.; Zhang, Q.; Pan, B.; Luo, Y.; Xie, Y. Atomic-Layer-Confined Doping for Atomic-Level Insights into Visible-Light Water Splitting. *Angew Chemie Int Ed* **2015**, *54* (32), 9266-9270.

(83) Chen, Z.; Jiang, X.; Zhu, C.; Shi, C. Chromium-Modified Bi4Ti3O12 Photocatalyst: Application for Hydrogen Evolution and Pollutant Degradation. *Appl Catal B Environ* **2016**, *199*, 241-251.

(84) Li, Y.; Wang, Z.; Xia, T.; Ju, H.; Zhang, K.; Long, R.; Xu, Q.; Wang, C.; Song, L.; Zhu, J.; et al. Implementing Metal-to-Ligand Charge Transfer in Organic Semiconductor for Improved Visible-Near-Infrared Photocatalysis. *Adv Mater* **2016**, *28* (32), 6959-6965.

(85) Du, C.; Yan, B.; Lin, Z.; Yang, G. Enhanced Carrier Separation and Increased Electron Density in 2D Heavily N-Doped $ZnIn_2S_4$ for Photocatalytic Hydrogen Production. *J*

Mater Chem A **2020**, *8* (1), 207-217.

(86)   Jing, L.; Zhu, R.; Phillips, D. L.; Yu, J. C. Effective Prevention of Charge Trapping in Graphitic Carbon Nitride with Nanosized Red Phosphorus Modification for Superior Photo(Electro)Catalysis. *Adv Funct Mater* **2017**, *27* (46), 1703484.

(87)   Goswami, T.; Yadav, D. K.; Bhatt, H.; Kaur, G.; Shukla, A.; Babu, K. J.; Ghosh, H. N. Defect-Mediated Slow Carrier Recombination and Broad Photoluminescence in Non-Metal-Doped $ZnIn_2S_4$ Nanosheets for Enhanced Photocatalytic Activity. *J Phys Chem Lett* **2021**, *12* (20), 5000-5008.

(88)   Goswami, T.; Bhatt, H.; Yadav, D. K.; Ghosh, H. N. Interfacing $g-C_3N_4$ Nanosheets with CdS Nanorods for Enhanced Photocatalytic Hydrogen Evolution: An Ultrafast Investigation. *J Phys Chem B* **2022**, *126* (2), 572-580.

(89)   Liang, J.; Yang, X.; Fu, H.; Ran, X.; Zhao, C.; An, X. Integrating Optimal Amount of Carbon Dots in $g-C_3N_4$ for Enhanced Visible Light Photocatalytic H_2 Evolution. *Int J Hydrogen Energy* **2022**, *47* (41), 18032-18043.

(90)   Zhu, C.; Wang, Y.; Jiang, Z.; Xu, F.; Xian, Q.; Sun, C.; Tong, Q.; Zou, W.; Duan, X.; Wang, S. CeO_2 Nanocrystal-Modified Layered $MoS_2/g-C_3N_4$ as 0D/2D Ternary Composite for Visible-Light Photocatalytic Hydrogen Evolution: Interfacial Consecutive Multi-Step Electron Transfer and Enhanced H_2O Reactant Adsorption. *Appl Catal B Environ* **2019**, *259*, 118072.

(91)   He, Z.; Zhang, J.; Li, X.; Guan, S.; Dai, M.; Wang, S. 1D/2D Heterostructured Photocatalysts: From Design and Unique Properties to Their Environmental Applications. *Small* **2020**, *16* (46), 2005051.

(92)   Li, J.; Zhao, L.; Wang, S.; Li, J.; Wang, G.; Wang, J. In Situ Fabrication of 2D/3D $g-C_3N_4/Ti_3C_2$ (MXene) Heterojunction for Efficient Visible-Light Photocatalytic Hydrogen Evolution. *Appl Surf Sci* **2020**, *515*, 145922.

(93)   Qin, Y.; Li, H.; Lu, J.; Feng, Y.; Meng, F.; Ma, C.; Yan, Y.; Meng, M. Synergy between van Der Waals Heterojunction and Vacancy in $ZnIn_2S_4/g-C_3N_4$ 2D/2D Photocatalysts for Enhanced Photocatalytic Hydrogen Evolution. *Appl Catal B Environ* **2020**, *277*, 119254.

(94)   Liu, X.; Zhang, Q.; Ma, D. Advances in 2D/2D Z-Scheme Heterojunctions for

Photocatalytic Applications. *Sol RRL* **2021**, *5* (2), 2000397.

(95) Tan, S.; Argondizzo, A.; Ren, J.; Liu, L.; Zhao, J.; Petek, H. Plasmonic Coupling at a Metal/Semiconductor Interface. *Nat Photonics* **2017**, *11* (12), 806-812.

(96) Wu, N. Plasmonic Metal–Semiconductor Photocatalysts and Photoelectrochemical Cells: A Review. *Nanoscale* **2018**, *10* (6), 2679-2696.

(97) Goswami, T.; Bhatt, H.; Yadav, D. K.; Saha, R.; Babu, K. J.; Ghosh, H. N. Probing Ultrafast Hot Charge Carrier Migration in MoS_2 Embedded CdS Nanorods. *J Chem Phys* **2021**, *156* (3), 34704.

(98) Goswami, T.; Rani, R.; Hazra, K. S.; Ghosh, H. N. Ultrafast Carrier Dynamics of the Exciton and Trion in MoS_2 Monolayers Followed by Dissociation Dynamics in Au@MoS_2 2D Heterointerfaces. *J Phys Chem Lett* **2019**, 3057-3063.

(99) Marcus, R. A. Electrostatic Free Energy and Other Properties of States Having Nonequilibrium Polarization. I. *J Chem Phys* **1956**, *24* (5), 979-989.

(100) Hsu, C.-P.; Hammarström, L.; Newton, M. D. 65 Years of Electron Transfer. *J Chem Phys* **2022**, *157* (2), 20401.

(101) Piechota, E. J.; Meyer, G. J. Introduction to Electron Transfer: Theoretical Foundations and Pedagogical Examples. *J Chem Educ* **2019**, *96* (11), 2450-2466.

Chapter 2

Synthesis and instrumentation

This chapter comprises all the synthetic procedures adopted and instrumental techniques utilized to carry out my thesis work. Special attention was given to transient absorption spectroscopy technique. We have employed a wide variety of synthesis procedures for the preparation of 2D materials and their heterojunctions, like chemical vapour deposition (CVD), liquid exfoliation, solvothermal method, hot injection synthesis etc. Detailed mechanisms of these procedures are discussed in the Introduction chapter. The basic characterisation of these materials was carried out employing X-ray diffraction (XRD), Raman spectroscopy and X-ray photoelectron spectroscopy (XPS), used in case-to-case basis. Transmission electron microscopy (TEM) was employed to realise the morphology of these materials, also for establishing the existence of any intimate contact between two systems in a hetero-composite. Atomic force microscopy (AFM) helped in elucidating thickness of these 2D architectures. The ground state optical behaviour of these materials was explored using steady state absorption and photoluminescence (PL) spectroscopy. Finally, detailed exploration of ultrafast photophysical processes were investigated using TA spectroscopy.

2.1. Synthesis techniques

2.1.1. Chemicals used in different synthesis procedures

Cadmium acetate dihydrate ($Cd(ac)_2.2H_2O$), bulk MoS_2 powder, Ascorbic acid, Sulphur (S) powder, bulk WS_2 powder, N-Methyl-2-Pyrrolidone (NMP), Zinc chloride ($ZnCl_2$), indium chloride ($InCl_3$), thioacetamide (TAA), polyvinyl pyrrolidine (PVP), N, N-dimethyl formamide (DMF), Di-Methyl Sulphoxide (DMSO), Copper (II) chloride ($CuCl_2$), sodium molybdate ($Na_2MoO_4.2H_2O$), thioacetamide (C_2H_5NS) (TAA), and ethylene glycol were purchased from Sigma Aldrich, India. MoO_3 powder was bought from Alfa Aesar. Thiourea was purchased from CDH, India. Ethylenediamine (EN) was purchased from Chemigeno, India. Triethanol amine was purchased from SRL, India. Analytical grade methanol, toluene, and inorganic acids (HCl, HNO_3) were purchased from Rankem for cleaning purpose. The deionized water (resistivity of 18 $M\Omega.cm$) was collected from a Millipore Milli-Q system.

2.1.2. Chemical vapour deposition

Chemical vapour deposition (CVD) is a thin film coating technique where the deposition initiates with the succession of few chemical reactions.[1,2] It is very different from the physical vapor deposition (PVD) techniques like, thermal evaporation, e-beam deposition, sputtering etc., where atoms or molecules are condensed on top of substrates following being evaporated, bombarded, or sputtered.[3,4] In case of CVD, the deposition completely relies on the chemical reactions, which obviously depend on many factors like pressure, temperature, mass flow etc. This brings in a clear advantage over the PVD techniques, as now we can control the deposition processes more efficiently.[3,5] CVD offers extensive tuning in the structure and properties of the deposited materials. Presently, it is considered to be one of the finest techniques available for the coating of highly crystalline materials on top of a heated substrate, via gaseous phase reaction of precursor substances. It is being widely used in the deposition of enormous low-dimensional materials like, graphene, TMDC, carbon nanotubes (CNT) etc.[6–9]

The basic principle of a CVD process stands on the gas phase chemical reactions at high temperature.[2] It is comprised of few elementary steps occurring inside the reaction tube, which is made of Quartz or Alumina in most cases.

(i) *Reactant*. At first, reactant gas molecules (precursor) are introduced into the tube. This is usually done with the help of an inert gas. In some cases, inert gas is used only for the mass flow. Reactant gas molecules are stemmed from the heating of solid or liquid reactants inside the chamber.

(ii) ***Diffusion and Adsorption***. These reactant molecules can undergo gas phase reactions in order to produce reactive intermediates, which would eventually diffuse and adsorbed on the substrate. On another way, the reactant molecules might be diffused directly to the substrate and being adsorbed.

(iii) ***Heterogeneous reaction***. Subsequently, a heterogeneous reaction takes place at the interface of gas and solid depositing a thin film on top of the substrate, via nucleation, growth, and coalescence phenomena. These reactions give rise to many by-products as well.

(iv) ***Desorption***. Next the unreacted molecules and the by-products are desorbed away from the substrate.
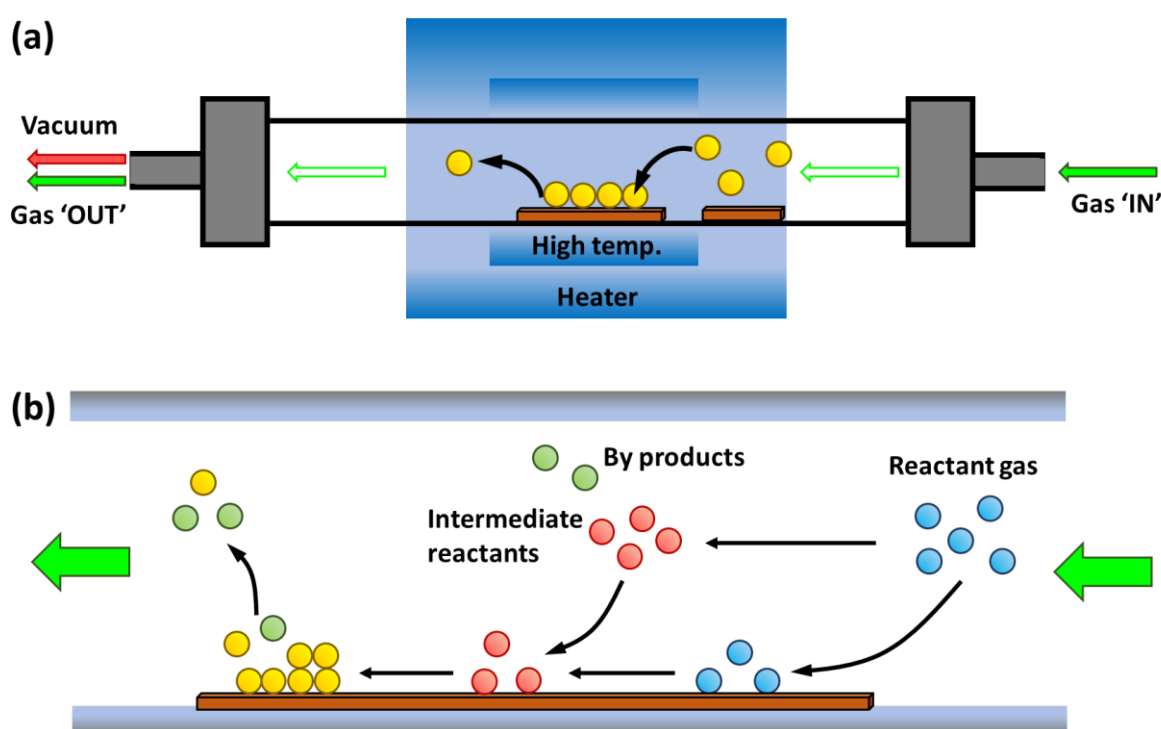
Figure 2.1: (a) Simple schematic representation of CVD technique using a quartz tube. **(b)** Stepwise representation of the chemical processes in a typical CVD deposition process.

These processes take place in a particular temperature, pressure, and mass flow. Any modification with these parameters will lead into different type of depositions. This will affect the crystallinity, shape, size, and purity of the deposited thin films. Also, the cleaning of the chamber is very important. Usually, before flowing reactant gas molecules into the chamber, the air inside the tube is suctioned out using a vacuum pump. All these parameters discussed here, would be different for the deposition of different materials.

2.1.2.1. Synthesis of monolayer MoS₂ flakes using CVD

During my thesis work, we have used this CVD technique to deposit monolayer MoS_2 flakes on top of SiO_2/Si substrate, using a two-zone thermal CVD.[10] MoO_3 and S powders were used as precursors, which were kept at different temperature zones inside the quartz tube. The mass flow was maintained by a continuous flow of Ar. Before initiating the deposition, the whole chamber was vacuumed using a rotary pump. The MoO_3 powders were poured in an alumina crucible and placed at the centre of the tube, where the temperature was fixed at 680 °C. The S powder was placed at the upstream of the tube maintaining temperature of 200 °C. For the deposition, 300 nm SiO_2/Si substrates were kept on top of the MoO_3 powders, upside down. Both the temperature zones were programmed in such way that those temperatures could be achieved at the exact same time. At this temperature, both MoO_3 and S powders are evaporated and form gaseous reactants. S reduces these oxides and form many reactive intermediates to finally obtain MoS_2 flakes on top of the substrate. Ar gas flow facilitates the diffusion of these reactants without interrupting in any chemical reaction. Our synthetic route produced monolayer flakes of MoS_2 with triangular shapes, which is the most common occurrence in such techniques owing to lowest edge formation energy of the triangular shape. These flakes were characterized using Raman and AFM, discussed in chapter 3.

2.1.3. Liquid phase exfoliation

Layered materials are comprised of 2D layers stacked upon each other through weak van der Waal interaction and appear as three-dimensional (3D) bulk structures.[11,12] Owing to this weak inter-layer interaction, it is very easy to break these bonds and produce individual layers. This production of segregated thin layers from a bulk layered material is usually termed as exfoliation or delamination.[13] There are mainly two types of exfoliation techniques, mechanical exfoliation, and liquid phase exfoliation (LPE). In mechanical one, the layers are peeled from the bulk system using scotch tape and highly crystalline thin layers are formed.[14] However, this method is suffered from very poor yield and wastage of the bulk material. On the other hand, LPE has the potential for easy production of mono- to few layered sheets, with highly scalable production in different solvent mixtures.[12,15]

LPE can be categorised into four different types,[13]

(i) **Oxidation**. In this method layered materials having low reduction potentials are oxidised using a suitable acid and subsequently dispersed in a solvent. It is widely used for exfoliating graphite into graphene.
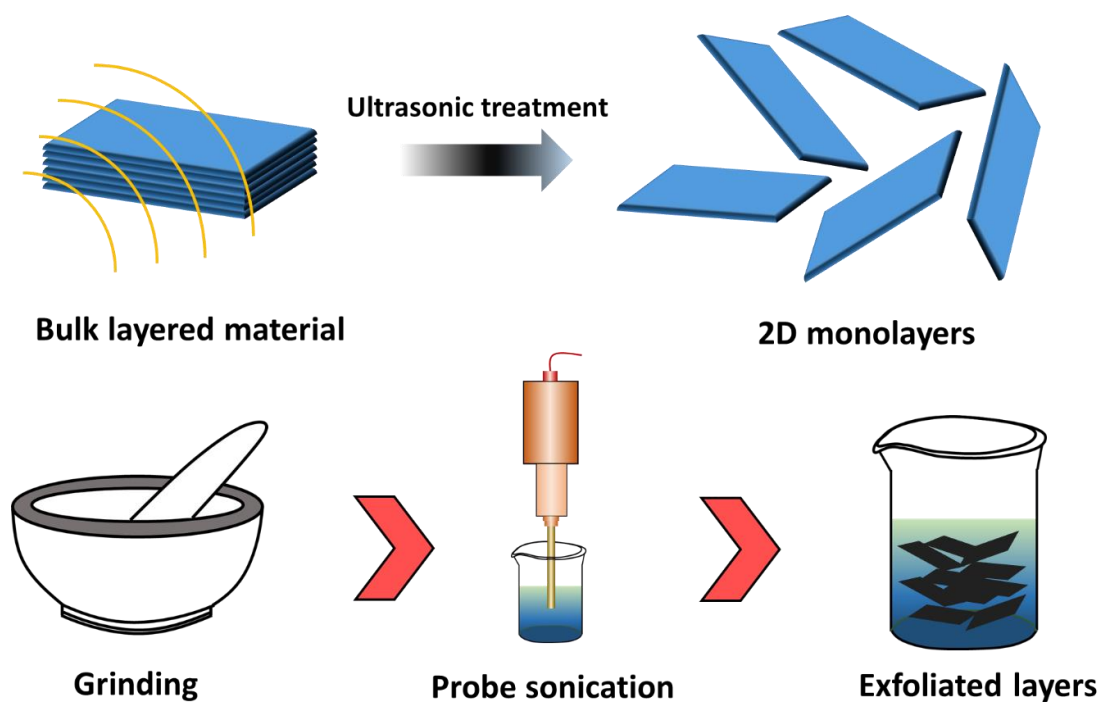
Figure 2.2: Liquid exfoliation process in a probe sonication method.

(ii) **Ion intercalation**. In this case, different ions are inducted between the layers of the material in a solution, which further weakens the van der Waal interactions. Subsequently, little agitation in form of heat, sonication etc. open all the layers. Layered materials are very prone adsorb alien molecules in between layers, which increases interlayer distance and brings down the interaction within layers. Although this method has the ability to decrease the exfoliation energy, it is not very stable at ambient conditions.

(iii) **Ion exchange**. This method is applicable in some special cases, where ions exist in between layers in order to balance the surface charge of the overall crystal. For exfoliations, these ions are chemically exchanged with larger ions to lower the interlayer interaction and subsequently agitated to form thin layer solutions. It is similar to intercalation process and sensitive in normal condition.

(iv) **Sonication in a solvent**. This is the most recent technique. Here, bulk layered particles are added to a suitable solvent and the solution is treated with ultrasonic waves for a particular time period. These waves produce cavitation bubbles in the solvent, which are transformed into very high energy jets, hitting in between the layers to yield segregated layers.[14] To prevent any reaggregation of these layers, the surface energy of the solvent must be similar to that of the material, so that there would be very little energy difference between the exfoliated and aggregated layers. So, it is very important to choose the solvent for a particular material.

2.1.3.1. Synthesis of few layered WS₂

In my thesis work, we have synthesised few layered WS_2 solution in NMP solvent[16] using ultrasonic treatment (**Figure 2.2**). At first, 80 mg bulk WS_2 powder was taken in a mortar and pestle and grinded for 30 mins. This would break the larger particles into smaller ones and would facilitate the exfoliation process. These crushed particles were taken in 15 mL NMP and sonicated in an ultrasonic bath sonicator for 30 mins, to make a fine solution. This black solution was further sonicated in a probe sonicator for 1h using an ice bath. Following the sonication, the colour of the solution was turned into greenish-black. Now the solution would contain both exfoliated and unexfoliated materials. To remove the unexfoliated particles, this mixture was centrifuged at 4000 rpm for 30 mins. The supernatant of this solution now contains exfoliated WS_2 nanosheets. It was carefully pipetted out and characterized. Raman and AFM measurements confirm the few layer nature of the sheets (Discussed in chapter 4).

2.1.4. Solvothermal synthesis

Solvothermal synthetic route is a bottom-up approach like CVD. It is a wet chemical synthesis process, where precursors are added to a suitable solvent and poured in closed Teflon autoclave (**Figure 2.3**).[17,18] The reaction takes place at an elevated temperature under high pressure (Usually much greater than 1 atm). The typical synthetic route is described in **figure 2.3**. At first precursors are carefully mixed in a suitable solvent to make a proper solution. Then this mixture is gently added in the Teflon lined reaction chamber and the chamber was closed inside a stainless-steel autoclave. This autoclave is kept in an oven and heated at a certain temperature for a particular time period. After that, the solution is cooled down naturally, which is now comprised with both product and unreacted precursors. This solution is washed, centrifuged, and dried to obtain desired nanomaterials. There are many factors, which decides the fate of the produced materials, like, concentration of the precursor solutions, oven temperature, heating time, the amount of the solution in the reaction chamber etc.[19]

When water is used as a solvent, this procedure is termed as hydrothermal synthesis. The advantage of this technique lies in the flexibility in controlling surface morphology, doping, composite fabrications, mass production etc., which are highly desired in photocatalytic, photo-electrocatalytic, gas sensing or energy storage applications.[17] Though the crystallinity of the solvothermal produced nanosheets are not that great, it would not be a problem for an application like photocatalysis. Nowadays, this method is most widely used protocol for synthesizing 2D nanosheets in industrial level applications.
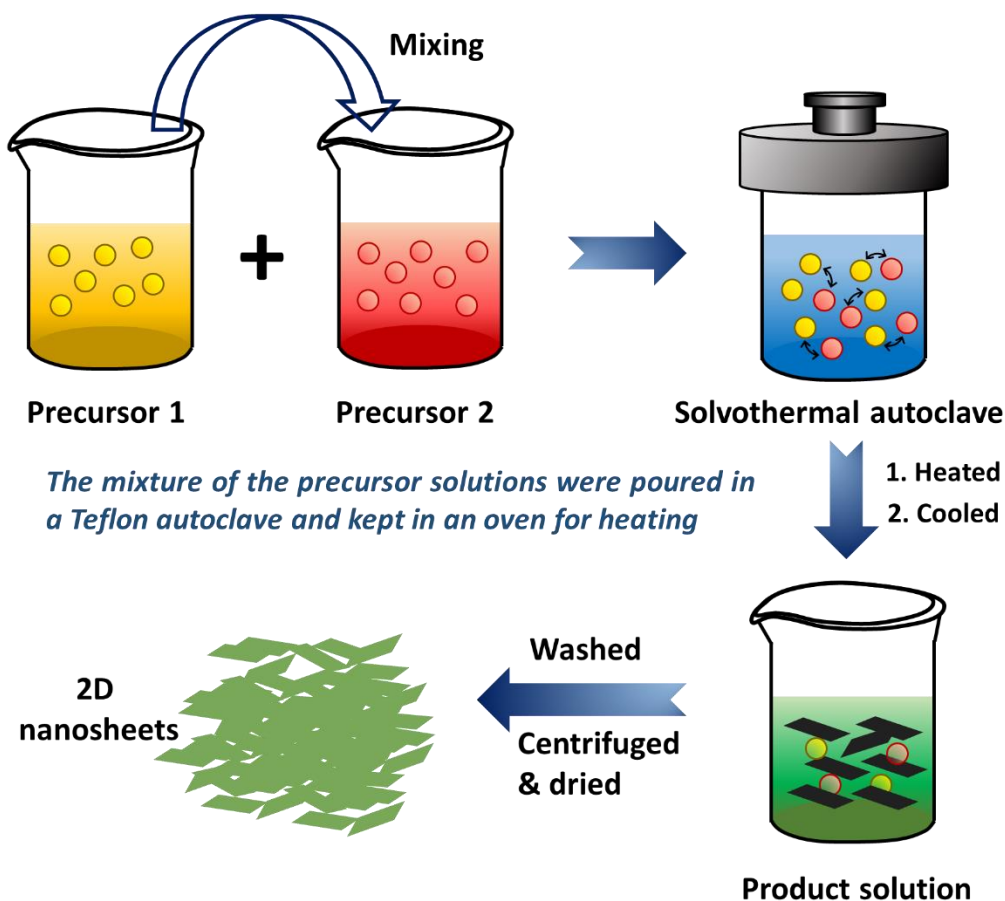
Figure 2.3: Simple schematic presentation of a solvothermal synthesis process.

2.1.4.1. Synthesis of O- and N-doped ZnIn₂S₄ nanosheets

We have opted hydrothermal synthetic procedure to synthesise thin $ZnIn_2S_4$ (ZIS) nanosheets.[20] At first, 1 mmol $ZnCl_2$, 2 mmol $InCl_3$, and 8 mmol TAA were added to 30 mL DI water and sonicated for 15 mins for homogeneous mixing. This is our precursor mixture solution. TAA acts as a reducing agent, as well as source of S^{2-} ions. Then this mixture was added to a Teflon lined stainless steel autoclave and heated in an oven at 180 °C for 20 h. Following that the autoclave was cooled naturally. The yellowish solution was then washed with absolute ethanol and DI water separately for 3-4 times each. Finally, the product was precipitated using a centrifuge machine (8000 rpm, 10 mins) and dried in a vacuum oven at 80 °C for 6 h.

O-doping: For the introduction of O atoms in the ZIS structure, we used PVP. In a typical process, 1 mmol $ZnCl_2$, 2 mmol $InCl_3$, 8 mmol TAA and 0.2 g PVP were added in 30 ml water-ethanol (1:1) mixture solvent and mixed with vigorous stirring for several mins. This precursor mixture was then decanted into a 50 mL Teflon lined stainless-steel autoclave system and

heated in an oven at 180 °C for 20 h, just like ZIS. The cooled product solution was of pale-yellow colour. It was washed, precipitated, and dried in a in a similar manner as of ZIS.

N-doping: In case of 'N', DMF was used. At first, 1 mmol $ZnCl_2$ 2 mmol $InCl_3$ and 8 mmol TAA were added in 30 ml DMF-water (3:1) mixture. The precursor solution was prepared with vigorous stirring for several mins. This solution was transferred into a 50 mL Teflon-lined stainless-steel autoclave and heated in an oven at 180 °C for 20 h. Then, the system was cooled down naturally. Finally, the product was obtained in similar way as discussed earlier.

2.1.4.2. Synthesis of CdS nanorods and CdS/MoS₂ composites

For synthesizing CdS nanorods (NRs) we opted a modified solvothermal route.[21] At first, 0.427g $Cd(ac)_2.2H_2O$ and 0.6089 g thiourea were mixed in 12 mL EN and properly dissolved by magnetic stirring for 30 mins. Then this homogeneous mixture was poured in a 25 mL Teflon lined stainless-steel autoclave and then heated at 180°C for 24h. After the reaction, the bright yellow solution was cooled naturally. In order to remove impurities, the product was washed several times with ethanol and finally dried in a vacuum oven at 60 °C.

For the synthesis of CdS/MoS₂ nanocomposite pristine MoS_2 sheets (0.2 g) were added to the as mentioned CdS precursor solution before transferring into the autoclave. All other conditions were kept same. The resultant composite was of greenish colour.

2.1.4.3. Synthesis of Cu₂MoS₄ nanosheets

Cu_2MoS_4 (CMS) is ternary metal chalcogenide system. It was prepared in two steps. First Cu_2O was made using a room temperature synthetic route. First, 3.333g PVP was dispersed in 100 mL distilled water taken in a beaker and mixed properly by continuous stirring. Then 1.12 mmol $CuCl_2$ powder was added to this mixture while stirring. It will form a homogeneous clear solution. 2M NaOH solution was prepared separately in 10 mL DI water. NaOH solution was added drop by drop to the main solution with continuous stirring. After that, an aqueous solution of ascorbic acid (10 mL, 0.6M) was added in the solution mixture drop by drop while stirring. This solution was kept at magnetic stirring for 1h. The colour of the final solution was turbid yellow. It was washed three times with 1:1 ratio of ethanol and water. The final precipitate was dried in a vacuum oven at 60 °C for 6h.

Next, solvothermal method was applied for the preparation of CMS. 30 mg sodium molybdate was properly dissolved in ethylene glycol solvent using ultrasonic treatment in an ultrasonic bath sonicator for 5 mins. Subsequently, 60 mg TAA and 20 mg as prepared Cu_2O powder was

added to this solution one by one and mixed in ultrasonication. After 5 mins, a greenish-brown colour was observed. This solution was poured into 50 mL Teflon-lined autoclave and heated at 200 °C for 24h. The obtained product solution was cooled naturally and washed with DI water and distilled ethanol, four times each. Finally, the product was precipitated and dried at 60 °C for 6h under vacuum condition.

2.1.5. Synthesis of gold nanoparticles via chemical reduction process

We have employed citrate reduction process for the synthesis of gold nanoparticles (Au NPs). It is a well-established technique for the synthesis of metal NPs.[22,23] At first 12 mL 1mM $HAuCl_4$ and 2 mL 2% trisodium citrate solution were separately prepared in DI water, which were preheated to 75 °C. Then the citrate solution was dropwise added to the Au precursor solution under vigorous stirring maintaining temperature at 75 °C. Followed by that the heating was continued for another 10 mins, when the colour of the solution changed from yellow to red. The heating was continued for another 20 mins for proper growth of the NPs.

2.2. Characterisation techniques

2.2.1. X-ray Diffraction (XRD)

X-ray diffraction (XRD) is one of the most widely used characterizing tool for the identification of the crystallite phase and unit cell parameters of a material.[24,25] It is the most basic characterization of any unknown material.
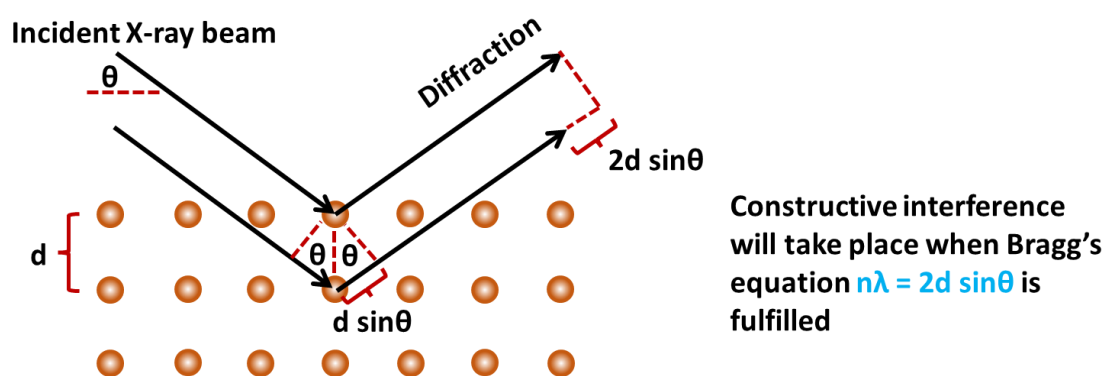
Figure 2.4: Basic principle of XRD measurement. Diffraction of X-ray beams are shown from different crystal planes, constituted with many atoms.

Principle: XRD is based on the constructive interference of a beam of monochromatic X-ray radiation and the crystalline material (**Figure 2.4**). When an X-ray beam falls upon a crystalline

material, it is diffracted by the crystalline planes within the material, at different angles following Bragg's law,[26]

$$n\lambda = 2dSin\theta$$

where, **n** is the diffraction order, λ is the incident X-ray wavelength, **d** is the interplanar distance for a particular crystal plane and θ is the angle of diffraction. These diffracted X-ray beams are detected and counted for further analysis. The connected computer system records a series of peaks arising at different angles (**2θ**), which corresponds to different planes. From the analysation of the diffraction angles for different crystal planes, we will get an idea of the periodic arrangement of atoms inside that material. Usually, the acquired data is matched with a standard database to confirm the material. The average particle size can also be calculated from the XRD peak width using Scherrer's equation,

$$r = \frac{K\lambda}{\beta cos\theta}$$

where, **r** is average particle size in Å, **K** is the shape factor (usually close to 1), β is FWHM of the peak and θ is the diffraction angle.
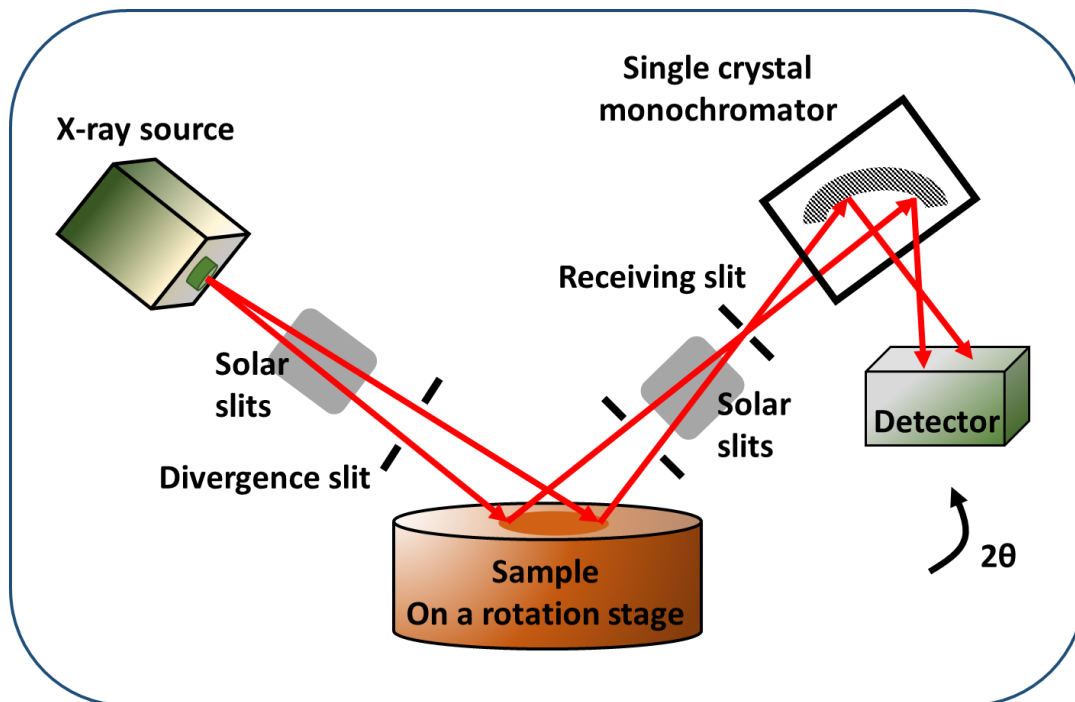
Figure 2.5: Basic structure of a XRD setup.

Instrumentation: The basic schematics of a XRD instrument is shown in **figure 2.5**, it is comprised with three basic components, X-ray source, X-ray detector and a sample holder. Inside the source, a cathode tube is heated to produce electrons, which are accelerated to hit

the target material via applying sufficient voltage. Electrons with enough energy (specific to the target material) removes inner shell electrons from the material and produces X-ray. This X-ray would be consisting of many wavelengths and appear as a spectrum, characteristic to the target material. Foils or crystal monochromators are used to filter this X-ray spectrum, generating monochromatic X-ray beam to bombard the material. The reflected X-ray beams are focussed at the detector via perfectly placed optics and a monochromator. The detector collects and process the signal to a count rate and send to the computer. When the bombarding X-ray beams satisfy Bragg's law, a constructive interference take place and a peak appears in the output data. During measurement, the sample and the X-ray source maintains an angle θ, whereas the detector maintains an angle 2θ. In my thesis work, we have used Bruker D8 ADVANCE PXRD set up with Cu Kα radiation (λ= 1.5418 Å), operating at an accelerating voltage of 40 kV and 25 mA current. The obtained XRD patters were matched with Joint Committee on Powder Diffraction Standards (JCPDS) or International Centre for Diffraction Data (ICDD) database.

2.2.2. Raman Spectroscopy

Raman spectroscopy is an inelastic scattering phenomenon, where incident photons interact with the vibrating molecules inside a material.[27] It is named after its inventor Dr. C. V. Raman, who demonstrated this scattering effect in 1928 along with his research partner Dr. K. S. Krishnan.[28] Today, this technique has emerged as one of the most important tools in all scientific sectors, physics, chemistry, material science, even in medicine and biology.[27,29] Even though raman spectroscopy is far less sensitive than absorption or PL spectroscopy, it is extensively used for its few unique advantages like, freedom to choose incident laser wavelength (No need to excite optical band gap), more relaxed selection rules (can monitor optically forbidden transitions), requirement of very little amount of sample etc.[27] Raman scattering is a very important characterizing tool for 2D materials; it can unambiguously confirm the material as well as predict its layer numbers.[30,31]

Principle: When a beam of light falls upon a material, it is either absorbed, transmitted, reflected, or scattered. Raman spectroscopy is the study of this scattered light. In most cases, the energy of the scattered photons is the same as that of the incident monochromatic light. It is called Rayleigh scattering, which is an elastic phenomenon. However, in some rare cases the

energy of the scattered photons is not same as of the incident light source, which is known as the Raman scattering.
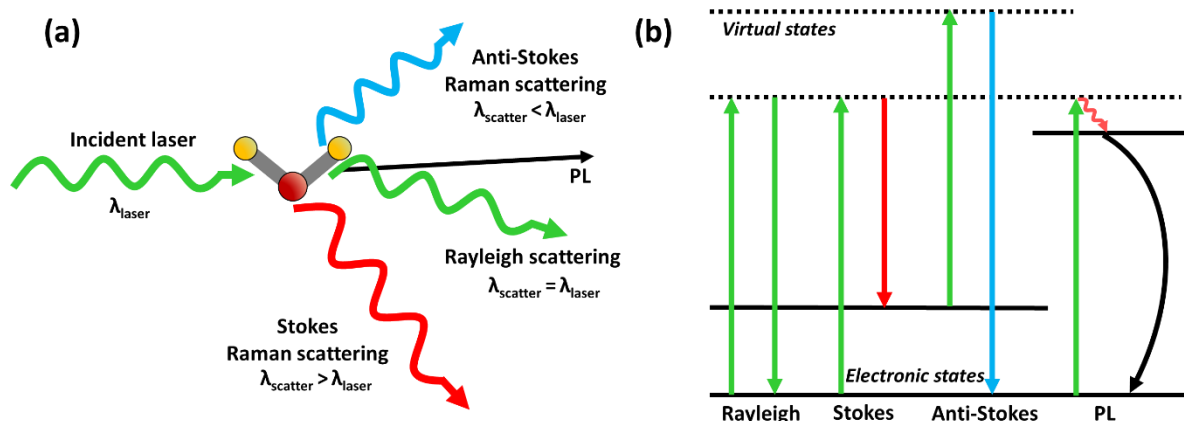
Figure 2.6: (a) Possible elastic and inelastic scattering processes when light falls on a molecule. **(b)** Emergence of different scattered lights and PL in a raman experiment.

If the scattered photon energy is lower than the incident one, the molecule gains energy from the photons and named as the Stokes Raman scattering. When the molecule loses its energy and the scattered photons possess higher energy than the incident photons, then that process is called Anti-stokes Raman scattering. We have shown these phenomena in **figure 2.6a**. In classical sense, raman scattering takes place when the oscillating electric field of the electromagnetic radiation induces a polarization in the molecule.[27] The electric field distorts the electron cloud and gives rise to a virtual state (Quantum theory). This state is very unstable and the system immediately returns to the ground state releasing scattered photons. Depending upon the energy of these transitions, we observe Stokes or Anti-Stokes Raman scattering, as described in **figure 2.6b**.

Instrumentation: A typical raman instrument is comprised of four basic components, (i) incident laser source, (ii) Objective microscope and the sample stage, (iii) filters, and (iv) the Spectrometer. The schematic of the apparatus is shown in **figure 2.7**. A modern-day laser set-up uses solid state lasers as source, with popular wavelengths of 514, 532, 633, 785, 830 and 1064 nm. Shorter wavelength lasers induce larger raman scattering cross-section and results in pronounced raman peaks. However, they are often associated with large scattering or PL induced broadening.
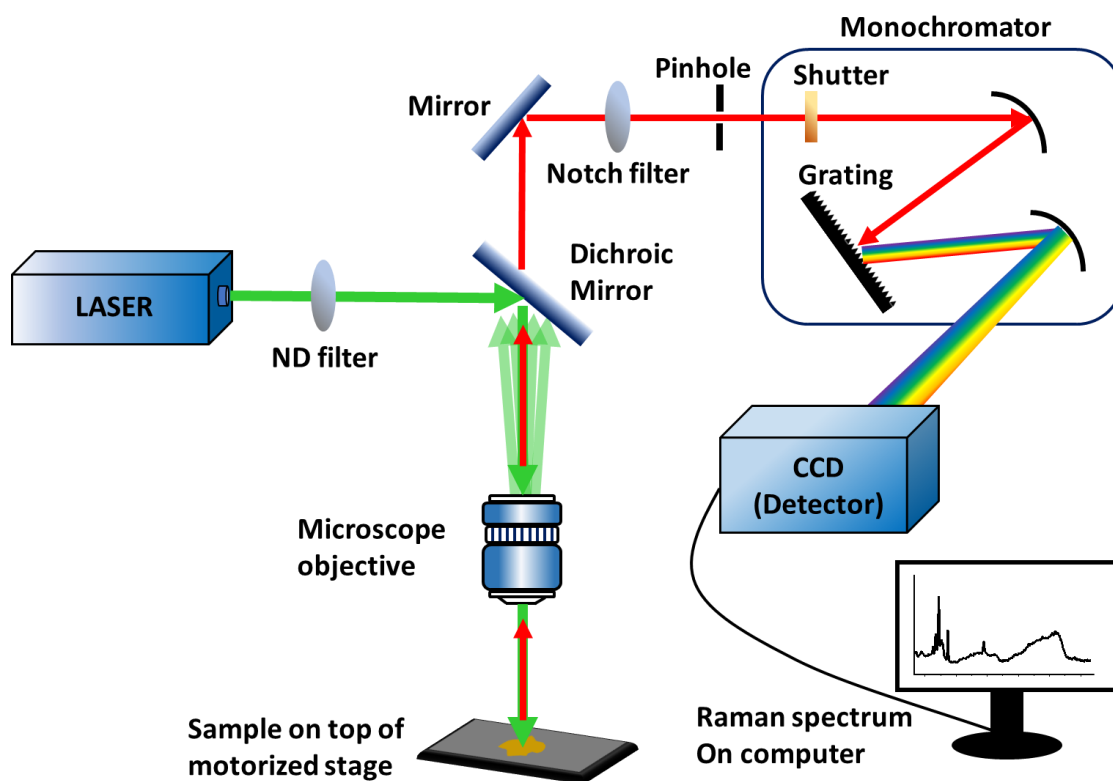
Figure 2.7: Outline of a Raman spectrometer.

Higher wavelengths produce more clearer spectra, although peak intensity gets affected. The resolution of the collected spectra depends on the bandwidth of the laser used. In most cases, the laser is a continuous wave. Pulsed lasers are used for time-dependent raman spectroscopy. Starting from the source, the laser falls upon objective microscope lens reflecting on a dichroic mirror. The microscope focusses the laser on the sample kept in a motorized stage, capable of lateral translation. Usually, one instrument uses many different microscopes of different resolution for focussing different type of samples. Once the light falls upon the sample, it gives rise to both Rayleigh and Raman scattered photons. Rayleigh photons are mostly reflected from the dichroic mirror, but Raman photons pass through. These scattered photons are directed toward the spectrometer with the help of few accurately placed mirrors. Before entering the spectrometer, a Notch filter is placed in the path of the laser to cut off any Rayleigh scattered stray photon. Spectrometer primarily consists of a monochromator and a detector. Inside the monochromator, a diffraction grating is placed, which disperses the scattered light into different components by their wavelengths. This wavelength range can be changed manually, according to our requirements. The resolution of the raman spectrum depends on the grating, specifically on the distance between the grooves on the grating. The dispersed light falls on a

cooled CCD (Charge-coupled device) detector, which records the signal and passes to the computer. In my thesis work, we have used a WITec alpha 300R Confocal Raman Microscope, with upright optical Microscope (Zeiss) and two laser sources of Nd-YAG 532 nm and He-Neon 633 nm, respectively.

2.2.3. X-ray Photo-electron Spectroscopy (XPS)

X-ray photoelectron spectroscopy (XPS) is a unique surface characterising tool where soft X-ray beams are used to study the material.[32,33] It was first developed by Kai Siegbahn and his group in the mid-1960s, which lead to his Nobel prize in 1981.
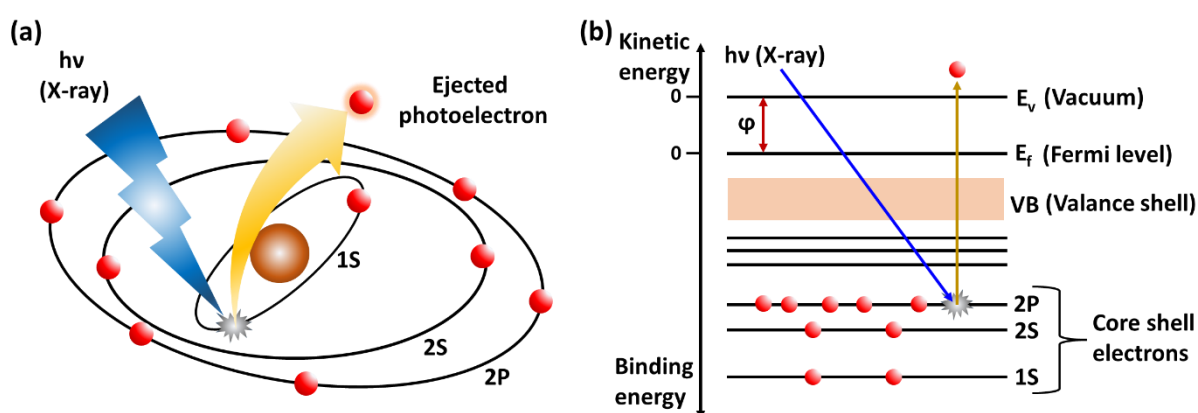
Figure 2.8: Basic principle of XPS.

Principle: XPS works on the principle of photoelectric effect. When monochromatic X-ray beams hit the sample surface, it releases electrons from the inner orbital of the atoms present in that material (**Figure 2.8**). These emitted electrons will have certain kinetic energy, which can be calculated from the Einstein's equation,

$$h\nu = BE + KE + \phi$$

where, $h\nu$ represents the energy of the of the X-ray radiation (h- Planck constant, ν- Frequency of the X-ray used), **BE** stands for binding energy of the emitted electron, **KE** is the kinetic energy of that electron and ϕ is the spectrometer work function. XPS primarily measures the KE of the electron, which gives us the binding energy of that electron, as other two parameters are known. Different electrons from orbitals and from different atoms would be having different BE. The XPS spectrum presents an intensity vs BE plot and provide us a quantitative idea about the material. The BE of the electrons also depend on the chemical environment of the atom, different bonding result in different BE for the same electron. So, the peak position in XPS spectrum also changes according to that, this is known as chemical shifting. Detailed

study of chemical shifting of peak positions gives lot of information about the bonding and structure of the material.[34]
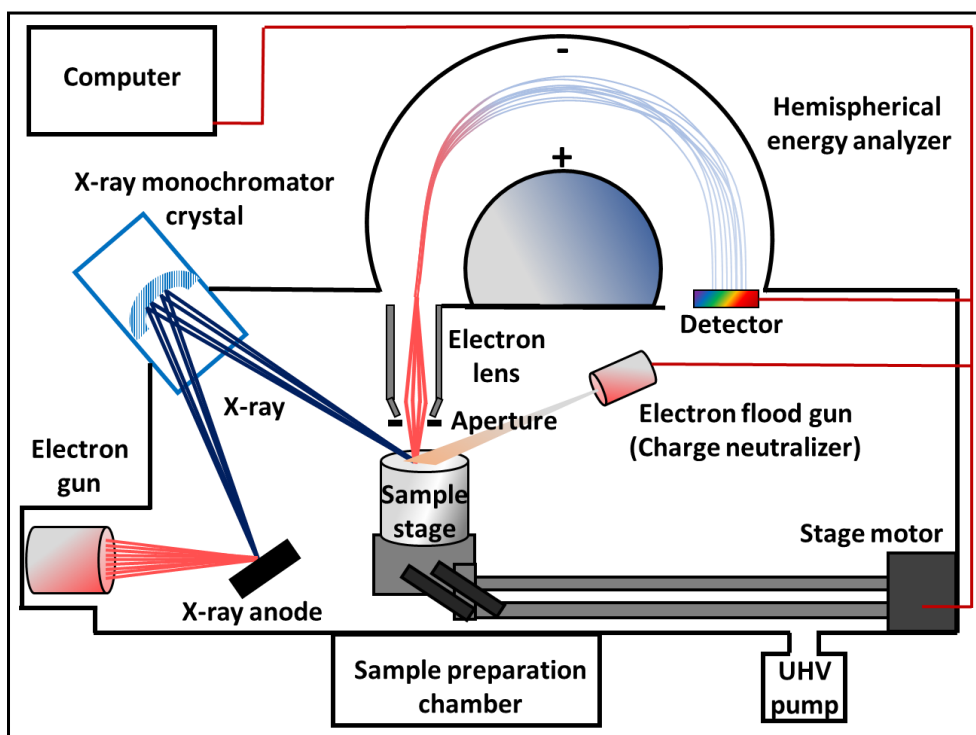
Figure 2.9: Basic outline of a XPS set up.

Instrumentation: A XPS setup is consisted with many important components (**Figure 2.9**),

(i) **Ultrahigh vacuum chamber** – In XPS, X-ray beams are bombarded on the sample to emit inner shell electrons, which will be having very low energy. Subsequently, they would have very small mean free Path in a presence of air particles. Hence, to monitor those electrons we need to suck out air from the chamber. Usually, 10^{-7} –10^{-9} mbar pressure is maintained while carrying out a XPS measurement.

(ii) X-ray source and monochromator – Generally, Al K_α (1486.6 eV) or Mg K_α (1253.6 eV) X-rays are used in XPS to excite the samples. Al or Mg plates are used as an anode inside the X-ray source, which is hit with an electron gun to produce characteristic X-rays. These X-ray beams are passes through a monochromator which allow only a particular energy of X-rays to fall on the sample.

(iii) Sample stage – The samples are placed on a motorized stage which is connected to the preparation chamber.

(iv) Electron energy analyser – The emitted electrons pass through few lenses and apertures to enter the Concentric Hemispherical Analyser (CHA), which separate out electrons with

different kinetic energy. These hemispheres are kept in a certain voltage, outer sphere being the more negative. This voltage can be modulated to control the passage of the electrons. The resolution of the analyser depends on its size, larger the size better the resolution.

(iv) **Multi-channel detector plate** – The detectors used in XPS are electron multipliers. Often multiple electron multipliers are employed to collect maximum number of electrons. These detectors send the data to a computer, which converts the electronic signal into a XPS spectra.

(v) **Ar ion gun** – It is used to remove the contaminations from the surface of the material before bombarding X-ray.

(vi) **Electron flood gun** – It is employed to minimize the effect of surface charging on the material while bombarded with X-ray beams.

In my thesis, we have used a Thermo Fisher Scientific made K-alpha XPS system, with Al K$_\alpha$ X-ray source having 1486.6 eV energy. The CHA pass energy was maintained at 200 eV and 500 eV for attaining a survey spectrum and a narrow scan, respectively. One rotary and two turbo ion pumps were used to maintain the ultrahigh vacuum.

2.2.4. Transmission Electron Microscopy (TEM)

An electron microscope (EM) is very similar to normal optical microscope, which is normally used to magnify the image of a small specimen. The major difference lies on the instrumentation and extremely high resolution of EM. It uses electron beam as light source and these are focussed on the sample with the help of electromagnets (lenses are used to focus visible light in optical microscope). As electrons possess extremely low effective wavelength, we can see very small objects (like atoms) using EM.[35] There are mainly three different EM techniques, Transmission Electron Microscopy (TEM), Scanning Electron Microscopy (SEM) and Scanning Tunnelling Microscopy (STM). They all operate in different ways. Here we are going to discuss only about TEM.

TEM is the most powerful electron microscopy technique still known, having resolution close to 1 nm. First experimental TEM setup was built by two German scientists Ernst Ruska and Max Knoll in the year 1931.[36] Ernst Ruska is hailed as the pioneer of electron microscopy and went on to win the Nobel prize in 1986. Nowadays, TEM is extensively used in the all the scientific sectors to visualise structure, morphology, defects etc. in any material.[37]

Principle and instrumentation: The principle of TEM is very similar to an optical Microscope. Electron beams released from the source is focussed on the sample with help of electromagnets,

transmitted through and fall on a fluorescence screen to produce an image. TEM setup is comprised with many different components (**Figure 2.10**),

Electron gun

First condenser lens

Second condenser lens

Condenser aperture

Sample

Objective lens

Objective aperture

First intermediate lens

Second intermediate lens

Projector lens

Projector screen
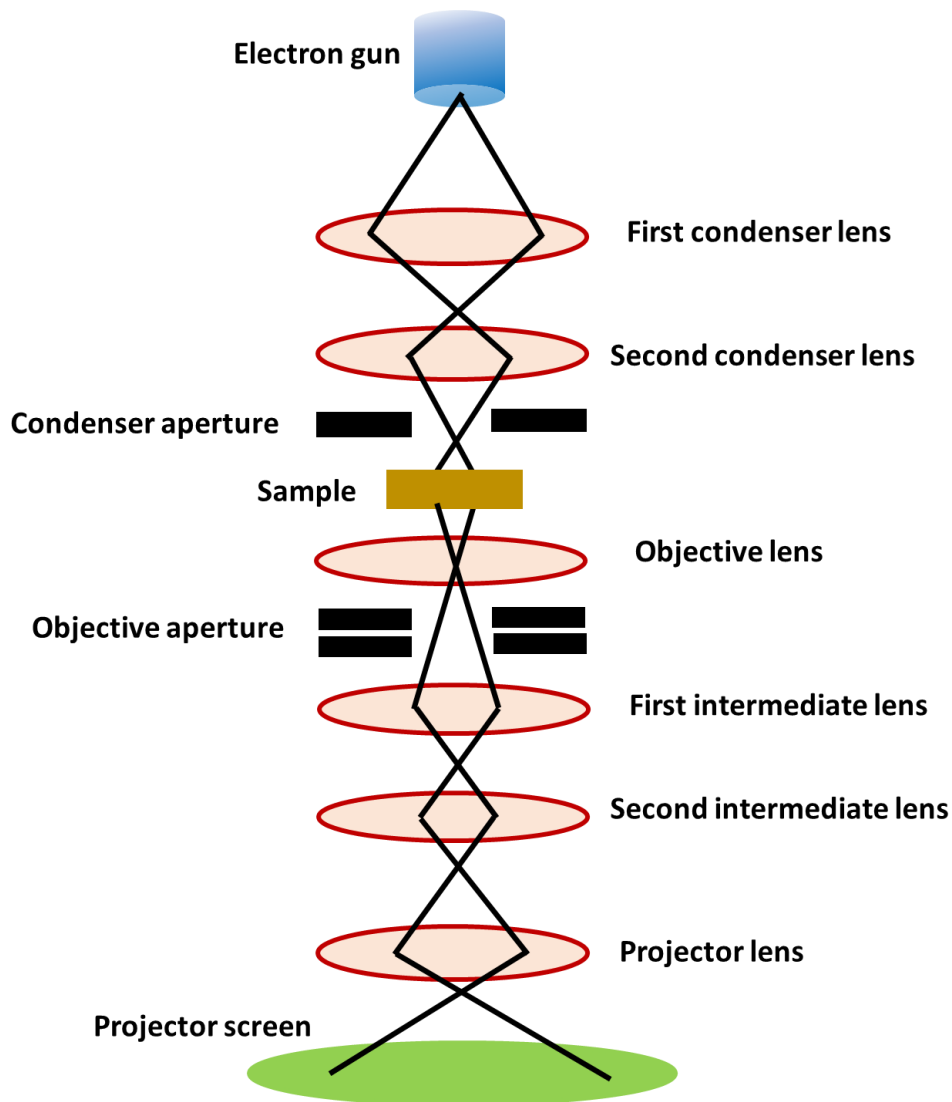
Figure 2.10: Simple schematic layout of a TEM instrument.

(i) **Electron gun** – It is the source of electrons and placed at the top of the TEM column. A filament is used as the cathode, which is connected to a voltage source. Usually, 50,000 to a few million volts of voltage is applied to the cathode in order to generate and accelerate the electrons from the cathode. The speed of the electrons is very important for this instrument, faster the electrons move, smaller the wavelengths they offer and the resolution is improved. Achieving the top speed, these electron beams are released from the gun via an anode plate and travel towards the lower side of the instrument.

(ii) **Electromagnetic coil** – It act as the lens for the electron beam and focusses the electrons. Mainly, three electromagnetic coils are used in the TEM column. The first lens (condenser

lens) focusses the parallel beam of electrons from the gun into a concentrated beam. Another condenser lens focusses the electrons on the sample as required. The second and third lens (objective and projector lens) help the transmitted electron beams to focus on the fluorescence screen.

(iii) **Aperture** – Apertures are small metallic plates, which help in excluding scattered or diffracted electrons from reaching the projector. With the help of these, the intensity of the electron beams can be controlled.

(iv) **Sample stage** – The samples are placed on a copper (usually) grid and inserted in between condenser and objective lens. It is equipped with an airlock system, so that the vacuum of the system does not break.

(v) **Vacuum system** – A TEM setup works only in high vacuum. Electrons cannot travel much in air. A proper vacuum will ensure less scattering between the electrons and the air particles.

(vi) **Imaging** – The transmitted electron beams are projected on a fluorescence plate, which produces the image of the sample area focussed during the measurement. A CCD camera is placed underneath this plate, which record the images and send it to the computer as micrographs. This bright field image is obtained purely due to the transmitted electrons only.

Today, TEM is not limited to imaging of samples, it is being used to quantitative analysis of the material as well. Energy dispersive X-ray Spectroscopy (EDS) studies the ejected X-ray beams from the material while bombarded with the electron beam and provide relative percentage of the elements present in the material. Selected area electron diffraction (SAED) technique uses diffracted electrons to monitor the crystal and phase structure of the material.

In our thesis work, the TEM and HRTEM measurements were carried out using a JEOL model 2100 instrument with an operating voltage of 200 kV.

2.2.5. Atomic Force Microscopy (AFM)

Atomic force microscopy (AFM) is one of the best-known techniques to study the morphology and topography of a material surface in nanoscale.[38–40] It is a special type of Scanning Probe Microscopy (SPM) with much higher resolution. IBM researchers Gerd Binnig, Christoph Gerber and Calvin Quate first demonstrated the imaging with AFM in 1986.[41] They received the prestigious Nobel prize in the same year along with Ernst Ruska. The Advantage of AFM imaging over STM like techniques is its ability to probe any material, be it metal, semiconductor, or any biological sample at extremely high resolution.[42,43]
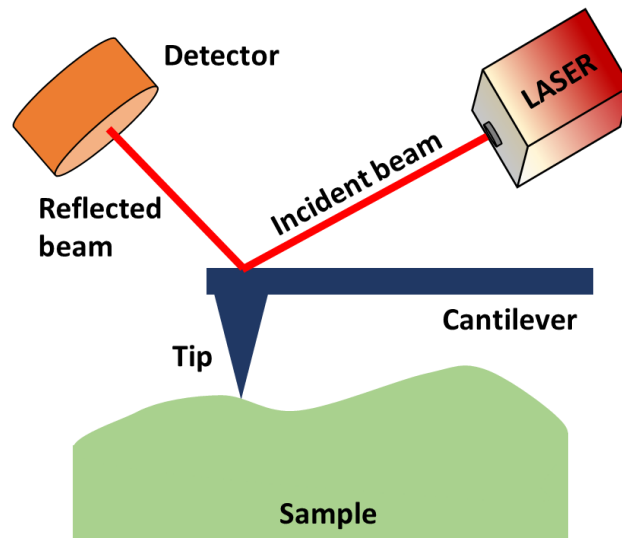
Figure 2.11: Outline of the AFM instrument.

Principle and instrumentation: AFM work on the principle of surface sensing with help of a sharp tip placed on a cantilever. This tip scans throughout the material surface and produce images. Though the operation of an AFM set up is different in case to case, it is primarily comprised of four components (**Figure 2.11**), (i) a laser source, (ii) cantilever with a sharp tip, (iii) sample stage and (iv) a photo-diode detector. The backside of the cantilever is coated with a highly reflective material, so the reflected beams from the laser source fall on the detector. This detector is extremely sensitive to the precise position of the laser on the cantilever and known as position sensitive photo-diode (PSPD). The cantilever works as a force sensor, it is stretched and compressed depending upon the type and amount of the force present. The detector tracks the movement of the cantilever and process it into an electronic signal. There are many kinds of forces inside the material, which influences the AFM process and can be detected. Some of these forces are chemical bond induced forces, mechanical forces, van der Waal forces, magnetic forces, electrostatic forces etc. When the force is attractive in nature it bends the AFM tip towards the surface, whereas a repulsive force bends it backwards.
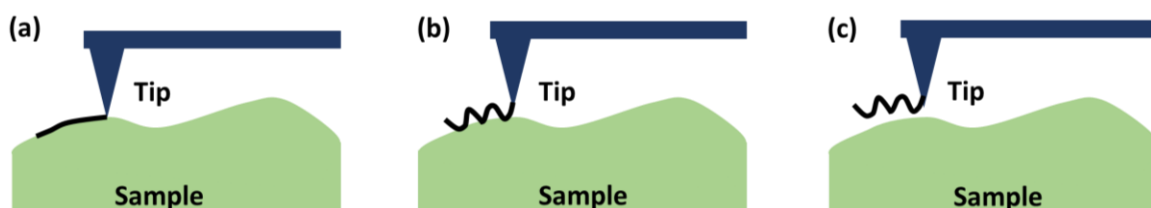
Figure 2.12: AFM working principle in three different modes, **(a)** contact mode, **(b)** tapping mode, and **(c)** non-contact mode.

AFM works on three different modes mainly (**Figure 2.12**),

(i) **Static mode (Contact mode)** – In this mode, the tip is placed on the material surface and dragged over the surface while scanning. Though this mode is very effective, it damages both the tip and the sample. It is only used to image hard samples.

(ii) **Dynamic mode (Tapping mode)** – In tapping mode, the tip touches the sample surface in a periodic manner. With the oscillation of the cantilever, the AFM tip encounters the surface frequently. This mode is widely used for different variety of samples owing to its minimal damaging.

(ii) **Dynamic mode (non-contact mode)** – In non-contact mode, the tip oscillates on top of the sample just like a sinusoidal motion, but never touches the surface. It is either driven by frequency or amplitude, applied to the cantilever. This mode is helpful in imaging soft materials, which are very prone to damage.

Today, AFM is not limited to only the study and imaging of a material surface. It is being employed in probing electrical, mechanical, thermal, magnetic, ferroelectric, and piezoelectric properties of certain materials by moulding the basic operational technique. Along with exceptional advantages of AFM technique, it is also having few drawbacks, like, small scan area, slow scan speed, sample damage etc.

We have done all our AFM measurements in tapping mode using Bruker Multimode 8 AFM with silicon cantilever from Bruker and Budget sensors (Tap 150Al-G).

2.3. Steady state optical instruments

Steady state optical measurement deals with the study of absorption or luminescence processes in a material recorded in a long-term average time scale. It gives us an overall idea about the electronic transitions inside the material on absorption of an optical radiation. These techniques are used to characterize the material as well. From the absorption or luminescence peak position, we also get a vague idea on the particle size of the material.

2.3.1. Absorption Spectroscopy

Absorption is a photo-physical phenomenon, which take place when a material absorbs an electromagnetic radiation and undergo an electronic transition to move from the ground state (**GS**) to the higher excited states (**ES**). It is one of the key results of light-matter interaction. If an incident monochromatic light of intensity I_0 passes through the material and have intensity

I (Transmitted intensity), the absorbance (**A**) and transmittance (**T**) of the material can be defined by (**Figure 2.13**),

$$A = \log\left(\frac{I_0}{I}\right) \text{ and } T = \frac{I}{I_0}$$

From the Beer-Lambert's law, this absorbance (**A**) depends on the concentration of the material (**c**) and the optical path length (**L**), as,

$$A = \varepsilon\,(\lambda)cL$$

Here, **ε (λ)** is the molar absorptivity, which depends on the wavelength (**λ**) of the radiation and the material itself. This equation is true for only low concentration solutions.
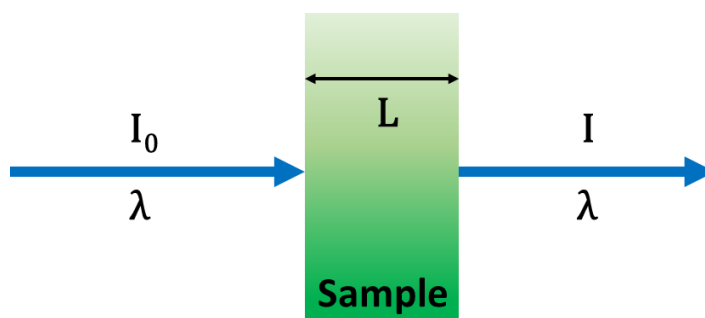
Figure 2.13: Absorption phenomenon.

Instrumentation: The basic set up of an absorption spectrometer is consisted with four major parts, light source, monochromator, sample stage and a detector (**Figure 2.14**). These parts are modulated according to the required wavelength range. Typically, Xenon lamps are capable of generating radiations throughout UV-Vis region. But they are very expensive and have stability issues. So, nowadays Deuterium arc lamps are used as the UV light source, coupled with tungsten or halogen lamps for the vis region. Next, a monochromator is placed in the path of this light to separate out different colours with the help of prisms and/or diffraction gratings. These selected wavelengths are splitted into two beams, which passes through sample solution and reference solvent, to avoid any solvent effect. These beams fall on a detector, which converts the absorption change in presence of the sample into an electronic signal and send it to a computer. The collected data shows a graph of absorbance (A) vs wavelength (λ), known as absorption spectrum.

In my thesis, we have used a Shimadzu made UV-2600 spectrometer having two set of lamps, Deuterium arc lamp and halogen lamp. It is capable of measuring 200-900 nm region (UV-Vis).
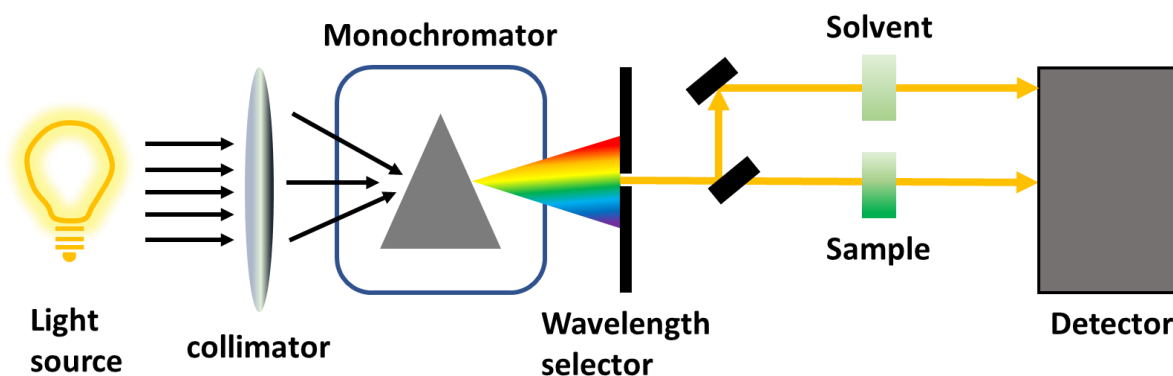
Figure 2.14: Basic components of an absorption spectrometer.

2.3.2. Photoluminescence (PL) Spectroscopy

Photoluminescence (PL) Spectroscopy is a complimentary technique of the absorption spectroscopy. Following the absorption of electromagnetic radiation, the excited charge carriers inside the material tend to relax down to the ground state. In course of that, they release their energy in form of light or heat, which are the results of radiative or non-radiative paths respectively. The study of these radiative phenomena is accomplished by PL spectroscopy (**Figure 2.15**). This technique reveals many important information related to the material, like, particle size, size distribution, band gap, charge transfer, defect concentration etc.[44–46] Based on the type of photoluminescence, PL spectroscopy is termed as Fluorescence or Phosphorescence spectroscopy.
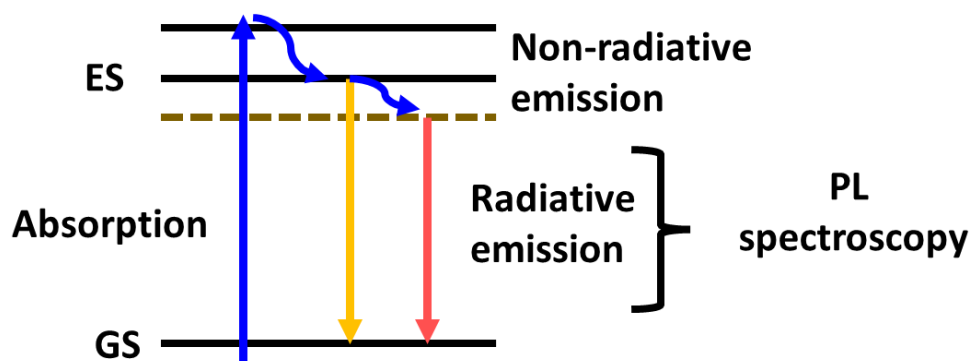
Figure 2.15: Principle of PL phenomenon and the PL spectroscopy.

Instrumentation: The instrument components of PL spectrometer is very similar to an absorption spectrometer. The basic layout of a PL spectrometer is shown in figure **2.16**. Usually, Xenon lamps are used as the light source, as its spectra is spread over a wide region,

UV to NIR. This radiation is first passed through an 'excitation monochromator' to select out wavelengths for particular excitations. Inside the monochromator, diffraction gratings are placed, which rotates according to the passage of a specific wavelength of light. The output of this monochromator acts as the excitation wavelength and causes radiative emission from the sample. This emission beam is directed into another monochromator (emission monochromator), which again separate out different wavelength before passing into the detector. The detector is usually a photomultiplier tube (PMT), which converts the optical changes in electronic signal and send to the computer. Unlike absorption spectrometer, the detector and the excitation source are not place in the same line here, in order to protect the detector from the intense excitation radiation. This could be possible in PL spectroscopy, as PL occurs in all directions. The collected data projects a graph of PL intensity vs wavelength.
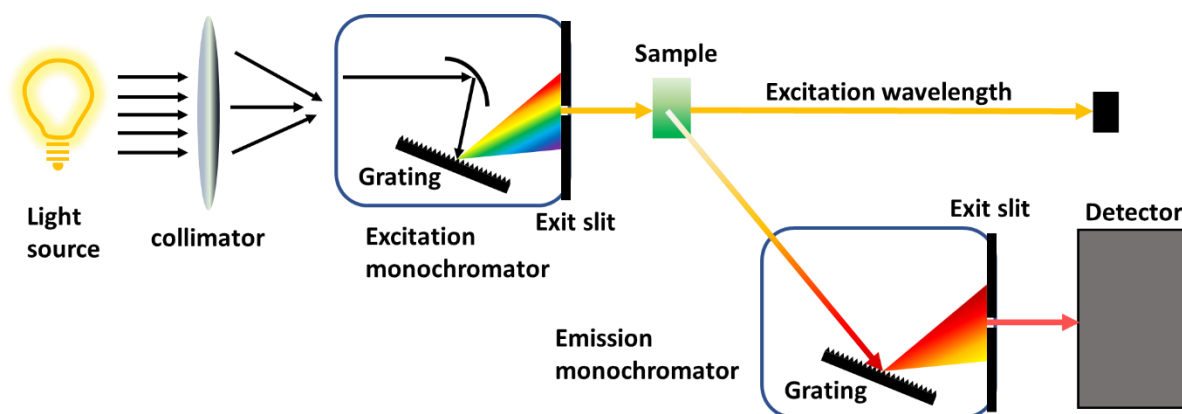
Figure 2.16: Basic components of a PL spectrometer.

In my thesis, we have used a Horiba Scientific made Fluorolog 3-221 spectrophotometer having 450W Xenon lamp and multi alkali PMT detector (200 – 800 nm).

2.4. Time-resolved optical instruments

The progression of scientific discoveries is intimately dependent on the advancement of instrumental techniques to comprehend the natural processes around us. In spectroscopy, the interaction of light and matter give rise to many photophysical processes inside the material, which decides the fate of this material in a light-based application. Most of these processes occur at very fast time scale, microsecond (µs), nanosecond (ns), picosecond (ps) or even femtosecond (fs) and attosecond (as). This is way beyond our visual limit of the eye, which is ~ 50 ms. So, to understand those processes we need some time resolved techniques, which will freeze the motion of the particles responsible for those photophysical phenomena, and give us

a clear idea about the material. From the discovery of a pump-probe technique in 1899,[47] the time resolved techniques have shown tremendous growth. Modern day time-resolved techniques have breached the barrier of attosecond and we are very close witness the dynamics of electronic motion. Time resolved techniques are mainly of two types based on the phenomenon these are structured, absorption or emission. There are two such widely popular techniques, Time resolved photoluminescence (TRPL) study or Time Correlated Single Photon Counting (TCSPC) and Transient Absorption Spectroscopy (TAS) for probing PL and absorption related photophysical processes in very short time scale. In my thesis work, we have deployed a Femtosecond Transient Absorption Spectroscopy (FTAS) set up in order to probe ultrashort photophysical processes in a 2D material.

2.4.1. Femtosecond Transient Absorption Spectroscopy (FTAS)

The journey of modern transient absorption spectroscopy started with the discovery of flash photolysis in the year 1949,[48] when two British chemists R. G. W. Norrish and G. Porter monitored reaction intermediates in the µs time range with the help of two light flashes (mercury vapour lamps). It leaded to their Nobel prize in 1967. Their work was based on the principle of 'pump-probe technique,' established by Abraham and Lemoine in 1899.[47] Since then, this area has been substantially developed over the years, thanks to the invention of state-of-the-art light sources. More shorter laser pulses are being developed and faster dynamical processes could be captured. D. R. Herschbach, Y. T. Lee, and J. C. Polanyi studied chemical dynamics in a reaction mixture applying 'ns' laser pulses and won the Nobel prize in the year 1986.[49] In 1988, Ahmed Zewail used 'ps' and 'fs' laser pulses to study the real time reaction dynamics and monitored the transition states, winning the Nobel prize in 1999.[50] This work started revolution in the pump-probe spectroscopy field. TAS is now being used to study the charge carrier dynamics and comprehend the inner photophysics of wide variety of materials. In my thesis work, we have employed short fs laser pulses (pulse width of 50-100 fs) to monitor ultrafast photophysical processes in various 2D materials.

2.4.1.1. Basic principle of TAS

TAS refers to the study of excited state photophysical processes on application of two ultrashort (mechanically or electronically delayed) laser pulses in atoms, molecules, and solid materials. These two pulses are named as pump and probe pulses, according their functions. Pump pulse create population in the excited state of the system and the dynamic evolution of that population

is monitored by the probe pulse, varying the delay line between pump and probe. In ideal case, a tunable pump pulse is employed in order to monitor different kind of transitions inside the material. On the other hand, probe pulses are broadband in nature so that all different processes can be traced. A simple schematic description of pump-probe TAS technique is shown in **figure 2.17a**.
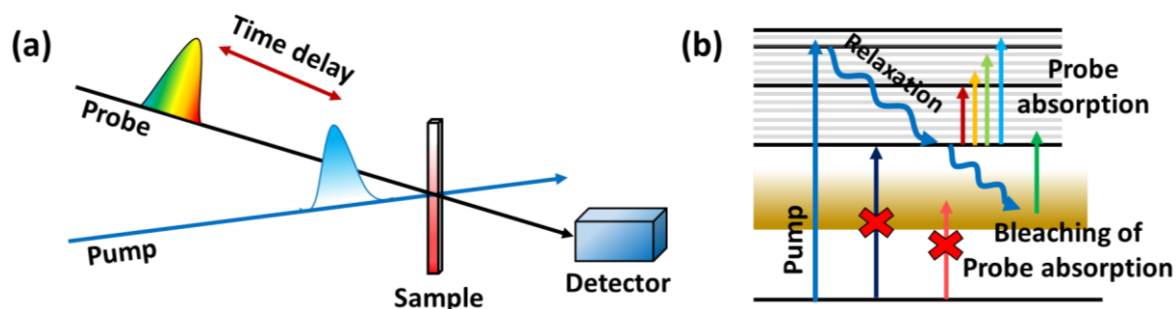
Figure 2.17: (a) Basic outline of a TAS experiment. **(b)** Different photophysical processes inside a material, on application of delayed pump and probe pulses.

Probe pulses are delayed from that of the pump pulses in time scale. Once the intense pump laser falls on the material, the ground state charge carriers are excited to higher energy states and delayed probe pulse monitor the dynamics of these excited charge carriers (**Figure 2.17b**). With the application of broadband pulses, a broad transient spectrum can be recorded, which will monitor many different phenomena simultaneously. Depending upon the monitoring transition, the absorption of probe can be either bleached or enhanced, resulting in negative and positive differential absorption (ΔA) signal in the transient spectra.

2.4.1.2. Instrumentation of a FTAS Setup

A FTAS setup is comprised of three primary components, a. Main laser, b. Optical parametric Amplifier (OPA) and c. Spectrometer.

a. Main laser: This is the most important component of any transient instrument, which generates requisite laser pulses to carry out a pump-probe phenomenon. In my thesis, we have used a Coherent Astrella laser system, having output of 800 nm laser pulses with ~ 50 fs pulse width, 1 kHz repetition rate and ~ 5 mJ/pulse energy. The basic parts of this laser system are TiS oscillator, multipass TiS amplifier and a Nd-YLF pump laser (**Figure 2.18**).

(i) *Ti-Sapphire (TiS) oscillator* – The oscillator in a modern-day laser setup consisted with Ti^{3+} doped Sapphire (Al_2O_3) gain medium, which is a well-known solid-state laser. Starting

from the invention in 1986, this laser system is being widely used for the generation of tunable and short pulsed lasers. TiS lasers have successfully replaced the Dye lasers, which were very common earlier. The properties which make these laser systems unique are, good thermal conductivity (can sustain high laser power), large gain bandwidth (helps in the generation of short laser pulses), tunable emission wavelength etc.
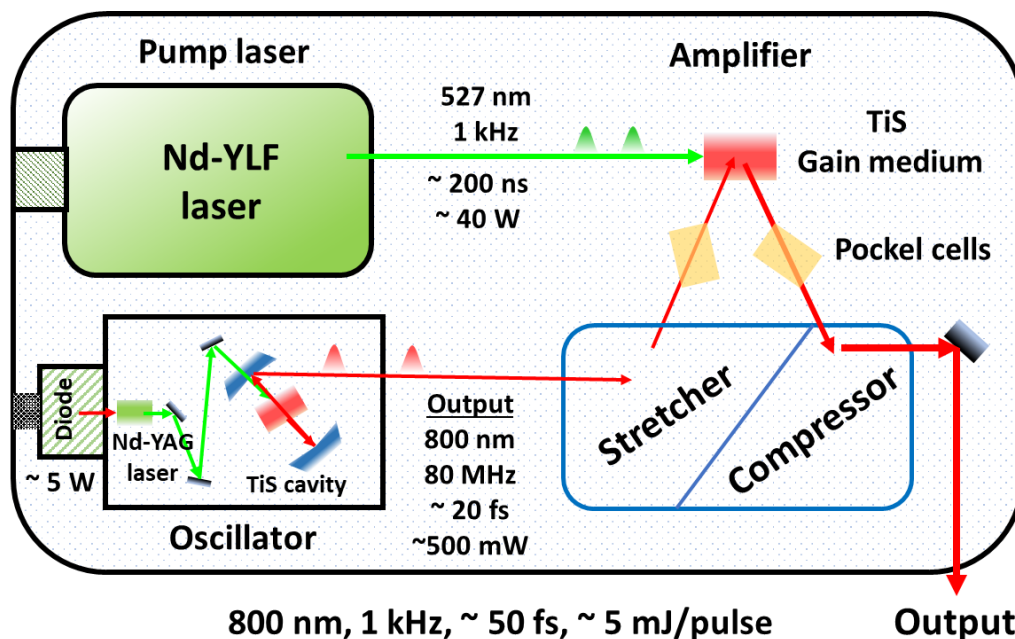
Figure 2.18: Basic outline scheme of the main laser setup.

The doping concentration of Ti^{3+} in sapphire is kept very low (0.15 – 0.25 %) in general, to maintain the crystallinity. TiS absorbs in the region of 400 to 600 nm and emits in broad regime of 650 to 1100 nm. The lifetime of TiS is quite short (3.2 μs), but the saturation power density is usually very high in these crystals. Hence, in order to pump TiS crystal we need a high intensity focussed laser beam. Earlier these crystals were pumped with Argon ion lasers (514 nm), which were large, expensive, and inefficient. So, later these were replaced by diode pumped solid-state lasers (DPSS). In our instrument, diodes are used to generate 532 nm continuous green laser from a Nd-YAG gain medium and this DPSS laser pump the TiS crystal. The basic alignment of the oscillator is shown in **figure 2.19**.

For the generation of ultrashort laser pulses, the TiS gain medium is placed inside a cavity (in between two or more mirrors) where the laser can be trapped for a requisite amount of time. Kerr lens mode-locking technique is employed in order to produce 'fs' or 'ps' laser pulses. When a highly intense laser beam propagates through a non-linear medium (Here TiS), the refractive index of the system is changed non-linearly, based on the following equation,

$$\eta(\nu) = \eta_0(\nu) + \eta_2(\nu)I$$

where, $\eta_0(\nu)$ is the refraction index of the medium in the normal condition, which is a function of frequency (ν), $\eta_2(\nu)$ is the non-linear coefficient deciding the coupling strength between the refraction index and the electric field of light.

In the laser cavity, the beam propagates as a gaussian distribution and the intensity of the passing electric field can be expressed as a function of distance ($\mathbf{r}$) from the centre of the beam,

$$I(r) = \exp(-gr^2)$$

where, $\mathbf{g}$ is the shape factor.
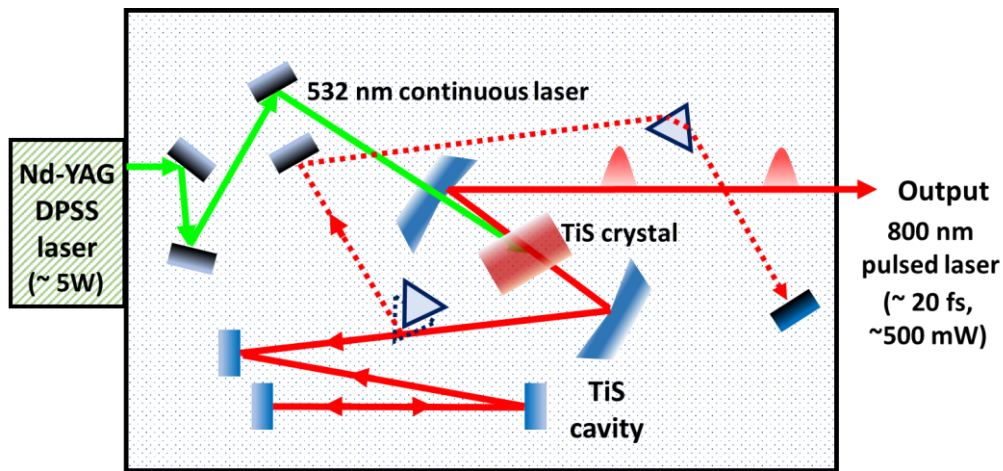
Figure 2.19: Basic components of the TiS oscillator.

So, upon illumination with a laser beam, the refractive index does not get distributed homogeneously. It is maximum at the centre of the beam and decreases toward the circumference. This phenomenon is known as '**Kerr effect**' and the medium is called '**Kerr medium**.' Due to this effect, only higher intense beams are able to transmit through the media. This intensity dependent loss of the radiation is repeated with every round trip of the laser beam through the Kerr medium. This process of producing pulsed laser is known as 'Kerr lens mode-locking' or 'Self mode-locking' as the medium itself takes part in the focussing process. Owing to large PL bandwidth of the gain media, TiS crystal is capable of generating extremely short pulses (< 6 fs). As the laser beam repeatedly travels inside the cavity, it will experience group velocity dispersion (GVD), which is neutralized by placing two prisms inside the cavity. Also, the polarisation of the laser gets hampered owing to bi-refringent property of the TiS medium. This is corrected by placing the crystal at Brewster angle.

In our main laser setup (Astrella, Coherent) a TiS oscillator (Vitara-T) is used to produce 'fs' laser pulses. The gain medium is pumped with DPSS laser (Verdi-G series), which is a

continuous wave of 532 nm wavelength and ~ 5 W average power. This green laser is generated from a Nd-YAG crystal which was pumped with a diode laser (808 nm). The oscillator produces < 20 fs laser pulses with 800 nm wavelength, 80 MHz repetition rate and ~ 500 mW average power. This output is known as the '**Seed laser**,' which will be further amplified in the multipass amplifier system.

(ii) *Multipass Ti-Sapphire amplifier* – The seed laser produced from the oscillator has very low intensity to carry out any pump-probe experiment. So, this intensity of these laser pulses needs to be amplified. In our instrument, a multipass TiS amplifier is used for enhancing the seed laser pulse intensity in several order of magnitudes. The components of this amplifier setup are, pulse stretcher, pulse picker, TiS amplifier, pulse compressor and synchronization electronics. This amplification process works on the principle of **chirped pulse amplification (CPA)**, shown in **figure 2.20**.
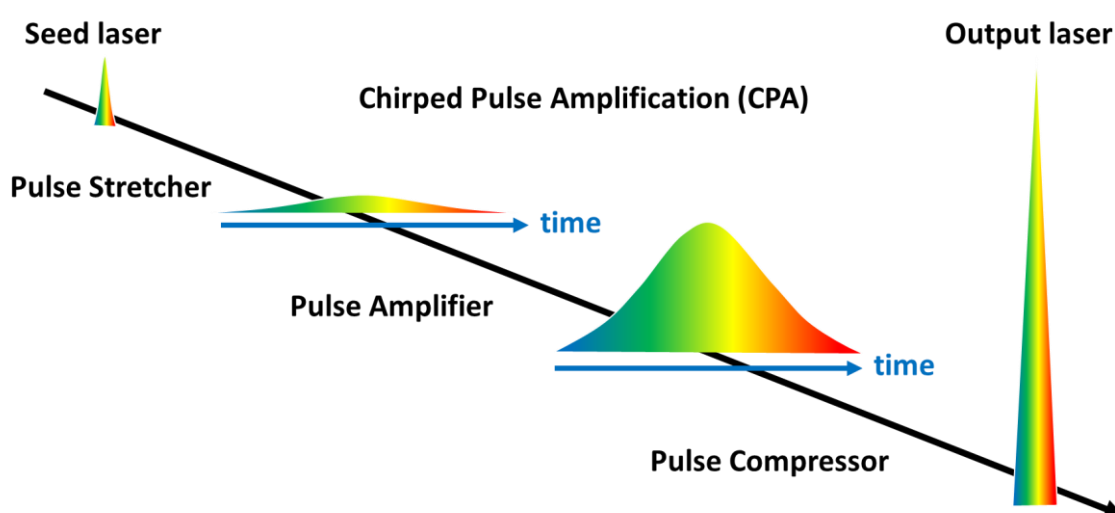
Figure 2.20: Basic principle of the CPA process.

<u>Pulse stretcher</u>

The seed laser first passes through a pulse stretcher box, which stretches the fs laser pulses into ps pulses, thereby diminishing the intensity of the pulses. This stretching of the pulses is very crucial for the overall amplification process. As the gain medium in the amplifier uses Kerr lens mode-locking principle, the TiS crystal tend to self-focus the laser beam. In the process of amplification, the average power of the laser reaches extremely high value and damages the crystal. To avoid this damage, pulses are temporally stretched before amplification, so that the peak pulse energy stay below the threshold limit of the TiS crystal while amplifying. The

schematics of the pulse stretcher is shown in **figure 2.21**. It is consisted with diffraction grating, spherical mirror, and plane mirrors. The stretching procedure works on the principle of GVD. The diffraction grating spread the pulse spectrum and the mirrors organize the beam path in such a way that bluer light components travel longer distance than the others. As a are result red beams leave the stretcher early than the blue ones and the pulses are stretched. A vertical retroreflector sends back the stretched pulses inside the stretcher and four passes are made to spatially reconstruct the stretched beam.
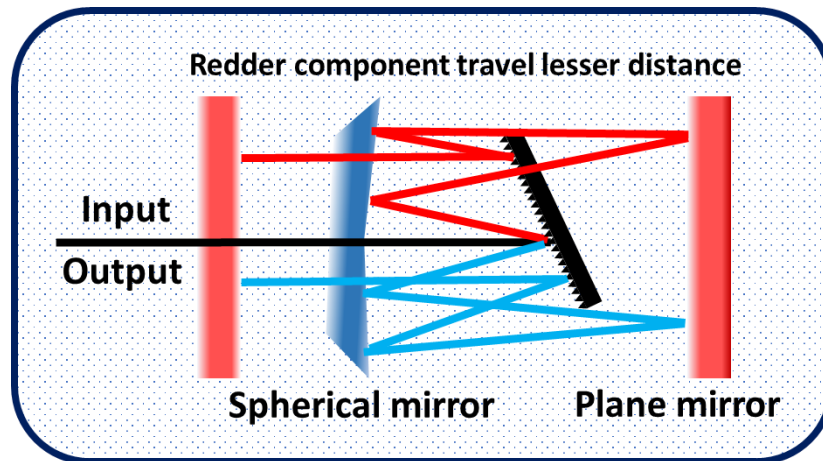
Figure 2.21: Basic outline of the femtosecond pulse stretcher.

Pulse Picker and Synchronization electronics

The stretched pulses pass through the pulse picker before hitting the amplifier, where the repetition rate of the pulses was decreased down from MHz to kHz. It works on the electro-optical pockel cell effect. When there is no voltage applied to the pockel cell, horizontal stretched pulses pass through the pulse picker as it is and dumped. But, on application of voltage the polarization of the pulses is changed to vertical and the pulses are now authorized to pass through the polariser, to be used for further amplification. The basic working principle of these pockel cells are shown in **figure 2.22**. In our system two pockel cells are placed, which act as quarter wave plates (effecting polarization change of λ/4) on application of voltage. These pockel cells act as the entry and exit gates of seed pulse trains to attain desired amplification. There are Synchronization electronics in place to control the application of voltage on the pockel cells, so that only requisite pulses can be picked from the whole pulse train and amplified further. These electronics are controlled by the SDG (Synchronisation and

Delay Generator) Elite unit, which maintains proper delay between the pockel cells by adjusting the applied voltage.
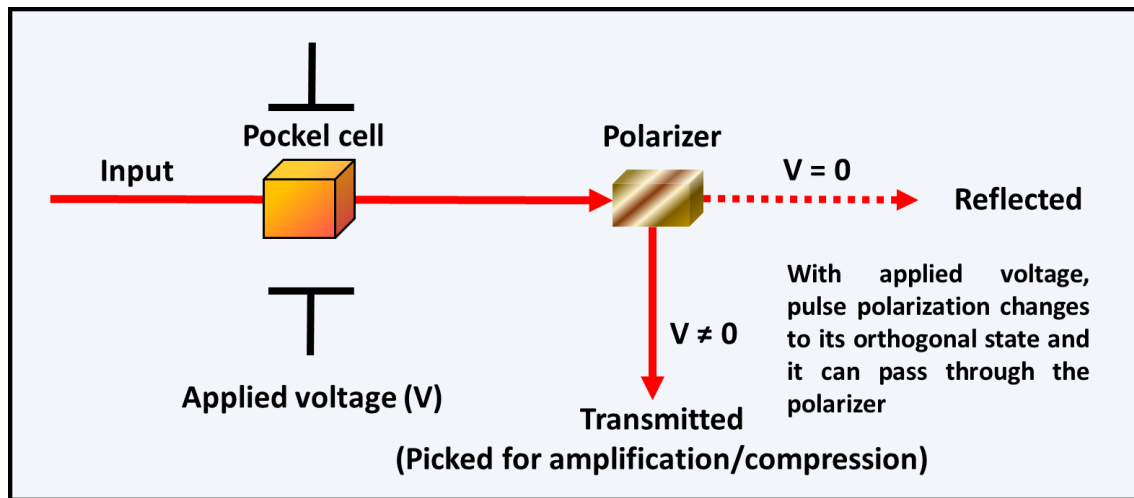
Figure 2.22: Basic working principle of a pockel cell.

TiS amplifier

The 1 kHz stretched seed pulse enters the amplifier arena where a TiS crystal is placed at the focal point of two concave mirrors. The basic outline of the amplifier is shown in **figure 2.23**. The TiS gain medium is pumped with a highly intense pump laser beam having the same repetition rate. This pump laser (Revolution, Diode pumped Q-switched laser) is made of a Nd-YLF crystal, which produces 527 nm pulsed laser with 1 kHz repetition rate, ~ 200 ns pulse width and ~ 40 W average power. The pump laser maintains the population inversion in the gain medium and enhance the stimulated emission. The concave mirrors construct a telescopic configuration and allow the seed pulse to pass inside the cavity several (six, eight or ten) times, focussing on the gain medium. The number passes are fixed according to the amplification requirement and damage threshold of the TiS crystal. With every pass, the laser beam intensity is amplified and falls close to the centre of the mirror (where exit slit present), finally comes out of the amplifier with completion of passes. The pump laser is focussed at the same spot on the crystal, as that of the seed laser.

Pulse compressor

Once the amplification is complete the pulses are compressed in order to get 'fs' laser output. The pulse compressor is comprised with two gratings, which are arranged in such a way that

redder components travel longer as compared to bluer ones (Opposite to that of the stretcher, **shown in figure 2.24**).
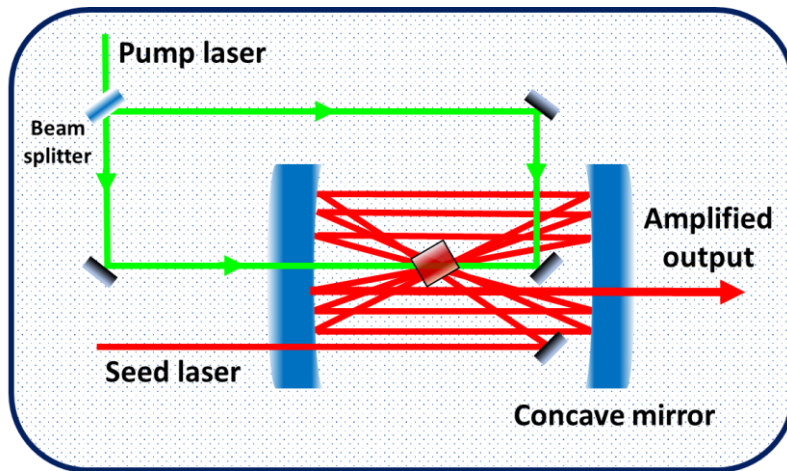
Figure 2.23: Basic outline of the TiS amplifier.

Varying the distance within those two gratings, the compressor unit is capable of generating similar pulse width as that of the initial seed pulse before stretching. Following the compression, the fs laser pulses come out of the main laser and used in pump probe spectroscopy. Our main laser setup produces 800 nm laser pulses with ~ 50 fs pulse width, 1 kHz repetition rate and ~ 5 mJ/pulse energy.
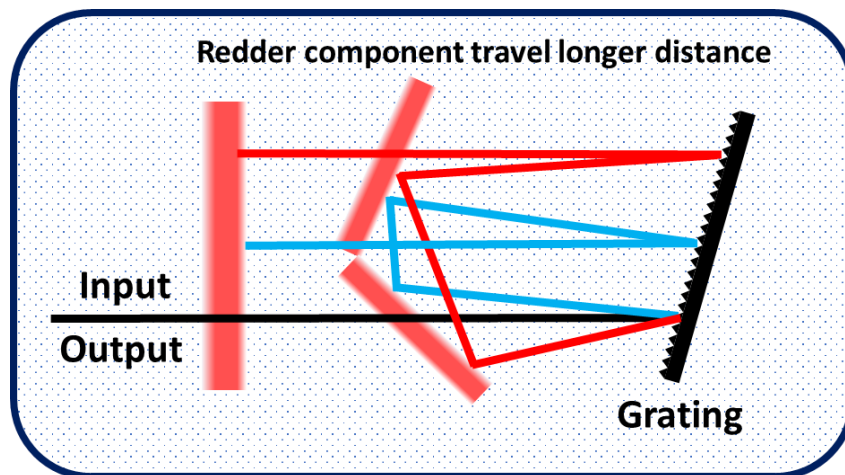
Figure 2.24: Basic outline of the femtosecond pulse compressor.

b. Optical parametric Amplifier (OPA): The output pulses from the main laser are splitted into two components using a beam splitter (65:35). The higher and lower energy components are named as pump and probe laser pulses. Pump laser is tuned into desired excitation wavelengths for exciting different transitions of a material, implying optical parametric

amplification (OPA) technique. OPA is the process of amplifying (or frequency modulating) an optical signal by means of parametric non-linearity and a pump laser. This method is widely popular for the generation of many wavelengths, which are usually not accessible due to lack of the appropriate gain mediums.

In my thesis, we have used an OPERA-SOLO setup which is a two-stage amplification system. At the first stage of amplification, the pump laser beam is splitted into two components using a beam splitter. The low energy beam passes through a sapphire crystal and generate white light continuum (WLC). This WLC and the other component (act as a pump) are focussed on a non-linear crystal, which are non-collinearly overlapped, spatially and temporally.
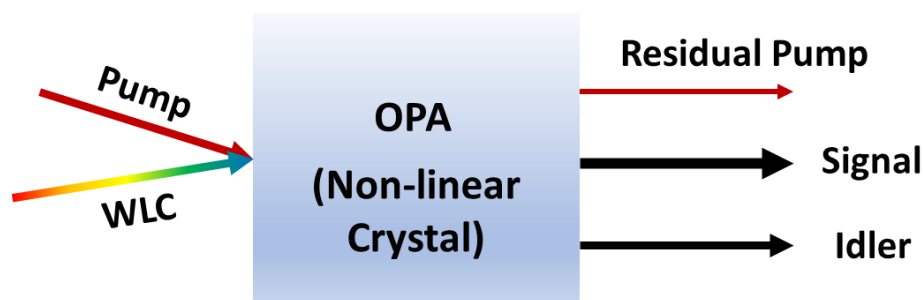
Figure 2.25: Basic principle of the OPA process.

This results in the signal and Idler beams. The frequency of the signal (ν_s), Idler (ν_i) and the pump (ν_p) beam is related as,

$$\nu_p = \nu_s + \nu_i$$

The residual pump beam and the Idler beam is blocked to only pass the signal beam into the second stage. This signal beam collinearly overlaps with a second pump pulse on another non-linear crystal, which again results in an amplified signal and Idler beams. These outputs give rise to our desired colour. According to the requirement of the output, the signal and pump beams are used applying requisite mirrors in their path. A general laser path in the OPERA-SOLO is shown in **figure 2.26**. The wavelength of the first signal pulse is modulated by adjusting the delay-1 line (delay between WLC and the first pump pulse) and the angle of the first crystal. The wavelength of the second signal and Idler pulses are adjusted by fine tuning first signal wavelength, delay-2 (delay between first signal beam and the second pump pulse) and the second crystal angle. All these adjustments can be done with the help of a software, synchronized with the OPERA-SOLO.
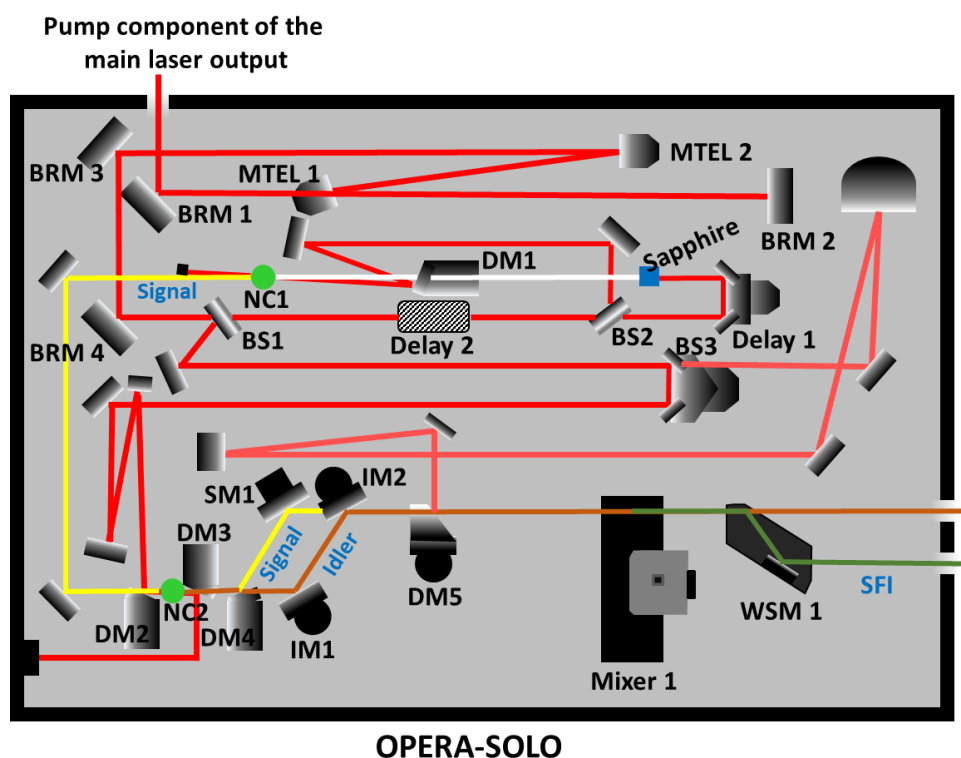
Figure 2.26: Basic outline of an OPERA-SOLO setup, where path of the pump laser is shown according to the generation of a Sum Frequency Idler (SFI) wavelength.

The frequency output from the OPA is further extended using frequency mixers (Mixer 1 in **figure 2.26**), which take part in second harmonic generation (SHG), sum frequency generation (SFG) and difference frequency generation (DFG) according to the wavelength requirement. These mixers are made up of several non-linear crystals cut at specific angles and placed in a rotation stage controlled by the software. These crystals are rotated with the software to a particular phase matching angle for the generation of a particular frequencies. In our system BBO crystal is installed in the mixers for converting signal and Idler pulses into their SHG frequencies. For the SHG process, horizontal polarization is needed, which is achieved by placing a Berek compensator before the mixer. The output pump laser beam is having vertical polarization. A wavelength separator (WSM) is used just after the mixer to separate out our desired frequency from the others (**Figure 2.26**).

c. Spectrometer (Helios-FIRE): Transient absorption spectrometer employs pump and probe pulses (separated beams from the main laser output) to produce spectral and dynamical data for the material under investigation. We have already discussed in the previous section how desired excitation wavelength is generated from the pump pulse. The probe pulse on the other

hand directly enters the spectrometer with the help of few properly placed mirrors. The basic layout of the Helios-FIRE spectrometer is shown in **figure 2.27**.
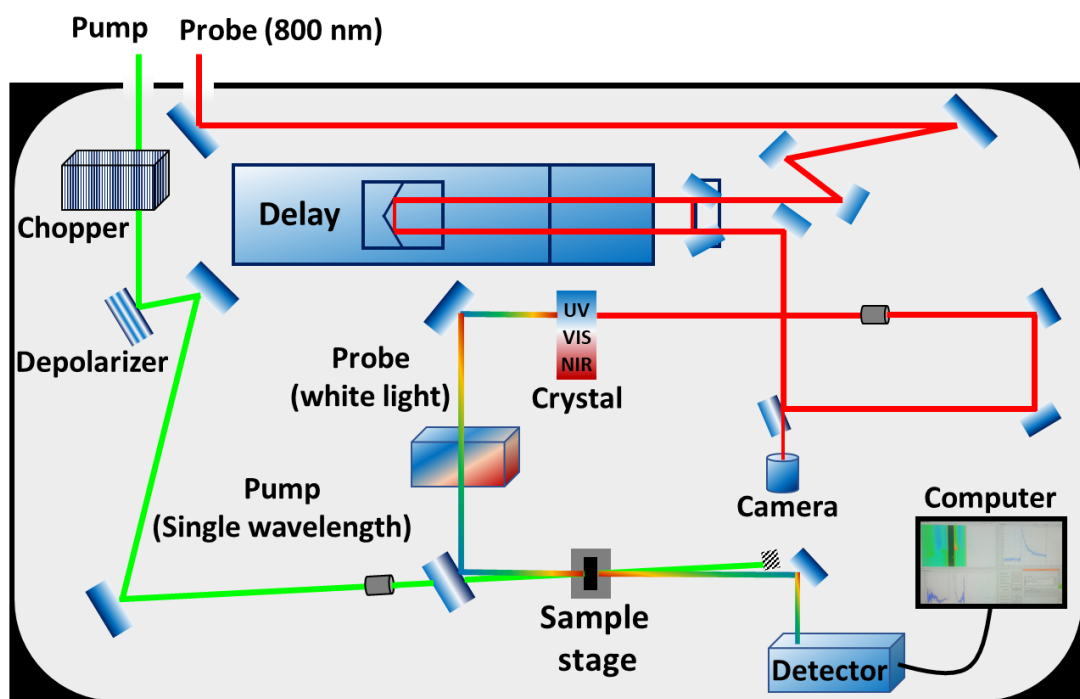
Figure 2.27: Basic layout of the Helios-FIRE spectrometer of the TA instrument.

At first, the pump pulse passes through a mechanical chopper to reduce the repetition rate of the laser to 500 Hz. Followed by that, a depolarizer is placed to depolarize the pump beam, in order to avoid any dipole-dipole interaction with the probe pulses. For polarization dependent experiments a half-wave plate and a polarizer is used in place of the depolarizer. On the other hand, 800 nm probe light is directed into a delay set up (A set of retro-reflectors and mirrors kept in a mechanical delay line) inside the spectrometer. This delayed probe pulse is focussed on appropriate crystals to produce white light continuums of different wavelength range. In our set up, CaF_2, Sapphire, and Yttrium Aluminium Garnet (YAG) crystals are used for the generation of UV-Vis, Vis and NIR probe pulses, respectively. The range of these three regions are 350-750 nm, 450-800 nm, and 800-1600 nm. For monitoring requisite wavelength region, those crystals are placed in the path of the probe with the help of the Helios-FIRE software. In fact, all the motors inside the spectrometer are connected electronically and can be controlled with the help of different softwares. The as produced white light passes through a filter and focussed on the sample. Pump beam is focussed on the same position on the sample as that of probe to attain spatial overlap. The sample stage is associated with optional rotation for the film samples. In case of solution phase samples, a magnetic stirrer is used to avoid any charging

effect. After transmitting through the sample, the pump beam is blocked and the probe beam is directed to a detector, connected with the computer. For UV-Vis and Vis lights a complementary metal-oxide semiconductor (CMOS) sensor is used, whereas for NIR detection INGaAs sensor is employed. Perfect spatial and temporal overlap of the pump and probe beam would result in a TA signal for the sample, which can be collected in the Helios-FIRE software.

White light generation (WLG)

White light continuum or sometimes referred to as supercontinuum is generated when a very short laser pulse is focussed on a transparent non-linear medium.[51] This phenomenon is observed in many non-linear solid and gaseous materials. It was first observed by Alfano and Shapiro in 1960s.[52] They focussed ps laser pulses on a glass substrate to observe a supercontinuum of Vis-NIR radiation. Later, in 1983 Fork et al. demonstrated a fs supercontinuum using an Ethylene Glycol film.[53] In general, the characteristics produced continuum depends on the medium and the input pulse properties. Also, there are many different theories behind the observation of this phenomenon, among which Self focussing and Self-phase modulation (SPM) is most widely accepted.[51] SPM is based on temporal modulation of the non-linear phase of a pulsed laser.[54,55] When an electric field propagates through a non-linear media along z-direction, it can be expressed as,

$$E_{in} = E_0 e^{i(knz-\omega_0 t)} = E_0 e^{i(\phi_0)}$$

As the intense laser beam propagates through the medium, refractive index of the medium modifies itself according to the self-focussing phenomenon ($n = n_0 + n_2 I$). If the laser pulse propagates through a distance L in the medium, the output electric field is modified as,

$$E_{out} = E_0 e^{i(kn_0 L + kn_2 I(t)L - \omega_0 t)} = E_0 e^{i(\phi_{NL} + \phi_0 t)}$$

Where ϕ_{NL} is the phase distribution in the non-linear media and can be expressed as,

$$\phi_{NL}(\tau) = \int_0^L n_2 I(z,\tau)\frac{\omega_0}{c} dz,$$

Here c is the speed of light.

The frequency of the laser pulses is changed with this time dependent phase modulation, the rate of increase or decrease of phase along the laser pulse distance.

$$\text{pulse frequency, } \omega = -\left[\frac{\partial(\phi_{NL}+\phi_0)}{\partial t}\right]$$

This results in a broad spectra both in the lower (Stokes) and higher (Anti-Stokes) energy regions of the incident laser frequency.

Origin of transient signal in the TA spectrometer

When a light passes through an absorbing medium, the absorbance can be expressed through Beer-Lambert's equation,

$$A = \log\left(\frac{I_0}{I}\right) = \varepsilon(\lambda)cL$$

Where, **ε** is the molar absorption coefficient, which depends on the material and the wavelength of the light. **c** is the molar concentration of the solution and **L** measures optical path length.

In TAS, two laser pulses (pump and probe) pass through the medium, maintaining a variable delay time. At first, pump laser falls on the sample and excite the system into the higher energy states. Probe laser monitor the subsequent relaxation and recombination processes take place inside the system. Detector only evaluates the change in intensity in the probe beam, in presence and in absence of the pump beam and results in a differential absorption (**ΔA**) signal.

ΔA is defined as,

$$\Delta A = A_{\text{with pump}} - A_{\text{without pump}}.$$

The intensity of the probe pulse in presence of pump can be given by,

$$I(\lambda, \Delta t) = I_0(\lambda)\, 10^{-\varepsilon(\lambda)N(\Delta t)L}$$

Here, $I_0(\lambda)$ is the intensity of probe pulse in absence of pump, and Δt refers to a certain delay time between pump and probe. $N(\Delta t)$ defines the excited state population in presence of pump, which is equivalent to the concentration of the solution.

So,

$$\Delta A\,(\Delta t) = \varepsilon(\lambda)N(\Delta t)L$$

Now, considering exponential decay of the transient population of the excited state $N(\Delta t)$ can be written as,

$$N(\Delta t) = N_0 e^{-(\Delta t/\tau)}$$

where, N_0 is the initial population (maximum) and τ refers to a time scale.

So, we have

$$\ln(\Delta A\,(\Delta t)) = \ln(\varepsilon_{\lambda_i} N_{(\Delta t)}L) - \frac{\Delta t}{\tau}$$

With the determination of the differential absorption, we can actually monitor the time dependent depletion of excited state population, for a particular wavelength λ (particular transition).

Now,

$$A_{\text{with pump}} = \log\left(\frac{I_0(\lambda)}{I(\lambda, \Delta t)}\right) \text{ and } A_{\text{without pump}} = \log\left(\frac{I_0(\lambda)}{I(\lambda)}\right)$$

Here, all the intensities are probe intensities. **Δt** is associated with the probe intensity in presence of pump.

So,

$$\Delta A = A_{\text{with pump}} - A_{\text{without pump}} = \log\left(\frac{I(\lambda)}{I(\lambda, \Delta t)}\right)$$

This is the fundamental equation of TAS, which decides the appearance of any signal in a TAS measurement. This ΔA value can be both negative and positive, resulting in negative and positive signal in TAS, which are referred as ground state bleach (**GSB**) and photoinduced absorption (**PIA**) or excited state absorption (**ESA**) respectively. **ΔA** will be negative when, I(λ) < I (λ, Δt); i.e., probe has higher intensity in presence of pump or probe is less absorbed in presence of pump. This is possible when there exists some ground state absorption or stimulated emission (**SE**) for that transition. In case of a ground state absorption, pump pulse excites the system to higher energy states and diminish the probe absorption in the similar transition region. This results in lower absorption of probe pulse in presence of pump. On the other hand, **ΔA** becomes positive when, I(λ) > I (λ, Δt). This occurs when pump helps in enhanced absorption of probe pulse (PIA case).
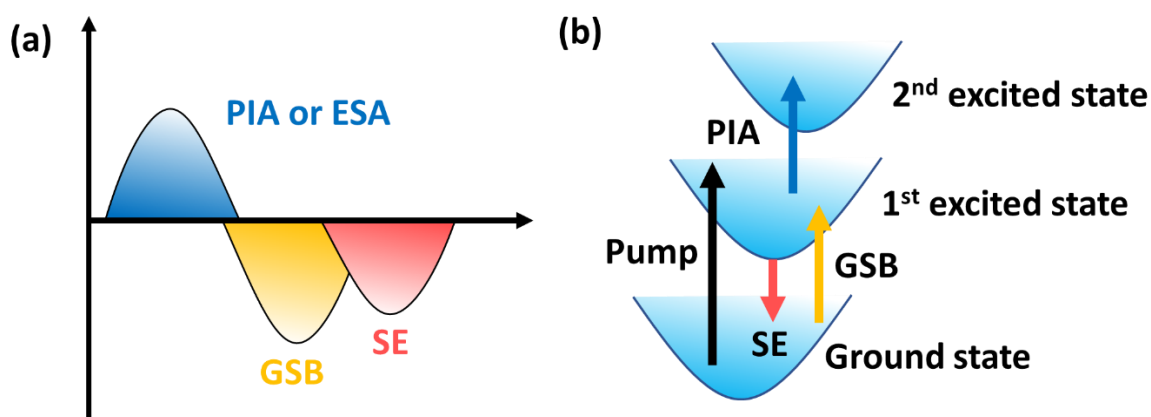
Figure 2.28: (a) Different types of signals in TAS and **(b)** their origins.

In our set up, the collected data were analysed and fitted with the help of a Surface Explorer (SX) software, which works via LabVIEW™ controls. SX is a simple and efficient data plotting software, which can simultaneously analyse transient spectra and dynamics, as well as 3D colour contour plot. This software is also associated with artifact correction tools like background correction, scattered light subtraction, time zero correction, chirp correction etc., to obtain clear and actual data. SX is capable of advanced fitting techniques like singular value decomposition (SVD) and global fitting. For fitting dynamic profiles, it uses a sum of convoluted exponentials in the form of,

$$S(t) = e^{-\left(\frac{t-t_0}{t_P}\right)^2} \sum_i A_i \, e^{-\frac{t-t_0}{t_i}}$$

$$\text{and } t_p = \frac{IRF}{2\ln 2}.$$

Here, **IRF** is the full width half maxima (FWHM) of instrument response function, which decides the temporal resolution of the instrument. In our instrument, it varies between 50 – 100 fs, depending upon the excitation wavelength. t_0 is the time zero, which commence the temporal overlap of pump and probe pulses. Starting from time zero, transient signal appears. A_i and t_i are the amplitude and time components for the ith exponential process. From the iteration of these three components (i, A_i and t_i), we can obtain a best fit for a dynamic profile, associated with the lower standard deviation value.

2.5. Temperature dependent studies

The electrical and optical properties of any material are often temperature dependent, owing to significant modulation of many parameters, like, dielectric constant, electronic band structure, charge carrier distribution, band gap, quasiparticle binding energy, electron-phonon coupling, phonon emission, defect density etc. with the variance of lattice temperature. So, in order to properly investigate the inner photophysics of any system, it is very important carry out all the measurements with the variance of lattice temperature.

In my thesis, we have used a closed cycle cryostat setup with the transient spectrometer in an ad hoc manner to carry out the temperature dependent measurements whenever required. This setup is capable of varying the temperature from 4K to 325K. The main workstation is made of Cryo industries of America Inc., which is assembled with a temperature controller from Lakeshore company (Model 335, 300mK- 1500K), an air-cooled Helium compressor from

Sumitomo cryogenics (HC- 4A Zephyr series) and a TPS-compact Turbo pumping system from Agilent Technologies.

2.6. References

(1)   Bryant, W. A. The Fundamentals of Chemical Vapour Deposition. *J Mater Sci* **1977**, *12* (7), 1285-1306.

(2)   Sun, L.; Yuan, G.; Gao, L.; Yang, J.; Chhowalla, M.; Gharahcheshmeh, M. H.; Gleason, K. K.; Choi, Y. S.; Hong, B. H.; Liu, Z. Chemical Vapour Deposition. *Nat Rev Methods Prim* **2021**, *1* (1), 5.

(3)   Abegunde, O. O.; Akinlabi, E. T.; Oladijo, O. P.; Akinlabi, S.; Ude, A. U. Overview of Thin Film Deposition Techniques. *AIMS Mater Sci* **2019**, *6* (2), 174-199.

(4)   Mahan, J. E. Physical Vapor Deposition of Thin Films; 2000.

(5)   Seshan, K. *Handbook of Thin-Film Deposition Processes and Techniques: Principles, Methods, Equipment and Applications*; Materials science and process technology series: Electronic materials and process technology; Noyes Publications/William Andrew Pub., 2002.

(6)   Cai, Z.; Liu, B.; Zou, X.; Cheng, H.-M. Chemical Vapor Deposition Growth and Applications of Two-Dimensional Materials and Their Heterostructures. *Chem Rev* **2018**, *118* (13), 6091-6133.

(7)   Mattevi, C.; Kim, H.; Chhowalla, M. A Review of Chemical Vapour Deposition of Graphene on Copper. *J Mater Chem* **2011**, *21* (10), 3324-3334.

(8)   Wang, J.; Li, T.; Wang, Q.; Wang, W.; Shi, R.; Wang, N.; Amini, A.; Cheng, C. Controlled Growth of Atomically Thin Transition Metal Dichalcogenides via Chemical Vapor Deposition Method. *Mater Today Adv* **2020**, *8*, 100098.

(9)   Pant, M.; Singh, R.; Negi, P.; Tiwari, K.; Singh, Y. A Comprehensive Review on Carbon Nano-Tube Synthesis Using Chemical Vapor Deposition. *Mater Today Proc* **2021**, *46*, 11250-11253.

(10)   Goswami, T.; Rani, R.; Hazra, K. S.; Ghosh, H. N. Ultrafast Carrier Dynamics of the Exciton and Trion in MoS_2 Monolayers Followed by Dissociation Dynamics in $Au@MoS_2$ 2D Heterointerfaces. *J Phys Chem Lett* **2019**, 3057-3063.

(11)   Coleman, J. N.; Lotya, M.; O'Neill, A.; Bergin, S. D.; King, P. J.; Khan, U.; Young, K.; Gaucher, A.; De, S.; Smith, R. J.; et al. Two-Dimensional Nanosheets Produced by Liquid Exfoliation of Layered Materials. *Science* **2011**, *331* (6017), 568-571.

(12)   Smith, R. J.; King, P. J.; Lotya, M.; Wirtz, C.; Khan, U.; De, S.; O'Neill, A.; Duesberg, G. S.; Grunlan, J. C.; Moriarty, G.; et al. Large-Scale Exfoliation of Inorganic Layered Compounds in Aqueous Surfactant Solutions. *Adv Mater* **2011**, *23* (34), 3944-3948.

(13)   Nicolosi, V.; Chhowalla, M.; Kanatzidis, M. G.; Strano, M. S.; Coleman, J. N. Liquid Exfoliation of Layered Materials. *Science* **2013**, *340* (6139), 1226419.

(14)   Yi, M.; Shen, Z. A Review on Mechanical Exfoliation for the Scalable Production of Graphene. *J Mater Chem A* **2015**, *3* (22), 11700-11715.

(15)   Xu, Y.; Cao, H.; Xue, Y.; Li, B.; Cai, W. Liquid-Phase Exfoliation of Graphene: An Overview on Exfoliation Media, Techniques, and Challenges. *Nanomaterials* **2018**, *8* (11), 942.

(16)   Goswami, T.; Bhatt, H.; Babu, K. J.; Kaur, G.; Ghorai, N.; Ghosh, H. N. Ultrafast Insights into High Energy (C and D) Excitons in Few Layer WS_2. *J Phys Chem Lett* **2021**, *12* (28), 6526-6534.

(17)   Ndlwana, L.; Raleie, N.; Dimpe, K. M.; Ogutu, H. F.; Oseghe, E. O.; Motsa, M. M.; Msagati, T. A. M.; Mamba, B. B. Sustainable Hydrothermal and Solvothermal Synthesis of Advanced Carbon Materials in Multidimensional Applications: A Review. *Materials*. 2021.

(18)   Yun, J.-H.; Wang, L.; Amal, R.; Ng, Y. H. One-Dimensional TiO_2 Nanostructured Photoanodes: From Dye-Sensitised Solar Cells to Perovskite Solar Cells. *Energies*. 2016.

(19)   Einarsrud, M.-A.; Grande, T. 1D Oxide Nanostructures from Chemical Solutions. *Chem Soc Rev* **2014**, *43* (7), 2187-2199.

(20)   Goswami, T.; Yadav, D. K.; Bhatt, H.; Kaur, G.; Shukla, A.; Babu, K. J.; Ghosh, H. N. Defect-Mediated Slow Carrier Recombination and Broad Photoluminescence in Non-Metal-Doped $ZnIn_2S_4$ Nanosheets for Enhanced Photocatalytic Activity. *J Phys Chem Lett* **2021**, *12* (20), 5000-5008.

(21) Goswami, T.; Bhatt, H.; Yadav, D. K.; Saha, R.; Babu, K. J.; Ghosh, H. N. Probing Ultrafast Hot Charge Carrier Migration in MoS_2 Embedded CdS Nanorods. *J Chem Phys* **2021**, *156* (3), 34704.

(22) Enustun, B. V; Turkevich, J. Coagulation of Colloidal Gold. *J Am Chem Soc* **1963**, *85* (21), 3317-3328.

(23) Polte, J.; Ahner, T. T.; Delissen, F.; Sokolov, S.; Emmerling, F.; Thünemann, A. F.; Kraehnert, R. Mechanism of Gold Nanoparticle Formation in the Classical Citrate Synthesis Method Derived from Coupled In Situ XANES and SAXS Evaluation. *J Am Chem Soc* **2010**, *132* (4), 1296-1301.

(24) Chauhan, A.; Chauhan, P. Powder XRD Technique and Its Applications in Science and Technology. *J Anal Bioanal Tech* **2014**, *5*, 1-5.

(25) Tan, W. L.; McNeill, C. R. X-Ray Diffraction of Photovoltaic Perovskites: Principles and Applications. *Appl Phys Rev* **2022**, *9* (2), 21310.

(26) BATTERMAN, B. W.; COLE, H. Dynamical Diffraction of X Rays by Perfect Crystals. *Rev Mod Phys* **1964**, *36* (3), 681-717.

(27) Shipp, D. W.; Sinjab, F.; Notingher, I. Raman Spectroscopy: Techniques and Applications in the Life Sciences. *Adv Opt Photonics* **2017**, *9* (2), 315-428.

(28) RAMAN, C. V; KRISHNAN, K. S. A New Type of Secondary Radiation. *Nature* **1928**, *121* (3048), 501-502.

(29) Das, R. S.; Agrawal, Y. K. Raman Spectroscopy: Recent Advancements, Techniques and Applications. *Vib Spectrosc* **2011**, *57* (2), 163-176.

(30) Liang, F.; Xu, H.; Wu, X.; Wang, C.; Luo, C.; Zhang, J. Raman Spectroscopy Characterization of Two-Dimensional Materials. *Chinese Phys B* **2018**, *27* (3), 37802.

(31) Cong, X.; Liu, X.-L.; Lin, M.-L.; Tan, P.-H. Application of Raman Spectroscopy to Probe Fundamental Properties of Two-Dimensional Materials. *npj 2D Mater Appl* **2020**, *4* (1), 13.

(32) Moulder, J. F.; Stickle, W. F.; Sobol, W. M.; Bomben, K. D. Handbook of X-Ray Photoelectron Spectroscopy; 1992.

(33) Addou, R.; Wallace, R. M. Using Photoelectron Spectroscopy in the Integration of 2D Materials for Advanced Devices. *J Electron Spectros Relat Phenomena* **2019**, *231*, 94-103.

(34) Penke, Y. K.; Anantharaman, G.; Ramkumar, J.; Kar, K. K. Aluminum Substituted Cobalt Ferrite (Co−Al−Fe) Nano Adsorbent for Arsenic Adsorption in Aqueous Systems and Detailed Redox Behaviour Study with XPS. *ACS Appl Mater Interfaces* **2017**, *9* (13), 11587-11598.

(35) Winey, M.; Meehl, J. B.; O'Toole, E. T.; Giddings, T. H. Conventional Transmission Electron Microscopy. *Mol Biol Cell* **2014**, *25* (3), 319-323.

(36) Freundlich, M. M. Origin of the Electron Microscope. *Science* **1963**, *142* (3589), 185-188.

(37) Chang, Y.-Y.; Han, H. N.; Kim, M. Analyzing the Microstructure and Related Properties of 2D Materials by Transmission Electron Microscopy. *Appl Microsc* **2019**, *49* (1), 10.

(38) McClelland, G. M.; Erlandsson, R.; Chiang, S. Atomic Force Microscopy: General Principles and a New Implementation BT - Review of Progress in Quantitative Nondestructive Evaluation; Thompson, D. O., Chimenti, D. E., Eds.; Springer US: Boston, MA, 1987; pp 1307-1314.

(39) Peng, J.; Guo, J.; Ma, R.; Jiang, Y. Water-Solid Interfaces Probed by High-Resolution Atomic Force Microscopy. *Surf Sci Rep* **2022**, *77* (1), 100549.

(40) Giessibl, F. J. Advances in Atomic Force Microscopy. *Rev Mod Phys* **2003**, *75* (3), 949-983.

(41) Binnig, G.; Quate, C. F.; Gerber, C. Atomic Force Microscope. *Phys Rev Lett* **1986**, *56* (9), 930-933.

(42) Alonso, J. L.; Goldmann, W. H. Feeling the Forces: Atomic Force Microscopy in Cell Biology. *Life Sci* **2003**, *72* (23), 2553-2560.

(43) Zhang, H.; Huang, J.; Wang, Y.; Liu, R.; Huai, X.; Jiang, J.; Anfuso, C. Atomic Force Microscopy for Two-Dimensional Materials: A Tutorial Review. *Opt Commun* **2018**, *406*, 3-17.

(44) Yu, Y.; Fan, G.; Fermi, A.; Mazzaro, R.; Morandi, V.; Ceroni, P.; Smilgies, D.-M.;

Korgel, B. A. Size-Dependent Photoluminescence Efficiency of Silicon Nanocrystal Quantum Dots. *J Phys Chem C* **2017**, *121* (41), 23240-23248.

(45)   Wang, Z.; Zeng, H.; Sun, L. Graphene Quantum Dots: Versatile Photoluminescence for Energy, Biomedical, and Environmental Applications. *J Mater Chem C* **2015**, *3* (6), 1157-1165.

(46)   Tebyetekerwa, M.; Zhang, J.; Xu, Z.; Truong, T. N.; Yin, Z.; Lu, Y.; Ramakrishna, S.; Macdonald, D.; Nguyen, H. T. Mechanisms and Applications of Steady-State Photoluminescence Spectroscopy in Two-Dimensional Transition-Metal Dichalcogenides. *ACS Nano* **2020**, *14* (11), 14579-14604.

(47)   Maiuri, M.; Garavelli, M.; Cerullo, G. Ultrafast Spectroscopy: State of the Art and Open Challenges. *J Am Chem Soc* **2020**, *142* (1), 3-15.

(48)   NORRISH, R. G. W.; PORTER, G. Chemical Reactions Produced by Very High Light Intensities. *Nature* **1949**, *164* (4172), 658.

(49)   Van Houten, J. A Century of Chemical Dynamics Traced through the Nobel Prizes. 1986: Dudley Herschbach, Yuan Lee, and John Polanyi. *J Chem Educ* **2002**, *79* (8), 926.

(50)   Dantus, M.; Rosker, M. J.; Zewail, A. H. Real-time Femtosecond Probing of '"Transition States'" in Chemical Reactions. *J Chem Phys* **1987**, *87* (4), 2395-2397.

(51)   Brodeur, A.; Chin, S. L. Ultrafast White-Light Continuum Generation and Self-Focusing in Transparent Condensed Media. *J Opt Soc Am B* **1999**, *16* (4), 637-650.

(52)   Alfano, R. R.; Shapiro, S. L. Emission in the Region 4000 to 7000 Å Via Four-Photon Coupling in Glass. *Phys Rev Lett* **1970**, *24* (11), 584-587.

(53)   Fork, R. L.; Shank, C. V; Hirlimann, C.; Yen, R.; Tomlinson, W. J. Femtosecond White-Light Continuum Pulses. *Opt Lett* **1983**, *8* (1), 1-3.

(54)   Marburger, J. H. Self-Focusing: Theory. *Prog Quantum Electron* **1975**, *4*, 35-110.

(55)   Shimizu, F. Frequency Broadening in Liquids by a Short Light Pulse. *Phys Rev Lett* **1967**, *19* (19), 1097-1100.

Chapter 3

Exciton and Trion Dynamics in Monolayer MoS$_2$ Flakes and in the Heterojunction of MoS$_2$/Au
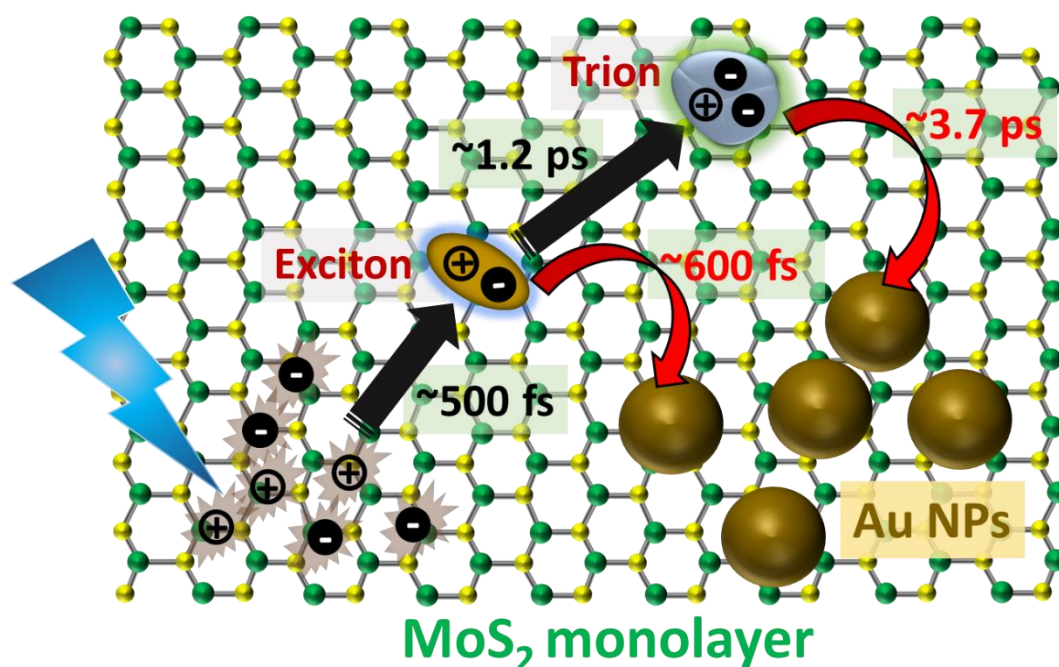
Adapted with permission from Goswami T., Rani R., Hazra K. S. and Ghosh H. N., Ultrafast Carrier Dynamics of the Exciton and Trion in MoS$_2$ Monolayers Followed by Dissociation Dynamics in Au@MoS$_2$ 2D Heterointerfaces, *J. Phys. Chem. Lett.*, 2019, 10, 3057-3063. **Copyright 2019 American Chemical Society**.

3.1. Introduction

2D TMDC materials are known to offer both fundamental and technological implications in various advanced electronic, optoelectronic and gas sensing devices, energy storage systems, photovoltaics and photo-catalysis[1–3]. Among these, MoS$_2$ is most extensively studied, owing to its high stability and easy synthesis routes and already showing promise in photo-transistors[4,5], transistors with high current switching[6], integrated circuits[7,8], sensing[9], LED[10], battery[11], solar cells[12,13], and catalysis[14,15]. On the other hand, Metal-2D hetero-structure based devices have gained significant limelight, where interaction between plasmon and exciton in metal-semiconductor (M-S) domain plays crucial role[16,17]. Metal nanoparticles are ideal light acceptors, due to presence of surface plasmons, which can restrain and manipulate light at nanoscale[18,19]. In this context, it is very important to study intrinsic physical properties of semiconductor system and charge transfer processes in metal-semiconductor heterojunction. Reduced dielectric constant in 2D monolayer semiconductor, results in strong interactions between quasiparticles, allowing formation of several many body states like excitons[20], bi-excitons[21], and trions[22]. Excitons and trions are stable even at room temperature, owing to their high coulombic interaction and large binding energies in the range of few hundred meV and tens of meV respectively[20,22,23]. Steady state luminescence studies and ultrafast pump probe spectroscopy, have been carried out to monitor excitonic population in 2D materials[20,24–27]. Unlike excitons, trions are not well reported for 2D materials, although they play a vital role in their intrinsic properties. There have been only few luminescence experiments conducted, where trions are reported at room temperature even in absence of any electrical or chemical doping[22,28–30]. Mak et al reported formation of tightly bound trions in monolayer MoS$_2$ at room temperature[22]. Lui *et al*. demonstrated separate contributions of photo-conductivity from the trion and electron, which provide direct evidence of trion transport[31]. Trion studies have become very interesting for both scientific and technological pursuits due to its transport properties, density and pseudo-spin which can be easily controlled by electric fields and polarization. In a metal-2D hetero-structure, we should consider both plasmon-exciton and plasmon-trion interaction, for better understanding its implications. To design and develop any efficient device out of these 2D materials, it is utmost important to understand the energy dissipation pathways, which includes formation and relaxation of free carriers, excitons, as well as trions, where most of the processes take place in fast and ultrafast time scale. Ultrafast pump-

probe spectroscopic study can play an important role in investigating these processes in very short time scale.

In this chapter, we are going to discuss the formation and relaxation dynamics of both exciton and trions in a monolayer MoS$_2$ system. We have monitored the carrier dynamics of monolayer MoS$_2$ deposited on SiO$_2$/Si substrate, before and after Au NP deposition, using broad band femtosecond transient absorption spectroscopy. Luminescence measurements confirm the presence of both exciton and trion in MoS$_2$ layers, which are drastically quenched after deposition of Au NPs, indicating photo-excited electron migration from MoS$_2$ to Au. Transient analysis revealed that, photogenerated free carriers form excitons and trions at an ultrafast time scale of ~500 fs and ~1.2 ps, respectively. Further, these quasiparticles were found to be dissociated in presence of Au, with time scale of ~600 fs and ~3.7 ps respectively.

3.2. Synthesis and experimental techniques

Monolayer MoS$_2$ was prepared on 300 nm SiO$_2$/Si substrate by CVD method, at 680 ^{0}C, using MoO$_3$ and Sulphur powder as precursor. Raman and PL characterization were carried out with 532 nm laser line by using WITEC alpha 300 R Raman spectrometer, having 600-line mm^{-1} grating. Bruker Multimode 8 AFM system was used for AFM imaging of MoS$_2$ in tapping mode, under ambient condition. Au NPs were synthesized by established citrate reduction method. HAuCl$_4$ solution (1mM) of 12 mL was boiled while adding 2mL of trisodium citrate (2%) under vigorous stirring. The colour of the solution turns yellow to red within 10 minutes, which indicates the formation of AuNP. The stirring of the solution was continuously maintained with heating, for another 20 min and then kept at room temperature under stirring condition.

Ultrafast transient absorption measurements of MoS$_2$ monolayers were executed using Ti: sapphire amplifier system (Astrella, Coherent, 800 nm, 2mJ/pulse energy, ~ 35 fs pulse width and 1 kHz repetition rate) and Helios Fire pump-probe spectrometer, already discussed in our previous article[46]. A Beam splitter was used to split the laser into two beams, Pump and Probe beam respectively. Frequency of the pump beam was converted into our desired excitation frequency by passing it through an Optical Parametric Amplifier (Coherent). Probe beam passes through a delay stage (designed to maintain perfect delay time between pump and probe pulses) and focussed on a Sapphire crystal to generate white light pulses ranging 400-750 nm. Pump beam passes through a mechanical chopper reducing its repetition rate to 500 Hz. Probe beam reflected upon the sample was detected by InGaAs detectors.

3.3. Results and discussion

3.3.1. Synthesis and characterisation of MoS$_2$ flakes and MoS$_2$/Au heterojunction

For the synthesis of MoS$_2$ monolayers, we have employed CVD method, which is known to be the most prominent technique to fabricate highly crystalline 2D materials. The optical image of the as grown MoS$_2$ is shown in **Figure 3.1a**, where monolayer flakes are abundant mostly in triangular shape. To know the number layer of MoS$_2$ deposited on SiO$_2$/Si substrate we have carried out Raman spectroscopic measurements. From the Raman characteristics of the MoS$_2$ flakes, it is found that the difference between two phonon vibration modes (in-plane E^1_{2g} and out-of-plane A_{1g}) is ~19.9 cm^{-1}, which confirmed the monolayer structure of MoS$_2$ (**Figure 3.1b**)[32].
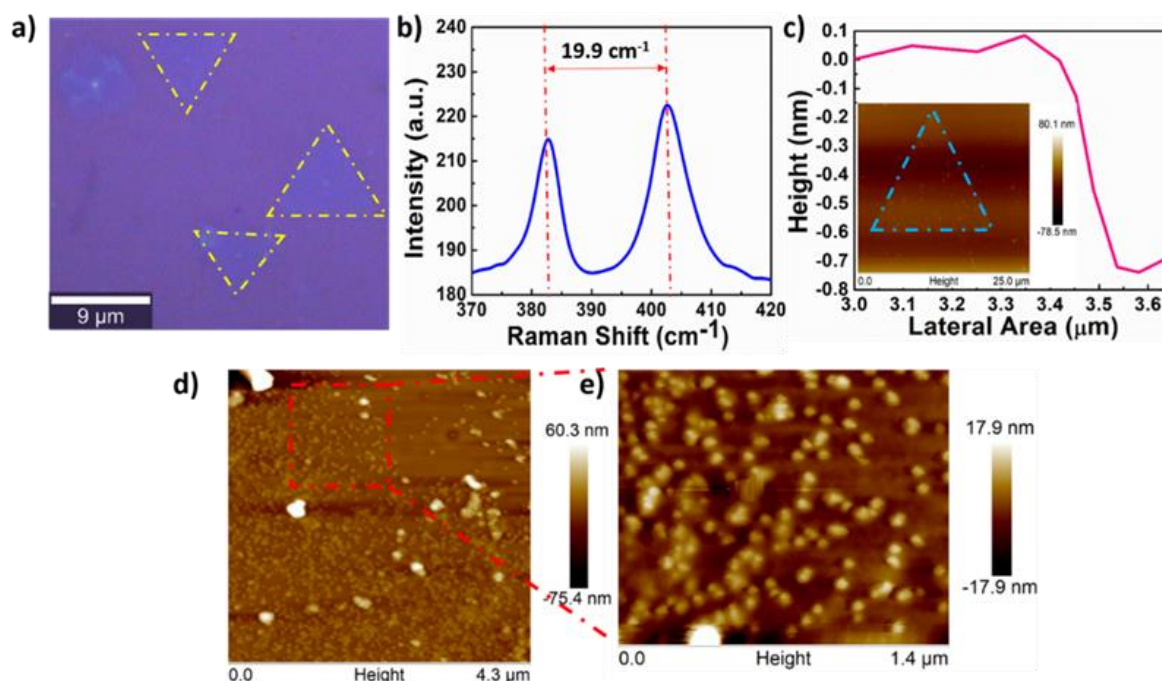
Figure 3.1: **(a)** Optical image of monolayer MoS$_2$ on SiO$_2$/Si substrate. **(b)** Raman characteristics spectra of MoS$_2$ where two peaks are separated by 19.9 cm^{-1} which confirms the monolayer of MoS$_2$; **(c)** AFM height profile of monolayer MoS$_2$ and inset image shows the AFM topography of monolayer MoS$_2$; **(d)** AFM topography image of distributed AuNPs on the surface of monolayer MoS$_2$; **(e)** Extended view of highlighted with red dotted area in figure **(d)** shows clear distribution of AuNPs on the MoS$_2$ flake.

To determine the thickness of the monolayer we have employed AFM technique, and thickness through AFM height image determined to be ~ 0.72 nm suggesting monolayer (**Figure 3.1c**). To make MoS$_2$/Au hetero-structure freshly prepared Au NP solutions of ~ 0.6 μL was drop-

casted over MoS_2 flakes on SiO_2/Si substrate and were put in vacuum for drying. The distribution of the AuNPs on MoS_2 flakes was examined by AFM image, and shown in **Figure 3.1d and 3.1e**. It is observed that Au nanoparticles are spread in high concentration mainly on the MoS_2 flake and not on the SiO_2 substrate, might be due to higher affinity of Au towards S. Enlarge view of AFM topography image (**Figure 3.1e**) shows uniform distribution of AuNP on the surface of MoS_2 flake. The size of the Au NPs was determined to be ~15 nm, from TEM measurements, as shown in **figure 3.2a**. HRTEM study confirmed the formation of Au NPs, with characteristic d-spacing of Au (111) lattice planes (**Figure 3.2b**). These metallic NPS possess a sharp plasmonic absorption band at 522 nm (**Figure 3.2c**).
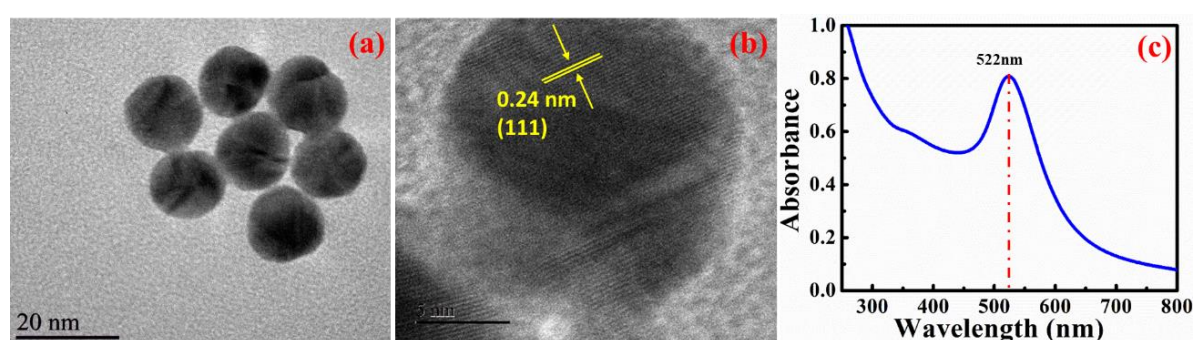
Figure 3.2: **(a)** TEM image of as prepared Au NPs; and **(b)** HRTEM image of an Au nanosphere; **(c)** UV-VIS absorption spectra of Au NPs.

3.3.2. Steady state optical investigation

Steady state photoluminescence study of pristine MoS_2 monolayers shows broad luminescence band with a peak at ~683 nm, with a hump at ~ 633 nm (**Figure 3.3a**), which can be attributed to the exciton A and exciton B peaks respectively[20,27]. The intense PL peaks are in accordance with the direct band gap of monolayer MoS_2. A and B excitonic peaks are generated due to direct band gap transitions between spin splitted valence band maxima and conduction band minima[20,33]. The splitting of the valence-band maximum in monolayer MoS_2, at the K point, is entirely due to the spin-orbit effect and the absence of any inversion symmetry in monolayer MoS_2. Valence band splitting is higher compared to the conduction band, because of, larger effective mass of holes, than electrons in the system[33].

Besides excitons, trion formation is also favourable in 2D transition metal dichalcogenides owing to their high coulombic interaction and large exciton and trion binding energy. Ideally a trion can be formed when either an electron or hole binds with an exciton and termed as negatively charged exciton or positively charge exciton respectively[34].
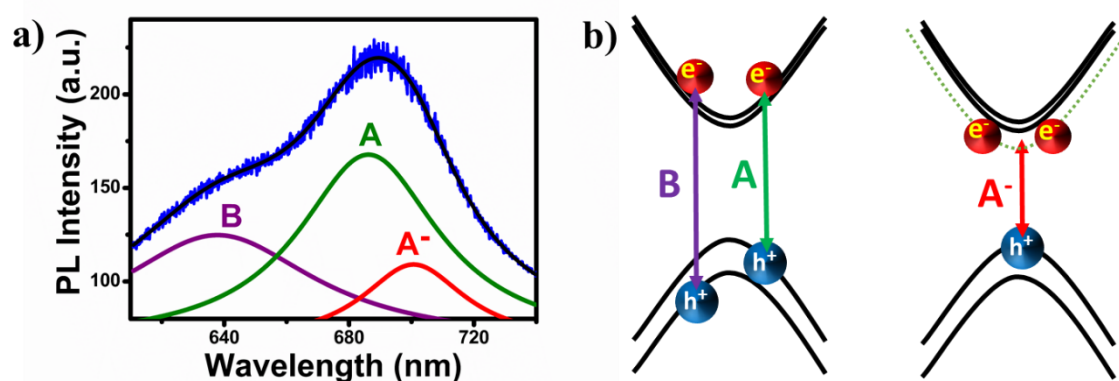
Figure 3.3: (a) Photoluminescence spectra of pristine MoS_2 monolayer, fitted with three Lorentzian functions, which have been attributed to exciton B, exciton A and charged exciton (trion) A^-; **(b)** Simplified energy band diagram of MoS_2, showing both B and A excitons and trion formation in MoS_2.

These extra charges, for the formation of trions, may come from defects, substrates or by doping or applied gating[35]. Formation of both negative and positive trions for $MoSe_2$ and WSe_2 are reported in literature[36,37]. In MoS_2, negative trions are usually observed, because of the intrinsic large electron density in MoS_2, doped unintentionally, which is too large to be completely defused by electronic back-gating of substrates[22]. These excess electrons can facilitate formation of trion after binding with excitons. As a result, a large number of trions can be formed even at room temperature. Separate photoluminescence peak due to negative trion (A^- Trion) in addition to both B Exciton and A Exciton have been observed by many authors[22,28–30]. In the present investigation we have observed a broad luminesce band with a hump which can be de-convoluted into three peaks at ~633 nm, ~683 nm and ~700 nm. We can attribute these peaks as luminescence due to B exciton, A exciton and A^- trion, respectively as shown in **figure 3.3a**. A simplified energy band diagram of MoS_2, manifesting exciton A and B, and trion A^-, shown in **figure 3.3b**.

3.3.3. Transient investigation of monolayer MoS₂

To understand the charge carrier dynamics of MoS_2, we have carried out broad-band femtosecond pump-probe spectroscopic measurements in pristine MoS_2 monolayer flakes. **Figure 3.4a** shows differential absorption spectrum of MoS_2 monolayer after excitation of 420 nm laser pulse. Transient spectra show two distinct bleach features (negative absorption bands) peaking at 620 nm and 675 nm.
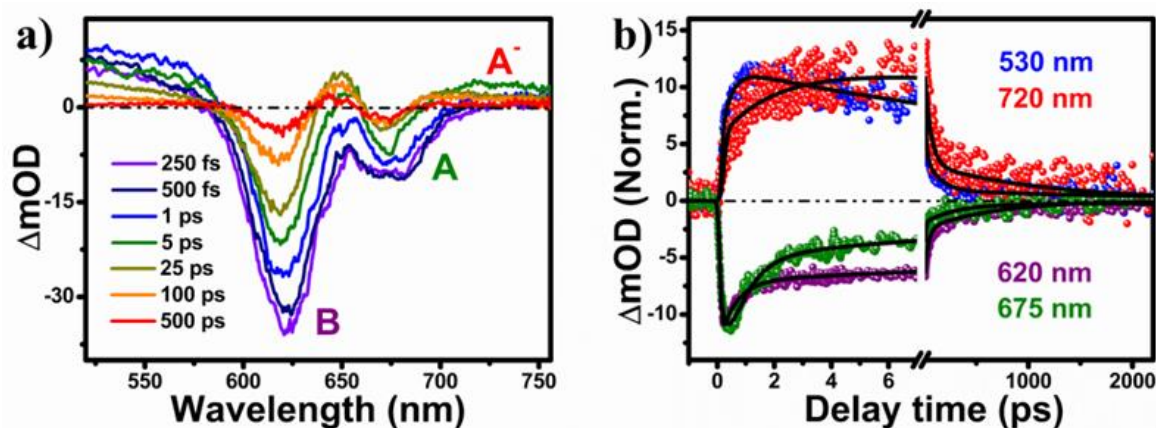
Figure 3.4: (a) Transient absorption spectra of monolayer MoS_2 on SiO_2 substrate, at different time delay, after exciting the samples at 420 nm; **(b**) Normalized bleach recovery kinetics of B and A exciton probing at 620 nm (B exciton) and 675 nm (A exciton) (**bottom panel**); Normalized transient absorption kinetics at 530 nm and 720 nm (**top panel**).

The negative absorption appeared at 620 nm and 675 nm can be attributed bleach due to B exciton and A exciton respectively[25,38]. Pogna et. al. described these spectral features as result of renormalization of both exciton binding energy and band gap, as well as state filling effect[39]. In addition to the bleach peaks due to B-exciton and A-exciton, positive absorption bands have also been observed in both blue and red regions of the spectra. To understand the charge carrier dynamics of photo-excited monolayer MoS_2 transient kinetics have been monitored at both A and B excitonic bleach positions (675 nm and 620 nm) and shown in **figure 3.4b** (bottom panel). Bleach kinetics for A and B excitons can be fitted multi-exponentially and the fitting parameters are reported in **Table 3.1**. It is quite evident to see that the temporal evolution of the transient kinetics of A and B excitonic transitions are very different from each other. The growth of A-exciton is marginally slower as compared to B-exciton and initial decay of B-exciton bleach is faster as compared to that of A-exciton. This can be explained as follows: on photo-excitation high energy photon (420 nm, 2.95 eV) as compared to band gap ($E_g^{MoS_2}$= 1.99 eV) photo-excited excite charge carriers (both electrons and holes) are generated in upper excitonic states of both conduction and valence band. Electrons very quickly (pulse width limited time) relaxed to the conduction band edge. Similarly, hole also relaxes to the lower valence band energy states and form B exciton. Within short time scale, these hot holes relaxed to the lower valence band, with the formation of A-exciton, where the holes are thermalized. This interesting observation can be attributed to "hole cooling" in single layer MoS_2. Hole

cooling process is clearly observed in the short time scale kinetics of A and B exciton (**Figure 3.5a)**.

Table 3.1. Exponentially fitted parameters for the kinetics of monolayer MoS$_2$ at different wavelengths after photoexcitation of 420 nm with 600 µJ/cm^2 fluence.

Probe (nm)	Growth	Recovery		
	τ_g	τ_1	τ_2	τ_3
620	< 0.1 ps	0.5 ps (42.4%)	34 ps (37%)	> 1 ns (20.6%)
675	0.2 ps	0.6 ps (55.9%)	3.9 ps (20.6%)	> 1 ns (24%)
530	0.3 ps	13.7 ps (63.8%)	131 ps (28.5%)	> 1 ns (7.7%)
720	1.2 ps	56.6 ps (72.7%)	> 1 ns (27.3%)	-

The time scale for this growth is attributed to the hole cooling time from upper valence state to lower valence state within the valence band, which was determined to be ~200 fs. The fastest decay component with major contribution for both excitonic bleaches were found to be in the range of 0.5–0.6 ps (**Table 3.1**). This time scale can be attributed mainly due to exciton formation. It has been reported in the literature that exciton formation time for mono-layer 2D materials like MoS$_2$, MoSe$_2$, WS$_2$, WSe$_2$ etc. are in the range of 0.3 to 0.5 ps[40].
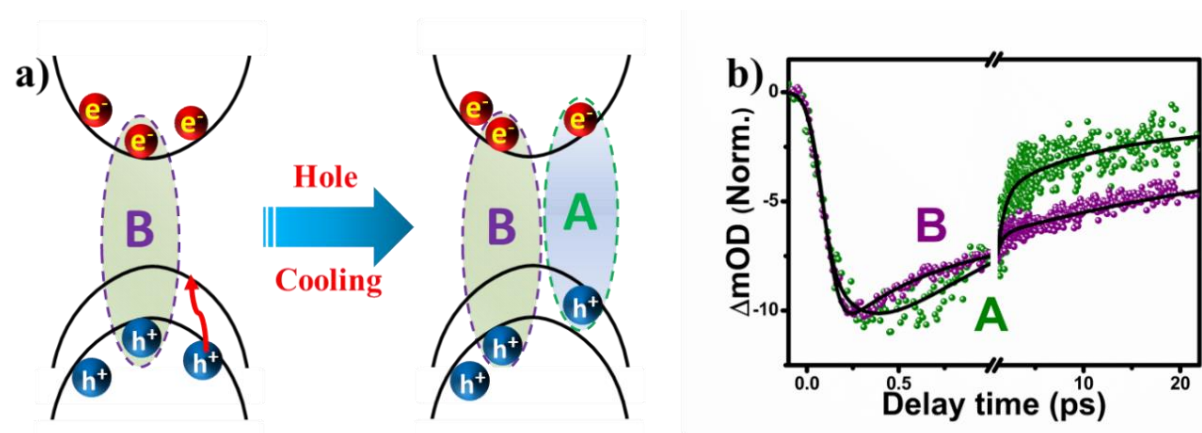
Figure 3.5: (a) Schematic representation of hole cooling before formation of A exciton upon excitation 420 nm excitation; and **(b)** Normalized kinetics of exciton A and B showing longer growth time for exciton A, confirming the hole cooling process.

To check whether the fast excitonic decay is due to exciton formation or any other decay process we have carried out transient experiments with different pump photon energy, with very high energy (420 nm), and with near band gap energy (580 nm). Large excitonic binding energy of 2D materials, restricts immediate exciton formation of the photoexcited electrons. When we excite with very high energy pump, electrons take longer time to come to the band edge and form exciton compared to lower energy pumps. So, the time responsible for the exciton formation should be very low, for near band gap excitation, as now we are injecting electrons near the band edge. In our experiment, we observed a fast excitonic decay only in case of 420 nm excitation, shown in **figure 3.6a and 3.6b**. This fast decay is not observed for 580 nm excitation. This study confirms that, this fast decay is associated with the exciton formation process, not any auger recombination or trap mediated recovery phenomenon.
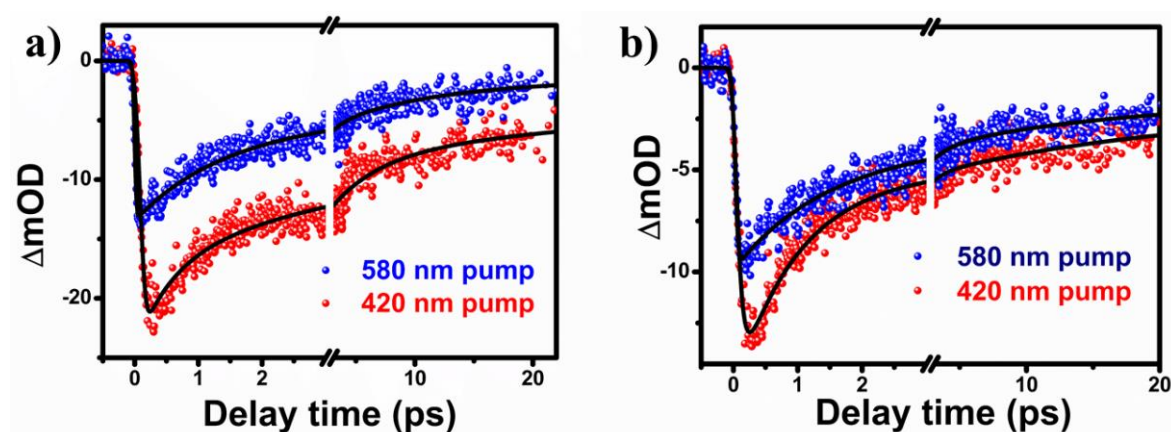
Figure 3.6: (a) Transient absorption kinetics of B exciton; and **(b)** A exciton, in MoS2 monolayers upon high energy (420 nm) photoexcitation and near band gap (580 nm) photoexcitation respectively.

The second component for both wavelengths (620 nm and 675 nm) in **table 3.1** is generally attributed to Auger recombination or exciton-exciton annihilation in the system[25]. In our case, it is quite evident that the second component for A-excitonic position is much faster, compared to that of B-excitonic position. We attribute this difference to the presence of another decay channel for exciton A, i.e., trion formation, making the decay much faster as compared to

exciton B. The long components (> 1ns) are due to radiative/non-radiative recombination of trapped carriers/excitons.

Further, we have monitored the positive absorption signal on the red- and blue-wavelength region of the excitonic bleaches and plotted in **Figure 3.4b**. Positive signals at early time scale have been attributed to the carrier induced peak broadening or pump induced exciton line width broadening[41,42]. In our study, longer lifetime of these features may indicate the presence of free/trapped quasi-particles in the system. Both growth and decay dynamics of these two features monitored at 530 nm and 720 nm and are found to be completely different. It clearly suggests that nature of particles responsible for the formation of these features are very different. Both positive bands are fitted with single-exponential growth and multi-exponential recovery as shown in **Table 3.1**. The growth component for 720 nm (1.2 ps) is much longer than that of 530 nm (0.3 ps). We attribute this slow growth, to the formation of trions. Kime et al mentioned this photo-induced feature to the negative trions present in the system[25]. They have reported much lower time scale than what we have observed, studying suspended MoS₂ nanoflakes. We assume this difference is due to presence of SiO₂ substrate or may be due to trapping of trions at the edges of MoS₂ monolayers. The longer decay components (56.6 ps, > 1 ns) are due to presence of radiative/non-radiative decay of trions and non-radiative decay of trapped trions, respectively. For 530 nm, the growth component (0.3 ps) may be attributed to the formation time for trapped carriers/trapped exciton and longer decay components (13.7 ps and 131 ps) can be radiative/non-radiative exciton-exciton annihilation and > 1ns component can be non-radiative decay of trapped excitons.
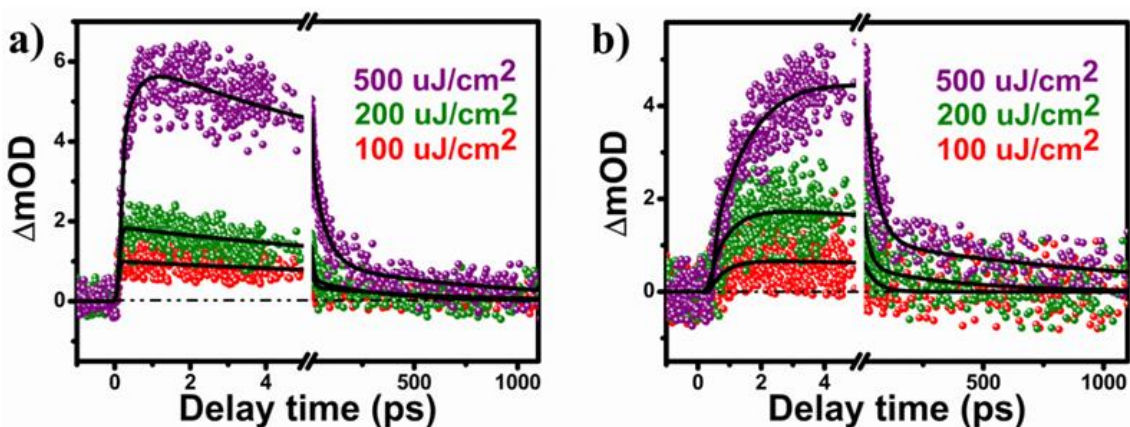
Figure 3.7: Fluence dependence transient absorption kinetics of monolayer MoS₂ on SiO₂/Si substrate at **(a)** 530 and **(b)** 720 nm after 420 nm photo-excitation. Laser fluence were kept 100, 200 and 500 μJ/cm².

Table 3.2. Exponentially fitted parameters for the kinetics of 2D monolayer MoS$_2$ at 530 nm after 420 nm photo-excitation with different laser intensity. Laser Intensity were kept 100 μJ/cm^2, 200 μJ/cm^2 and 500 μJ/cm^2.

Pump fluence (μJ/cm^2)	Growth	Recovery		
	τ_g	τ_1	τ_2	τ_3
100	< 0.1 ps	12.6 ps (-64.7%)	> 1 ns (-35.3%)	-
200	< 0.1 ps	2.32 ps (-28.5%)	22.6 ps (-54.1%)	> 1 ns (-17.4%)
500	0.38 ps	5.22 ps (-37.8%)	63 ps (-47%)	> 1 ns (-15.2%)

Table 3.3. Exponentially fitted parameters for the kinetics of 2D monolayer MoS$_2$ at 720 nm after 420 nm photo-excitation with different laser intensity. Laser Intensity were kept 100 μJ/cm^2, 200 μJ/cm^2 and 500 μJ/cm^2.

Pump Fluence (μJ/cm^2)	Growth	Recovery	
	τ_g	τ_1	τ_2
100	0.48 ps	47.2 ps (100%)	-
200	0.66 ps	26 ps (-71.84%)	390 ps (-28.16%)
500	1.23 ps	46.1 ps (-77.68%)	> 1 ns (-22.32%)

To ascertain whether these transient absorptions at 530 nm and 720 nm are due to trapped carriers/trapped exciton and trions respectively, we have carried out fluence dependent transient absorption studies, keeping the pump fluence at 100, 200 and 500 μJ/cm^2 and are shown in **Figure 3.7**. **Figure 3.7a** indicates the transient growth and decay kinetics at 530 nm at different laser fluence. It is clearly observed from our experiment that with increasing laser fluence, transient signal increases. Kinetics are fitted multi-exponentially, shown in **Table 3.2 and 3.3**. Trion formation depends upon availability of free electrons in the system, increasing

fluence should drastically enhance the trion signal, as now we are exciting more no of electrons in the system. The growth time of 530 nm, transient signal changes from < 0.1 ps to 0.38 ps, as we increase the laser fluence from 100 to 500 µJ/cm^2, whereas, for 720 nm, the growth time increases from 0.48 ps to 1.23 ps, in similar laser fluences. This drastic change in growth time, for 720 nm positive feature, supports our claim. This positive signal is not due to formation of trapped carriers or excitons, but because of presence of trions in the system.

3.3.4. Transient investigation of MoS₂/Au heterojunction

One of our main aim of this present study is to investigate the ultrafast charge carrier dynamics of MoS$_2$ monolayers, following the deposition of Au NPs on top of it. Earlier Bhanu et. al. discussed photoluminescence quenching in MoS$_2$/Au hybrid nanoflakes, where they suggested photo-excited electron transfer from MoS$_2$ to Au NP as the process is thermodynamically viable[43]. The conduction band level ($E_{CB}^{MoS_2} = -4.46$ eV)[35,44] of MoS$_2$ is energetically higher, compared to the Fermi level of Au ($E_F^{Au} = -5.1$ eV)[45]. However, the electron transfer dynamics was never been reported in MoS$_2$/Au interface. In the present investigation we have deposited Au NPs (~ 15 nm) on the MoS$_2$ monolayer flakes and recorded photoluminescence and shown in **figure 3.8a**. It is clearly seen that in presence of Au NPs photoluminescence of MoS$_2$ is completely quenched. We suggest this quenching of photoluminescence attributes to the electron transfer from MoS$_2$ to Au region. To investigate this electron transfer process, in ultrafast time scale and to monitor the excited-state properties in MoS$_2$/Au hetero-interface, we have carried out femtosecond transient absorption measurements, by exciting the samples with a 420 nm laser pulse. **Figure 3.8b** shows transient absorption spectra of Au deposited MoS$_2$ monolayers, at different time delay. This transient spectra of MoS$_2$/Au are clearly different compared to pure MoS$_2$ and signal intensity was drastically reduced here. A broad bleach is observed, peaking at 620 nm (B-excitonic peak) with a hump around 550 nm and a small intensity bleach peak at 675 nm (A-excitonic peak).

In addition to that, two low intensity positive absorption bands appear below 510 nm and above 710 nm. These absorptions are due to presence of free carriers/excitons and trions respectively, as we have already discussed in case of pure MoS$_2$. The negative absorption at 550 nm (hump) can be attributed to the bleach due to Au Plasmon. At 420 nm excitation majority of the laser light is absorbed by MoS$_2$ monolayer, however still some portion of the light can be absorbed by the Au NPs, as a result Au plasmonic bleach at 550 nm has been observed. Also, MoS$_2$ to Au electron migration could result in a plasmonic bleach. To find out, we carried separate

transient studies, exciting only Au NPs deposited over SiO₂/Si substrate, with 420 nm laser pulse, where we observed a distinct bleach at 550 nm due to Au surface Plasmon (**Figure 3.9a**).
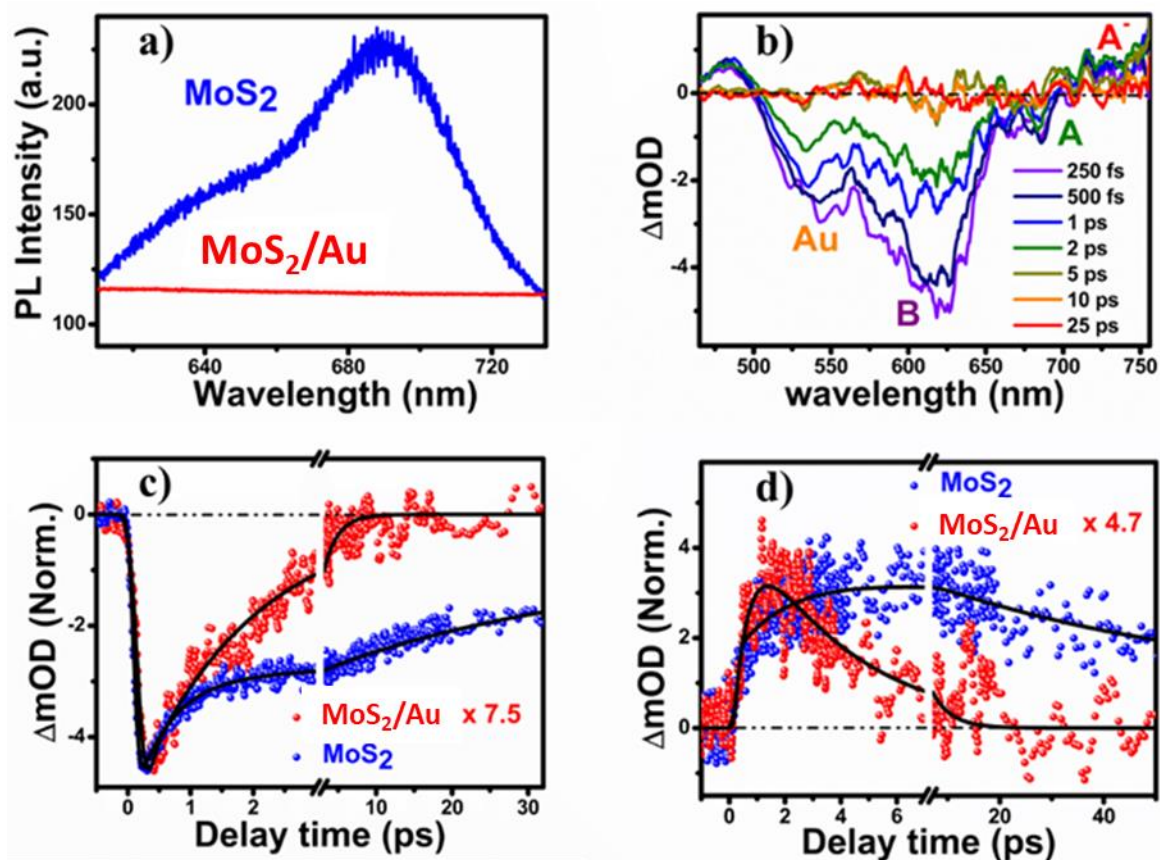
Figure 3.8: **(a)** Photoluminescence spectra of MoS₂ monolayer in absence and in presence of Au NPs; **(b)** Transient absorption spectra of Au deposited MoS₂ monolayers; **(c)** Normalized kinetics of exciton B, probing at 620 nm, before and after Au deposition; **(d)** Normalized kinetics of trion, before and after Au deposition, upon 420 nm photoexcitation, probing at 720 nm.

Comparative charge carrier dynamics of Au NPs over SiO₂ and MoS₂ are plotted in **figure 3.9b**. Enhanced bleach intensity in case of MoS₂/Au heterosystem confirms the increment in electron population in the Au region. Now to understand charge carrier dynamics of excitons and trions in photo-excited MoS₂/Au, we have monitored the transient kinetics at different wavelengths and compared with pure MoS₂ monolayer. **Figure 3.8c** represents the normalized recovery kinetics B exciton at 620 nm, in absence and presence of Au NP. In presence of Au NP, 620 nm bleach recovers very fast and can be fitted multi-exponentially with time constants $\tau_1 = 600$ fs (96.8%) and 1.28 ps (3.2%) **(Table 3.4)**. Here the fastest recovery time constant (600 fs) can be ascribed to the electron transfer from MoS₂ exciton to Au NP. Drastic decrement

of excitonic bleach intensity (7.5 times) for MoS_2/Au system, can be accredited to the pulse-width limited transfer of electrons (when they exist as free carriers) from MoS_2 to Au NP.
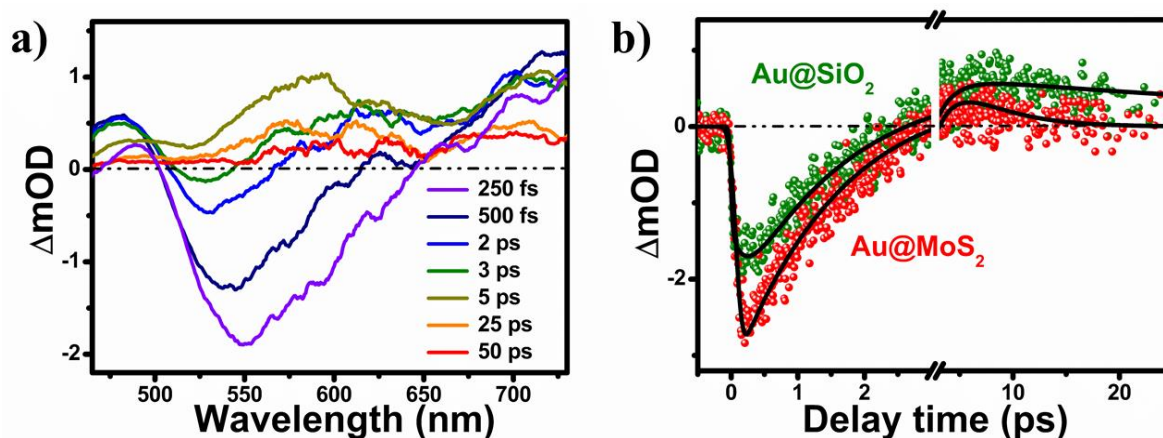
Figure 3.9: (a) Transient absorption spectra Au solution deposited over SiO_2; and **(b)** Comparative evolution of Au plasmonic bleach for Au solution deposited over bare SiO_2 substrate and MoS_2 monolayers respectively, probing at 550 nm upon 420 nm photoexcitation.

Table 3.4. Exponentially fitted parameters for the kinetics of 2D monolayer MoS_2 after depositing Au NP at different wavelengths after exciting the samples at 420 nm.

Probe Wavelength (nm)	Growth	Recovery	
	τ_g	τ_1	τ_2
620	< 0.1 ps	0.6 ps (-96.8%)	1.3 ps (-3.2%)
720	0.55 ps	3.7 ps (-100%)	-

Figure 3.8d shows the normalized transient absorption kinetics of pristine MoS_2 monolayer and Au deposited MoS_2 at 720 nm. It is clearly seen that, in presence of Au NPs, transient signal decay much faster and can be fitted with single exponential growth time with 0.55 ps and decays single exponentially with time constant of 3.7 ps (100%). This fast dissociation of trion also supports, electron transfer from MoS_2 to Au region. Trion formation depends upon the abundance of free electrons in the system. In presence of Au, free electrons are removed from 2D MoS_2 monolayer. At lower free electron density, trion signal starts decaying very early, and becomes zero within ~20 ps. We attribute this single exponential decay with time constant of 3.7 ps to the trion dissociation time, in presence of Au NP.

3.4. Conclusions

In summary, we have synthesized monolayer MoS_2 on SiO_2 using CVD method and Au NPs were drop-casted over it. Uniform distribution of Au NPs on monolayer MoS_2 was confirmed by AFM topography. Steady state photoluminescence studies show formation of B-exciton, A-exciton, and A^--trion (negatively charged exciton) in 2D monolayer MoS_2. Luminescence of MoS_2 monolayers was found to be completely quenched after depositing Au NPs, which has been attributed due to photo-excited electron transfer from MoS_2 monolayer to Au NPs. Femtosecond transient absorption spectroscopy unravel the ultrafast charge carrier dynamics of photo-excited MoS_2, which suggests, with photo-excitation free carriers are generated in the 2D monolayer and within 500-600 fs both excitons are formed and finally after capturing an electron, some of the excitons turned into trions, with a time scale of ~1.2 ps. After depositing Au NPs on MoS_2 monolayer, majority of the free carriers are captured by Au NPs. As a result, excitons and trions are dissociated in presence of Au NPs, with the timescale of ~600 fs and ~3.7 ps respectively. We expect this detailed study of exciton and trion dynamics in MoS_2, within ultrafast timescale, will be a great help to design and develop devices not only based on MoS_2 but also other 2D materials.

3.5. References

(1)   Liu, B.; Abbas, A.; Zhou, C. Two-Dimensional Semiconductors: From Materials Preparation to Electronic Applications. *Adv. Electron. Mater.* **2017**, *3* (7), 1–17.

(2)   Henan, L.; Yumeng, S.; Ming-Hui, C.; Lain-Jong, L. Emerging Energy Applications of Two-Dimensional Layered Transition Metal Dichalcogenides. *Nano Energy* **2015**, *18*, 293–305.

(3)   Li, X.; Shan, J.; Zhang, W.; Su, S.; Yuwen, L.; Wang, L. Recent Advances in Synthesis and Biomedical Applications of Two-Dimensional Transition Metal Dichalcogenide Nanosheets. *Small* **2017**, *13* (5), 1–28.

(4)   Lin, M.; Kravchenko, I. I.; Fowlkes, J.; Li, X.; Puretzky, A. A.; Rouleau, C. M.; Geohegan, D. B.; Xiao, K. Thickness-Dependent Charge Transport in Few-Layer MoS_2 Field-Effect Transistors. *Nanotechnology* **2016**, *27* (16), 165203.

(5)   Das, S.; Chen, H.-Y.; Penumatcha, A. V; Appenzeller, J. High Performance Multilayer MoS2 Transistors with Scandium Contacts. *Phys. Rev. B* **1987**, *36* (2), 100–105.

(6)   Chang, H.; Yang, S.; Lee, J.; Tao, L.; Hwang, W.; Jena, D.; Lu, N.; Akinwande, D. High-Performance , Highly Bendable MoS$_2$ Transistors with High - K Dielectrics for Flexible Low-Power systems. *ACS Nano* **2013**, *7* (6), 5446–5452.

(7)   Radisavljevic, B.; Whitwick, M. B.; Kis, A. Integrated Circuits and Logic Operations Based on Single-Layer MoS$_2$. *ACS Nano* **2013**, *7* (4), 3729.

(8)   Dubey, M.; Li, L.-J.; Chin, M. L.; Kong, J.; Palacios, T.; Yu, L.; Lee, Y.-H.; Hsu, A.; Shi, Y.; Wang, H. Integrated Circuits Based on Bilayer MoS$_2$ Transistors. *Nano Lett.* **2012**, *12* (9), 4674–4680.

(9)   Friedman, A. L.; Jernigan, G. G.; Campbell, P. M.; Jonker, B. T.; Cobas, E.; Perkins, F. K. Chemical Vapor Sensing with Monolayer MoS$_2$. *Nano Lett.* **2013**, *13* (2), 668–673.

(10)   Yin, Z.; Zeng, Z.; Zhang, H.; Zheng, B.; Yang, H. Y.; Zhang, X.; Chen, J.; Cai, Y.; Wong, J. I.; Wu, J.; Zeng, Z.; Zhang, H. Preparation of MoS$_2$-MoO$_3$ Hybrid Nanomaterials for Light-Emitting Diodes. *Angew. Chemie Int. Ed.* **2014**, *53* (46), 12560-12565.

(11)   Cho, J.; Hwang, H.; Kim, H. MoS$_2$ Nanoplates Consisting of Disordered Graphene-like Layers for High Rate Lithium Battery Anode Materials. *Nano Lett.* **2011**, 4826–4830.

(12)   Yue, G.; Lin, J. Y.; Tai, S. Y.; Xiao, Y.; Wu, J. A Catalytic Composite Film of MoS$_2$/Graphene Flake as a Counter Electrode for Pt-Free Dye-Sensitized Solar Cells. *Electrochim. Acta* **2012**, *85*, 162–168.

(13)   Su, S.-H.; Tsai, M.-L.; Chen, C.-H.; Tsai, D.-S.; Li, L.-J.; He, J.-H.; Chang, J.-K.; Chen, L.-J.; Wu, C.-I. Monolayer MoS$_2$ Heterojunction Solar Cells. *ACS Nano* **2014**, *8* (8), 8317–8322.

(14)   Wang, L.; Luo, S.; Xu, Y.; Tang, Y.; Zeng, Y.; Liu, C.; Zhang, S.; Liu, Y. Vertical Single or Few-Layer MoS$_2$ Nanosheets Rooting into TiO$_2$ Nanofibers for Highly Efficient Photocatalytic Hydrogen Evolution. *Appl. Catal. B Environ.* **2014**, *164*, 1–9.

(15)   Yang, Y.; Ng, D. H. L.; Zhang, N.; Wang, G.; Li, Q. High Efficiency Photocatalysis for Pollutant Degradation with MoS$_2$/C$_3$N$_4$ Heterostructures. *Langmuir* **2014**, *30* (29), 8965–8972.

(16)   Li, Z.; Xiao, Y.; Gong, Y.; Wang, Z.; Kang, Y.; Zu, S.; Ajayan, P. M.; Nordlander, P.;

Fang, Z. Active Light Control of the MoS$_2$ Monolayer Exciton Binding Energy. *ACS Nano* **2015**, *9* (10), 10158–10164.

(17) Jariwala, D.; Sangwan, V. K.; Lauhon, L. J.; Marks, T. J.; Hersam, M. C. Emerging Device Applications for Semiconducting Two-Dimensional Transition Metal Dichalcogenides. *ACS Nano* **2014**, *2*, 1102–1120.

(18) Lee, Y. K.; Jung, C. H.; Park, J.; Seo, H.; Somorjai, G. A.; Park, J. Y. Surface Plasmon-Driven Hot Electron Flow Probed with Metal-Semiconductor Nanodiodes. *Nano Lett.* **2011**, 4251–4255.

(19) Chalabi, H.; Schoen, D.; Brongersma, M. L. Hot-Electron Photodetection with a Plasmonic Nanostripe Antenna. *Nano Lett.* **2014**, *14*, 1374−1380.

(20) Scheuschner, N.; Ochedowski, O.; Kaulitz, A.-M.; Gillen, R.; Schleberger, M.; Maultzsch, J. Photoluminescence of Freestanding Single- and Few-Layer MoS$_2$. *Phys. Rev. B* **2014**, *89* (12), 125406.

(21) Sie, E. J.; Frenzel, A. J.; Lee, Y.; Kong, J.; Gedik, N. Intervalley Biexcitons and Many-Body Effects in Monolayer MoS$_2$. *Phys. Rev. B* **2015**, *92*, 125417.

(22) Heinz, T. F.; Mak, K. F.; He, K.; Lee, C.; Shan, J.; Hone, J.; Lee, G. H. Tightly Bound Trions in Monolayer MoS$_2$. *Nat. Mater.* **2012**, *12* (3), 207–211.

(23) Kylänpää, I.; Komsa, H. P. Binding Energies of Exciton Complexes in Transition Metal Dichalcogenide Monolayers and Effect of Dielectric Environment. *Phys. Rev. B - Condens. Matter Mater. Phys.* **2015**, *92* (20), 1–6.

(24) Mak, K. F.; Lee, C.; Hone, J.; Shan, J.; Heinz, T. F. Atomically Thin MoS$_2$: A New Direct-Gap Semiconductor. *Phys. Rev. Lett.* **2010**, *105* (13), 136805.

(25) Kime, G.; Leontiadou, M. A.; Brent, J. R.; Savjani, N.; O'Brien, P.; Binks, D. Ultrafast Charge Dynamics in Dispersions of Monolayer MoS$_2$ Nanosheets. *J. Phys. Chem. C* **2017**, *121* (40), 22415–22421.

(26) Sim, S.; Park, J.; Song, J. G.; In, C.; Lee, Y. S.; Kim, H.; Choi, H. Exciton Dynamics in Atomically Thin MoS$_2$: Interexcitonic Interaction and Broadening Kinetics. *Phys. Rev. B - Condens. Matter Mater. Phys.* **2013**, *88* (7), 1–5.

(27) Voiry, D.; Fujita, T.; Chhowalla, M.; Eda, G.; Yamaguchi, H.; Chen, M.

Photoluminescence from Chemically Exfoliated MoS$_2$. *Nano Lett.* **2011**, *12* (1), 526–526.

(28)   Christopher, J. W.; Goldberg, B. B.; Swan, A. K. Long Tailed Trions in Monolayer MoS$_2$: Temperature Dependent Asymmetry and Resulting Red-Shift of Trion Photoluminescence Spectra. *Sci. Rep.* **2017**, *7* (1), 1–8.

(29)   Zhang, S.; Qin, Q.; Pei, J.; Lu, Y.; Wang, X.; Jiang, W.; Myint, Y. W.; Yang, J.; Zeng, Y.-H.; Xu, R.; et al. Exciton and Trion Dynamics in Bilayer MoS$_2$. *Small* **2015**, *11* (48), 6384–6390.

(30)   Mouri, S.; Miyauchi, Y.; Matsuda, K. Tunable Photoluminescence of Monolayer MoS$_2$ via Chemical Doping. *Nano Lett.* **2013**, *13* (12), 5944–5948.

(31)   Lui, C. H.; Frenzel, A. J.; Pilon, D. V.; Lee, Y.-H.; Ling, X.; Akselrod, G. M.; Kong, J.; Gedik, N. Trion-Induced Negative Photoconductivity in Monolayer MoS$_2$. *Phys. Rev. Lett.* **2014**, *113* (16), 166801.

(32)   Li, H.; Zhang, Q.; Yap, C. C. R.; Tay, B. K.; Edwin, T. H. T.; Olivier, A.; Baillargeat, D. From Bulk to Monolayer MoS$_2$: Evolution of Raman Scattering. *Adv. Funct. Mater.* **2012**, *22* (7), 1385–1390.

(33)   Cheiwchanchamnangij, T.; Lambrecht, W. R. L. Quasiparticle Band Structure Calculation of Monolayer, Bilayer, and Bulk MoS$_2$. *Phys. Rev. B - Condens. Matter Mater. Phys.* **2012**, *85* (20), 1–4.

(34)   Berkelbach, T. C.; Hybertsen, M. S.; Reichman, D. R. Theory of Neutral and Charged Excitons in Monolayer Transition Metal Dichalcogenides. *Phys. Rev. B - Condens. Matter Mater. Phys.* **2013**, *88* (4), 1–6.

(35)   Radisavljevic, B.; Radenovic, A.; Brivio J.; Giacometti V.; Kis, A. Single-Layer MoS$_2$ Phototransistors. *Nature Nanotechnology* **2011,** *6*, 147–150.

(36)   Ross, J. S.; Wu, S.; Yu, H.; Ghimire, N. J.; Jones, A. M.; Aivazian, G.; Yan, J.; Mandrus, D. G.; Xiao, D.; Yao, W.; et al. Electrical control of neutral and charged excitons in a monolayer semiconductor. *Nature Comm.* **2013**, *4*, 1–6.

(37)   Jones, A. M.; Yu, H.; Ghimire, N. J.; Wu, S.; Aivazian, G.; Ross, J. S.; Zhao, B.; Yan, J.; Mandrus, D. G.; Xiao, D.; et al. Optical Generation of Excitonic Valley Coherence

in Monolayer WSe$_2$. *Nature Nanotechnology* **2013**, *8*, 634–638.

(38)   Tsokkou, D.; Yu, X.; Sivula, K.; Banerji, N. The Role of Excitons and Free Charges in the Excited-State Dynamics of Solution-Processed Few-Layer MoS$_2$ Nanoflakes. *J. Phys. Chem. C* **2016**, *120* (40), 23286–23292.

(39)   Pogna, E. A. A.; Marsili, M.; De Fazio, D.; Dal Conte, S.; Manzoni, C.; Sangalli, D.; Yoon, D.; Lombardo, A.; Ferrari, A. C.; Marini, A.; et al. Photo-Induced Bandgap Renormalization Governs the Ultrafast Response of Single-Layer MoS$_2$. *ACS Nano* **2016**, *10* (1), 1182–1188.

(40)   Ceballos, F.; Cui, Q.; Bellus, M. Z.; Zhao, H. Exciton Formation in Monolayer Transition Metal Dichalcogenides. *Nanoscale* **2016**, *8* (22), 11681–11688.

(41)   Nie, Z.; Long, R.; Sun, L.; Huang, C.; Zhang, J.; Xiong, Q. Ultrafast Carrier Thermalization and Cooling Dynamics in Few-Layer MoS$_2$. *ACS Nano* **2014**, *8* (10), 10931–10940.

(42)   Shi, H.; Yan, R.; Bertolazzi, S.; Brivio, J.; Gao, B.; Kis, A.; Jena, D. Exciton Dynamics in Suspended Monolayer and Few-Layer MoS$_2$ 2D Crystals. *ACS Nano* **2013**, *7* (2), 1072–1080.

(43)   Bhanu, U.; Islam, M. R.; Tetard, L.; Khondaker, S. I. Photoluminescence Quenching in Gold-MoS$_2$ Hybrid Nanoflakes. *Sci. Rep.* **2014**, *4*, 1–5.

(44)   Lee, G.-H.; Lee, D.-Y.; Hone, J.; Hwan Lee, S.; Sup Choi, M.; Jong Yoo, W.; Yu, Y.-J.; Kim, P. Controlled Charge Trapping by Molybdenum Disulphide and Graphene in Ultrathin Heterostructured Memory Devices. *Nat. Commun.* **2013**, *4* (1), 1–7.

(45)   Eastman, D. E. Photoelectric Work Functions of Transition, Rare-Earth, and Noble Metals. *Phys. Rev. B* **1970**, *2* (1).

Chapter 4

Formation and relaxation dynamics of all four excitonic features (A, B, C, D) in few layer WS$_2$
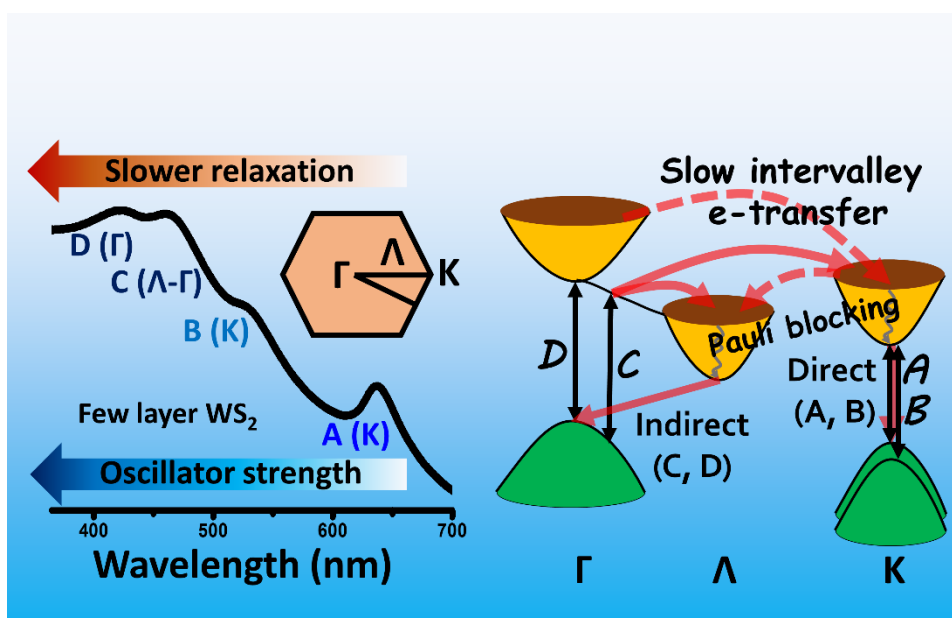
Adapted with permission from Goswami, T.; Bhatt, H.; Babu, K. J.; Kaur, G.; Ghorai, N.; Ghosh, H. N. Ultrafast Insights into High Energy (C and D) Excitons in Few Layer WS$_2$. *J. Phys. Chem. Lett.* 2021, *12*, 6526-6534. **Copyright 2021 American Chemical Society**.

4.1. Introduction

Opto-electronic response of any material has profound reliance on the efficient absorption of electromagnetic radiation and subsequent relaxation of the photogenerated hot carriers in the system.[1,2] The efficacy of an quantum system in various opto-electronic applications like light-emitting diodes,[3] photodetectors,[4,5] opto-valleytronics[6,7] or energy harvesting devices[8] could possibly be improved by slowing down the relaxation of hot carriers or by exploiting broader absorption range[5]. Detailed understanding of the excitonic features generated in an extended range of the radiation would be crucial for developing advanced photonic devices out of any material.

Nowadays, layered TMDCs are being projected as semiconducting equivalent of Graphene[9,10] and they confer great potential towards ultrathin and flexible opto-electronic devices.[11,12,13] As the 2D structure of TMDC approaches the monolayer limit, diverse electronic and optical properties emerge in the system, like exceptionally strong coulombic interactions,[14] increment in the electronic band gap,[15,16] strong spin-orbit coupling,[17,18,19] efficient light-matter interactions, fascinating spin-valley physics[20,21] *etc*. The optical absorption spectrum of mono- and few layer TMDC materials are generally comprised of four excitonic signals usually labelled as A, B, C, D in energetic order,[22,23] where the spectrum is dominated by the C, D, suggested to be formed in a parallel band structure arrangement in their density of states and largely affected by band nesting phenomena.[24,25] The oscillator strengths of these excitons are surprisingly higher than those low energy ones, even greater than monolayer graphene[26] yet, the PL quantum efficiency was found to be very low.[24] This indicates that the relaxation processes associated with these high energy excitons must be very different from those of fundamental excitons (A, B), which are well reported in the literature.[27,28,29,30,31] Dominance of phonon mediated hot carrier relaxation could be one of the key reasons behind this poor quantum efficiency. D. Kozawa *et al*. reported that the photogenerated carriers (electron/hole) in the band-nesting region exhibit fast intraband relaxation towards nearest excited states (Λ valley/Γ hill), followed by a relatively slow non-radiative decay to reach K/K′ state in monolayer MoS$_2$.[24] They attributed this fast relaxation to the spontaneous charge separation in the momentum space (Band Nesting effect), which eventually restricts the quantum efficiency of the C excitonic state. Moreover, as 2D systems undergo bulk to monolayer transition, the relaxation processes are modified accordingly, attributing to the increased carrier interactions in reduced coulombic environment, bandgap renormalization and indirect to direct band gap

transition. Hence, it is very important to study these excitonic species in different dimensionality. Earlier, N. Kumar *et al.* employed transient absorption microscopy in bulk MoS$_2$ and observed efficient inter-valley carrier transfer (K to Γ) of K excitons due to weak exciton binding energy in bulk (25 meV) and significant indirect gap effect in the energy band structure.[32] In 2015, T. Borzda *et al.* reported for the very first time the relaxation dynamics of C excitons along with A, B in case of few layer MoS$_2$.[23] Later on, few other articles surfaced where C-exciton dynamics were studied and quantified in monolayer MoS$_2$. L. Wang *et al.* observed very slow C exciton relaxation in the parallel energy band arrangement and discussed this behaviour as a consequence of excited state coulombic nature along K and Γ space.[33] Y. Li. et al. reported relatively faster C exciton dynamics in monolayer MoS$_2$ attributing to the slow inter-valley carrier transfer.[34] However, the formation characteristics of C excitons has never been discussed in femtosecond time scale. Also, there are no reports regarding D excitonic behaviour in these layered materials. Despite, D exciton does have individual identity in the steady state absorption of WS$_2$ and should have independent effect over optical behaviours in these materials. Henceforth, independent study toward the nature of these high energy excited states and underlying photophysical processes in reduced dimensionality could be of key importance towards better implications of these materials in broadband photonic devices.

In this article, we present a spectroscopic overview of the high energy C, D excitons along with A, B in few layer WS$_2$, elucidating formation as well as relaxation dynamics ranging in a broad UV-Visible region. We have observed low intensity high energy C, D excitonic bleach signals along with A, B excitonic bleaches in the transient absorption spectra. We have explored the excitonic behaviour of both C and D excitons and correlated with the A, B excitonic behaviours. Detailed spectral analysis proposed a tentative position for D excitons, closer to Γ and not in a parallel band arrangement like C exciton. We elucidated that, in few layer WS$_2$ C, D excitons follow Λ-Γ indirect relaxation pathway, contrary to direct K-K recombination of A, B excitons. Both C, D relaxations are much slower in nature due to the involvement of inter-valley scattering process as well as state filling induced Pauli blocking effect in K and Λ valley.

4.2. Synthesis and experimental techniques

4.2.1. Synthesis

Bulk WS$_2$ powder and NMP were purchased from Sigma-Aldrich. Liquid exfoliation technique was employed to prepare few layer WS$_2$ nanosheets. First, 80 mg WS$_2$ powder was crushed with the help of a mortar and pestle for 30 mins to make fine uniform powder. These crushed powders were solvated in 15 ml of NMP and subsequently sonicated for 4h in an ultrasonic bath sonicator. Then, dispersions were probe sonicated for 1h and centrifuged at 4000 rpm for 30 mins. The above three-fourth part of supernatant containing few layers of WS$_2$, were carefully pipetted off and collected for further studies.

4.2.2. Material characterisation

As prepared WS$_2$ sheets were characterised using Raman, AFM and TEM measurements. Raman spectra were collected with a 532 nm laser line using a WITEC alpha 300 R Raman spectrometer. A Bruker Multimode 8 AFM system was used for AFM imaging of WS$_2$ flakes in tapping mode under ambient conditions. The morphological features of the WS$_2$ layers were obtained using Transmission Electron Microscope (TEM, JEOL JEM 2100) at an accelerating voltage of 200 kV. The steady state absorption spectra were collected with a Shimadzu UV-2600 UV-vis spectrophotometer.

4.2.3. Femtosecond transient absorption spectroscopy

The ultrafast setup was comprised of a Ti: sapphire amplifier system (Astrella, Coherent, 800 nm, 3mJ/pulse energy, ~ 35 fs pulse width and 1 kHz repetition rate) and Helios Fire pump-probe spectrometer.[35.] With the help of two beam splitters the output laser pulses were cleaved into pump (95% of the output) and probe (remaining 5%) beams. Optical Parametric Amplifier (OPerA-SOLO) was in place of pump beam to produce required wavelength for the photo-excitation of the sample. A delay stage is operating in path of probe beam to maintain a perfect delay between pump and probe in temporal sense throughout the experimental procedure. Monochromatic probe light passes through a CaF$_2$ crystal generating UV-Visible probe pulses. Probe beam passes through sample dispersion and falls upon fibre coupled CMOS detectors connected with the computer system. The diameter of pump and probe beam spot sizes are ~ 250 and ~ 60 µm. The average power of the probe pulses (white light) was ~ 30 µW. WS$_2$ few layer solutions in a 2 mm quartz cuvette were taken as sample. All the experimental measurements were carried out at room temperature. The collected TA data were chirped and fitted multi-exponentially using surface explorer software.

4.3. Results and discussion

4.3.1. Basic characterisation

WS$_2$ few layers were exfoliated in NMP using Liquid exfoliation method, a simple, inexpensive, and mass productive technique in comparison to the generally used CVD or mechanical exfoliation methods. Raman spectra of few layer WS$_2$ are shown in **Figure 4.1a, b**. Exfoliated WS$_2$ dispersions were extremely diluted to minimize aggregation of nanosheets and spin coated over SiO$_2$/Si substrate for carrying out Raman and AFM experiments. **Figure 4.1a** represents typical Raman spectrum of WS$_2$ nanosheets on top of a SiO$_2$/Si substrate[36,37,38], following excitation at 532 nm laser. The spectrum is dominated by sharp E$^1_{2g}$ (Γ) and A$_{1g}$ (Γ) peaks of WS$_2$, with the presence weak Si signal around 520 cm^{-1}. [36] Weak LA (M) peak is observed at 178 cm^{-1}. In TMDC, E$^1_{2g}$ mode emerges from the in-plane opposite direction oscillation of W and S atoms, whereas A$_{1g}$ mode generates from out of plane vibration of S atoms[37]. Multi-peak Lorentzian fitting reveals four distinct closely spaced peaks for WS$_2$, 2LA (M)- E$^2_{2g}$ (Γ), 2LA (M), E$^1_{2g}$ (Γ) and A$_{1g}$ (Γ) at 324.4, 351.7, 357.7 and 420.2 cm^{-1} respectively (**Figure 4.1b**)[39]. 532 nm laser excitation induces strong electron-phonon coupling in the system and results in many second-order and multi-photon peaks in the Raman spectrum[36, 39]. Intensity of these second order peaks, specially 2LA (M) mode is amplified with decreasing layer numbers in WS$_2$ system and reaches maximum in monolayer[36]. Presence of 2LA mode very close to E$^1_{2g}$ hinders precise determination of peak positions and it is very difficult to assess the number of layers from the peak difference.
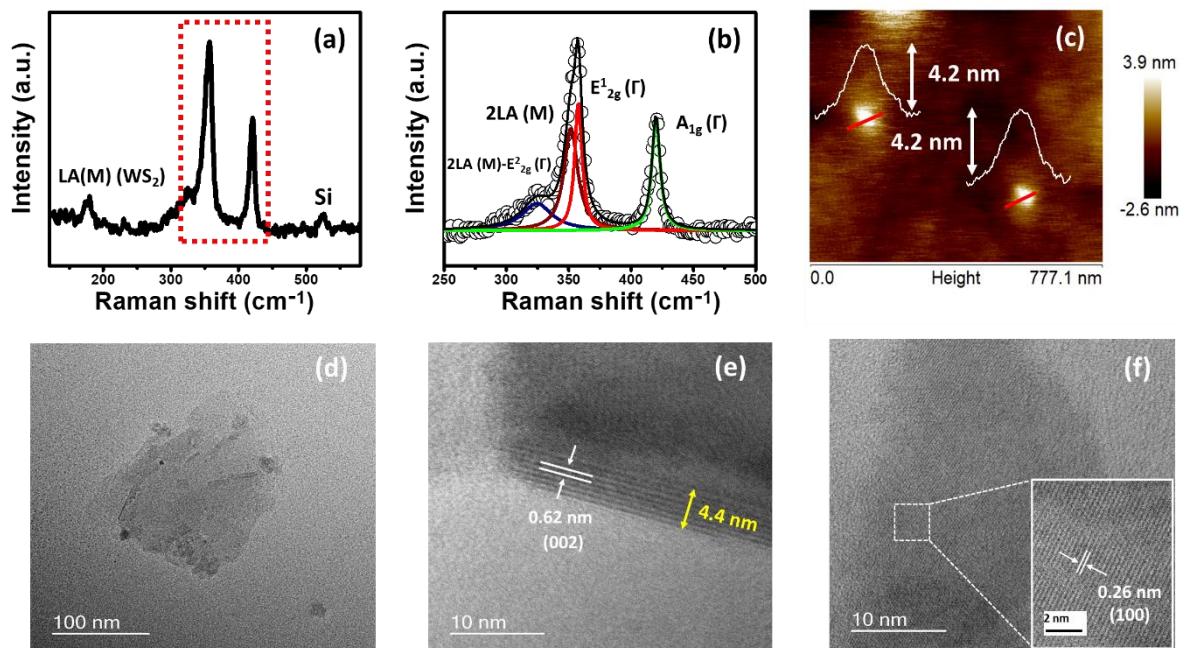
Figure 4.1: (a) Room temperature Raman spectrum of few layer WS$_2$ deposited over SiO$_2$/Si substrate, using 532 nm laser excitation. Red dotted lines focus significant peaks of WS$_2$. **(b)** Lorentzian fitting of WS$_2$ peaks, portraying both the characteristic raman modes, E$^1_{2g}$ (Γ) and A$_{1g}$ (Γ), along with 2LA (M) and 2LA (M)- E$^2_{2g}$ (Γ), represented by red, green, brown, and blue lines. **(c)** AFM topographic image of WS$_2$ nanosheets on top of SiO$_2$/Si substrate, along with cross-sectional height profile along the red lines in the image. **(d)** Low resolution TEM images of WS$_2$ sheets. **(e)** HRTEM images of multilayer WS$_2$ showing 002 planes. **(f)** HRTEM images representing 100 planes of WS$_2$.

AFM images of WS$_2$ nanosheets are presented in **figure 4.1c**, which focuses upon two small flakes. The thickness of these grains were determined along the red line marked in the image. The thickness of the WS$_2$ nanosheets was found to be ~ 4.2 nm, which is analogous to 5-6 layers[40], considering monolayer thickness of ~ 0.7 nm[41]. In **figure 4.1d, e, f**, we have represented TEM and HRTEM images of layered WS$_2$. **Figure 4.1b** confirms the multilayer nature of the sheets and depicted loading of WS$_2$ (002) planes[42], having interplanner spacing of 0.62 nm. The approximate thickness of the nanosheets was calculated to be 4.4 nm from **figure 4.1b**[43], which corresponds to around 6 layers of WS$_2$. This result well corroborates with our AFM analysis. In planner orientation, characteristic (100) planes are observed, with interplanner distance of 0.26 nm (**figure 4.1c**).

4.3.2. Steady state optical measurements and the generation of the excitons

The optical signature of a material reveals the basic features of their energy band structure. **Figure 4.2a** displays the absorption spectra of few layer WS$_2$, presenting all four excitonic peaks, i.e., A, B, C, D at around 636, 530, 462 and 423 nm respectively (Peaks are labelled following their usual convention[23,44]). Quantum confinement with lower dimensionality and strong coulomb interaction ensures dominance of excitonic features in the steady state absorption spectra. Here, the spectrum is primarily dominated by strong absorptions from high energy excitons (C, D), which is quite common in low-dimensional TMDC materials.

In **Figure 4.2b** we discussed a simplified optical band diagram for few layer WS$_2$, representing A, B, C, D excitonic transitions. In layered TMDC systems, interlayer interaction plays significant role in defining electronic band structures of the system. In monolayer, conduction band minima (CBM) and valence band maxima (VBM) both lie in K/K' region of the Brillouin zone. However, with increasing no of layers Λ valley shifts downwards and Γ hill shifts

upwards, leaving K/K' valley or hills almost unaltered, as a result of which CBM now resides in Λ valley and VBM in Γ hill.[45,46] A and B peaks originate from the excitonic transitions at the K/K' spaces between conduction band minima and spin splitted valence band maxima.[13,47]
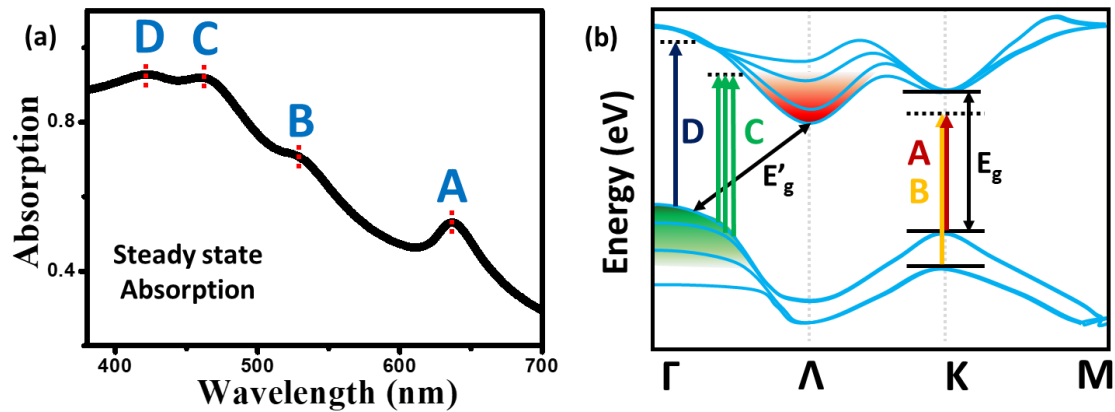
Figure 4.2: (a) Steady state absorption spectra of few layer WS₂. **(b)** Quasiparticle optical band structure of few layer WS₂, adapted from previous reports on TMDC.[25,45] E_g and E'_g represent direct and indirect optical band gap (In few layer $E_g > E'_g$).

On the other hand, the high energy exciton (C) arises from nearly-degenerate excitonic states associated with the van Hove singularity in the joint density of state (JDOS) diagram, between Λ and Γ space.[34,48] The locally parallel band near Λ space gives rise to local minima in optical band structure with the formation of C exciton.[48] However, we could not find any specific report regarding momentum space position for the D excitonic state. S. H. Aleithan *et al.* suggested that the D excitonic state could be originating from a higher energy conduction band valley close to C (Λ valley), or could be the result of another band nesting effect in JDOS.[49] They anticipated that, C and D excitonic states would also have bound states shifted by a binding energy ~ 500 meV below conduction band minima in the optical band structure, just like A and B excitons. Although, these assumptions were never been corroborated with any experimental findings. Transient absorption spectroscopy can help us to find a closer look on the formations of C, D excitons and might be able to make a concrete statement on those assumptions.

4.3.3. Transient study

The transient responses were collected with non-resonant high energy excitation (370 nm, 3.35 eV) probing at different pump-probe delay time and displayed in **figure 4.3a, b**. There are four photo-induced transient bleaches appeared in 2D colour contour plot peaking at around 636,

532, 464 and 422 nm, corresponds to A, B, C and D excitonic transition, as discussed in steady state absorption spectra in **figure 4.2a**. Herein 370 nm pump provides sufficient photon energy to generate different excitonic states of WS_2 as shown in **figure 4.3a and b**. The intensity of C and D excitonic bleach signal is significantly lower as compared to that of A and B excitonic bleach signals, which is contrary to the fact that C, D possess higher oscillator strength than that of A, B.[26] The spectral amplitude (S) of a transient feature is necessarily proportional to the product of injected carrier concentration / exciton density in a particular state (n) and oscillator strength of the corresponding optical transition (f), i.e., S α n.f.[50]
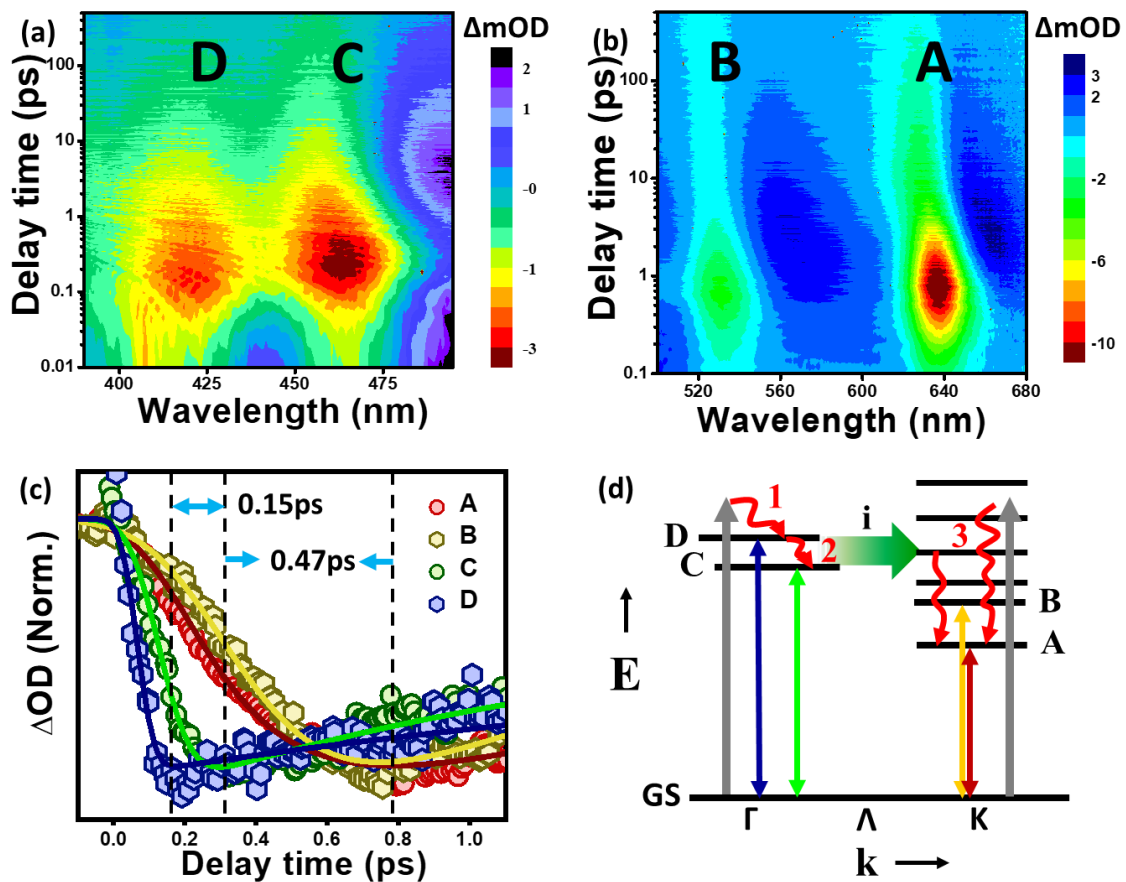
Figure 4.3: (a, b) 2D colour contour plot of D, C, B, A excitonic features representing their spectral and temporal evolution in few layer WS_2, with 370 nm (3.35 eV) photoexcitation and 100 μJ/cm² excitation fluence. Colour intensity represents the intensity of the respective transient signal for a certain probe wavelength and pump-probe delay time. **(c)** Normalized growth profiles of all four excitonic features probed at bleach maxima at 636 nm, 532 nm, 464 nm and 422 nm for D, C, B, A exciton respectively. **(d)** Simple energy diagram representing probable thermalization of hot plasma into corresponding excitonic states. 1, 2, 3 are intra-

valley thermalization associated with D, C and A excitons respectively. 'i' denotes inter-valley electron transfer from C, D towards A, B states.

Hence, the reason behind this lower spectral intensity in the high energy regime could be due to lower carrier density. Gradual enhancement of only C exciton intensity (when 'A' intensity was nearly constant) with increment of carrier density in monolayer MoS_2[34] also justifies this remark. We assume that, large proportion of the electron-hole plasma generated at this blue regime (photo-excited with high energy 370 nm pump), would migrate to the lower energy valleys (K, Λ) through inter-valley phonon scattering, and contributes towards the formation of A, B excitons.

Figure 4.3c depicts the growth profiles of different transient excitonic bleaches. Exciton dynamics are monitored by tuning the probe wavelength at the photoinduced bleach maxima, i.e., band-edge of different excitonic states. We found that there exists a distinct time offset in the growth dynamics of these four excitons, where high energy excitons appear at much faster time scale (at least 0.45 ps) as compared to that of A, B. In addition to that, there is slight difference in growth time scales within C and D also. Earlier, D. Kozawa *et al*. reported independent inter-valley thermalization phenomena for A exciton emission in bilayer MoS_2 and WS_2 with excitation of the photo carriers at the band nesting region (C-resonant excitation).[24] In the present investigation we are exciting the system with much higher energy as compared to this report. Henceforth we expect generation of hot electrons closer to Γ plateau in the optical band structure and we cannot neglect the possibility of inter-valley transfer in A/B excitonic growth. So the slow rise time of the A/B excitonic signals would be resultant of both intra-valley (within K-valley itself) and inter-valley thermalization process (from Γ states as well as band nesting region to K space) (**Figure 4.3d**). Very low spectral amplitude of C, D implies that inter-valley thermalization triumphs over the intra one, influencing this extended growth time of A/B. Significant enhancement of A excitonic signal rise time with excitation higher or close to C, D states, confirms immense dependence of A/B exciton formation over Γ-K inter-valley scattering (**will be discussed later**). For high energy excitons C, D, rise time would refer to mainly intra-valley thermalization where photoexcited carriers form bound pairs, followed by fast relaxation to the excitonic band edge lying in the similar valley or hill as that of photoexcited carriers. As pump photon energy is very close to the C, D energy levels, the contribution of the intra-valley scattering process would be minimal in thermalization

towards the band edge. To further analyse different excitonic behaviours in WS_2 we employed wide range of photon energy pumps to excite the system.

4.3.4. Pump dependent TA measurements

The intensity map plotted in **figure 4.4a**, b illustrates the evolution of the D, C, A exciton respectively, for a range of pump excitation (1.95- 4.13 eV) (B exciton is excluded as it behaves like A). The high energy excitons are still visible even on application of much lower excitation photon energy. Significant overlap in between C excitonic states and K-space excited states makes this up-conversion possible.[33,49] If we excite with a lower energy pump (below C excitonic resonance), we inject photocarriers in the K-valley. These photocarriers undergo probe induced photo-absorption to K high energy states and would subsequently be delocalised into C-excitonic states for the formation of C excitons. The exciton intensities in all three cases deplete with the decrement of photon energy. This behaviour correlates well with the fact that, high photon energy is capable of populating with higher number of charge carriers influencing the phase space filling, responsible for the excitonic bleach formation[51].
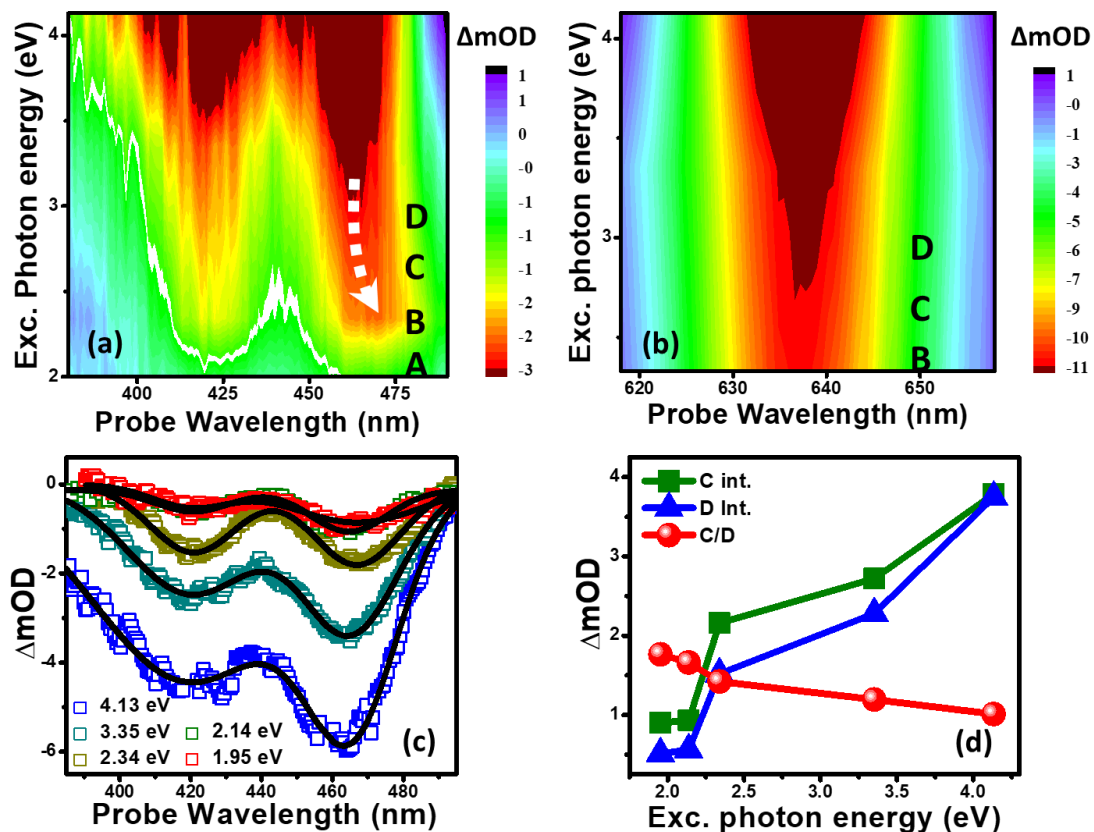
Figure 4.4: 2D intensity map of transient absorption spectra at 0.25 ps, simulated from different energy pump excitations for **(a)** C, D and **(b)** A exciton. The A, B, C, D notations in

the colour map signifies the corresponding excitonic positions of these excitons. **(c)** Transient absorption spectra of high energy C, D exciton at 0.25 ps delay time for pump energy 1.95, 2.14, 2.34, 3.35 and 4.13 eV. The solid lines represent Gaussian fitting of the experimental data points. **(d)** C/D intensity ratio plotted as a function of pump photon energy. Individual C, D exciton intensity is also plotted for the reference.

Interestingly, the position of C excitonic bleach show anomalous behaviour with different pump wavelength. Specifically, the position of C excitonic signal undergoes a red shift with lowering of pump photon energy. This characteristic red shift indicates towards involvement of different energy levels for the exciton formation on application of different pump energy. Unlike other excitons, C exciton formation occurs within parallel band arrangement in between Λ-Γ space and is not involved with any extreme points in the conduction and valence band structure. At the same time, the parallel bands pass through an emergence of local minima with the formation of bound pairs in this region. With implication of higher energy photons mainly higher order states get involved in order to create the minima with the formation of C excitons. Whereas, for lower energy pump excitations photoexcited carriers near K-space travel through Λ region to reach C, D excitonic states. Charge carriers ejected from the lower energy pump can only place itself in the lower side of the energy levels and generate C excitons with a significant red shift. On the other hand, the position of D excitonic signal does not necessarily depend on pump photon energy. This observation indicates that, D excitons do not necessarily form in a parallel band arrangement like C. They originate in a valley-hill arrangement like A, B.

Figure 4.4c describes evolution of excitonic intensity and broadening of transient absorption spectra of C, D excitons for pump energy 1.95, 2.14, 2.34, 3.35 and 4.13 eV. It is evident that the shape of the transient spectra merely changes with pump photon energy. Although, with decrement of photon energy, C excitonic peaks get broader while D gets narrower. This broadening in case of C excitons reaches maximum at 1.95 eV excitation. We expect this as a resultant of the involvement of lower energy states in the band nesting regime with the formation of C bound pairs in low energy excitations. This again confirms the fact that energy bands corresponding to the formation of C exciton formation strongly dependant on the applied photon energy. The intensity of C and D excitons are extracted and plotted as a function of pump photon energy in **figure 4.4d**. We used maximum bleach intensity as it directly correlates maximum exciton population in the respective excitonic band edge. As we decrease the pump

photon energy, intensity of the bleach signals decreases, where D exciton intensity decreases at much faster rate than C. An almost linear increment of C/D bleach intensity ratio was observed in our pump photon energy range. This indicates that, with lower pump energy, C exciton formation probability is much higher than D exciton. The reason behind this could be the incapability of lower energy pump in providing hot carriers into the D excitonic states. Lower energy pump can easily promote charge carriers into C excitonic states, but the same with D states is not that feasible.
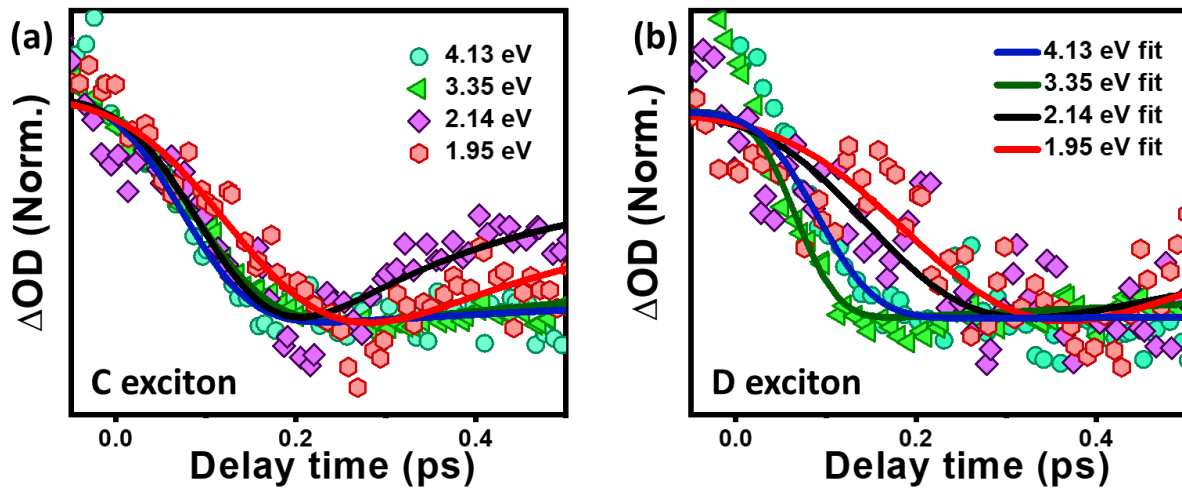
Figure 4.5: Transient growth profiles of **(a)** C and **(b)** D excitons with application of 4.13, 3.35, 2.14 and 1.95 eV pump energy.

To analyse pump photon energy induced effect on the formation of WS$_2$ excitons, we compared transient growth signal of these excitonic features in different pump photon energy. **Figure 4.5a, b** presents growth features of C, D excitons respectively, with excitation of 4.13, 3.35, 2.14 and 1.95 eV pump photon energy, which will be further reffered as higher energy photons, HEP (4.13 and 3.35 eV); and lower energy photons, LEP (2.14 and 1.95 eV). C, D bleach maxima experience anomolous change in rise time much unlike A (**Figure 4.6**) with increasing energy of photons. All the excitation energies are higher corresponding to the energitical position of A exciton (1.95 eV). Hence, the growth fetaures in this figure picturize the thermalization of photo-generated hot carriers corresponding to the A excitons following different excitation photon energy. The instantateneous bleach signal growth in case of near resonant excitation extends itself in a much slower phenomena with increasing photon energy (**Figure 4.6a**). We observed a significant jump in the rise time for HEP compared to LEP. This observation stands over the immense dependence of fundamental K-space excitons on high energy exciton population, deterioration of C, D bound pairs generates enormous amount of

hot excited carriers which will eventually accumulate in the band edge regions forming A, B excitons.

On the other hand, for all the excitations, C exhibits almost identical rise time (except 1.95 eV), while there is a distinct difference in the rise times for D at different pump photon energy. In order to explain these events we need to understand how HEP and LEP excitations work for C, D formation. In case of HEP, photocarriers are excited in the high energy levels, from where they thermalize themselves at the excitonic band edges. Whereas in LEP scenario, C, D states are populated from K excited state mediated tunneling. So, the growth time observed here would be collective potrayal of excitation of carriers in the K space and subsequent tunneling. Hence, the observed growth process of C excitonic signal in LEP would corresponds to the probe mediated absorption of photocarriers into the C-hybridised K states from the lower energy states in K-valley (considering there is no phonon mediated phenomenon involved).
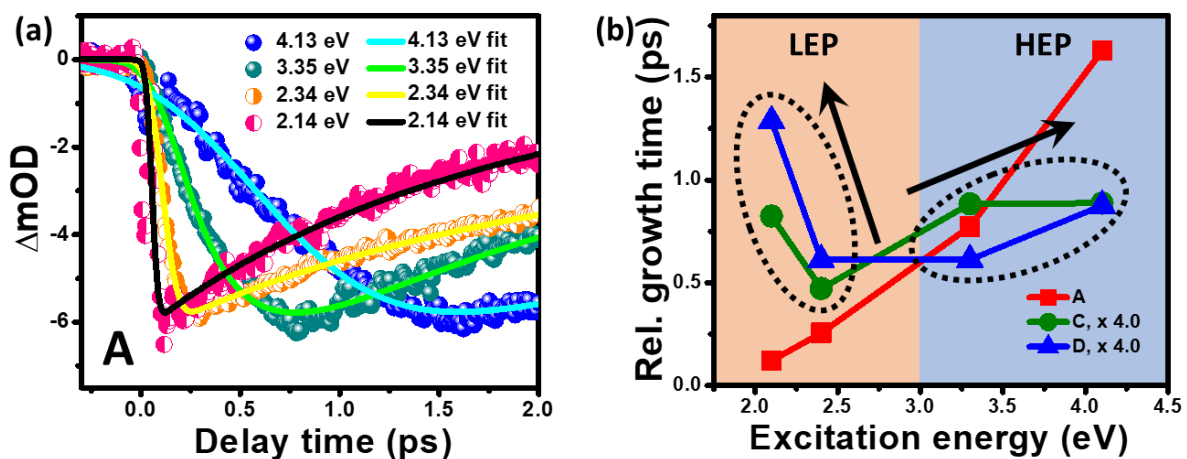
Figure 4.6: (a) Growth profiles of A with application of 4.13, 3.35, 2.34 and 2.14 eV pump energy. **(b)** Plot of relative growth values for A, C and D exciton for different pump excitation energy. C, D data points are rescaled (multiplied 4 times) to be comparable with A.

For HEP excitation, C exciton rise time is a compilation of of C exciton formation and opposite propagation of electron and hole in the parallel band arrangement, as dicussed earlier. Identical rise time for 3.35 and 4.13 eV excitation implies that band nesting propagation does not necessarily depend on the energy of photons. Whereas, on increasing photoexcitation energy from 3.35 to 4.13 eV, D exciton exhibits enhancemement in the signal rise time, in contrast to the indifferent behaviour of C exciton. Similar observation was recorded for A, B excitons. This proves that, D excitons are different than C excitons. In LEP scenario, D excitonic growth is substantially enhanced. The growth time scales are even bigger than C excitons. This

indicates that D excitons do not emerge in the similar energy levels as of C, because in that case growth time scales of both the excitons would be similar in the LEP regime. We have already discussed, how electron delocalisation from the K high energy states to C excitonic states play important role for the formation of C excitons in LEP case. It is very clear that similar phenomena are not sufficient to produce D excitons. And we can conclude that, there is no excitonic overlap between D states and K high energy states and K-Γ tunnelling to D states is not viable. There must be some phonon mediated up-conversion process is involved in the generation of D excitons, which slow down the growth as we decrease the pump photon energy.

4.3.5. Recombination pathway

In **figure 4.7a** transient kinetic profile of exciton A is directly compared with that of high energy excitonic features (C, D). These decay profiles were fitted with multi-exponential time constants and are shown in **table 4.1** where all the fitting parameters are listed. The decay time components τ_2, τ_3, and τ_4 are also marked in three different background
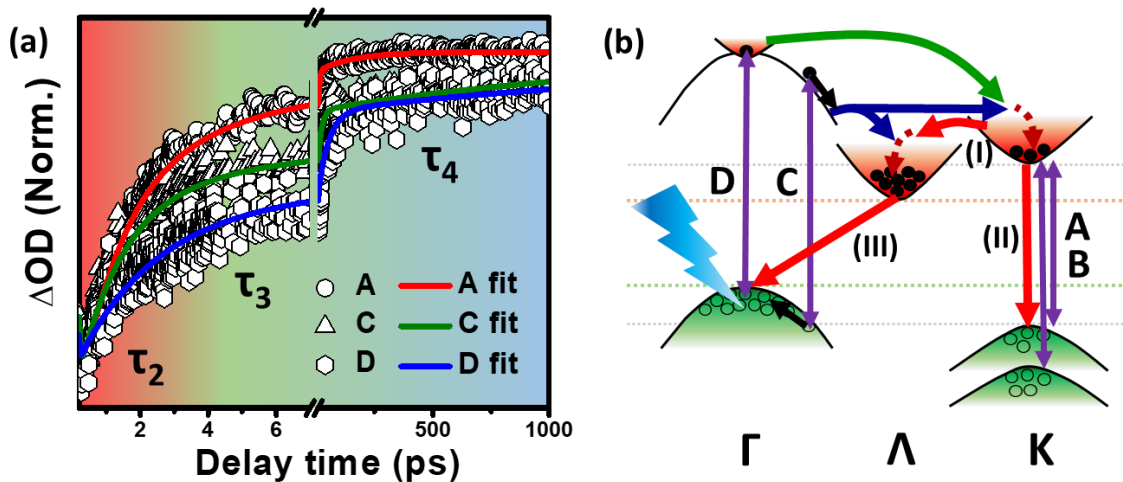
Figure 4.7: (a) Normalized kinetic traces of A, C, D probed at excitonic bleach maxima (636, 464 and 422 nm) following 3.35 eV photoexcitation. The solid lines are multiexponential fitting results of the experimental data. **(b)** Schematic optical valley diagram of few layer WS₂ and possible relaxation pathways for the excitons following 370 nm photoexcitation. Here, only Γ space excitations are considered for the sake of simplicity. Also, less-probable processes are omitted here. Green arrows represent inter-valley electron transfer from D states, whereas blue arrows symbolize electronic delocalisation of C excitons into Λ and K valley. C excitonic propagation due to band nesting effect is shown with two antiparallel black arrows for electron

and hole. Red arrows present subsequent migration of electrons (common for all the excitons), where (I) inter-valley scattering of electrons from K to Λ valley, (II) K-K direct recombination and (III) Λ-Γ indirect recombination. Red dotted lines are intra-valley thermalization processes in K and Λ valley.

colours in **figure 4.7a**. B exciton dynamics is excluded from the discussion, as it is strongly influenced by the surrounding photo-induced absorption signals. The decay dynamics of C and D excitonic signals, are much slower as compared to A, despite having very low spectral intensity. Previously few articles reported similar slow relaxation of C excitons compared to A/B in monolayer MoS$_2$, and elucidated that slow inter-valley electron transfer from Λ to K valley would be responsible for the slow dynamical nature of C transient signal.[33,34] However, in few layer case the scenario would not be the same. Here, the electronic band structure modifies itself with increasing layers, placing CBM at Λ valley and VBM in Γ hill, in contrast to the monolayer TMDC. This adversely affect the direct K-K transition, favouring indirect Λ-Γ and K-Γ transitions. Now, in case of C excitons, following the formation of the bound pair, the electron and hole start propagating in opposite direction towards Λ and Γ respectively (Band nesting effect). This migration of electrons could end up in Λ valley, owing to closer proximity of C excitonic states with Λ valley compared to K and subsequently being thermalized to the Λ valley edge. However, C electrons could also easily migrate towards the K regime as C excitonic states and K excited states enjoy significant overlap,[33,52] as we have shown in our previous discussion. Hot electrons in K valley would either be transferred into the Λ valley through K-Λ inter-valley scattering or would undergo intra-valley thermalization in K valley itself and help in formation of A/B excitons. In room temperature PL measurements for different layers of WS$_2$, Zhao et al. showed that indirect Λ-Γ PL peaks are enhanced with increasing layer numbers, however the PL spectrum is also comprised of PL peaks corresponding to the direct K-K recombination[46]. However, they failed to observe any indirect PL peak corresponding to the K-Γ recombination at room temperature. From this instance, we can assume that Λ-Γ indirect pathway may be the most feasible channel for the relaxation of WS$_2$ excitons, although K-K direct recombination cannot be neglected. D excitons would also end up in K valley rather in Λ, as Γ-K inter-valley scattering would be much stronger than the Γ-Λ one, as K valley lies closer to Γ valley than that of Λ.[46] Subsequently D excitons would follow C relaxation pathway. In **figure 4.7b** we presented a simple energy valley schematics of few layer WS$_2$ portraying electronic transitions corresponding to all four excitonic features following 370 nm photo-excitation (**Check figure 4.8 for more clear representation**).
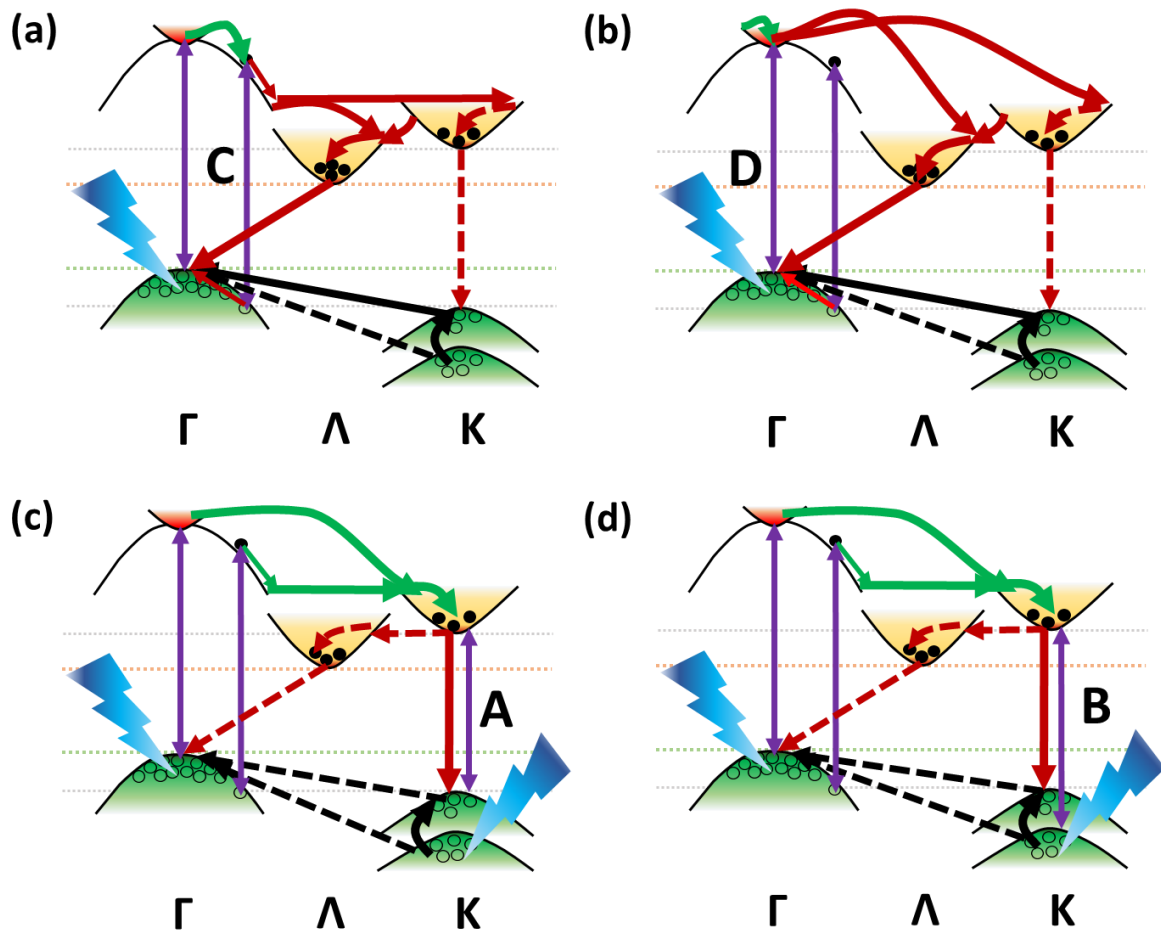
Figure 4.8: Graphical representation of different excitonic relaxations in few layer WS$_2$ for a high energy (370 nm, 3.35 eV) excitation in case of **(a)** C, **(b)** D, **(c)** A and **(d)** B excitons. Optical valleys are shown as per main paper discussion. Here, green, and red lines represent photo-physical processes responsible in formation and decay of the respective excitons in terms of electrons. Hole migrations are presented with black lines. Dotted lines are the representation of less-plausible pathways.

From multi-exponential fitting, decay time components for the transient bleach signals were found to be, $\tau_2 \sim 1.4 \pm 0.1$ ps (62.2 %), $\tau_3 \sim 15.8 \pm 5.6$ ps (18.6 %) and $\tau_4 > 1$ ns (19.2 %) for C excitons and $\tau_2 \sim 2.4 \pm 0.2$ ps (53.3 %), $\tau_3 \sim 46.6 \pm 12.3$ ps (27.8 %) and $\tau_4 > 1$ ns (18.9 %) in case of D. The final decay component ($\tau_4 > 1$ ns) resembles with slow dynamical nature of indirect recombination processes observed in bulk samples.[33,52]

Table 4.1. Transient fitting components of different excitonic features for 3.35 eV pump excitation. The kinetic profiles are fitted with surface explorer software as a summation of convoluted exponentials.

Probe wavelength, nm	Growth		Decay	
	τ_1 , ps	τ_2 , ps	τ_3 , ps	τ_4 , ns
636 (A)	0.15 ± 0.1	1.8 ± 0.2 (78.9 %)	8.4 ± 4.2 (15.3 %)	0.15 ± 0.1 ns (5.8 %)
532 (B)	0.14 ± 0.1	1.0 ± 0.1 (83.1 %)	3.9 ± 1.2 (13.1 %)	> 1 ns (3.8 %)
464 (C)	< 0.1 (IRF limited)	1.4 ± 0.1 (62.2 %)	15.8 ± 5.6 (18.6 %)	> 1 ns (19.2 %)
422 (D)	< 0.1 (IRF limited)	2.4 ± 0.2 (53.3 %)	46.6 ± 12.3 (27.8 %)	> 1 ns (18.9 %)

Hence, we can consider Λ-Γ indirect recombination channel to be the main recombination pathway for C, D excitons, as compared to direct K-K recombination. Based on our previous discussion we ascribe τ_2, τ_3 and τ_4 as inter-valley electron transfer (Γ-K for D and K-Λ for C), intra-valley thermalization in Λ and Λ-Γ indirect recombination, respectively. τ_2 and τ_3 is much slower in case of D excitons than that of C, mainly because of pauli blocking effect in K valley in course of Γ(D)-K inter-valley electron transfer and in intra-valley thermalization process, as the states are already filled from either C or A/B electrons. Contrary to C and D, A exciton exhibit very fast decay ($\tau_4 \sim 150 \pm 94$ ps). This intrigues us to think that, K-K direct recombination process is the significant contributor for the relaxation of A[53], and defect states are playing very important role in that. The possible reason would be the lower probability of K-Λ inter-valley scattering for K band edge electrons, owing to less kinetic energy of band edge electrons as compared to the high energy ones[54]. Although we could not analyse B exciton dynamics separately, we expect relaxation of B would follow A excitons, as these two are immensely dependent on each other.

4.4. Conclusions

In summary, we explained the formation and relaxation behaviours of high energy excitonic features, in reference of their low energy counterparts for few layer WS₂ in room temperature. Our ultrafast measurements reveal weak C, D excitonic bleach formation at the blue region of the transient spectra along with A, B excitonic bleach signal at the red region irrespective of the applied excitation photon energy. With high energy excitation, large number of photo-

excited electrons generated in the Γ space, undergo Γ-K inter-valley transfer prior to the formation of C, D bound pairs and greatly influence A, B exciton formation. D exciton emerges in a valley-hill arrangement close to Γ, more like A, B and shows no effect of band nesting, unlike C exciton. We elucidated that, C exciton formation strongly depends on pump photon energy. In course of relaxation, C, D follow the bulk route, first inter-valley electron transfer from Γ to K valley and K to Λ valley, subsequently slower intra-valley thermalization in Λ valley and finally indirect recombination in Λ-Γ route. Involvement of inter-valley scattering processes towards the filled states of K, Λ retard the relaxation of these high energy excitons. Pauli blocking in intra-valley thermalization and slow indirect recombination channel also serves as a bottleneck in C, D relaxation pathway and extends their charge separation. D excitons are most severely affected from the pauli blocking in both K and Λ valley and results in very slow relaxation. Contrary to these high energy excitons, the primary relaxation channel for A, B was found to be direct K-K recombination. We expect that, our detailed analysis on WS$_2$ excitonic features in a broad range of the electromagnetic spectrum would inspire more studies on valley based exciton formations in atomically thin TMDC systems. Large absorption coefficient and slow relaxation behaviour of these high energy excitons would be of great help in constructing hot carrier based broadband opto-electronic devices.

4.5. References

(1)   Saeed, S.; de Jong, E. M. L. D.; Dohnalova, K.; Gregorkiewicz, T. Efficient Optical Extraction of Hot-Carrier Energy. *Nat. Commun.* **2014**, *5*, 4665.

(2)   Gabor, N. M.; Song, J. C. W.; Ma, Q.; Nair, N. L.; Taychatanapat, T.; Watanabe, K.; Taniguchi, T.; Levitov, L. S.; Jarillo-Herrero, P. Hot Carrier–Assisted Intrinsic Photoresponse in Graphene. *Science* **2011**, *334*, 648 LP - 652.

(3)   Yang, W.; Shang, J.; Wang, J.; Shen, X.; Cao, B.; Peimyoo, N.; Zou, C.; Chen, Y.; Wang, Y.; Cong, C.; Huang, W.; Yu, T. Electrically Tunable Valley-Light Emitting Diode (VLED) Based on CVD-Grown Monolayer WS$_2$. *Nano Lett.* **2016**, *16*, 1560-1567.

(4)   Lee, H. S.; Min, S.-W.; Chang, Y.-G.; Park, M. K.; Nam, T.; Kim, H.; Kim, J. H.; Ryu, S.; Im, S. MoS$_2$ Nanosheet Phototransistors with Thickness-Modulated Optical Energy Gap. *Nano Lett.* **2012**, *12*, 3695-3700.

(5)   Yin, Z.; Li, H.; Li, H.; Jiang, L.; Shi, Y.; Sun, Y.; Lu, G.; Zhang, Q.; Chen, X.; Zhang, H. Single-Layer MoS$_2$ Phototransistors. *ACS Nano* **2012**, *6*, 74-80.

(6)   Plechinger, G.; Nagler, P.; Arora, A.; Schmidt, R.; Chernikov, A.; Lupton, J.; Bratschitsch, R.; Schüller, C.; Korn, T. Valley Dynamics of Excitons in Monolayer Dichalcogenides. *Phys. status solidi – Rapid Res. Lett.* **2017**, *11*, 1700131.

(7)   Cao, T.; Wang, G.; Han, W.; Ye, H.; Zhu, C.; Shi, J.; Niu, Q.; Tan, P.; Wang, E.; Liu, B.; Feng, J. Valley-Selective Circular Dichroism of Monolayer Molybdenum Disulphide. *Nat. Commun.* **2012**, *3*, 887.

(8)   Bernardi, M.; Palummo, M.; Grossman, J. C. Extraordinary Sunlight Absorption and One Nanometer Thick Photovoltaics Using Two-Dimensional Monolayer Materials. *Nano Lett.* **2013**, *13*, 3664-3670.

(9)   Radisavljevic, B.; Radenovic, A.; Brivio, J.; Giacometti, V.; Kis, A. Single-Layer MoS$_2$ Transistors. *Nat. Nanotechnol.* **2011**, *6*, 147-150.

(10)   Ramakrishna Matte, H. S. S.; Gomathi, A.; Manna, A. K.; Late, D. J.; Datta, R.; Pati, S. K.; Rao, C. N. R. MoS$_2$ and WS$_2$ Analogues of Graphene. *Angew. Chemie Int. Ed.* **2010**, *49*, 4059-4062.

(11)   Bonaccorso, F.; Colombo, L.; Yu, G.; Stoller, M.; Tozzini, V.; Ferrari, A. C.; Ruoff, R. S.; Pellegrini, V. Graphene, Related Two-Dimensional Crystals, and Hybrid Systems for Energy Conversion and Storage. *Science* **2015**, *347*, 1246501.

(12)   Xia, F.; Wang, H.; Xiao, D.; Dubey, M.; Ramasubramaniam, A. Two-Dimensional Material Nanophotonics. *Nat. Photonics* **2014**, *8*, 899-907.

(13)   Wang, Q. H.; Kalantar-Zadeh, K.; Kis, A.; Coleman, J. N.; Strano, M. S. Electronics and Optoelectronics of Two-Dimensional Transition Metal Dichalcogenides. *Nat. Nanotechnol.* **2012**, *7*, 699-712.

(14)   Steinhoff, A.; Rösner, M.; Jahnke, F.; Wehling, T. O.; Gies, C. Influence of Excited Carriers on the Optical and Electronic Properties of MoS$_2$. *Nano Lett.* **2014**, *14*, 3743-3748.

(15)   Splendiani, A.; Sun, L.; Zhang, Y.; Li, T.; Kim, J.; Chim, C.-Y.; Galli, G.; Wang, F. Emerging Photoluminescence in Monolayer MoS$_2$. *Nano Lett.* **2010**, *10*, 1271-1275.

(16) Mak, K. F.; Lee, C.; Hone, J.; Shan, J.; Heinz, T. F. Atomically Thin MoS$_2$: A New Direct-Gap Semiconductor. *Phys. Rev. Lett.* **2010**, *105*, 136805.

(17) Xiao, D.; Liu, G.-B.; Feng, W.; Xu, X.; Yao, W. Coupled Spin and Valley Physics in Monolayers of MoS$_2$ and Other Group-VI Dichalcogenides. *Phys. Rev. Lett.* **2012**, *108*, 196802.

(18) Cheiwchanchamnangij, T.; Lambrecht, W. R. L. Quasiparticle Band Structure Calculation of Monolayer, Bilayer, and Bulk MoS$_2$. *Phys. Rev. B* **2012**, *85*, 205302.

(19) Ochoa, H.; Roldán, R. Spin-Orbit-Mediated Spin Relaxation in Monolayer MoS$_2$. *Phys. Rev. B* **2013**, *87*, 245421.

(20) Rivera, P.; Seyler, K. L.; Yu, H.; Schaibley, J. R.; Yan, J.; Mandrus, D. G.; Yao, W.; Xu, X. Valley-Polarized Exciton Dynamics in a 2D Semiconductor Heterostructure. *Science* **2016**, *351*, 688-691.

(21) Feng, S.; Cong, C.; Konabe, S.; Zhang, J.; Shang, J.; Chen, Y.; Zou, C.; Cao, B.; Wu, L.; Peimyoo, N.; Zhang, B.; Yu, T. Engineering Valley Polarization of Monolayer WS$_2$: A Physical Doping Approach. *Small* **2019**, *15*, 1805503.

(22) Bellani, S.; Wang, F.; Longoni, G.; Najafi, L.; Oropesa-Nuñez, R.; Del Rio Castillo, A. E.; Prato, M.; Zhuang, X.; Pellegrini, V.; Feng, X.; Bonaccorso, F. WS$_2$-Graphite Dual-Ion Batteries. *Nano Lett.* **2018**, *18*, 7155-7164.

(23) Borzda, T.; Gadermaier, C.; Vujicic, N.; Topolovsek, P.; Borovsak, M.; Mertelj, T.; Viola, D.; Manzoni, C.; Pogna, E. A. A.; Brida, D.; Antognazza, M. R.; Scotognella, F.; Lanzani, G.; Cerullo, G.; Mihailovic, D. Charge Photogeneration in Few-Layer MoS$_2$. *Adv. Funct. Mater.* **2015**, *25*, 3351-3358.

(24) Kozawa, D.; Kumar, R.; Carvalho, A.; Kumar Amara, K.; Zhao, W.; Wang, S.; Toh, M.; Ribeiro, R. M.; Castro Neto, A. H.; Matsuda, K.; Eda, G. Photocarrier Relaxation Pathway in Two-Dimensional Semiconducting Transition Metal Dichalcogenides. *Nat. Commun.* **2014**, *5*, 4543.

(25) Carvalho, A.; Ribeiro, R. M.; Castro Neto, A. H. Band Nesting and the Optical Response of Two-Dimensional Semiconducting Transition Metal Dichalcogenides. *Phys. Rev. B* **2013**, *88*, 115205.

(26)   Kumar, R.; Verzhbitskiy, I.; Eda, G. Strong Optical Absorption and Photocarrier Relaxation in 2-D Semiconductors. *IEEE J. Quantum Electron.* **2015**, *51*, 1-6.

(27)   Sie, E. J.; Frenzel, A. J.; Lee, Y.-H.; Kong, J.; Gedik, N. Intervalley Biexcitons and Many-Body Effects in Monolayer MoS₂. *Phys. Rev. B* **2015**, *92*, 125417.

(28)   Fan, P.; Zheng, B.; Sun, X.; Zheng, W.; Xu, Z.; Ge, C.; Liu, Y.; Zhuang, X.; Li, D.; Wang, X.; Zhu, X.; Jiang, Y.; Pan, A. Trion-Induced Distinct Transient Behaviour and Stokes Shift in WS₂ Monolayers. *J. Phys. Chem. Lett.* **2019**, *10*, 3763-3772.

(29)   Wang, L.; Wang, W.; Wang, Q.; Chi, X.; Kang, Z.; Zhou, Q.; Pan, L.; Zhang, H.; Wang, Y. Correction: Study on Photoelectric Characteristics of Monolayer WS₂ Films. *RSC Adv.* **2019**, *9* (67), 38943-38943.

(30)   Cunningham, P. D.; McCreary, K. M.; Jonker, B. T. Auger Recombination in Chemical Vapor Deposition-Grown Monolayer WS₂. *J. Phys. Chem. Lett.* **2016**, *7*, 5242-5246.

(31)   Chowdhury, R. K.; Nandy, S.; Bhattacharya, S.; Karmakar, M.; Bhaktha, S. N. B.; Datta, P. K.; Taraphder, A.; Ray, S. K. Ultrafast Time-Resolved Investigations of Excitons and Biexcitons at Room Temperature in Layered WS₂. *2D Mater.* **2018**, *6*, 15011.

(32)   Kumar, N.; He, J.; He, D.; Wang, Y.; Zhao, H. Charge Carrier Dynamics in Bulk MoS₂ Crystal Studied by Transient Absorption Microscopy. *J. Appl. Phys.* **2013**, *113*, 133702.

(33)   Wang, L.; Wang, Z.; Wang, H.-Y.; Grinblat, G.; Huang, Y.-L.; Wang, D.; Ye, X.-H.; Li, X.-B.; Bao, Q.; Wee, A.-S.; Maier, S. A.; Chen, Q.-D.; Zhong, M.-L.; Qiu, C.-W.; Sun, H.-B. Slow Cooling and Efficient Extraction of C-Exciton Hot Carriers in MoS₂ Monolayer. *Nat. Commun.* **2017**, *8*, 13906.

(34)   Li, Y.; Shi, J.; Chen, H.; Mi, Y.; Du, W.; Sui, X.; Jiang, C.; Liu, W.; Xu, H.; Liu, X. Slow Cooling of High-Energy C Excitons Is Limited by Intervalley-Transfer in Monolayer MoS₂. *Laser Photon. Rev.* **2019**, *13*, 1800270.

(35)   Goswami, T.; Rani, R.; Hazra, K. S.; Ghosh, H. N. Ultrafast Carrier Dynamics of the Exciton and Trion in MoS₂ Monolayers Followed by Dissociation Dynamics in Au@MoS₂ 2D Heterointerfaces. *J. Phys. Chem. Lett.* **2019**, *10*, 3057-3063.

(36)   Berkdemir, A.; Gutiérrez, H. R.; Botello-Méndez, A. R.; Perea-López, N.; Elías, A. L.; Chia, C.-I.; Wang, B.; Crespi, V. H.; López-Urías, F.; Charlier, J.-C.; Terrones, H.;

Terrones, M. Identification of Individual and Few Layers of WS$_2$ Using Raman Spectroscopy. *Sci. Rep.* **2013**, *3*, 1755.

(37)   Wang, F.; Kinloch, I. A.; Wolverson, D.; Tenne, R.; Zak, A.; O'Connell, E.; Bangert, U.; Young, R. J. Strain-Induced Phonon Shifts in Tungsten Disulfide Nanoplatelets and Nanotubes. *2D Mater.* **2016**, *4*, 15007.

(38)   Cheng, Y.; Peng, J.; Xu, B.; Yang, H.; Luo, Z.; Xu, H.; Cai, Z.; Weng, J. Passive Q-Switching of a Diode-Pumped Pr:LiYF$_4$ Visible Laser Using WS$_2$ as Saturable Absorber. *IEEE Photonics J.* **2016**, *8*, 1-6.

(39)   Li, D.-H.; Zheng, H.; Wang, Z.-Y.; Zhang, R.-J.; Zhang, H.; Zheng, Y.-X.; Wang, S.-Y.; Zhang, D. W.; Chen, L.-Y. Dielectric Functions and Critical Points of Crystalline WS$_2$ Ultrathin Films with Tunable Thickness. *Phys. Chem. Chem. Phys.* **2017**, *19*, 12022-12031.

(40)   Hu, S.; Wang, X.; Meng, L.; Yan, X. Controlled Synthesis and Mechanism of Large-Area WS$_2$ Flakes by Low-Pressure Chemical Vapor Deposition. *J. Mater. Sci.* **2017**, *52*, 7215-7223.

(41)   Adilbekova, B.; Lin, Y.; Yengel, E.; Faber, H.; Harrison, G.; Firdaus, Y.; El-Labban, A.; Anjum, D. H.; Tung, V.; Anthopoulos, T. D. Liquid Phase Exfoliation of MoS$_2$ and WS$_2$ in Aqueous Ammonia and Their Application in Highly Efficient Organic Solar Cells. *J. Mater. Chem. C* **2020**, *8*, 5259-5264.

(42)   Rout, C. S.; Joshi, P. D.; Kashid, R. V; Joag, D. S.; More, M. A.; Simbeck, A. J.; Washington, M.; Nayak, S. K.; Late, D. J. Superior Field Emission Properties of Layered WS$_2$-RGO Nanocomposites. *Sci. Rep.* **2013**, *3*, 3282.

(43)   Chen, D.; Ji, G.; Ding, B.; Ma, Y.; Qu, B.; Chen, W.; Lee, J. Y. In Situ Nitrogenated Graphene–Few-Layer WS$_2$ Composites for Fast and Reversible Li$^+$ Storage. *Nanoscale* **2013**, *5*, 7890-7896.

(44)   Vega-Mayoral, V.; Vella, D.; Borzda, T.; Prijatelj, M.; Tempra, I.; Pogna, E. A. A.; Dal Conte, S.; Topolovsek, P.; Vujicic, N.; Cerullo, G.; Mihailovic, D.; Gadermaier, C. Exciton and Charge Carrier Dynamics in Few-Layer WS$_2$. *Nanoscale* **2016**, *8*, 5428-5434.

(45)   Zeng, H.; Liu, G.-B.; Dai, J.; Yan, Y.; Zhu, B.; He, R.; Xie, L.; Xu, S.; Chen, X.; Yao,

W.; Cui, X. Optical Signature of Symmetry Variations and Spin-Valley Coupling in Atomically Thin Tungsten Dichalcogenides. *Sci. Rep.* **2013**, *3*, 1608.

(46)   Zhao, W.; Ribeiro, R. M.; Toh, M.; Carvalho, A.; Kloc, C.; Castro Neto, A. H.; Eda, G. Origin of Indirect Optical Transitions in Few-Layer MoS_2, WS_2, and WSe_2. *Nano Lett.* **2013**, *13*, 5627-5634.

(47)   Ramasubramaniam, A. Large Excitonic Effects in Monolayers of Molybdenum and Tungsten Dichalcogenides. *Phys. Rev. B* **2012**, *86*, 115409.

(48)   Klots, A. R.; Newaz, A. K. M.; Wang, B.; Prasai, D.; Krzyzanowska, H.; Lin, J.; Caudel, D.; Ghimire, N. J.; Yan, J.; Ivanov, B. L.; Velizhanin, K. A.; Burger, A.; Mandrus, D. G.; Tolk, N. H.; Pantelides, S. T.; Bolotin, K. I. Probing Excitonic States in Suspended Two-Dimensional Semiconductors by Photocurrent Spectroscopy. *Sci. Rep.* **2014**, *4*, 6608.

(49)   Aleithan, S. H.; Livshits, M. Y.; Khadka, S.; Rack, J. J.; Kordesch, M. E.; Stinaff, E. Broadband Femtosecond Transient Absorption Spectroscopy for a CVD MoS_2 Monolayer. *Phys. Rev. B* **2016**, *94*, 35445.

(50)   Cha, S.; Sung, J. H.; Sim, S.; Park, J.; Heo, H.; Jo, M.-H.; Choi, H. 1s-Intraexcitonic Dynamics in Monolayer MoS_2 Probed by Ultrafast Mid-Infrared Spectroscopy. *Nat. Commun.* **2016**, *7*, 10768.

(51)   Pogna, E. A. A.; Marsili, M.; De Fazio, D.; Dal Conte, S.; Manzoni, C.; Sangalli, D.; Yoon, D.; Lombardo, A.; Ferrari, A. C.; Marini, A.; Cerullo, G.; Prezzi, D. Photo-Induced Bandgap Renormalization Governs the Ultrafast Response of Single-Layer MoS_2. *ACS Nano* **2016**, *10*, 1182-1188.

(52)   Shi, H.; Yan, R.; Bertolazzi, S.; Brivio, J.; Gao, B.; Kis, A.; Jena, D.; Xing, H. G.; Huang, L. Exciton Dynamics in Suspended Monolayer and Few-Layer MoS_2 2D Crystals. *ACS Nano* **2013**, *7*, 1072-1080.

(53)   Sie, E. J.; Steinhoff, A.; Gies, C.; Lui, C. H.; Ma, Q.; Rösner, M.; Schönhoff, G.; Jahnke, F.; Wehling, T. O.; Lee, Y.-H.; Kong, J.; Jarillo-Herrero, P.; Gedik, N. Observation of Exciton Redshift–Blueshift Crossover in Monolayer WS_2. *Nano Lett.* **2017**, *17*, 4210-4216.

(54)   Stanton, C. J.; Bailey, D. W. Rate Equations for the Study of Femtosecond Intervalley

Scattering in Compound Semiconductors. *Phys. Rev. B* **1992**, *45*, 8369-8377.

Chapter 5

Temperature dependent charge carrier dynamics in thin Cu₂MoS₄ nanoflakes
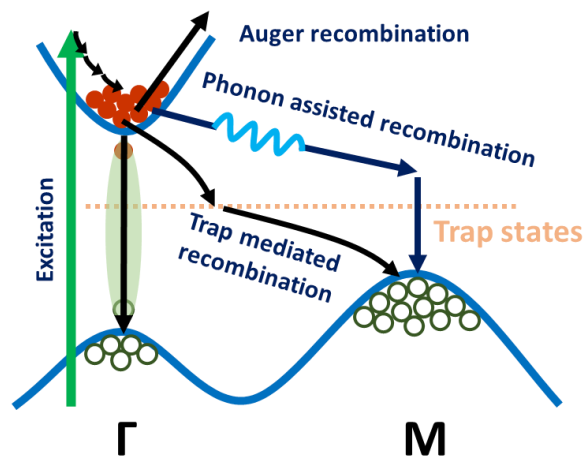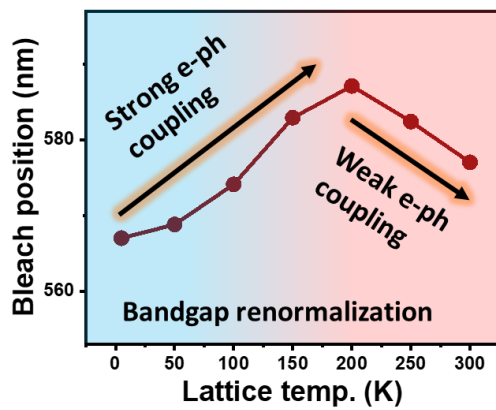
5.1. Introduction

In recent times, the research on two-dimensional transition metal chalcogenides (2D TMCs) have been established as one of the hottest research topics in the field of nanoscience and nanotechnology, owing to many exotic physical, chemical, and optoelectronic properties, such as, strong light-matter interaction, tunable crystal structure and band structures, suitable birefringence value for nonlinear optoelectronics, high carrier mobility, high surface to volume ratio in ultrathin sheet like morphology, large photo-responsivity etc[1,2,3,4,5,6,7]. These layered chalcogenide systems have already proven their candidature in many advanced photovoltaic and photocatalytic applications like, photodetectors, solar cells, energy storage and conversion, spintronics, lasers, catalysis, valleytronics and nonlinear optical devices.[8,9,10,11,12,13,2] The journey of these material started with binary systems like MoS_2, WS_2, $MoSe_2$, WSe_2 etc.[14,15,16], which are extensively investigated over the years. Though these binary systems are blessed with several advantages[14,17], they possess few shortcomings as well which are concerning for an optical device fabrication. Like, it is very difficult to maintain appropriate band alignment and restrict charge carrier recombination simultaneously in a single binary TMC[18]. Also, it is not easy to tune the band gap of most of the binary TMCs[19] These drawbacks can be easily lifted if we introduce another element in the binary system. Henceforth, the 2D materials field is gradually moving on towards ternary systems which offer many new optical and electronic properties. The ternary transition metal chalcogenides (TTMCs) family blooming day by day with materials like, Ta_2NiS_5, Ta_2NiSe_5, $CuFeS_2$, $ZnIn_2S_4$ and $Mo_{(1-x)}W_xS_2$ etc.[20,21,12,22] Contrary to the binary systems, ternary compounds possess a new degree of freedom with the addition of third element. In TMCs, the orbitals of transition metals mainly contribute in the formation of conduction and valence bands[23]. So, the band structure of TTMCs can be tuned by varying the elemental composition, which boost their optoelectronic performance. Song and Yang observed the band gap increment with the higher order of Cu deficiency in $CuInS_2$ system. $CuInS_2$/ZnS heterosystem with Cu/In = ¼ ratio was found the best LED material with luminous efficiency of 63.4 lm/W at a forward current of 20 mA among all compositions[24]. Also, the presence of third element helps in slowing down the electron-hole recombination process[18], which makes them better photocatalyst than binary TMCs. Li et. al., investigated that $Zn_{1-x}Cd_xS$ solid solutions with x=0.5 shows highest H_2 evolution rate of 7.42 mmolh^{-1}g^{-1} among all solid solution with different Zn/Cd molar ratios. The photocatalytic activity of $Zn_{0.5}Cd_{0.5}S$ was found to be 24 and 54 times higher than pristine CdS and ZnS samples and even much greater than Pt loaded CdS[25]. Along with those advantages, some TTMCs possess

no phase separation, good stability and low mixing free energy[19]. Among different TTMCs, AB_2X_4 (where A and B = transition metals, X = S, Se, and Te) family exhibits some unique properties. Like, this class of compounds possesses tetragonal crystal structure which is different from the conventional 2D materials with hexagonal lattice structure. Also, their structural diversity, tunable band gap, smaller charge diffusion length and kinetic stability[2,25,26] make them ideal for optoelectronics applications, as well as in the photocatalytic applications. Cu_2MoS_4 (CMS) is one such a promising layered material, which is part of a comparatively new family of TTMC, Cu_2MX_4 (M= Mo, W and X= S, Se)[27]. It possesses an indirect band gap and exhibits diverse electronic band structure and phonon dispersion[28]. This family of materials usually have two different types of allotropes with space groups of I42m (I-phase) and P42m (P-phase)[27]. Atomically, the single layer of CMS is encompassed by two closed square lattice of transition metal atoms (Cu and Mo), which are tetrahedrally coordinated with the S atoms, forming the square shaped layer of Cu and Mo atoms sandwiched between the layers of S atom[26]. Owing the visible region band gap, CMS has already shown its capability to harvest the solar energy as a visible light driven photocatalyst.[26,29,30,31] Liang and Guo synthesized Cu_2MoS_4 by the robust hydrothermal method at different reaction temperatures and reported their photocatalytic activity for the first time.[32] Along with photocatalysis, CMS is potent to unleash breakthrough in many other photovoltaic, or biological applications[33,34]. In order to achieve superior efficiency in those applications, it is very important to understand the inner photophysics of the material. Appropriate understanding of the excited state charge carrier dynamics would be utmost necessary for pursuing these materials in light related applications. But for CMS like materials, it was never been explored properly. We found very few reports of optical absorption and photoluminescence (PL) spectra of CMS in the literature[30,27,35]. Recently, Qin et. al investigated the electron-phonon (e-ph) interaction in CMS nanoflakes with the help of Raman spectroscopy and observed up to the fourth order of LO phonons under the above band gap photoexcitation. This indicates the presence of strong e-ph coupling due to the domination of Frohlich interactions between localized longitudinal optical (LO) phonons and respective charge carriers[28]. The energy exchange between carriers and quasi particles as well as other photophysical processes is usually observed to be ultrafast to fast time scale in the range of picosecond (ps) or sub-ps time scales. The femtosecond pump-probe spectroscopy is a well-equipped spectroscopic tool to monitor the excited states charge carriers dynamics of the photoexcited materials[36,37]. To the best of our knowledge, the charge carrier dynamics in

the CMS type TTMCs is never reported in the literature. Our first spectroscopic investigation will boost the candidature of 2D TTMC based advanced optoelectronic and photonics devices. In this work, we have synthesized a ternary chalcogenide material CMS using simple hydrothermal technique. Steady state Raman analysis confirmed the existence of strong e-ph coupling in the system. This material absorbs a broad region of the visible light, having maximum peak at around 576 nm. The PL spectrum of the material is comprised of two features, band gap emission and trap state mediated emission. Using TA spectroscopy, we explored all the possible excitonic features emerging in this material following absorption of visible light photons. Fluence dependent measurements revealed the influence of auger phenomenon in the kinetics of excitonic features in this material at high charge carrier density. With the lowering of external temperature, the band gap of the material was found to be enhanced with accelerated the exciton dynamics, owing to strong e-ph coupling at lower temperatures. The excited state charge carrier dynamics of CMS was found to be extremely influenced by the e-ph interactions in the material, which is temperature dependent.

5.2. Synthesis and experimental techniques

5.2.1. Synthesis of Cu₂O

The primary precursor for the synthesis of CMS is Cu_2O. We prepared Cu_2O previously reported method with slight modification at room temperature. PVP (3.333 g) was dispersed in 100 mL distilled water followed by continuous stirring. Then, $CuCl_2$ (1.12 mmole) was added to the above solution followed by continuous stirring to form a homogeneous and clear solution. Afterward, 10 ml of 2M aqueous solution of NaOH was added drop by drop followed by continuous stirring. After that, 10 ml of 0.6 M aqueous solution of ascorbic acid were prepared and added dropwise followed by stirring for 1h. Immediately, a turbid yellow liquid is formed. The obtained product was collected by centrifugation followed by subsequently washing with a 1:1 ratio of ethanol and water. The precipitate was kept in a vacuum for dried at 60°C for 6h.

5.2.2. Synthesis of Cu₂MoS₄

Further, for the synthesis of CMS, 30 mg of sodium molybdate was dissolved in ethylene glycol with ultrasonic treatment for 5 min. Then, 60 mg of TAA was added to the homogeneous solution followed by continuous ultrasonic treatment. After that, 20 mg of the prepared Cu_2O yellow powder was dispersed in the above suspension, followed by ultrasonic treatment for 5

min. The colour of the liquid changed from yellow to greenish-brown. The well-mixed solution was kept for ultrasonic treatment for another 5 min. Then, the obtained suspension was transferred to a 50 mL Teflon-lined autoclave and maintained at 200 °C for 24h. The product was collected by centrifugation at 8000 rpm for 10 min followed by washing with deionized water four times and then with distilled ethanol three times. Finally, the obtained product was kept under vacuum for drying at 60 °C for 6 h.

5.3. Results and discussion

5.3.1. Characterisation and steady state optical measurements

Two-dimensional CMS nanoflakes were prepared using simple hydrothermal synthetic route. hThe morphology of the as prepared CMS was investigated using transmission electron microscopy (TEM) and high-resolution TEM (HRTEM) images at different magnifications (**Figure 5.1a-c**).
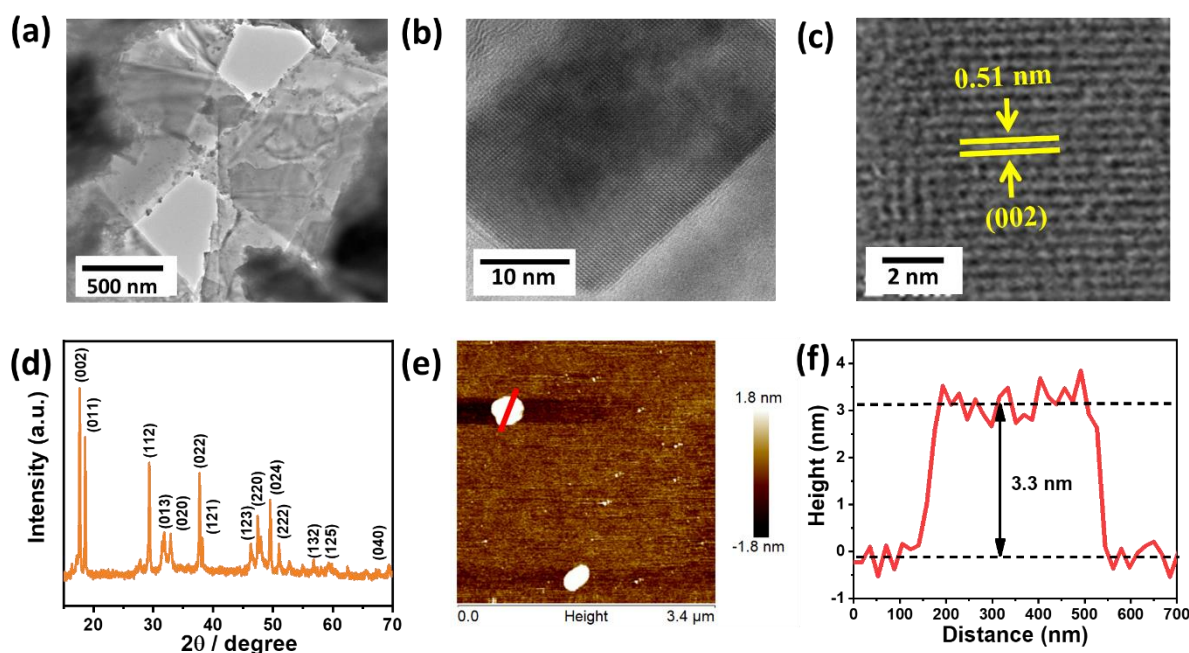
Figure 5.1: (**a, b**) TEM micrographs of CMS system presenting random flake morphology. (**c**) HRTEM image of a CMS flake showing characteristic d-spacing of the material. (**d**) PXRD patterns CMS nanoflakes. (**e**) AFM topographic image of CMS flakes. (**f**) AFM height profile of a nanoflake with thickness of 3.3 nm.

Figure 5.1a confirms the 'sheet' morphology of the material. **Figure 5.1b** and **c** displays the HRTEM image of these nanosheets. Further, **figure 5.1c** reveals the well-resolved lattice

spacing 0.51 nm which corresponds to (002) plane of CMS[31]. Moving on, powder X-ray diffraction (XRD) technique was implied to analyse the phase and structure of material (**Figure 5.1d**). The XRD pattern of CMS is having diffraction peaks at 17.6, 18.5, 29.3, 31.8, 32.9, 37.8, 46.4, 47.6, 49.5, 51.1, 52.7, 55, 56.7, 58.1, 59.1, 59.7, 62.6, 65.5 and 69.2, corresponding to (002), (011), (112), (013), (020), (022), (121), (123), (220), (024), (222), (221), (006), (132), (003), (125), (116), (231), (026) and (040) lattice planes of CMS, respectively[27]. The XRD pattern confirmed the formation of the body-centred tetragonal phase of Cu_2MoS_4 (space group: I-42m). In **figure 5.1e**, the AFM topographical image of CMS is presented. From the height profile, the thickness of these nanosheets were acquired to be ~ 3.5 nm, which would correspond to 2-3 layers (**Figure 5.1f**)[26]. Now, we will explore these atomically thin CMS nanoflakes with the help of different steady state and time-resolved spectroscopic techniques.

Figure 5.2a represents the room temperature Raman spectra of CMS nanosheets on application of 514 nm laser. This spectrum is comprised with bunch of intense peaks around 400 nm, with most intense one at 433 cm^{-1}. This peak could be assigned to the longitudinal optical (LO) phonon modes in this system[28]. This LO mode was also accompanied by its second, third and fourth order harmonics at 866, 1299 and 1732 cm^{-1}. Amongst these three, second order peak signature is very strong, but third and fourth order is almost indistinguishable.
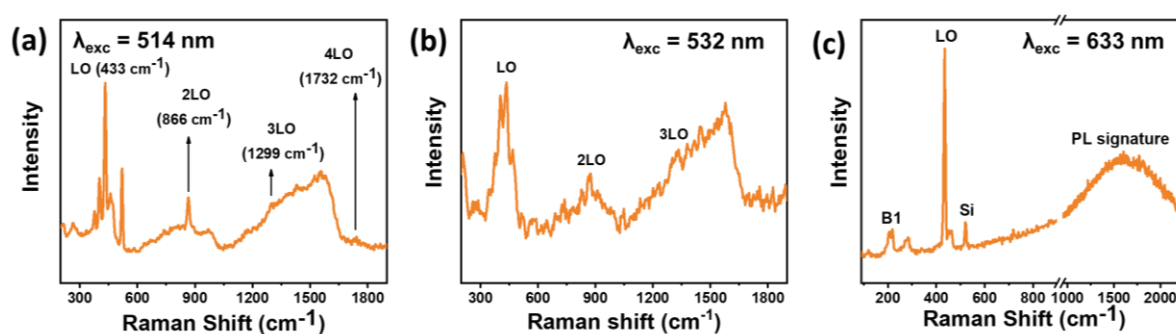
Figure 5.2: Unpolarized Raman spectrum of CMS following **(a)** 514, **(b)** 532, and **(c)** 633 nm laser excitations.

This spectrum is very similar to the earlier reports of CMS raman investigations[28,38]. Presence of LO overtones in the Raman spectra indicates toward strong e-ph coupling in this material. Further, we have recorded the Raman spectra with the implication of two other lesser energy excitations, 532 nm, and 633 nm. For 532 nm excitation, the spectra possess LO, 2LO and 3LO peaks at the same position as that of 514 nm (**Figure 5.2b**). However, 633 nm excitation could produce only LO signature at the same position (**Figure 5.2c**). Considering the band gap of

CMS around ~ 2.03 eV[26], 514 and 532 nm pumps are both above band gap excitations and able to produce n-LO signatures in the Raman spectrum. So, multi-phonon generation was only possible when excited with above band gap photon energy. This observation agrees with earlier reports[28,39]. In application of band edge energy or lower, the energy difference between the incident photon and the outgoing photon is very less, so the possibility of multi-phonon generation diminishes.
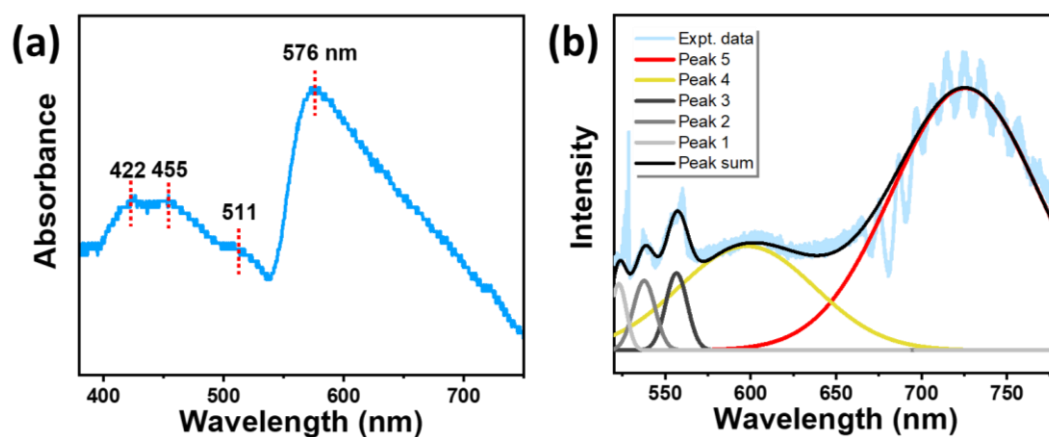
Figure 5.3: (a) Steady state absorption spectra of this system, comprising a strong peak at 576 nm and a group of few small peaks forming a hump at the higher energy region. **(b)** CMS PL spectra for 514 nm laser excitation.

The optical UV-vis spectra of CMS nanosheets are presented in **figure 5.3a**. CMS possess a wide absorption in the visible light region with absorption maxima around 576 nm. The spectrum is quite broad in nature and extended toward the NIR region. This could be the result of high density of defect induced energy states in the interband gap region of CMS. The lowest energy transition is indirect in nature in this type of material, which might as well take part in the broadening of the spectra. The peak maximum is arising with the direct transition from the valence band at Γ point to the conduction band minima (CBM) at the same point in the electronic band structure of CMS[26]. Along with this maximum peak, there are many other peak-like signatures were found in the spectrum, mainly at the higher energy region. In fact, these peaks are very close to each other and clubs into a broad hump around 420-450 nm region. So, there is a possibility of many other direct transitions in this material, which possesses much higher energy. These small peaks could be originating from these direct transitions. Existence of several peaks of similar energy indicates that there are many close by energy states in this region. The PL spectrum of this material is also very complex in nature and comprised of many peaks. **Figure 5.3b** presents PL spectrum of CMS following 514 nm laser excitation. For, better

understanding, we have fitted the spectrum with five gaussian functions, which are located at 523, 538, 556, 598 and 725 nm respectively.

These three small peaks at the high energy region cannot be attributed to PL signatures, rather they might be originating from Raman scattering induced broadening. As PL spectrum of this material was collected in a Raman spectrometer, both Raman and PL peaks would be present in the spectra. The 598 nm PL feature must be originating from the recombination of electron and hole at the direct band gap in Γ position. The most significant peak of the spectra is located at 725 nm, which could be originating from some inter band gap trap states. Till date, most of the reports regarding the optical properties of this material were confined to steady state absorption and PL spectra, which were not discussed properly. Our report aims for comprehensive optical analysis of CMS, which is never reported in the literature. Also, we could not find any time dependent studies of this material, which would be utmost beneficiary in realizing full potential of this material in optical applications. In course of that, we have employed transient absorption spectroscopy (TAS) technique, to explore time-resolved optical processes, like the relaxation and recombination of photoexcited charge carriers at very short time scale (ps or sub-ps).

5.3.2. TA measurements

Figure 5.4a represents 2D colour contour plot of CMS on application of 350 nm (3.5 eV) pump. These pump photons possess very high energy and possibly excite the charge carriers close to the continuum edge. Following that the photo-excited charge carriers would relax down to the band gap edge and eventually get recombined. The contour diagram presents most significant signal in the range of 500-600 nm, a negative and a positive signature dominates the TA spectra. This could be more clearly realized in the TA spectra plotted in **figure 5.4b**. The TA spectra are dominated by the photoinduced bleach signal and a sharp positive signal, peaking at 573 and 542 nm respectively. Along with that, many weak bleach features appeared in the TA spectra at the high energy region. These bleach features correspond to the small humps as observed in the steady state absorption spectra, which could be stemming from the state filling transitions of the high energy states.

The photoinduced bleach signal at 573 nm originates from the accumulation of charge carriers at the direct band gap edge, which give rise to the peak maximum in the steady state absorption

spectra. So, monitoring the dynamics of this feature one could explore the relaxation and recombination processes of the photoexcited charge carries in this layered material.
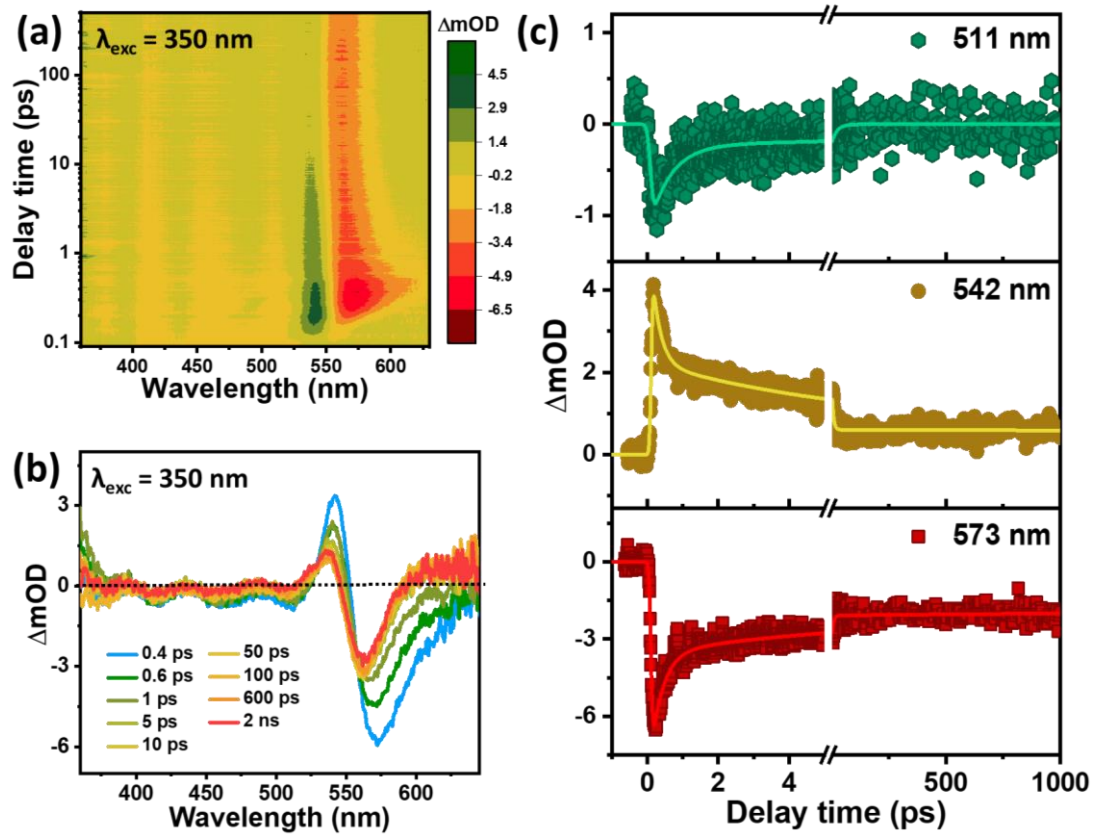
Figure 5.4: (a) 2D colour contour plot of CMS on application of 350 nm laser pulses. **(b)** TA spectra of CMS system for few pump-probe delay times. **(c)** TA dynamic profiles of the intense bleach feature at 573 nm, sharp positive signal at 542 nm and weak bleach at 511 nm.

The positive feature at 542 nm is not broad enough to be considered as the high-density defect induced positive absorption. Rather, it is a very sharp feature and must be originating from the high energy absorption from a localized state. In order to draw further conclusions, the dynamic profiles of all these features were analysed. In **figure 5.4c**, we have presented dynamics of three different transient features in three rows, weak bleach signal at 511 nm, sharp positive signal at 542 nm and band edge bleach feature at 573 nm. We have presented the kinetics of 511 nm bleach only among all other small bleach signals; just to compare these with the band edge bleach signal. We are not going discuss much about these features, as the intensity of these signals is very less to draw any conclusion. These dynamic profiles are fitted with three-exponential time scales and the fitting components were presented in **table 5.1**.

We found that the dynamical nature of 573 nm bleach and 542 nm positive signal are very similar and both the feature might be originating from the same set of energy states. As we have already discussed the origin of this bleach signal to be the state filling of band edge states, the positive one might be stemming from the transition of band edge charge carriers to the high energy states. This again substantiates the presence of many high energy states in this system, where viable optical transitions are possible. Both these features rise instantaneously, limited to instrument response function (IRF). This indicates very fast relaxation of charge carriers from the continuum edge towards the band edge. Following the emergence, these signals undergo a very fast decay, which might be indicating the presence Auger recombination[40] or exciton-exciton annihilation[41] or defect trapping[42] in this system. Also, there is a slight possibility that this positive signal could be the signature of multi-exciton generation in the system. To verify these possibilities and figure out the inherent photophysical processes involved in the relaxation and recombination of charge carriers in this material, we have varied the pump fluence in a certain range.

5.3.3. Fluence dependent TA measurements

Figure 5.5a shows pump fluence-dependent TA spectra at a particular pump-probe delay time of 0.3 ps for 350 nm pump excitation. The spectra undergo substantial change with the variation of pump fluence, both in peak intensity and broadening. The band edge bleach signal was found to be most severely affected by the variation of pump fluence. This negative feature is accompanied with significant red shift throughout the applied fluence range, which could be the resultant of the charge carrier induced stark effect, change in the exciton binding energy or band gap renormalization process[43,44]. It is possible that all three processes are simultaneously active in the high fluence range, generating this broad bleach signal. Broadened bleach signal necessarily points toward the higher distribution of charge carrier density near the band gap edge in injection of higher charge carrier population. Contrary to that, the positive signal holds nearly constant peak position in different fluence. Slight blue shift in high energy fluence case might be originating from the excessive broadening of the adjacent bleach signal. Hence, one can assume that this positive feature is not influenced by any of stark effect, band filling effect or band gap renormalization phenomena.

Figure 5.5b represents the increased peak amplitudes of the band edge bleach and the positive signal as a function of excitation density. This excitation energy dependence can be fitted with saturation absorber model[40,41],

$$\Delta T/T_0 \propto n/ (n + n_s)$$

where n and n_s signify excitation density and corresponding saturation density of the material, respectively. $\Delta T/T_0$ represents differential change in the transmission, which is inversely proportional to ΔOD in TA data.
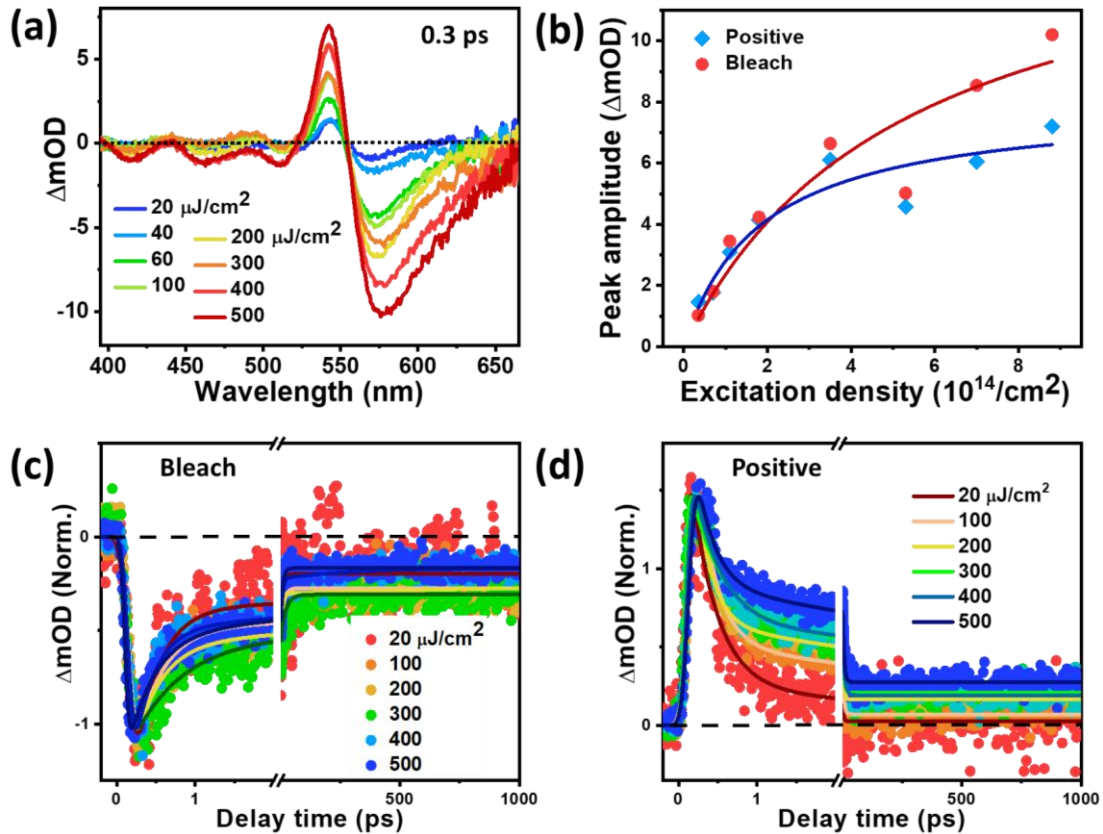
Figure 5.5: (a) TA spectra of CMS on application of different pump fluence at a particular pump-probe delay time (0.3 ps). Pump fluence was varied from 20 to 500 µJ/cm². **(b)** Peak amplitudes of the bleach and the positive signal as a function of excitation density. The data points are fitted with a saturation absorber model, discussed in the text. Normalized dynamic profiles of **(c)** the intense bleach feature and **(d)** the sharp positive signal for different pump fluence. Pump wavelength was kept 350 nm in all cases.

From the fitting of this model, the saturation density was calculated to be $5.3 \pm 0.7 \times 10^{14}$ and $1.8 \pm 0.3 \times 10^{14}$ photons/cm² for the bleach and positive signal respectively. This saturation of the transient features could be prompted by approaching Mott density of the material and one can assume that mott density of CMS would fall in the similar excitation region. It is very evident that the positive signal approaches the saturation limit much faster than the bleach one. So, the decay processes involved in these two signals must be different, so does the

recombination channels. Hence, one cannot really be sure about the involvement of same set of energy states for the generation of these two features, as we predicted earlier. As, the bleach signal directly corresponds to the exciton density or band edge charge carrier population, we can safely assume that the mott density would lie close to $5.3 \pm 0.7 \times 10^{14}$ photons/cm^2.
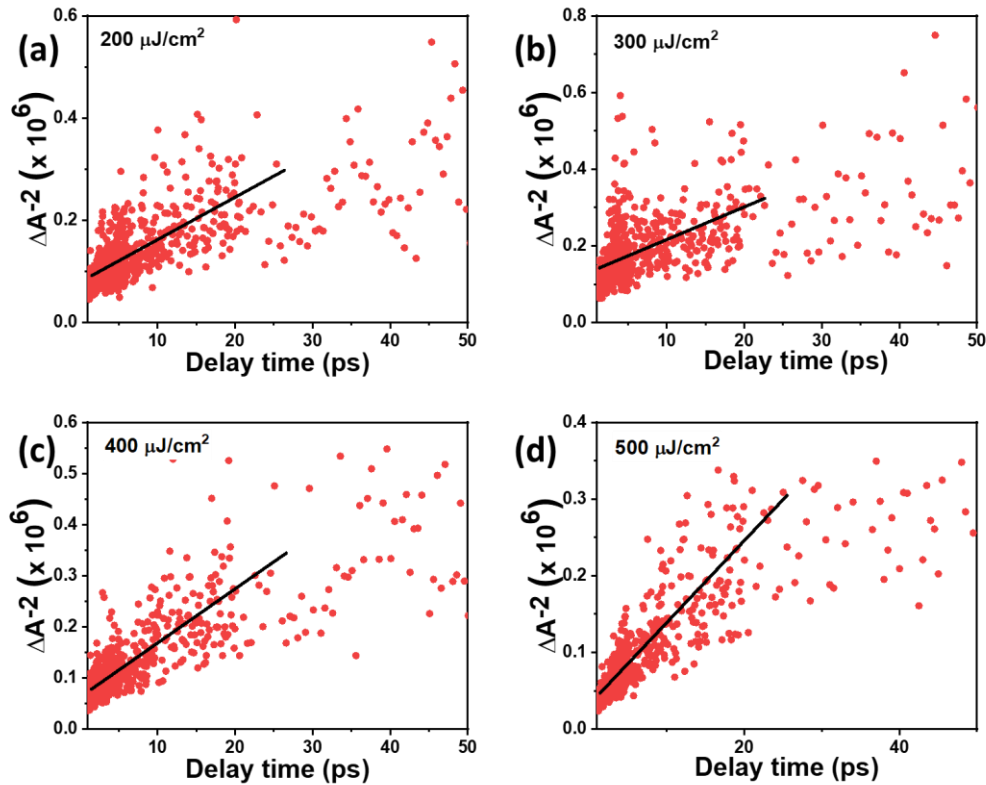
Figure 5.6: Auger fitting in case of the band edge bleach signature for **(a)** 200, **(b)** 300, **(c)** 400 and **(d)** 500 µJ/cm^2 applied pump fluence.

Similar conclusions can be drawn from the dynamical plot of these features in **figures 5.5c and d**. All the decay curves were fitted with multiexponential functions, and the fitting parameters are listed in **Table 5.1**. On increasing fluence, the bleach dynamic profiles were found to be slower up to a certain excitation density (300 µJ/cm^2 or 5.3×10^{14} photons/cm^2). Beyond that, the bleach signals show faster decay dynamics. Interestingly, these regions also fall beyond saturation limit, where many body processes like auger recombination, bi-exciton formation, two-photon absorption etc[45,46,40,47]. dominate the recovery channels of the transient features. It is possible that auger induced non-radiative decay play dominant role in the faster dynamics of the bleach feature at high fluence regime. **Figure 5.6** depicts the linear dependence of ΔA^{-2} versus delay time, confirming involvement of Auger recombination phenomenon at early (up to 25 ps) delay time scales.

Table 5.1: Transient fitting parameters of the band edge bleach signature for different pump fluences.

Pump fluence ($\mu J/cm^2$)	Excitation density ($10^{14}/cm^2$)	Probe Wavelength (nm)	Growth τ_g (ps)	Recovery τ_1 (ps)	τ_2 (ps)	τ_3 (ps)
20	0.3	570	< 0.1	0.3 (75.5 %)	15.1 (11.8 %)	> 1000 (12.7 %)
60	1.1	572.4	< 0.1	0.3 (69.5 %)	12.6 (20.3 %)	> 1000 (10.2 %)
100	1.8	571.2	< 0.1	0.3 (63.6 %)	17.3 (15.9 %)	> 1000 (20.5 %)
200	3.5	574.1	< 0.1	0.5 (57.4 %)	17.6 (21.5 %)	> 1000 (21.1 %)
300	5.3	575.3	< 0.1	0.6 (52.4 %)	23.4 (20.9 %)	> 1000 (26.7 %)
400	7.0	576.5	< 0.1	0.3 (64.6 %)	15.1 (19.6 %)	> 1000 (15.8 %)
500	8.8	579.4	< 0.1	0.3 (57.1 %)	12.4 (29.1 %)	> 1000 (13.8 %)

In case of the positive signal though, we did not find any auger induced acceleration in the decay features. Rather, the signals are getting slower on increasing pump fluence. This observation indicates toward the presence of surface trap induced decay channels in the dynamics of the positive feature[42]. As these defect states tend to get populated over increased fluence, the recombination of the photoexcited carriers get blocked owing to pauli blocking[45]. We believe that, both auger and trap mediated processes are involved in the decay of both the features. In case of bleach signal, the auger phenomenon dominates, whereas positive signal decay is only influenced by trap mediated recombinations. Henceforth, we assign the fast decay time scale to the auger recombination and defect mediated recombination for the bleach and positive signal respectively. In order to further investigate the charge carrier recombination

processes, the TA experiments were performed at different lattice temperatures, ranging from 5K to 300K.

5.3.4. Temperature dependent TA measurements

Figure 5.7a, b represents TA spectra of CMS maintaining lattice temperature at 5K and 200K. Pump wavelength and fluence were kept at 350 nm and 200 µJ/cm^2 respectively for all the temperature dependent studies. TA spectra for all other temperatures are shown in **figure 5.8**. We found the spectral shape and intensities were very different at 5K and 200K. At higher temperatures, the TA spectra were much broader as compared to that of lower temperatures, also the transient bleach is red-shifted in high temperatures. This type of shifting is very common in temperature dependent studies, as observed in many PL and TA studies earlier[48]. At high temperatures, thermal excitations reduce the charge carrier population in the bound states and defect/impurity mediated signatures dominate the spectra, resulting in a broad and dispersive signature. Whereas, at low temperature a sharp bleach feature arises owing to the optical transitions mainly from the bound states. In **figure 5.7c**, we have plotted the peak positions of the bleach and positive feature at different temperatures. Interestingly, as we increase temperature both the signals show red-shift up to 200K, and beyond that a marginal blue shift was observed. As the bleach feature predominantly corresponds to the direct band gap transitions in CMS, this shifting phenomenon could be associated with the variation of band gap with temperature. So, one can assume that the direct band gap of the material undergoes substantial downfall with increasing temperature. The band gap of a semiconducting system primarily depends on two factors, e-ph interaction, and thermal expansion effect[49,50,51]. Usually in conventional semiconductors, both these parameters possess negative value and correspondingly band gaps are found to be decreased with the increase of temperature[50,52]. But that is not always true. There are many other reports where opposite trends were observed[53,51]. In our system, two different trends are observed at separate temperature regions, which possibly indicates that both these factors influence the band gap renormalization of CMS, but with opposite signs. In CMS, the e-ph coupling strength decreases with the increment of temperature.

The Huang-Rhys factor (S, e-ph coupling strength parameter) in CMS was found to be maximum around 100K and gradually decreases with temperature[28].
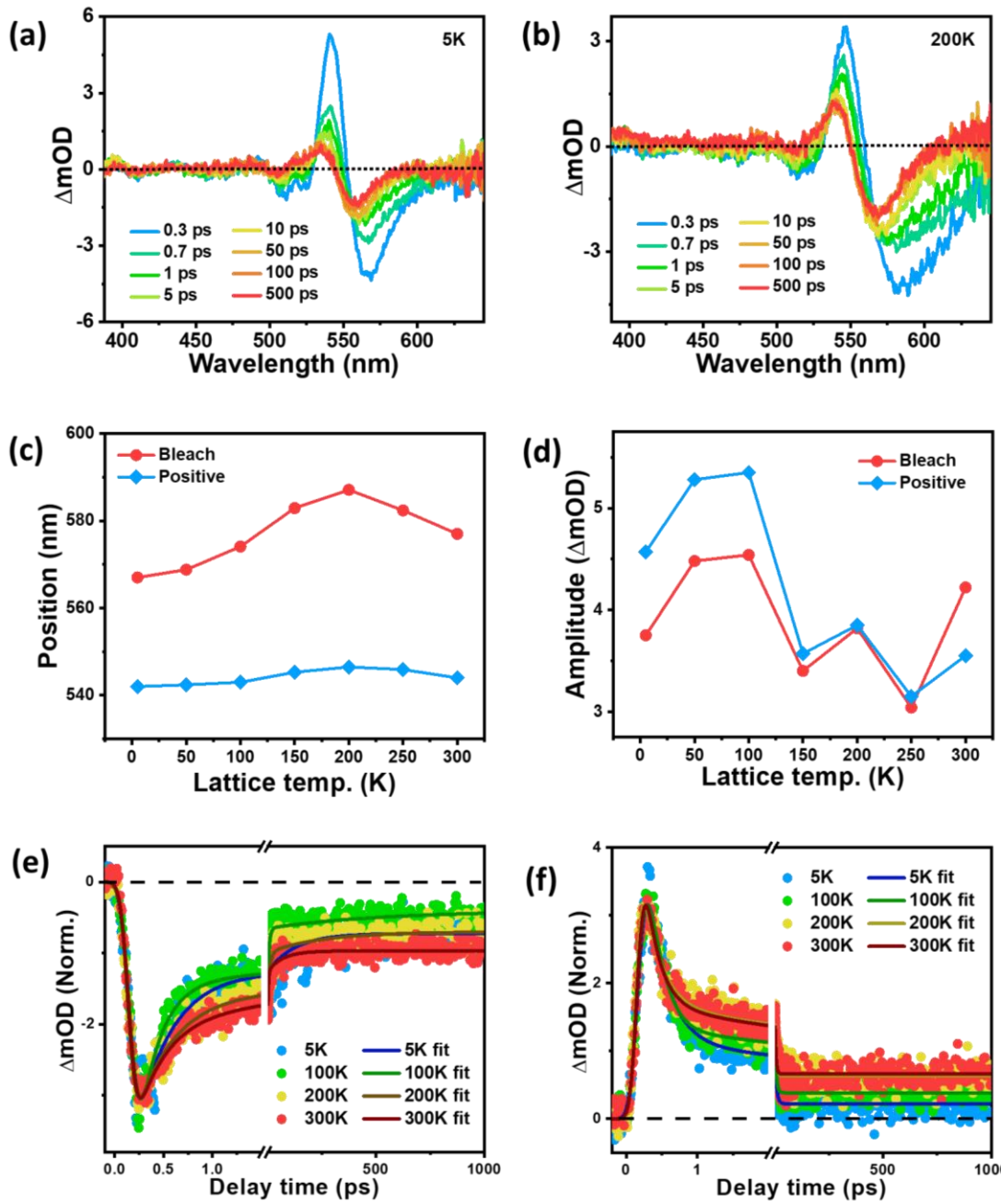
Figure 5.7: TA spectra of CMS collected at lattice temperature of **(a)** 5K and **(b)** 200K, on application of 350 nm pump with 200 µJ/cm^2 fluency. Plots of respective **(c)** peak positions and **(d)** amplitude values of the bleach and positive features for a range of lattice temperatures. The lines are only guide to the eye. Normalized dynamic profiles of **(e)** the intense bleach feature and **(f)** the sharp positive signal for different lattice temperatures, for 350 nm pump and 200 µJ/cm^2 applied fluence.

So, it is possible that, the e-ph interaction parameter is the major contributor for the renormalization of band gap at low temperatures (below 200K) and its contribution is negative for this material. At very high temp (beyond 200K), e-ph interaction becomes negligible and the thermal expansion factor decides the band gap. At this high temperature region, band gap increases with temperature; means thermal expansion parameter possess a positive value. This abnormal trend was earlier observed in many d-orbital based semiconductors like, copper halides, metal halide pervoskites, silver chalcopyrites etc.[54,52]

The signal intensities of the positive and negative features, also undergo a decreasing trend with increasing temperature (**Figure 5.7d**). This is quite possible considering higher charge carrier population in the bound states at lower temperatures, also responsible for the sharper bands discussed earlier. The interesting part is that the positive features are now having higher signal intensity than that of the bleach signals. In our previous discussion on fluence variance, we found out that the dynamics of the positive signal is predominantly dependent on the trap mediated recombination channels, then that of the bleach one. So, these signals would depend on the defect density of the system. As, lower temperature induces less no of defect mediated trap states in any material, the effect of these traps would have negligible effect on the transient signal in the lower temperature region. This is resulting in higher signal intensity of positive signals as compared to bleach features.
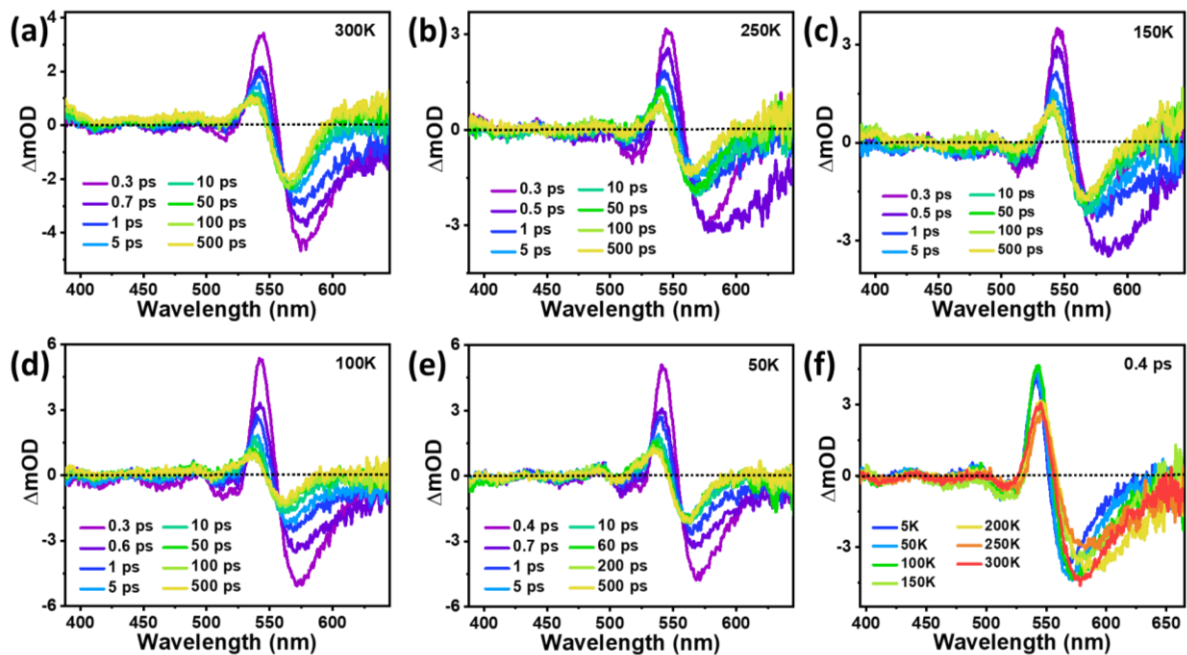
Figure 5.8: TA spectra of CMS with 350 nm and 200 µJ/cm^2 pump excitation having lattice temperature of **(a)** 300K, **(b)** 250K, **(c)** 150K, **(d)** 100K and **(e)** 50K. **(f)** Comparative TA spectra of CMS for different lattice temperature case, at a particular pump-probe delay time (0.4 ps).

Table 5.2: Transient fitting parameters of the band edge bleach signature for different lattice temperatures.

Lattice temperature (K)	Probe Wavelength (nm)	Growth τ_g (ps)	Recovery		
			τ_1 (ps)	τ_2 (ps)	τ_3 (ps)
5	567.0	< 0.1	0.4 (57.4 %)	23.2 (10.7 %)	> 1000 (31.9 %)
50	568.8	< 0.1	0.3 (51.8 %)	18.4 (16.7 %)	> 1000 (31.5 %)
100	574.1	< 0.1	0.2 (54.7 %)	9.5 (24.3 %)	> 1000 (21.0 %)
150	582.9	< 0.1	0.4 (49.8 %)	20.4 (21.4 %)	> 1000 (28.8 %)
200	587.1	< 0.1	0.4 (49.3 %)	25.2 (21.4 %)	> 1000 (29.3 %)
250	582.4	< 0.1	0.2 (53.3 %)	17.3 (20.9 %)	> 1000 (25.8 %)
300	577.0	< 0.1	0.6 (48.2 %)	18.4 (16.9 %)	> 1000 (34.9 %)

The temperature dependent decay processes of these transient features were further explored via detailed analysis of the time dependent dynamic profiles of the bleach and positive signals. **Figure 5.7e and f** represent transient kinetics of the respective bleach and positive signals. These dynamic profiles were fitted with three-exponential decay parameters as well and listed in **Table 5.2**. Both the features show almost similar trend with respect to temperature. At lower temperature the decay processes were found to be accelerated, which could be due to very strong e-ph coupling at low temperature. CMS is associated with lowering of dielectric constant in the lattice with temperature decrement, which induces stronger e-ph interaction in the

system. This leads into enhanced phonon emission and subsequent faster dissipation of phonon energy to the surroundings[55]. These phenomena would result in faster dynamics and that is what observed in our low temperature TA experiments. So, our study substantiates the existence of stronger e-ph coupling in low temperature for CMS. Also, CMS possess an indirect band gap and the direct band gap charge carriers would recombine via indirect band that involves e-ph interaction. So, e-ph interaction must be the most influencing factor in the recombination of photoexcited charge carriers in CMS. In **figure 5.9**, we have shown all the possible relaxation and recombination processes in CMS with the help of an electronic energy band diagram of CMS.
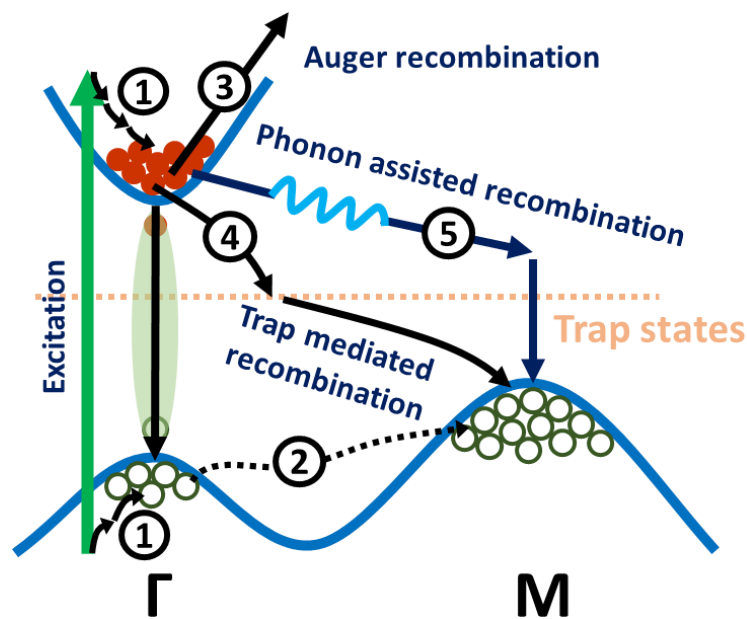
Figure 5.9: Probable decay channels for the recombination CMS direct band gap exciton emerged at the Γ space of electronic band structure. Five different relaxation and recombination channels dictate the decay of charge carrier recombination in CMS, 1) Hot carrier relaxation, 2) Inter-hill hole cooling, 3) auger process 4) inter band gap trap state mediated recombination, and 5) phonon mediated indirect recombination.

Following the high energy photoexcitation (350 nm, 3.5 eV), the charge carriers are placed at higher energy levels as compared to the direct band gap excitation (close to 573 nm, 2.16 eV). These charge carriers relax to the direct band edge within ultrafast time scale (< 0.1 ps). Following that, these holes are further cooled the valence band maxima at 'M' space, as this valley possess lowest energy. At this situation, there are three possibilities for the recombination of those electron and holes; auger recombination, inter-band gap trap state mediated recombination and normal photon mediated indirect recombination. Both the auger

and trap mediated channels could also be influenced by phonons, as this material showed strong e-ph coupling even at room temperature. From the transient measurement as well, we found the effect of strong e-ph coupling in the temperature dependent charge carrier dynamics. Also, the bleach dynamics is predominantly affected by auger recombination. So, we can postulate that, the main recombination channel in this system would be phonon mediated auger process, as observed earlier in indirect band gap semiconductors[56]. This kind of experimental validation regarding the existence of e-ph coupling in a material like CMS is rare in the literature. The knowledge of the temperature dependence of the e-ph interaction in CMS and subsequent variation of charge carrier dynamics would be beneficiary in CMS based optical device fabrication.

5.4. Conclusions

In summary, we have successfully synthesized an exquisite ternary chalcogenide Cu_2MoS_4, which is confined in only one direction (2D material). CMS flakes were found to be assembled from the van der Waal stacking of 2-3 monolayers. These atomically thin 2D systems were investigated in steady state Raman spectroscopy, revealing the presence of very strong e-ph coupling. CMS was also found to absorb a broad region of the electromagnetic radiation. The absorption maximum was located at 576 nm, corresponding to the direct transition at the Γ space of the electronic band structure. The PL spectra is comprised of two broad peaks, corresponding to direct band gap emission and inter-band gap trap state mediated radiative recombinations. Steady state optical studies confirmed the huge effect of intrinsic defect states in the properties of these materials. Transient study further explored the excited state charge carrier dynamics of CMS. The TA spectra primarily composed of a strong bleach signal and a sharp PIA signature, corresponding to the state filling of the conduction band edge and excited state absorption into the higher energy states. The spectra also feature many weak bleach signatures at the high energy end, indicating the possibility of several closely spaced high energy transitions in the CMS band structure. Pump fluence dependent measurements disclose the saturation density of the material lies in the range of $5.3 \pm 0.7 \times 10^{14}$ photons/cm^2, beyond this limit auger recombination predominates. We found Auger recombination to be an integral part of the photophysical processes involved in the decay of photoexcited charge carriers. Whereas trap mediated recombinations play more dominant role in the decay dynamics of the positive signal. These dynamical features are very much dependent on the lattice temperature. At lower temperature e-ph coupling strength peaks, accelerating the decay of the TA signals.

Stronger e-ph interaction at the at low temperature range might as well responsible for the increment the optical band gap of the material. e-ph interaction was found to be most important factor for the recombination of CMS excitons. Our measurements indicate toward the phonon assisted auger recombination as the most feasible recombination channel in CMS. Overall, this study aims to gain an exclusive insight of the optical properties of CMS, which was never been reported in literature to the best of our knowledge. This detailed spectroscopic investigation would draw more attention toward the unexplored optical properties of ternary 2D chalcogenides and help in the construction of state-of-the-art optoelectronic devices.

5.5. References

(1)   Zeng, H.; Liu, G.-B.; Dai, J.; Yan, Y.; Zhu, B.; He, R.; Xie, L.; Xu, S.; Chen, X.; Yao, W.; Cui, X. Optical Signature of Symmetry Variations and Spin-Valley Coupling in Atomically Thin Tungsten Dichalcogenides. *Sci. Rep.* **2013**, *3*, 1608.

(2)   Chen, H.; Wei, W.-B.; Lin, H.; Wu, X.-T. Transition-Metal-Based Chalcogenides: A Rich Source of Infrared Nonlinear Optical Materials. *Coord. Chem. Rev.* **2021**, *448*, 214154.

(3)   Liu, B.; Ma, Y.; Zhang, A.; Chen, L.; Abbas, A. N.; Liu, Y.; Shen, C.; Wan, H.; Zhou, C. High-Performance WSe$_2$ Field-Effect Transistors via Controlled Formation of In-Plane Heterojunctions. *ACS Nano* **2016**, *10*, 5153-5160.

(4)   Goswami, T.; Bhatt, H.; Babu, K. J.; Kaur, G.; Ghorai, N.; Ghosh, H. N. Ultrafast Insights into High Energy (C and D) Excitons in Few Layer WS$_2$. *J. Phys. Chem. Lett.* **2021**, *12*, 6526-6534.

(5)   Jacobs-Gedrim, R. B.; Shanmugam, M.; Jain, N.; Durcan, C. A.; Murphy, M. T.; Murray, T. M.; Matyi, R. J.; Moore, R. L.; Yu, B. Extraordinary Photoresponse in Two-Dimensional In2Se3 Nanosheets. *ACS Nano* **2014**, *8*, 514-521.

(6)   Zhuang, G.; Yan, J.; Wen, Y.; Zhuang, Z.; Yu, Y. Two-Dimensional Transition Metal Oxides and Chalcogenides for Advanced Photocatalysis: Progress, Challenges, and Opportunities. *Sol. RRL* **2021**, *5*, 2000403.

(7)   Huang, Y. H.; Chen, R. S.; Zhang, J. R.; Huang, Y. S. Electronic Transport in NbSe$_2$ Two-Dimensional Nanostructures: Semiconducting Characteristics and Photoconductivity. *Nanoscale* **2015**, *7*, 18964-18970.

(8)   Lopez-Sanchez, O.; Lembke, D.; Kayci, M.; Radenovic, A.; Kis, A. Ultrasensitive Photodetectors Based on Monolayer MoS$_2$. *Nat. Nanotechnol.* **2013**, *8*, 497-501.

(9)   Tsai, M.-L.; Su, S.-H.; Chang, J.-K.; Tsai, D.-S.; Chen, C.-H.; Wu, C.-I.; Li, L.-J.; Chen, L.-J.; He, J.-H. Monolayer MoS$_2$ Heterojunction Solar Cells. *ACS Nano* **2014**, *8*, 8317-8322.

(10)   Goswami, T.; Yadav, D. K.; Bhatt, H.; Kaur, G.; Shukla, A.; Babu, K. J.; Ghosh, H. N. Defect-Mediated Slow Carrier Recombination and Broad Photoluminescence in Non-Metal-Doped ZnIn$_2$S$_4$ Nanosheets for Enhanced Photocatalytic Activity. *J. Phys. Chem. Lett.* **2021**, *12*, 5000-5008.

(11)   Mak, K. F.; Shan, J. Photonics and Optoelectronics of 2D Semiconductor Transition Metal Dichalcogenides. *Nat. Photonics* **2016**, *10*, 216-226.

(12)   Li, Y.; Wang, Y.; Pattengale, B.; Yin, J.; An, L.; Cheng, F.; Li, Y.; Huang, J.; Xi, P. High-Index Faceted CuFeS$_2$ Nanosheets with Enhanced Behaviour for Boosting Hydrogen Evolution Reaction. *Nanoscale* **2017**, *9*, 9230-9237.

(13)   Francis, B. M.; Ponraj, J. S.; Dhanabalan, B.; Manavalan, R. K.; Veluswamy, P.; Yin, P.; Al-Hartomy, O. A.; Al-Ghamdi, A.; Wageh, S.; Zhang, H.; Dhanabalan, S. C. Two-Dimensional Material-Based Printed Photonics: A Review. *2D Mater.* **2022**, *9*, 42003.

(14)   Zhang, X.; Lai, Z.; Ma, Q.; Zhang, H. Novel Structured Transition Metal Dichalcogenide Nanosheets. *Chem. Soc. Rev.* **2018**, *47*, 3301-3338.

(15)   Goswami, T.; Rani, R.; Hazra, K. S.; Ghosh, H. N. Ultrafast Carrier Dynamics of the Exciton and Trion in MoS$_2$ Monolayers Followed by Dissociation Dynamics in Au@MoS$_2$ 2D Heterointerfaces. *J. Phys. Chem. Lett.* **2019**, *10*, 3057-3063.

(16)   Pradhan, N. R.; Garcia, C.; Holleman, J.; Rhodes, D.; Parker, C.; Talapatra, S.; Terrones, M.; Balicas, L.; McGill, S. A. Photoconductivity of Few-Layered *p*-WSe$_2$ Phototransistors via Multi-Terminal Measurements. *2D Mater.* **2016**, *3*, 41004.

(17)   Goswami, T.; Bhatt, H.; Yadav, D. K.; Saha, R.; Babu, K. J.; Ghosh, H. N. Probing Ultrafast Hot Charge Carrier Migration in MoS$_2$ Embedded CdS Nanorods. *J. Chem. Phys.* **2021**, *156*, 34704.

(18)   Rahman, A.; Khan, M. M. Chalcogenides as Photocatalysts. *New J. Chem.* **2021**, *45*, 19622-19635.

(19)   Wang, L.; Hu, P.; Long, Y.; Liu, Z.; He, X. Recent Advances in Ternary Two-Dimensional Materials: Synthesis, Properties and Applications. *J. Mater. Chem. A* **2017**, *5*, 22855-22876.

(20)   Tan, C.; Yu, P.; Hu, Y.; Chen, J.; Huang, Y.; Cai, Y.; Luo, Z.; Li, B.; Lu, Q.; Wang, L.; Liu, Z.; Zhang, H. High-Yield Exfoliation of Ultrathin Two-Dimensional Ternary

Chalcogenide Nanosheets for Highly Sensitive and Selective Fluorescence DNA Sensors. *J. Am. Chem. Soc.* **2015**, *137*, 10430-10436.

(21) Bhatt, H.; Goswami, T.; Yadav, D. K.; Ghorai, N.; Shukla, A.; Kaur, G.; Kaur, A.; Ghosh, H. N. Ultrafast Hot Electron Transfer and Trap-State Mediated Charge Carrier Separation toward Enhanced Photocatalytic Activity in g-C_3N_4/$ZnIn_2S_4$ Heterostructure. *J. Phys. Chem. Lett.* **2021**, *12*, 11865-11872.

(22) Zhang, W.; Li, X.; Jiang, T.; Song, J.; Lin, Y.; Zhu, L.; Xu, X. CVD Synthesis of $Mo_{(1−x)}W_xS_2$ and $MoS_{2(1−x)}Se_{2x}$ Alloy Monolayers Aimed at Tuning the Bandgap of Molybdenum Disulfide. *Nanoscale* **2015**, *7*, 13554-13560.

(23) Xiao, D.; Liu, G.-B.; Feng, W.; Xu, X.; Yao, W. Coupled Spin and Valley Physics in Monolayers of MoS_2 and Other Group-VI Dichalcogenides. *Phys. Rev. Lett.* **2012**, *108*, 196802.

(24) Song, W.-S.; Yang, H. Efficient White-Light-Emitting Diodes Fabricated from Highly Fluorescent Copper Indium Sulfide Core/Shell Quantum Dots. *Chem. Mater.* **2012**, *24*, 1961-1967.

(25) Li, Q.; Meng, H.; Zhou, P.; Zheng, Y.; Wang, J.; Yu, J.; Gong, J. $Zn_{1−x}Cd_xS$ Solid Solutions with Controlled Bandgap and Enhanced Visible-Light Photocatalytic H_2-Production Activity. *ACS Catal.* **2013**, *3*, 882-889.

(26) Gan, L.-Y.; Schwingenschlögl, U. Two-Dimensional Square Ternary Cu_2MX_4 (M = Mo, W; X = S, Se) Monolayers and Nanoribbons Predicted from Density Functional Theory. *Phys. Rev. B* **2014**, *89*, 125423.

(27) Chen, W.; Chen, H.; Zhu, H.; Gao, Q.; Luo, J.; Wang, Y.; Zhang, S.; Zhang, K.; Wang, C.; Xiong, Y.; Wu, Y.; Zheng, X.; Chu, W.; Song, L.; Wu, Z. Solvothermal Synthesis of Ternary Cu_2MoS_4 Nanosheets: Structural Characterization at the Atomic Level. *Small* **2014**, *10*, 4637-4644.

(28) Qin, L.; Wen, Z.; Zhang, X.; Zhang, K.; Lin, Y.; Song, L.; Wu, X.; Qiu, X. Multiphonon Raman Scattering and Strong Electron–Phonon Coupling in 2D Ternary Cu_2MoS_4 Nanoflakes. *J. Phys. Chem. Lett.* **2020**, *11*, 8483-8489.

(29) Zhang, K.; Lin, Y.; Wang, C.; Yang, B.; Chen, S.; Yang, S.; Xu, W.; Chen, H.; Gan, W.; Fang, Q.; Zhang, G.; Li, G.; Song, L. Facile Synthesis of Hierarchical Cu_2MoS_4 Hollow Sphere/Reduced Graphene Oxide Composites with Enhanced Photocatalytic Performance. *J. Phys. Chem. C* **2016**, *120*, 13120-13125.

(30) Zhang, K.; Chen, W.; Wang, Y.; Li, J.; Chen, H.; Gong, Z.; Chang, S.; Ye, F.; Wang,

T.; Chu, W.; Zou, C.; Song, L. Cube-like Cu₂MoS₄ Photocatalysts for Visible Light-Driven Degradation of Methyl Orange. *AIP Adv.* **2015**, *5*, 77130.

(31)   Ma, J.; Zhu, F.; Ji, P.; Zou, Q.; Wang, H.; Xu, G. Enhanced Visible-Light Photocatalytic Performance of Co/Ni Doped Cu₂MoS₄ Nanosheets for Rhodamine B and Erythromycin Degradation. *J. Alloys Compd.* **2021**, *863*, 158612.

(32)   Liang, H.; Guo, L. Synthesis, Characterization and Photocatalytic Performances of Cu₂MoS₄. *Int. J. Hydrogen Energy* **2010**, *35*, 7104-7109.

(33)   Yu, L. D.; Wen, Y. X.; Zhang, X. Y.; Li, N. B.; Luo, H. Q. Signal-off Photoelectrochemical Determination of MiRNA-21 Using Aptamer-Modified In₂O₃@Cu₂MoS₄ Nanocomposite. *Microchim. Acta* **2020**, *187*, 561.

(34)   Chang, M.; Hou, Z.; Wang, M.; Wang, M.; Dang, P.; Liu, J.; Shu, M.; Ding, B.; Al Kheraif, A. A.; Li, C.; Lin, J. Cu₂MoS₄/Au Heterostructures with Enhanced Catalase-Like Activity and Photoconversion Efficiency for Primary/Metastatic Tumors Eradication by Phototherapy-Induced Immunotherapy. *Small* **2020**, *16*, 1907146.

(35)   Rameshbabu, R.; Vinoth, R.; Navaneethan, M.; Harish, S.; Hayakawa, Y.; Neppolian, B. Visible Light Responsive Cu₂MoS₄ Nanosheets Incorporated Reduced Graphene Oxide for Efficient Degradation of Organic Pollutant. *Appl. Surf. Sci.* **2017**, *418*, 128-137.

(36)   Goswami, T.; Bhatt, H.; Yadav, D. K.; Ghosh, H. N. Interfacing g-C₃N₄ Nanosheets with CdS Nanorods for Enhanced Photocatalytic Hydrogen Evolution: An Ultrafast Investigation. *J. Phys. Chem. B* **2022**, *126*, 572-580.

(37)   Goswami, T.; Bhatt, H.; Yadav, D. K.; Ghosh, H. N. Atomically Thin 2D Photocatalysts for Boosted H₂ Production from the Perspective of Transient Absorption Spectroscopy. *Phys. Chem. Chem. Phys.* **2022**, *24*, 19121-19143.

(38)   Chen, H.; Zhang, K.; Chen, W.; Ali, I.; Wu, P.; Liu, D.; Song, L. Raman Scattering of Single Crystal Cu₂MoS₄ Nanosheet. *AIP Adv.* **2015**, *5*, 37141.

(39)   Yadav, H. K.; Katiyar, R. S.; Gupta, V. Modified Cascade Model of Resonant Raman Scattering: A Case Study of UV Raman Scattering in Zn₁₋ₓMnₓO Thin Films. *J. Raman Spectrosc.* **2011**, *42*, 2126-2131.

(40)   Cunningham, P. D.; McCreary, K. M.; Jonker, B. T. Auger Recombination in Chemical Vapor Deposition-Grown Monolayer WS₂. *J. Phys. Chem. Lett.* **2016**, *7*, 5242-5246.

(41)   Kumar, N.; Cui, Q.; Ceballos, F.; He, D.; Wang, Y.; Zhao, H. Exciton-Exciton Annihilation in MoSe₂ Monolayers. *Phys. Rev. B* **2014**, *89*, 125427.

(42)   Wang, H.; Zhang, C.; Rana, F. Ultrafast Dynamics of Defect-Assisted Electron–Hole Recombination in Monolayer MoS$_2$. *Nano Lett.* **2015**, *15*, 339-345.

(43)   Borzda, T.; Gadermaier, C.; Vujicic, N.; Topolovsek, P.; Borovsak, M.; Mertelj, T.; Viola, D.; Manzoni, C.; Pogna, E. A. A.; Brida, D.; Antognazza, M. R.; Scotognella, F.; Lanzani, G.; Cerullo, G.; Mihailovic, D. Charge Photogeneration in Few-Layer MoS$_2$. *Adv. Funct. Mater.* **2015**, *25*, 3351-3358.

(44)   Pogna, E. A. A.; Marsili, M.; De Fazio, D.; Dal Conte, S.; Manzoni, C.; Sangalli, D.; Yoon, D.; Lombardo, A.; Ferrari, A. C.; Marini, A.; Cerullo, G.; Prezzi, D. Photo-Induced Bandgap Renormalization Governs the Ultrafast Response of Single-Layer MoS$_2$. *ACS Nano* **2016**, *10*, 1182-1188.

(45)   Zhang, T.; Wang, J. Defect-Enhanced Exciton–Exciton Annihilation in Monolayer Transition Metal Dichalcogenides at High Exciton Densities. *ACS Photonics* **2021**, *8*, 2770-2780.

(46)   Cunningham, P. D.; Hanbicki, A. T.; McCreary, K. M.; Jonker, B. T. Photoinduced Bandgap Renormalization and Exciton Binding Energy Reduction in WS$_2$. *ACS Nano* **2017**, *11*, 12601-12608.

(47)   Liu, H.; Wang, C.; Liu, D.; Luo, J. Neutral and Defect-Induced Exciton Annihilation in Defective Monolayer WS$_2$. *Nanoscale* **2019**, *11*, 7913-7920.

(48)   Yan, T.; Qiao, X.; Liu, X.; Tan, P.; Zhang, X. Photoluminescence Properties and Exciton Dynamics in Monolayer WSe$_2$. *Appl. Phys. Lett.* **2014**, *105*, 101901.

(49)   Yu, C.; Chen, Z.; J. Wang, J.; Pfenninger, W.; Vockic, N.; Kenney, J. T.; Shum, K. Temperature Dependence of the Band Gap of Perovskite Semiconductor Compound CsSnI$_3$. *J. Appl. Phys.* **2011**, *110*, 63526.

(50)   Rubino, A.; Francisco-López, A.; Barker, A. J.; Petrozza, A.; Calvo, M. E.; Goñi, A. R.; Míguez, H. Disentangling Electron–Phonon Coupling and Thermal Expansion Effects in the Band Gap Renormalization of Perovskite Nanocrystals. *J. Phys. Chem. Lett.* **2021**, *12*, 569-575.

(51)   Kaur, G.; Babu, K. J.; Ghosh, H. N. Temperature-Dependent Interplay of Polaron Formation and Hot Carrier Cooling Dynamics in CsPbBr$_3$ Nanocrystals: Role of Carrier-Phonon Coupling Strength. *J. Phys. Chem. Lett.* **2020**, *11*, 6206-6213.

(52)   Francisco-López, A.; Charles, B.; Weber, O. J.; Alonso, M. I.; Garriga, M.; Campoy-Quiles, M.; Weller, M. T.; Goñi, A. R. Equal Footing of Thermal Expansion and Electron–Phonon Interaction in the Temperature Dependence of Lead Halide Perovskite

Band Gaps. *J. Phys. Chem. Lett.* **2019**, *10*, 2971-2977.

(53) Sebastian, M.; Peters, J. A.; Stoumpos, C. C.; Im, J.; Kostina, S. S.; Liu, Z.; Kanatzidis, M. G.; Freeman, A. J.; Wessels, B. W. Excitonic Emissions and Above-Band-Gap Luminescence in the Single-Crystal Perovskite Semiconductors $CsPbBr_3$ and $CsPbCl_3$. *Phys. Rev. B* **2015**, *92*, 235210.

(54) Serrano, J.; Schweitzer, C.; Lin, C. T.; Reimann, K.; Cardona, M.; Fröhlich, D. Electron-Phonon Renormalization of the Absorption Edge of the Cuprous Halides. *Phys. Rev. B* **2002**, *65*, 125110.

(55) Hintermayr, V. A.; Polavarapu, L.; Urban, A. S.; Feldmann, J. Accelerated Carrier Relaxation through Reduced Coulomb Screening in Two-Dimensional Halide Perovskite Nanoplatelets. *ACS Nano* **2018**, *12*, 10151-10158.

(56) Yuan, L.; Huang, L. Exciton Dynamics and Annihilation in WS_2 2D Semiconductors. *Nanoscale* **2015**, *7*, 7402-7408.

Chapter 6

Tracking hot carrier migration in a 1D/2D heterojunction: CdS/MoS$_2$
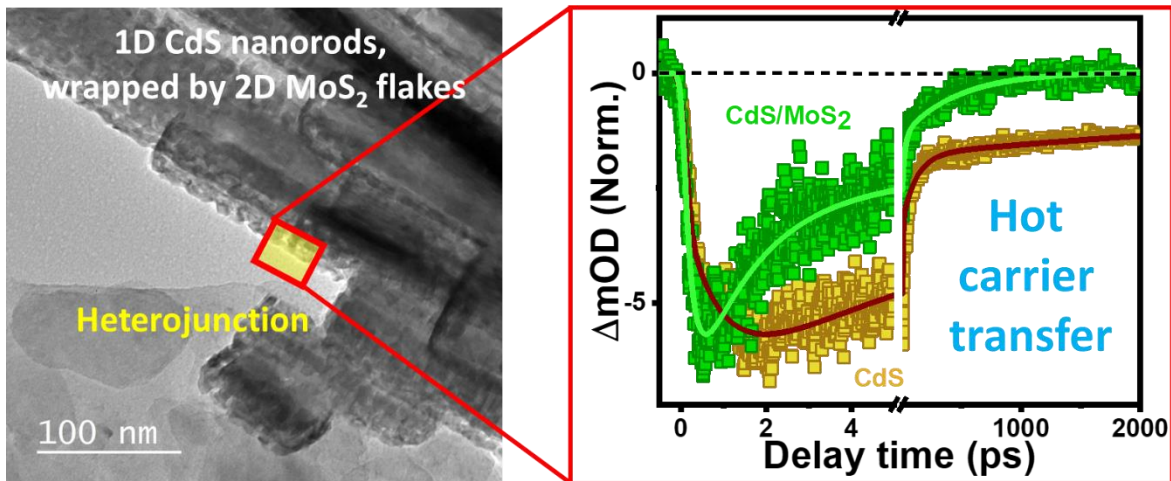
Adapted with permission from Goswami T., Bhatt H., Yadav D. K., Saha R., Babu K. J. and Ghosh H. N., Probing ultrafast hot charge carrier migration in MoS$_2$ embedded CdS nanorods, *J. Chem. Phys.*, 2021, 156, 34704, **Copyright 2021 AIP Publishing**.

6.1. Introduction

Phonon bottleneck mediated slow relaxation of hot charge carriers provides extra boost toward the device efficiency of a semiconducting material, owing to longer time range for the extraction of those carriers. It is expected that efficient utilization of hot carriers would enhance the efficiency of solar cells up to 66% under 1 sun illumination.[1] Among many other techniques, a heterojunction formation is one of the best-known methods for the extraction of hot carriers in a system.[2,3] In recent times, numerous heterojunctions are being fabricated and designed to form state of the art optoelectronic devices.[4,5,6,7,8,9] The efficiency of these heterosystem can possibly be improved from detailed knowledge of the excited state behaviour of hot carriers, [2, 10] as well as the formation of important quasiparticles like exciton, bi-exciton, trion[11] etc. at the interface of those quantum materials. Hence, it is utmost important to explore the charge carrier dynamics of all possible heterosystems suggested to have potential in advancing the optoelectronic research.

Cadmium Sulfide (CdS) is a versatile II-VI semiconductor[12] and a widely known photocatalyst[13] owing to its easy synthetic routes and outstanding optical and catalytic properties. Some of its properties important for catalytic applications are like suitable direct bandgap (~2.4 eV) for visible light harvesting, good chemical and thermal stability, appropriate redox potential etc.[14, 15, 16] Along with these fascinating properties, low dimensional CdS nanostructures endows some fundamental properties like high charge carrier mobilities, relatively low work function and large exciton binding energy.[17, 18] CdS based nanostructures hold great promise as a host material in high technology optoelectronic applications like photovoltaics, transistors, light emitting diodes, photochemical devices, photodetectors, etc.[18, 19, 20] Amid all nanostructures of CdS, 1D nanorods (NRs) is the hottest field of nanotechnology in recent times due to their unique optoelectronic properties.[18, 21] Now, for the fabrication of an efficient device for the extraction of hot carriers, a thermodynamically suitable material has to be integrated with CdS, so that hot carrier extraction (HCE) phenomena overpowers the hot carrier cooling process.[22] Usually, the hot carriers dissipate their energies non-radiatively in form of heat, and can only be made useful by slowing down their relaxation process and simultaneous extraction.[23] In this quest, MoS$_2$ could be a good choice as an absorbing semiconductor of hot electrons due to their tunable band gap (1.3 eV to 1.8 eV) and layer dependent electronic band structure.[11] It is a 2D TMDC system and possess hexagonal crystal structure just like CdS,[13] which ensures an intimate interface between these two. Also, MoS$_2$

conduction band level lies such that CdS electrons can easily migrate into MoS$_2$,[24] which is utmost important for efficient extraction of CdS hot carriers. On the other hand, MoS$_2$ itself a very good photocatalyst owing to its band positions, very high charge carrier mobility and huge number of active edge site in the 2D architecture.[25, 26, 27, 28] Hence the extracted charge carriers from CdS system would join MoS$_2$ carriers in the active sites and take part in the catalysis reactions enhancing the activity of overall heterosystem. In 2010, Zong et. al., reported that calcined MoS$_2$/CdS catalysts are capable of very high photocatalytic activity, even better than Pt/CdS.[29] Following that, many scientists around the globe have been trying to design a heterojunction photocatalyst comprised of CdS and MoS$_2$.[24, 30, 31, 32, 33, 34] Although, there have been many attempts on device fabrication, the basic understanding of the charge carrier dynamics is almost rare in the literature. There are very few examples in the literature where the respective charge carrier dynamics was studied to get an insight of the mechanistic pathways in a CdS-MoS$_2$ based architecture.[35, 36] However, the detailed spectroscopic investigation at the interface of these two exquisite nanomaterials are still absent in the literature. Also, there have been no reports on the hot carrier dynamics in these kinds of systems. In this scenario, we thought it would be very important to explore all possible optical phenomena staging in this type of 1D-2D interface in a detailed manner, which are responsible for the photocatalytic activity in these heterosystems.

In this chapter, we will be discussing a 1D-2D hetero-composite system, based on CdS nanorods (1D) and MoS$_2$ flakes (2D). The composition provides a type-I heterojunction, such that in photoexcitation of CdS, both the electron and holes can migrate toward MoS$_2$. From the steady state photoluminescence spectroscopy, we found that CdS charge carriers are effectively transferred to MoS$_2$ following photoexcitation. Transient absorption (TA) studies revealed that the heterosystem consists of both CdS and MoS$_2$ signatures, where MoS$_2$ signals are enhanced but CdS bleach intensity was drastically decreased as compared to their pristine signatures. We found that hot charge carrier migration is much more effective than band edge one here and effectively enhance charge carrier population in the MoS$_2$ region. Pump energy dependent measurements discloses the importance of photon energy on the migration process and the hot carrier transfer.

6.2. Synthesis and experimental techniques

6.2.1. Synthesis of CdS Nanorods and CdS/MoS$_2$ nanocomposite

CdS nanorods were prepared through a simple solvothermal method.[16, 37] For synthesis of CdS nanorods, Cd(ac)$_2$.2H$_2$O (0.4269 g) and thiourea (0.6089 g) were dissolved in 12 mL ethylenediamine followed by magnetic stirring. After stirring for 30 min, the mixture was transferred to Teflon-lined stainless-steel autoclave with a capacity of 25 mL and then kept at 180°C for 24 h. After natural cooling the autoclave to room temperature, the obtained product was collected by centrifugation and washed four to five times with ethanol, followed by drying in an oven at 60°C. The preparation of CdS/MoS$_2$ nanocomposite was like that of CdS nanorods, only MoS$_2$ sheets (0.2 g) were added to the CdS precursors before the reaction procedure. The multilayer sheets were prepared by exfoliating bulk MoS$_2$ in DMSO using a bath sonicator for 1h.

6.2.2. Basic characterisation and optical measurements

Powder X-ray diffraction (PXRD) patterns of the as-synthesized samples were collected on a Bruker D8 ADVANCE X-ray diffractometer with a Cu Kα line of 1.542 Å. TEM and HRTEM measurements were conducted on (JEOL JEM 2100) operating at an accelerating voltage of 200 kV to get the morphologies and structures of the samples. UV-Vis absorption spectra were recorded with a Shimadzu UV-2600 UV-vis spectrophotometer. PL spectra were recorded on Fluorolog 3-221 fluorimeter in solid state.

6.2.3. Femtosecond transient absorption (TA) spectroscopy

TA measurements were executed with the help of a Ti: sapphire amplifier system (Astrella, Coherent, 800 nm output wavelength, ~ 3W average power, pulse width of ~ 35 fs and 1 kHz repetition rate) and a Helios Fire pump-probe spectrometer.[38] The output laser beam was splitted into pump and probe using an appropriate beam splitter. Pump beam passes through an Optical Parametric Amplifier (Coherent) to produce desired wavelengths for pumping the system. Probe beam generates white light passing thorough a Sapphire crystal. A mechanical delay was placed in the pump beam path to maintain proper pump-probe delay throughout the experiment. The experimental data were fitted using surface explorer software.

6.3. Results and discussion

6.3.1. Characterisation and basic optical measurements

We have synthesized CdS and CdS/MoS$_2$ nanocomposites using robust and cost-effective solvothermal route. The basic idea was to fabricate a heterojunction between these two 1D and 2D systems, as shown in the schematics in **figure 6.1a**.
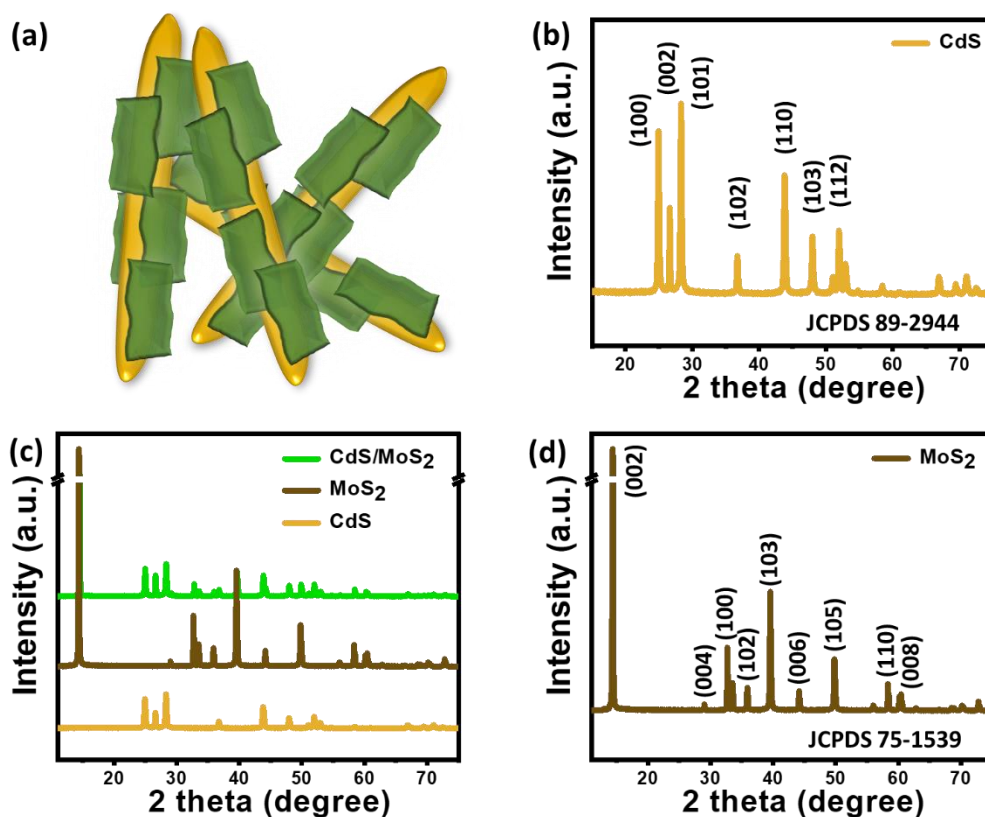
Figure 6.1: (a) Graphical representation of an 1D/2D heterocomposite of CdS and MoS$_2$. **(b)** XRD patterns of pristine CdS nanorods. **(c)** Comparative XRD patterns of pristine CdS, MoS$_2$ and CdS/MoS$_2$ nanocomposites along with detailed lattice planes of **(d)** MoS$_2$ nanosheets.

The PXRD pattern was used to distinguish the crystal structure and phase purity of pristine CdS, MoS$_2$ and CdS/MoS$_2$. The diffraction pattern of bare CdS, having lattice constants a = 4.14 Å and c = 6.704 Å, shows good agreement with the standard pattern of hexagonal wurtzite-structured CdS[16] (**Figure 6.1b**). Comparing with CdS nanorods, the nanocomposite XRD patterns in **figure 6.1c**, shows additional reflections for MoS$_2$ as expected. The reflection peaks at 2θ values of 14.40º, 33.48º, and 58.34º are attributed to the reflection plane (002), (100) and (110) of MoS$_2$ in the XRD pattern of CdS/MoS$_2$ heterostructure[36] (**Figure 6.1d**). No impurity diffraction peaks related to Cd, S and Mo were observed in the composite, which confirms the high purity of CdS/MoS$_2$ nanocomposite.[24]
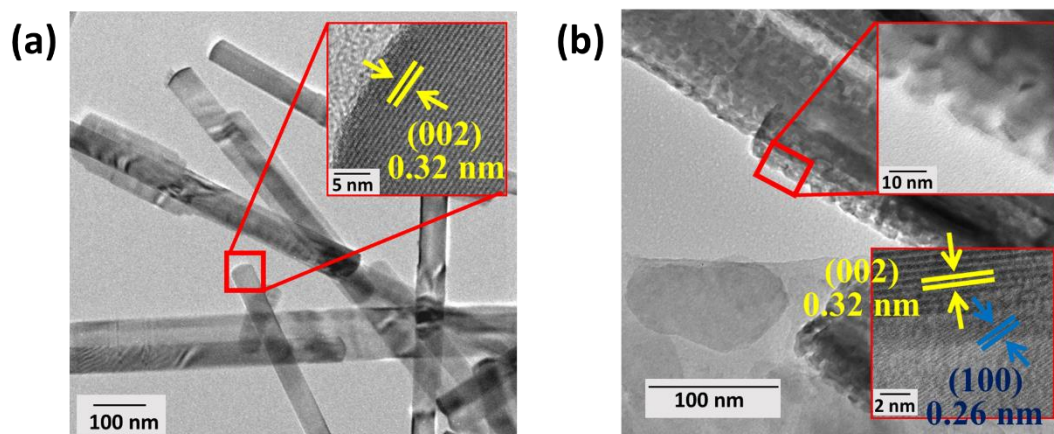
Figure 6.2: TEM and HRTEM images of **(a)** CdS and **(b)** CdS/MoS$_2$.

The surface morphology and microstructure of the prepared CdS and CdS/MoS$_2$ nanocomposite were investigated using TEM and HRTEM shown in **Figure 6.2a and b**, respectively. As can be seen from the TEM image (**Figure 6.2a**), the bare CdS exhibits rod-like morphology. The average diameter and length of bare CdS has been calculated to be 50-60 nm and 600-700 nm, respectively. Inset of **figure 6.2a** shows the crystal lattice planes of CdS nanorods with interplanar spacing of 0.32 nm, which corresponds to (002) plane of hexagonal CdS.[16] The above findings confirm the single-crystalline nature of CdS NRs. The TEM image shown in **figure 6.2b** and inset, reveals the presence MoS$_2$ flakes at the end of CdS nanorod in the synthesized nanocomposite. Inset of **figure 6.2b** shows the HRTEM image of CdS/MoS$_2$ nanocomposite. The HRTEM image of nanocomposite disclosed that the lattice fringes of CdS nanorods ((002), 0.32nm) and MoS$_2$ nanosheet ((100), 0.26 nm)[36] are closely spaced which ensures a clear interface between MoS$_2$ nanosheets and CdS NRs.

Figure 6.3a depicts steady state optical absorption spectra of CdS nanorods and CdS/MoS$_2$ composite systems. CdS absorption spectrum displays a broad absorption peak around 500 nm, comprised with two closely spaced peaks, arising from 1Σ (1σ_e−1σ_h) and 2Σ (2σ_e−2σ_h) excitonic transitions.[39] Large diameter of the nanorods induces very little effect of quantum confinement (behaves more like bulk), that the energy bands are very closely spaced (energy difference ~ 0.07 eV). As a result, the peaks overlap each other and could not be deconvoluted in the absorption spectrum. In the nanocomposite, CdS peaks appear at the same energetic position, implies that nanorods maintain their usual size distribution in the heterosystem. Although the overall absorption of the system is enhanced, particularly at the red region of the

spectrum. Both A, B MoS$_2$ excitonic peaks are clearly visible in the nanocomposite spectrum (**Figure 6.3b**).
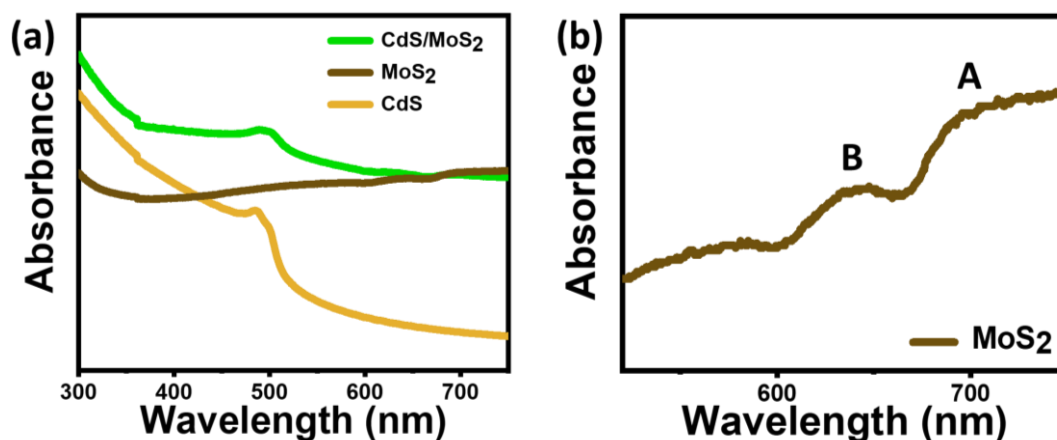
Figure 6.3: (a) Absorption spectra of CdS, MoS$_2$ and CdS/MoS$_2$ nanocomposites. **(b)** Enlarged absorption spectrum of MoS$_2$, representing both A and B excitonic features at ~ 680 and ~ 620 nm respectively.

Next, to realise the charge carrier characteristics in CdS and CdS/MoS$_2$, these systems were investigated with the help of steady state PL spectroscopy. **Figure 6.4a** represents PL spectra of these two materials following 400 nm photoexcitation. The PL spectrum of CdS exhibits a broad peak around 530 nm, along with a strong signature extending beyond 730 nm. These two features can be assigned to the radiative recombination of photoexcited charge carriers from band edge and inter band gap trap states respectively.[40]
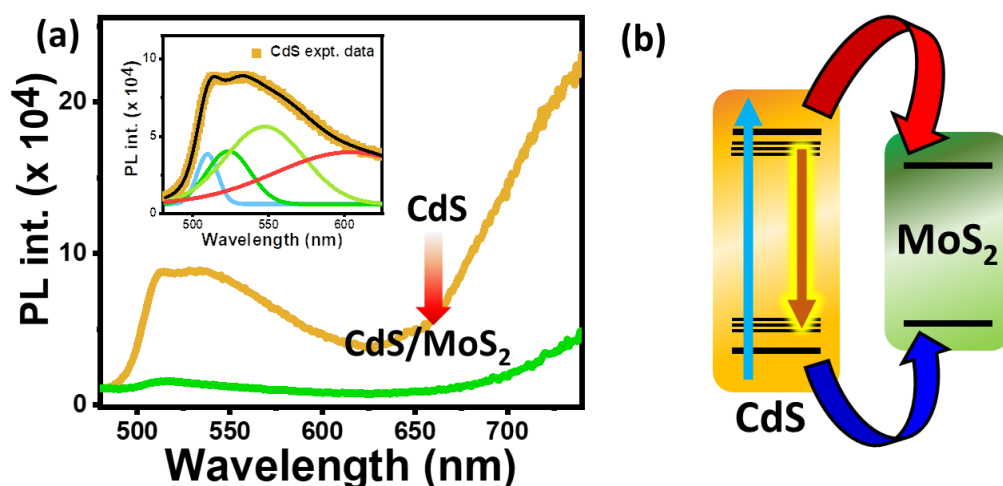
Figure 6.4: (a) Steady state photoluminescence spectra of CdS and CdS/MoS$_2$ heterocomposites. Inset: De-convoluted PL spectra of CdS in the band edge regime (480 to 620

nm). (**b**) Comparative band levels of CdS nanorods and MoS₂ sheets representing migration of charge carriers from CdS to MoS₂.

Moreover, the peak around 530 nm is quite broad and cannot represent only band edge recombinations. Recombinations from near band edge trap states are also contributing to this signal. To further elucidate this broad band, we deconvoluted this feature using four gaussian functions. Four different peaks were observed at 510, 524, 548 and 604 nm (**Figure 6.4a** INSET). The 510 nm peak is necessarily arising from the radiative recombination phenomena within CdS conduction and valence band. The other three and the strongest PL signature at 740 nm are associated with the inter band gap trap states of CdS. Following addition of MoS₂, the CdS PL intensity is substantially quenched (**Figure 6.4a**), pointing toward migration of charge carriers from CdS to MoS₂ (**Figure 6.4b**). The respective band positions of CdS and MoS₂ were calculated from Mott Schottky analysis and DRS spectra, giving rise to a type-I band alignment (**Figure 6.5**), which confirms the thermodynamic viability of CdS charge carrier migration toward MoS₂.
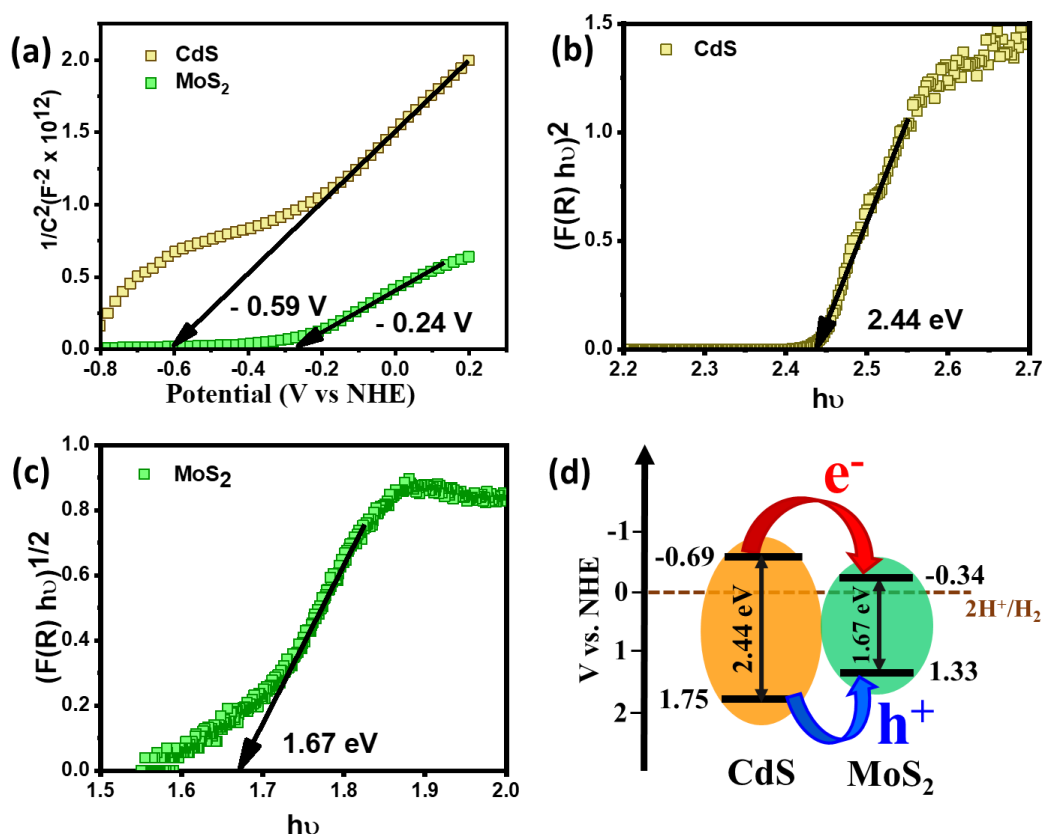
Figure 6.5: (**a**) Mott Schottky plot and estimated conduction band edges for CdS nanorods and MoS₂ nanosheets. (**b**) Band gap calculation of CdS from the respective DRS spectrum. (**c**)

Band gap calculation of MoS$_2$ from the respective DRS spectrum. **(d)** Respective band level positions of CdS and MoS$_2$, calculated from Mott Schottky plot and optical band gap, representing the possibility of charge carrier migration from CdS to MoS$_2$.

6.3.2. TA study of CdS nanorods

To elucidate the excited state characteristics of CdS NRs, femtosecond transient absorption spectroscopy was employed for the nanorod solution in DMSO. **Figure 6.6a, c** portrays transient spectra of CdS NRs at different pump probe delay time, following photoexcitation with 400 nm pump. The spectra display a strong photoinduced bleach at 499 nm with a hump around 488 nm, which are assigned to the band edge 1Σ transition and weakly populated 2Σ transition, respectively. The 2Σ signal is more pronounced at the early and longer time scale of the spectra.
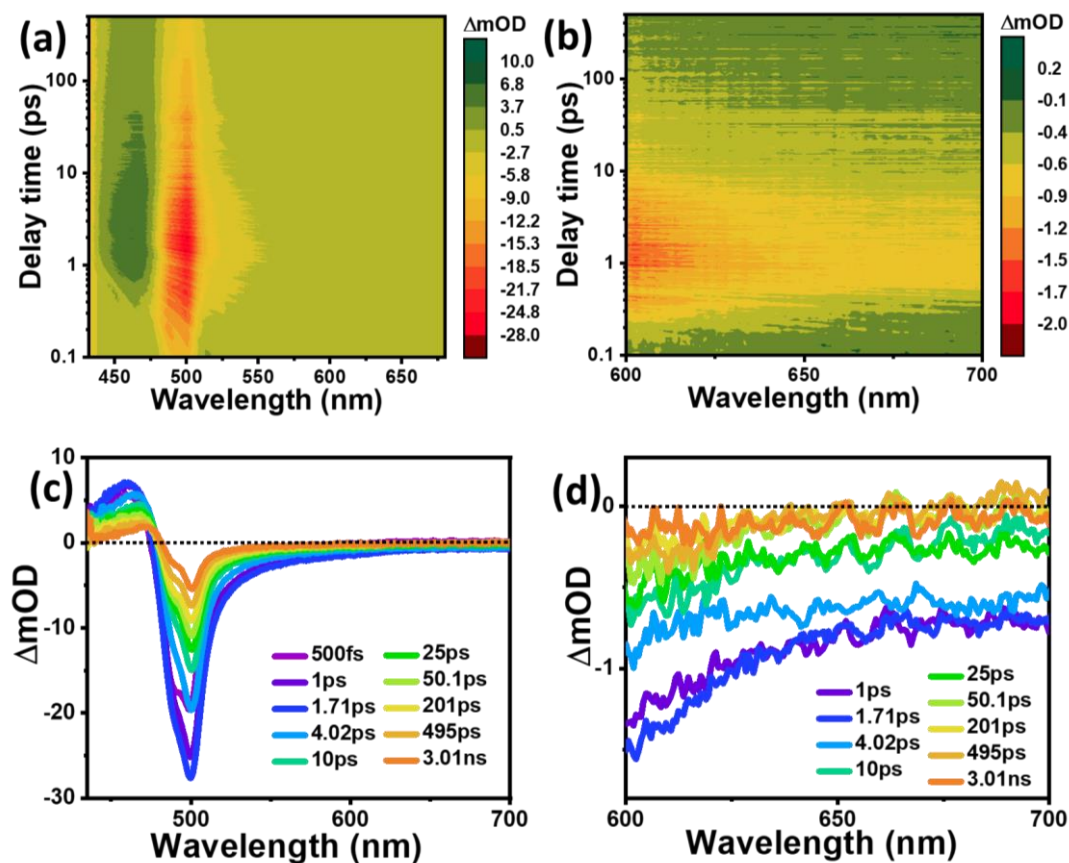
Figure 6.6: **(a)** 2D colour contour plot of pristine CdS nanorods as a function of pump-probe delay time with 400 nm photoexcitation. **(b)** Enlarged contour plot of low intensity signal at the red wing of the spectra. **(c, d)** Corresponding TA spectra CdS NRs for certain pump probe delay time scales.

Possibly high intensity of the 1Σ signal masks the 2Σ feature in other time regimes, owing to high charge carrier population at the band edge states. In addition to these two, we observed a strong photoinduced absorption signal at the blue wing, peaking around 460 nm and a broad as well as weak bleach feature at the red side of the spectra, covering wide region of the electromagnetic spectra. The intense 1Σ, 2Σ bleach features appear due to state filling effect in 1σ$_e$ band and dominated by electrons,[41] owing to lighter effective mass of electrons and higher degeneracy in valence band states in nanorod architecture of CdS.[42] Hence, the broad range (550-700 nm) negative feature in the spectra (Shown in **figure 6.6b, d**) must be arising from filling of inter-band-gap states with photo-excited electrons in the system.[43] Earlier, Yan et al. observed Similar transient features in case of CdS nanorods.[35] There are also report of CdS nanorods, where a weak photoinduced signature was observed instead of bleach.[40] Although those nanorods are much more quantum confined owing to their small sizes, prepared from long chain ligand mediated hot injection method. To further elucidate the origins of different transient features in our system, we have studied the dynamics at different wavelengths of the spectra.
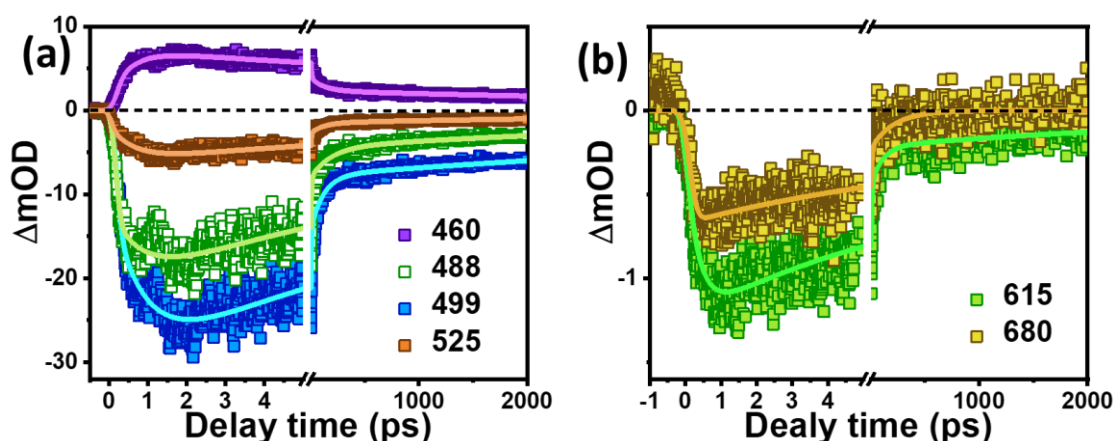
Figure 6.7: (a) Transient decay profiles of CdS probing at 460, 488, 499 and 525 nm for the blue wing photoinduced absorption, high energy excitonic bleach, band edge excitonic bleach and trap mediated bleach signal respectively. **(b)** TA dynamics of the red region of the spectra monitoring at 615 and 680 nm.

In **figure 6.7a and 6.7b**, we have presented the transient decay profiles of CdS nanorods probing at blue and red region of the spectra, respectively, continuing from the above discussion. The dynamic profiles are fitted with multi-exponential functions and the fitting parameters are listed in **table 6.1**. The excitonic signals (1Σ and 2Σ) possess maximum intensity amongst the bleach features, also associated with largest growth time scales, 0.55 ps and 0.44

ps respectively. This infers the dominance of excitonic features in the TA signal of CdS NRs. 400 nm pump has sufficient energy to excite the charge carriers into higher energy states of CdS, as compared to 1Σ and 2Σ excitonic states in the system. These high energy electrons (well known as hot electrons) are quickly thermalized and cooled down to lower energy states. The growth time scales of the transient bleach signal estimate these colling processes. The rate constant k_{int} ($k_{internal\ relaxation}$) corresponding to these hot carrier cooling processes for 1Σ and 2Σ states was calculated to be 1.82 ps^{-1} (τ_{growth} ~ 0.55 ps) and 2.27 ps^{-1} (τ_{growth} ~ 0.44 ps) from the following equation,[44]

$$\tau_{growth} = 1/k_{int}$$

Again, both the intensity and growth time scales are substantially higher in case of the band edge exciton than that of the higher energy excitons. This is possible due to the spontaneous cooling of photoexcited charge carriers from 2Σ states toward 1Σ band edge. The dynamics of the weak bleach signature is much faster than that of the 1Σ and 2Σ signals (**Figure 6.7b**). Earlier in the steady state experiments, we observed high concentration of inter-band-gap defect states in the system, which will certainly take part in the TA spectra. In our previous article as well, we observed similar defect mediated signals in ZnIn$_2$S$_4$ nanosheets and established their role in the photocatalytic activity of this material.[43] These defect states are necessarily shallow in nature and reside very close to the band edge and possess very fast dynamics, owing to higher de-trapping nature of these states.[45] Following the trapping of charge carriers in these states, de-trapping phenomena comes into play and minimises the state filling effect. As we go down to the higher wavelength region, the trap induced signal becomes weaker, possessing shorter growth time scales as well as faster decay (**Table 6.1**). This is possible because, lower energy states are more closely spaced to the band edge and charge carriers are easily de-trapped from these states.

6.3.3. TA study of MoS$_2$ and CdS/MoS$_2$ nanocomposites

Next, in order to investigate the interfacial interaction in between CdS nanorods and MoS$_2$ sheets, TA spectroscopy was employed in the CdS/MoS$_2$ nanocomposite. **Figure 6.8a, c** portrays both CdS and MoS$_2$ excitonic features in the nanocomposite spectra following photoexcitation of 400 nm, in a wide range of pump-probe delay time. The spectra are comprised of pronounced 1Σ CdS excitonic bleach at 502 nm very similar to pristine CdS, along with characteristic A, B excitonic peaks of MoS$_2$ at 680 and 620 nm, respectively (**Figure**

6.8b, d). This is possible because, 400 nm pump can photoexcite both MoS$_2$ and CdS band edge excitons.

The TA spectra in **figure 6.8a and b** monitors the changes in CdS and MoS$_2$ bleach signals simultaneously. Interestingly, transient study of pristine MoS$_2$ produces very weak signatures A, B excitonic peaks (**Figure 6.9a, b**) even with higher pump fluence (400 µJ/cm^2), owing to weak exciton binding energy and high defect concentration in multi-layered MoS$_2$ sheets.[46, 47] On the other hand, in presence of CdS nanorods, stronger excitonic signals are visible in the MoS$_2$ region (**figure 6.8d**) in much lower pump fluence (100 µJ/cm^2). The intensity of A, B excitonic signals are now enhanced in presence of CdS (**Figure 6.9c, d**), which infers increased carrier population in the MoS$_2$ regime in the heterosystem. In **figure 6.10a** we have plotted the dynamic profiles of CdS 1Σ excitonic bleach signal in absence and presence of MoS$_2$ for 400 nm pump excitation. Interestingly, the bleach signal intensity is almost diminished (decreased from 25 mOD to 5.6 mOD) in presence of MoS$_2$.

Table 6.1. Fitting parameters corresponding to the dynamic profiles of the transient signal of CdS nanorods, in different probe wavelengths for 400 nm photoexcitation.

Probe wavelength (nm)	τ_1 (ps) (Growth)	τ_2 (ps) (Decay)	τ_3 (ps) (Decay)	τ_4 (ns) (Decay)
460	0.43	7.7 (44.6%)	124 (21.7%)	> 1 ns (33.7%)
488	0.44	7.8 (57%)	118 (18.4%)	> 1 ns (24.6%)
499	0.55	8.1 (49.1%)	130 (21.9%)	> 1 ns (29%)
525	0.45	6.7 (51.7%)	111 (21.4%)	> 1 ns (26.9%)
615	0.28	6.5 (61.8%)	102 (19.8%)	> 1 ns (18.4%)
680	0.12	7.8 (68.2%)	211 (21.4%)	–
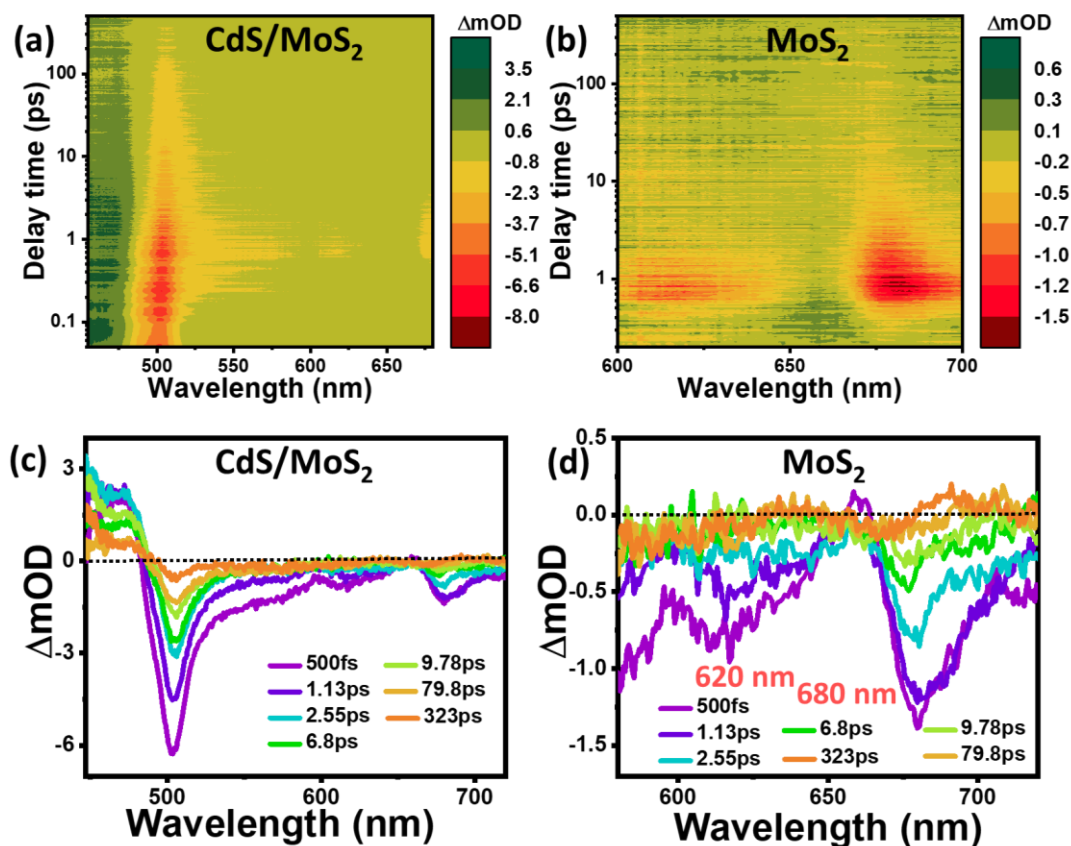
Figure 6.8: **(a)** 2D colour contour plot of pristine CdS/MoS$_2$ nanocomposites as a function of pump-probe delay time with 400 nm photoexcitation. **(b)** Enlarged contour plot of low intensity signal at the red wing of the spectra, representing emergence of A, B excitons of MoS$_2$. **(c, d)** TA spectra of CdS/MoS$_2$ nanocomposites and MoS$_2$ respectively as a function of few selected pump-probe delay times with 400 nm photoexcitation.

This indicates decrement of electron population in the $1\sigma_e$ band edge. Also, there is possibility of energy transfer from CdS to MoS$_2$, considering the overlap of CdS PL spectrum and MoS$_2$ absorption spectrum. Here, we will focus on the migration of charge carriers only. In the composite system, the relaxation of CdS hot electrons to the band edge gets hampered due to the competition from another thermodynamically viable process, i.e., hot electron transfer into the MoS$_2$ conduction band. The decrease in the probability of internal relaxation of CdS electrons in the band edge leads to small intensity of the CdS signal in presence of MoS$_2$. The growth time scale of the 1Σ excitonic bleach signal was found to be 0.15 ps here (**Table 6.2**), which corresponds to the factor, $1/(k_{int} + k_{hot})$. Hence, the time scale ($\tau_{hot} = 1/k_{hot}$) corresponding to the hot carrier transfer was calculated to be 0.21 ps ($k_{hot} \sim 4.85$ ps^{-1}).
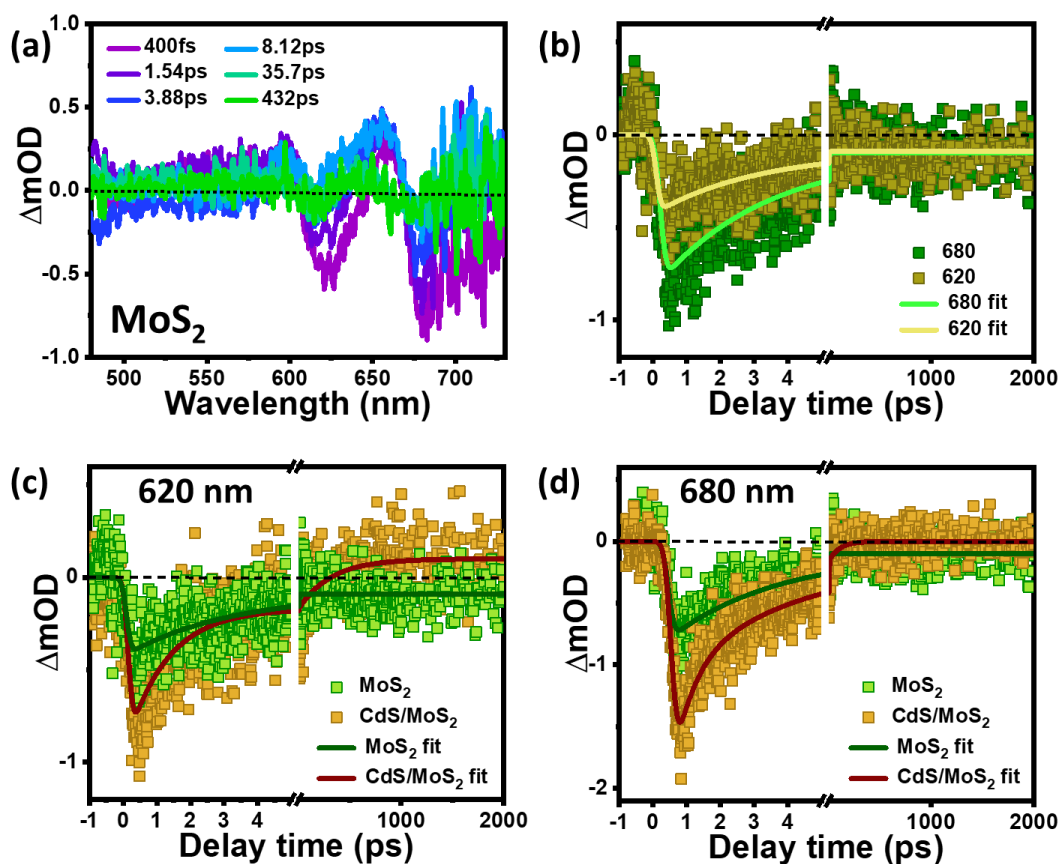
Figure 6.9: **(a)** TA spectra of pristine MoS$_2$ nanosheets as a function of pump-probe delay time with 420 nm photoexcitation with 400 µJ/cm^2 pump fluence. **(b)** Transient decay profiles of exciton A and B in MoS$_2$, monitoring at 680 and 620 nm. Comparative decay profiles of **(c)** exciton B and **(d)** A in MoS$_2$ and CdS/MoS$_2$, monitoring at 620 and 680 nm, respectively.
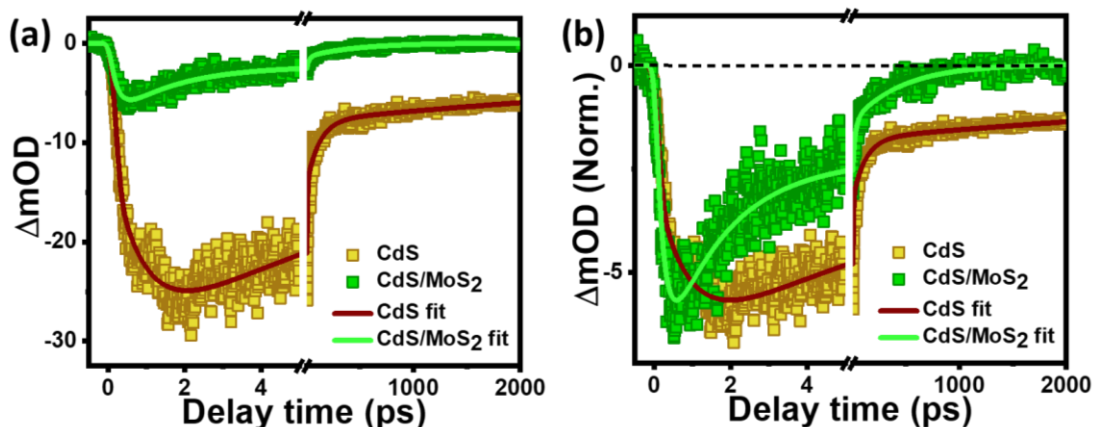
Figure 6.10: **(a)** Evolution of transient dynamics probing at the band edge exciton of CdS NRs in absence and presence of MoS$_2$. **(b)** Normalized bleach recovery kinetics at the band edge

exciton of CdS NRs in absence and presence of MoS_2, indicating transfer of charge carriers from CdS to MoS_2.

Table 6.2. Fitting parameters corresponding to the dynamic profiles of the transient signal of CdS/MoS₂ heterosystem, in different probe wavelengths for 400 nm photoexcitation.

Probe wavelength (nm)	τ_1 (ps) (Growth)	τ_2 (ps) (Decay)	τ_3 (ps) (Decay)	τ_4 (ns) (Decay)
502	0.15	1.6 (57.1%)	27.7 (34.6%)	> 1 ns (8.3%)
620	0.14	0.7 (69.4%)	90.4 (30.6%)	> 1 ns (100%)
680	0.14	0.4 (50%)	3.7 (40%)	0.49 ns (10%)

We found that, the signal in the heterosystem decays at a much faster rate as compared to the pristine one (**figure 6.10b**), implying shorter lifetime of CdS $1\sigma_e$ electrons in presence of MoS_2. The fast recovery of MoS_2 based CdS bleach confirms migration of photoexcited electrons from CdS domain to MoS_2. The decay of bare CdS bleach signal was found to be 8.1 ps (τ_2, Table 6.1), which is significantly reduced to 1.6 ps in presence of MoS_2 (**Table 6.2**). This difference would give rise to electron transfer time scale from CdS to MoS_2.[39] So, the band edge electron transfer (BET) rate constant,

$$k_{BET} = (1.6 \text{ ps})^{-1} - (8.1 \text{ ps})^{-1} = 0.49 \text{ ps}^{-1}$$

Subsequently, the electron transfer time scale from the $1\sigma_e$ band edge can be calculated to be 2 ps.

A simplified picture of this competition of cooling and extraction processes of hot carriers are shown in **figure 6.11**. The 400 nm pump excites the charge carriers at high energy states of CdS, which are eventually cooled to the band edge by means of phonon emissions. In presence of MoS_2, these hot carriers are extracted from CdS high energy states at very fast time scale and can be used for further catalytic processes from MoS_2. Hot carrier extraction (HCE) brings down the waste of charge carriers and improves device efficiency of the heterosystem.
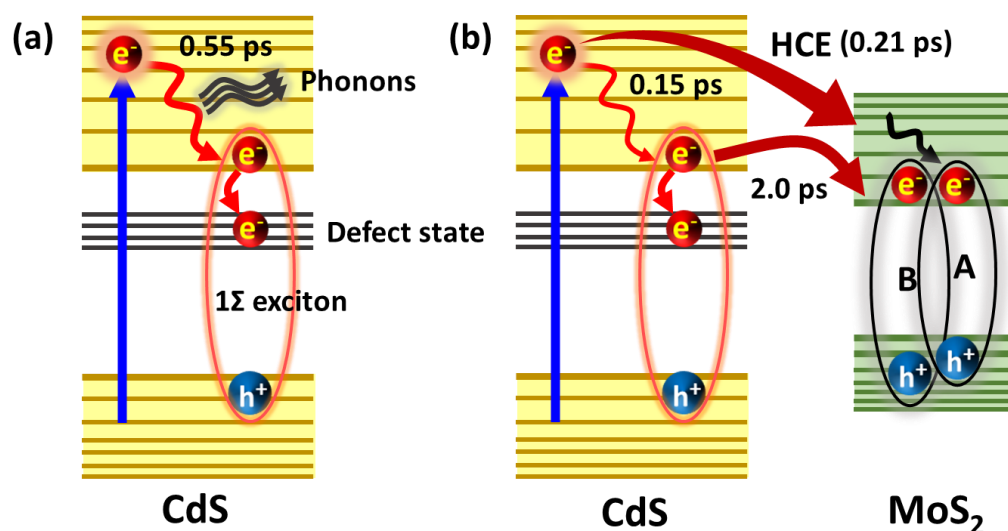
Figure 6.11: Schematic illustration of excited state behaviour of photogenerated charge carriers in **(a)** CdS and **(b)** CdS/MoS₂ on application of 400 nm pump. The scheme represents how hot carrier extraction triumphs over hot carrier cooling of CdS in presence of MoS₂. Only electronic migrations are shown here for the sake of simplicity and little contribution of holes in the TA signal of CdS.

6.3.4. Pump dependent TA study

To further elucidate the hot electron transfer process in CdS/MoS₂ nanocomposites, we employed different pump photon energy to excite CdS and CdS/MoS₂ systems. The idea was to probe the dependency of charge carrier migration at the CdS/MoS₂ interface on the energy of pump photons. In **figure 6.12a** we have plotted the dynamic profiles of 1Σ excitons in CdS nanorods for 360, 400 and 450 nm pump excitations. The growth time scale of 450 signal was found to be 0.34 ps (**Table 6.3**), lower than that of 400 nm. As, 450 nm pump can only excite the electrons in the lower energy states than that of 400 nm, the electrons take shorter time to reach the1Σ excitonic band edge from the higher energy states. The rise time of the 2Σ excitons were extremely fast in this case, found to be IRF limited. The corresponding rate constant corresponding to this cooling processes was calculated to be 2.94 ps^{-1} ($\tau_{growth} \sim 0.34$ ps). In presence of MoS₂ this 1Σ growth time is drastically decreased and found to be extremely fast (< 0.1 ps, **Table 6.4**). However, the growth time scale of 360 nm excitation is very similar to that of 400 nm (**Figure 6.12a, Table 6.3**). This is contradictory to what we generally observe in a quantum material. Usually, higher energy pump enjoys longer signal rise time in transient absorption spectroscopy.[48] Unless we are exciting close to the continuum states of the system and the cooling time is almost unchanged. This could be the result of poor quantum effect in

these CdS nanorods, which is expectable from the large diameter of the rods. In case of CdS/MoS$_2$, the dynamical change of 1Σ exciton for different pumps is very similar to that of the pristine CdS (**Figure 6.12b**). The rise time of 360 nm excitation is again similar to 400 nm. So, one may interpret from these observations that the hot electron transfer would not depend on the pump wavelengths, if we are exciting the materials with very high energy photons in this type of CdS nanorods. In order confirm this statement, we probed A exciton dynamics in the MoS$_2$ regime (**Figure 6.12c**). Very interestingly, the growth time scales are now very different from each other for different pump excitations.
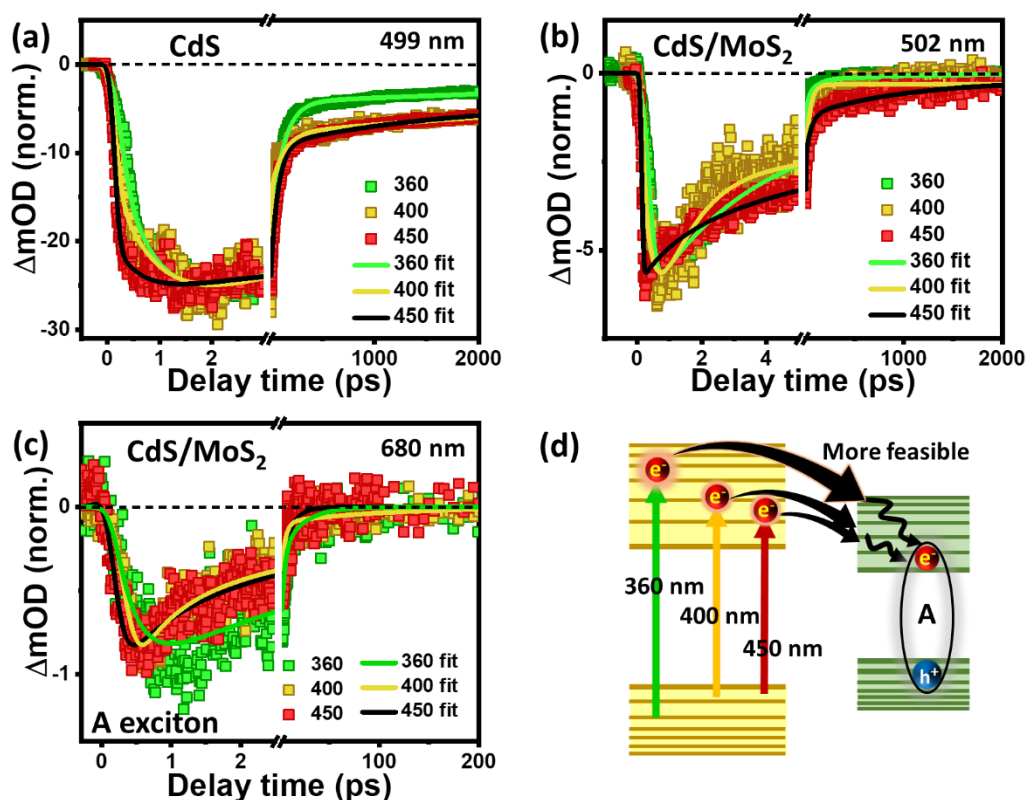
Figure 6.12: Normalized decay profiles of CdS 1Σ excitons in **(a)** pristine CdS at 499 nm and **(b)** CdS/MoS$_2$ composite system at 502 nm, on excitation of different pump wavelengths (360, 400 and 450 nm). **(c)** Normalized decay profiles of MoS$_2$ A excitons (at 680 nm) in CdS/MoS$_2$ nanocomposite on excitation of similar pump wavelengths. **(d)** Simple schematic of the CdS/MoS$_2$ interface representing higher probability of electronic migration on application of higher energy pump photons.

Figure 6.12c represents the dynamic profiles of MoS$_2$ A excitonic signal in CdS/MoS$_2$ for 360, 400 and 450 nm. The rise time of this excitonic feature maintains a steady increment with the pump photon energy. The rise time for 450 nm (0.11 ps) is increased to 0.15 ps in 400 nm and

further jumped into 0.28 ps in case 360 nm (**Table 6.5**). So, even the cooling time of CdS does not offer any change and gets saturated above photon energy of 400 nm, it is not the case for MoS$_2$. The most plausible reason would be the transfer of CdS electrons into different energy states of MoS$_2$ before being thermalized into the band edge forming A excitons. Higher energy photon places the electrons in the higher energy states of MoS$_2$ and in turn increase the cooling time corresponding to A excitons. This would be extra bonus for extraction of hot carriers from this heterosystem. Not only that, the decay profiles are now much slower in high energy pump photon case. This infers higher charge carrier population in MoS$_2$ region in presence of CdS after exciting at higher energy pump photons.

Table 6.3. Fitting parameters corresponding to the dynamic profiles of the 1Σ excitonic bleach signal of CdS nanorods, for different pump excitation.

Pump wavelength (nm)	τ_1 (ps) (Growth)	τ_2 (ps) (Decay)	τ_3 (ps) (Decay)	τ_4 (ns) (Decay)
360	0.53	7.2 (35.9%)	137 (47.9%)	> 1 ns (16.2%)
400	0.55	8.1 (49.1%)	130 (21.9%)	> 1 ns (29%)
450	0.34	44.3 (60.8%)	325.7 (14.1%)	> 1 ns (25.1%)

These instances strongly establish the fact that higher energy pumps are capable of stronger charge carrier separation in CdS/MoS$_2$ hetero-interface and opens new avenue for optical applications. We have discussed charge carrier migration phenomena in the interface of CdS/MoS$_2$ composite system, on applications of pump photons from different regimes of the electromagnetic spectra. This study would pave a unique journey in the research of heterojunction based photocatalysts, particularly in a 1D-2D arrangement.

Table 6.4. Fitting parameters corresponding to the dynamic profiles of the 1Σ excitonic bleach signal in CdS/MoS$_2$ heterosystem, for different pump excitation.

Pump wavelength (nm)	τ_1 (ps) (Growth)	τ_2 (ps) (Decay)	τ_3 (ps) (Decay)	τ_4 (ps) (Decay)	τ_5 (ns) (Decay)
360	0.15	3.2 (78.3%)	28 (15.6%)	645 6.1%)	-
400	0.15	1.6 (57.1%)	27.7 (34.6%)	> 1 ns (8.3%)	-
450	< 0.1	0.7 (31.7%)	4.4 (30.1%)	62.1 (20.6%)	> 1 ns (17.6%)

Table 6.5. Fitting parameters corresponding to the dynamic profiles of the A excitonic bleach signal (680 nm) in CdS/MoS$_2$ heterosystem, for different pump excitation.

Pump wavelength (nm)	τ_1 (ps) (Growth)	τ_2 (ps) (Decay)	τ_3 (ps) (Decay)	τ_4 (ns) (Decay)
360	0.28	2.1 (73.2%)	20.4 (26.8%)	-
400	0.15	0.4 (50%)	3.7 (40%)	0.49 ns (10%)
450	0.11	1.2 (68.3%)	15.7 (31.7%)	-

6.4. Conclusions

A 1D-2D heterocomposite, CdS/MoS$_2$ was fabricated using simple, inexpensive hydrothermal synthetic route. HRTEM measurements show CdS nanorods are covered with small MoS$_2$ flakes in the composite system. CdS/MoS$_2$ absorption spectrum is comprised of both the signature of CdS 1Σ, 2Σ excitons and MoS$_2$ A, B excitons. The CdS PL spectrum is substantially quenched in presence of MoS$_2$, which indicate transfer of photoexcited charge carriers from CdS to MoS$_2$. Decrement of both band edge and defect mediated PL signals testifies for the efficient charge migration in the heterosystem. Transient absorption spectroscopy reveals a strong overlapped bleach signal corresponding to 1Σ and 2Σ excitons,

along with a weak defect induced bleach signal spread in a wide region of the spectra. The lifetime of hot carrier relaxation for these two excitons were calculated from the rise time of the transient signals and found to be 0.45 and 0.55 ps. CdS/MoS$_2$ spectra shows presence of both the systems in the nanocomposite, CdS bleach appears at 502 nm and MoS$_2$ excitons appear at 620 and 680 nm, similar to their pristine systems. But the intensity and rise time of the CdS bleach signal is drastically decreased in the composite, indicating toward hot carrier transfer in the system, which was confirmed from the enhanced intensity of MoS$_2$ bleach signals. The hot carrier transfer time scale was calculated to be 0.21 ps (rate constant, k_{hot} ~ 4.85 ps^{-1}). The charge carriers are also get migrated from the CdS band edges and the corresponding rate constant was found to be 0.49 ps^{-1} (2.0 ps) which is much lower than the hot carrier transfer one. Pump dependent analysis suggests that the charge migration process is immensely dependent on the pump photon energy. Increment in photon energy directly result in enhanced hot carrier injection in the MoS$_2$ high energy states. This detailed spectroscopic analysis is unique and would be extremely impactful on fabricating a 1D-2D heterojunction based optical devices, where efficient extraction of hot charge carriers plays pivotal role.

6.5. References

(1)   Ross, R. T.; Nozik, A. J. Efficiency of Hot-carrier Solar Energy Converters. *J. Appl. Phys.* **1982**, *53*, 3813-3818.

(2)   Li, Y.; Zhou, H.; Chen, Y.; Zhao, Y.; Zhu, H. Efficient Hot-Electron Extraction in Two-Dimensional Semiconductor Heterostructures by Ultrafast Resonant Transfer. *J. Chem. Phys.* **2020**, *153*, 44705.

(3)   Paul, K. K.; Kim, J.-H.; Lee, Y. H. Hot Carrier Photovoltaics in van Der Waals Heterostructures. *Nat. Rev. Phys.* **2021**, *3*, 178-192.

(4)   Shim, J.; Kang, D.-H.; Kim, Y.; Kum, H.; Kong, W.; Bae, S.-H.; Almansouri, I.; Lee, K.; Park, J.-H.; Kim, J. Recent Progress in Van Der Waals (VdW) Heterojunction-Based Electronic and Optoelectronic Devices. *Carbon N. Y.* **2018**, *133*, 78-89.

(5)   Ahn, S.; Chung, H.; Chen, W.; Moreno-Gonzalez, M. A.; Vazquez-Mena, O. Optoelectronic Response of Hybrid PbS-QD/Graphene Photodetectors. *J. Chem. Phys.* **2019**, *151*, 234705.

(6)   Wang, X.; Zhang, X.; Gao, W.; Sang, Y.; Wang, Y.; Liu, H. Self-Reduction Derived

Nickel Nanoparticles in CdS/Ni(OH)$_2$ Heterostructure for Enhanced Photocatalytic Hydrogen Evolution. *J. Chem. Phys.* **2020**, *152*, 214701.

(7) Flöry, N.; Ma, P.; Salamin, Y.; Emboras, A.; Taniguchi, T.; Watanabe, K.; Leuthold, J.; Novotny, L. Waveguide-Integrated van Der Waals Heterostructure Photodetector at Telecom Wavelengths with High Speed and High Responsivity. *Nat. Nanotechnol.* **2020**, *15*, 118-124.

(8) Li, X.; Chen, W.; Zhang, S.; Wu, Z.; Wang, P.; Xu, Z.; Chen, H.; Yin, W.; Zhong, H.; Lin, S. 18.5% Efficient Graphene/GaAs van Der Waals Heterostructure Solar Cell. *Nano Energy* **2015**, *16*, 310-319.

(9) Liu, Z.; Zhu, Y.; El-Demellawi, J. K.; Velusamy, D. B.; El-Zohry, A. M.; Bakr, O. M.; Mohammed, O. F.; Alshareef, H. N. Metal Halide Perovskite and Phosphorus Doped g-C$_3$N$_4$ Bulk Heterojunctions for Air-Stable Photodetectors. *ACS Energy Lett.* **2019**, *4*, 2315-2322.

(10) Pandey, A.; Guyot-Sionnest, P. Hot Electron Extraction From Colloidal Quantum Dots. *J. Phys. Chem. Lett.* **2010**, *1*, 45-47.

(11) Goswami, T.; Rani, R.; Hazra, K. S.; Ghosh, H. N. Ultrafast Carrier Dynamics of the Exciton and Trion in MoS$_2$ Monolayers Followed by Dissociation Dynamics in Au@MoS$_2$ 2D Heterointerfaces. *J. Phys. Chem. Lett.* **2019**, *10*, 3057-3063.

(12) Karan, N. S.; Mandal, A.; Panda, S. K.; Pradhan, N. Role of Fatty Acid in Controlling Nucleation and Growth of CdS Nanocrystals in Solution. *J. Phys. Chem. C* **2010**, *114*, 8873-8876.

(13) Liu, F.; Wang, Z.; Weng, Y.; Shi, R.; Ma, W.; Chen, Y. Black Phosphorus Quantum Dots Modified CdS Nanowires with Efficient Charge Separation for Enhanced Photocatalytic H$_2$ Evolution. *ChemCatChem* **2021**, *13*, 1355-1361.

(14) Shi, R.; Ye, H.-F.; Liang, F.; Wang, Z.; Li, K.; Weng, Y.; Lin, Z.; Fu, W.-F.; Che, C.-M.; Chen, Y. Interstitial P-Doped CdS with Long-Lived Photogenerated Electrons for Photocatalytic Water Splitting without Sacrificial Agents. *Adv. Mater.* **2018**, *30*, 1705941.

(15) Chava, R. K.; Do, J. Y.; Kang, M. Smart Hybridization of Au Coupled CdS Nanorods with Few Layered MoS$_2$ Nanosheets for High Performance Photocatalytic Hydrogen

Evolution Reaction. *ACS Sustain. Chem. Eng.* **2018**, *6*, 6445-6457.

(16)   Zhang, K.; Fujitsuka, M.; Du, Y.; Majima, T. 2D/2D Heterostructured CdS/WS₂ with Efficient Charge Separation Improving H₂ Evolution under Visible Light Irradiation. *ACS Appl. Mater. Interfaces* **2018**, *10*, 20458-20466.

(17)   Zhang, M.; Shao, Z.; Jiang, T.; Wu, X.; Zhang, B.; Zhang, X.; Xia, F.; Jie, J. Tuning Electrical and Raman Scattering Properties of Cadmium Sulfide Nanoribbons via Surface Charge Transfer Doping. *J. Phys. Chem. C* **2019**, *123*, 15794-15801.

(18)   Li, H.; Wang, X.; Xu, J.; Zhang, Q.; Bando, Y.; Golberg, D.; Ma, Y.; Zhai, T. One-Dimensional CdS Nanostructures: A Promising Candidate for Optoelectronics. *Adv. Mater.* **2013**, *25*, 3017-3037.

(19)   Deng, K.; Li, L. CdS Nanoscale Photodetectors. *Adv. Mater.* **2014**, *26*, 2619-2635.

(20)   Pal, B. N.; Ghosh, Y.; Brovelli, S.; Laocharoensuk, R.; Klimov, V. I.; Hollingsworth, J. A.; Htoon, H. 'Giant' CdSe/CdS Core/Shell Nanocrystal Quantum Dots As Efficient Electroluminescent Materials: Strong Influence of Shell Thickness on Light-Emitting Diode Performance. *Nano Lett.* **2012**, *12*, 331-336.

(21)   Yang, P.; Yan, R.; Fardy, M. Semiconductor Nanowire: What's Next? *Nano Lett.* **2010**, *10*, 1529-1536.

(22)   Kaur, G.; Saha, R.; Babu, K. J.; Shukla, A.; Ghosh, H. N. Unravelling the Underlying Hot Carrier Transfer and Relaxation Pathways in Type-1 CsPbBr₃–PbS System. *J. Phys. Chem. C* **2021**, *125*, 10516-10525.

(23)   Grimaldi, G.; Crisp, R. W.; ten Brinck, S.; Zapata, F.; van Ouwendorp, M.; Renaud, N.; Kirkwood, N.; Evers, W. H.; Kinge, S.; Infante, I.; Siebbeles, L. D. A.; Houtepen, A. J. Hot-Electron Transfer in Quantum-Dot Heterojunction Films. *Nat. Commun.* **2018**, *9*, 2310.

(24)   He, J.; Chen, L.; Wang, F.; Liu, Y.; Chen, P.; Au, C.-T.; Yin, S.-F. CdS Nanowires Decorated with Ultrathin MoS₂ Nanosheets as an Efficient Photocatalyst for Hydrogen Evolution. *ChemSusChem* **2016**, *9*, 624-630.

(25)   Yang, X.; Liu, W.; Han, C.; Zhao, C.; Tang, H.; Liu, Q.; Xu, J. Mechanistic Insights into Charge Carrier Dynamics in MoSe₂/CdS Heterojunctions for Boosted Photocatalytic

Hydrogen Evolution. *Mater. Today Phys.* **2020**, *15*, 100261.

(26)   Li, G.; Zhang, D.; Qiao, Q.; Yu, Y.; Peterson, D.; Zafar, A.; Kumar, R.; Curtarolo, S.; Hunte, F.; Shannon, S.; Zhu, Y.; Yang, W.; Cao, L. All The Catalytic Active Sites of MoS₂ for Hydrogen Evolution. *J. Am. Chem. Soc.* **2016**, *138*, 16632-16638.

(27)   Radisavljevic, B.; Radenovic, A.; Brivio, J.; Giacometti, V.; Kis, A. Single-Layer MoS₂ Transistors. *Nat. Nanotechnol.* **2011**, *6*, 147-150.

(28)   Shi, X.; Fujitsuka, M.; Kim, S.; Majima, T. Faster Electron Injection and More Active Sites for Efficient Photocatalytic H2 Evolution in g-C₃N₄/MoS₂ Hybrid. *Small* **2018**, *14*, 1703277.

(29)   Zong, X.; Wu, G.; Yan, H.; Ma, G.; Shi, J.; Wen, F.; Wang, L.; Li, C. Photocatalytic H₂ Evolution on MoS₂/CdS Catalysts under Visible Light Irradiation. *J. Phys. Chem. C* **2010**, *114*, 1963-1968.

(30)   Chang, K.; Li, M.; Wang, T.; Ouyang, S.; Li, P.; Liu, L.; Ye, J. Drastic Layer-Number-Dependent Activity Enhancement in Photocatalytic H₂ Evolution over nMoS₂/CdS (n ≥ 1) Under Visible Light. *Adv. Energy Mater.* **2015**, *5*, 1402279.

(31)   Yin, X.-L.; Li, L.-L.; Jiang, W.-J.; Zhang, Y.; Zhang, X.; Wan, L.-J.; Hu, J.-S. MoS₂/CdS Nanosheets-on-Nanorod Heterostructure for Highly Efficient Photocatalytic H₂ Generation under Visible Light Irradiation. *ACS Appl. Mater. Interfaces* **2016**, *8*, 15258-15266.

(32)   Iqbal, S.; Pan, Z.; Zhou, K. Enhanced Photocatalytic Hydrogen Evolution from in Situ Formation of Few-Layered MoS₂/CdS Nanosheet-Based van Der Waals Heterostructures. *Nanoscale* **2017**, *9*, 6638-6642.

(33)   Wu, A.; Tian, C.; Jiao, Y.; Yan, Q.; Yang, G.; Fu, H. Sequential Two-Step Hydrothermal Growth of MoS₂/CdS Core-Shell Heterojunctions for Efficient Visible Light-Driven Photocatalytic H₂ Evolution. *Appl. Catal. B Environ.* **2017**, *203*, 955-963.

(34)   Chen, J.; Wu, X.-J.; Yin, L.; Li, B.; Hong, X.; Fan, Z.; Chen, B.; Xue, C.; Zhang, H. One-Pot Synthesis of CdS Nanocrystals Hybridized with Single-Layer Transition-Metal Dichalcogenide Nanosheets for Efficient Photocatalytic Hydrogen Evolution. *Angew. Chemie Int. Ed.* **2015**, *54*, 1210-1214.

(35)   Yan, Z.; Du, L.; Lee Phillips, D. Multilayer Core–Shell MoS$_2$/CdS Nanorods with Very High Photocatalytic Activity for Hydrogen Production under Visible-Light Excitation and Investigation of the Photocatalytic Mechanism by Femtosecond Transient Absorption Spectroscopy. *RSC Adv.* **2017**, *7*, 55993-55999.

(36)   Cho, J.; Suwandaratne, N. S.; Razek, S.; Choi, Y.-H.; Piper, L. F. J.; Watson, D. F.; Banerjee, S. Elucidating the Mechanistic Origins of Photocatalytic Hydrogen Evolution Mediated by MoS$_2$/CdS Quantum-Dot Heterostructures. *ACS Appl. Mater. Interfaces* **2020**, *12*, 43728-43740.

(37)   Lou, Z.; Zhu, M.; Yang, X.; Zhang, Y.; Whangbo, M.-H.; Li, B.; Huang, B. Continual Injection of Photoinduced Electrons Stabilizing Surface Plasmon Resonance of Non-Elemental-Metal Plasmonic Photocatalyst CdS/WO$_{3-x}$ for Efficient Hydrogen Generation. *Appl. Catal. B Environ.* **2018**, *226*, 10-15.

(38)   Goswami, T.; Bhatt, H.; Babu, K. J.; Kaur, G.; Ghorai, N.; Ghosh, H. N. Ultrafast Insights into High Energy (C and D) Excitons in Few Layer WS$_2$. *J. Phys. Chem. Lett.* **2021**, *12*, 6526-6534.

(39)   Jiang, Z.-J.; Kelley, D. F. Hot and Relaxed Electron Transfer from the CdSe Core and Core/Shell Nanorods. *J. Phys. Chem. C* **2011**, *115*, 4594-4602.

(40)   Wolff, C. M.; Frischmann, P. D.; Schulze, M.; Bohn, B. J.; Wein, R.; Livadas, P.; Carlson, M. T.; Jäckel, F.; Feldmann, J.; Würthner, F.; Stolarczyk, J. K. All-in-One Visible-Light-Driven Water Splitting by Combining Nanoparticulate and Molecular Co-Catalysts on CdS Nanorods. *Nat. Energy* **2018**, *3*, 862-869.

(41)   Wu, K.; Zhu, H.; Liu, Z.; Rodríguez-Córdoba, W.; Lian, T. Ultrafast Charge Separation and Long-Lived Charge Separated State in Photocatalytic CdS–Pt Nanorod Heterostructures. *J. Am. Chem. Soc.* **2012**, *134*, 10337-10340.

(42)   Klimov, V. I. Optical Nonlinearities and Ultrafast Carrier Dynamics in Semiconductor Nanocrystals. *J. Phys. Chem. B* **2000**, *104*, 6112-6123.

(43)   Goswami, T.; Yadav, D. K.; Bhatt, H.; Kaur, G.; Shukla, A.; Babu, K. J.; Ghosh, H. N. Defect-Mediated Slow Carrier Recombination and Broad Photoluminescence in Non-Metal-Doped ZnIn$_2$S$_4$ Nanosheets for Enhanced Photocatalytic Activity. *J. Phys. Chem. Lett.* **2021**, *12*, 5000-5008.

(44)   Okuhata, T.; Katayama, T.; Tamai, N. Ultrafast and Hot Electron Transfer in CdSe QD–Au Hybrid Nanostructures. *J. Phys. Chem. C* **2020**, *124*, 1099-1107.

(45)   Choudhury, B.; Dey, M.; Choudhury, A. Shallow and Deep Trap Emission and Luminescence Quenching of TiO$_2$ Nanoparticles on Cu Doping. *Appl. Nanosci.* **2014**, *4*, 499-506.

(46)   Saigal, N.; Sugunakar, V.; Ghosh, S. Exciton Binding Energy in Bulk MoS$_2$: A Reassessment. *Appl. Phys. Lett.* **2016**, *108*, 132105.

(47)   Strait, J. H.; Nene, P.; Rana, F. High Intrinsic Mobility and Ultrafast Carrier Dynamics in Multilayer Metal-Dichalcogenide MoS$_2$. *Phys. Rev. B* **2014**, *90*, 245402.

(48)   Mandal, S.; Mukherjee, S.; De, C. K.; Roy, D.; Ghosh, S.; Mandal, P. K. Extent of Shallow/Deep Trap States beyond the Conduction Band Minimum in Defect-Tolerant CsPbBr$_3$ Perovskite Quantum Dot: Control over the Degree of Charge Carrier Recombination. *J. Phys. Chem. Lett.* **2020**, *11*, 1702-1707.

Chapter 7

Transient Investigation of Enhanced Photocatalytic Activity in ZnIn$_2$S$_4$ Nanosheets Following Elemental Doping
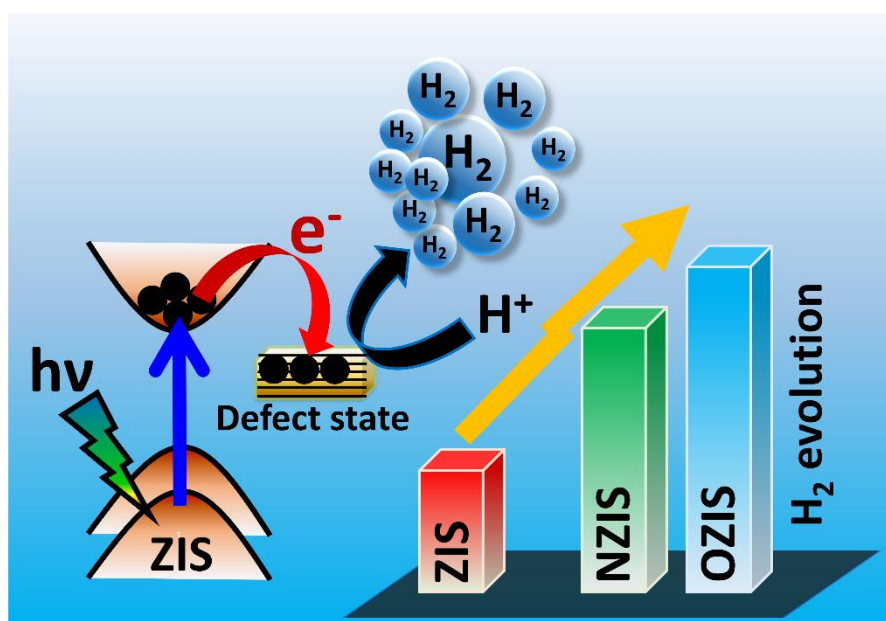
Adapted with permission from Goswami T., Yadav D. K., Bhatt H., Kaur G., Shukla A., Babu K. J. and Ghosh H. N., Defect-Mediated Slow Carrier Recombination and Broad Photoluminescence in Non-Metal-Doped ZnIn$_2$S$_4$ Nanosheets for Enhanced Photocatalytic Activity, *J. Phys. Chem. Lett.*, 2021, 12, 5000-5008. **Copyright 2021 American Chemical Society**.

7.1. Introduction

Photocatalytic H$_2$ evolution stands out to be the next possible alternative source of energy ahead of the scientific community in course of replacing non-renewable and toxic energy sources like coal, petroleum, etc.[1] Numerous semiconducting and metallic systems [2,3] are being used to convert earth-abundant waters into chemical fuel H$_2$ using solar energy. Though these materials show immense potential, we are far from the stage where we can commercialize this energy. At this instant, proper knowledge of the photophysical processes, like photoinduced behaviour of charge carriers and subsequent relaxation processes involved in the phenomena of H$_2$ evolution would be extremely helpful in designing efficient and cost-effective photocatalytic materials.

Currently, ZIS is considered to be one of the best photocatalysts due to its low cost, high stability, low toxicity and tunable bandgap (2.06 eV-2.85 eV).[4-6] It offers a wide range of applications like charge storage, solar cell, photodetectors, photo-electrochemical and photocatalysis.[7-12] ZIS nanosheets usually exhibit in two crystal phases; cubic and hexagonal, where hexagonal phase happens to show better photocatalytic performance as compared to its cubic counterpart.[13] In bulk ZIS systems, the photocatalytic activity is hampered due to both surface and bulk recombination of photo-excited charge carriers.[14] While in the atomically thin system these bulk recombinations are diminished riding upon the emerging quantum confinement phenomena.[15,14] Particularly, in the few layer ZIS nanosheets, a large fraction of surface Sulphur atoms are exposed in the sunlight and offer more active sites. Reduced diffusion length of charge carriers helps in rapid transport towards the surface-active sites before recombination. As a result, few layer ZIS shows much better photocatalytic activity than bulk.[16,17] However, it is often observed that fast recombination of charge carriers limits the photocatalytic performance even in few layer ZIS nanosheets.[4] In this scenario elemental doping emerged to be an effective strategy to improve the photocatalytic activity by surface modification and tuning the electronic structure.[18] Various metallic cations like Cu^{2+}, Ni^{2+} etc.[19-21] are being doped to enhance the light absorption range which helps in the improvement of photocatalytic activity. However, there is a probability of trapping the photoinduced charge carriers in the metal centers as well, which can diminish the photocatalytic yield.[22] Contrary to that, elemental (O, N, P, etc.) doping is more preferable for better photocatalytic performance.[16] Recently, O- and N-doped ZIS systems are reported to showcase much higher photocatalytic activity than that of pristine ZIS systems. Yang *et. al.* reported that O-doped ZIS exhibit 4.5

times higher photocatalytic activity than pristine ZIS.[5] Furthermore, Du *et. al.*, demonstrated 13.8 times improved photocatalytic hydrogen evolution rate (11086 μmolg^{-1}h^{-1}) in N-doped ZIS as compared to that of pristine ZIS.[16]

Now, to understand the emergence of photocatalytic activity in few layer ZIS and the effect of doping, it is really important to study its charge carrier characteristics through spectroscopical investigation. Though, ZIS is a widely used material in photocatalytic application, detailed knowledge of charge carrier photo-physics is still unexplored. Ultrafast transient absorption (TA) spectroscopy is a powerful technique to monitor the dynamics of charge carriers and their ultrafast radiative and non-radiative recombination pathways in optically excited materials. To date only a few reports are available, where TA spectroscopy is applied to study intrinsic optical properties in ZIS nanosheets.[23,5,16] They addressed the effect of defect states in the enhanced photocatalytic activity of ZIS, which sits well with the reports where defect states help in boosted photocatalysis.[24-26] However, these reports discuss charge carrier dynamics only for a particular wavelength, which is neither complete nor conclusive. To understand the comprehensive charge carrier characteristics in a system, it is really important to monitor it in a wide range of the electromagnetic spectrum. In fact, to make any rational comment on the effect of inter bandgap states, a separate analysis should be carried out for band edge states and inter bandgap states, which is completely missing in the literature. In this scenario, detailed TA spectroscopy of ZIS is the need of the hour for a complete understanding of its charge carrier characteristics and corresponding photocatalytic activity.

In this chapter, we have presented a comprehensive spectroscopic study of charge carrier dynamics in pristine ZIS and its O- and N-doped counterparts using femtosecond broadband pump-probe spectroscopy. The materials were successfully synthesized using an easy and robust hydrothermal route. XPS measurements were carried out to analyse the effect of non-metal doping in the pristine ZIS system. The photocatalytic activity was seen to be substantially enhanced in doped ZIS nanosheets. Doped ZIS systems possess enhanced charge carrier population and higher charge carrier lifetime to be used for H$_2$ evolution, as probed by steady state PL and ultrafast transient studies. Transient absorption spectroscopy demonstrated that the reduction phenomenon corresponding to the H$_2$ evolution process occurs mainly from the inter-bandgap defect states of ZIS, not from the conduction band edge.

7.2. Synthesis and experimental techniques

7.2.1. Synthesis of ZIS nanosheets

The ZIS nanosheets were synthesized via typical hydrothermal route. Hydrothermal method is a versatile and eco-friendly technique to synthesize photocatalytic materials. A solution of 30 mL H_2O with stoichiometric amount of $ZnCl_2$ (1.0 mmol; 0.136g), $InCl_3$ (2.0 mmol; 0.442g) and excessive thioacetamide (TAA) (8.0 mmol; 0.601g) were sonicated for 15 min. Then, the solution was poured into 50 mL Teflon-lined stainless-steel autoclave and kept in oven at 180 °C for 20 h. After 20 h, the autoclave was cooled down naturally. The yellow product was obtained by centrifugation at 8000 rpm. The obtained precipitate was washed with absolute ethanol and distilled water several times to remove unreacted impurities. Finally, the precipitate was dried at 80 °C for 6 h in oven.

7.2.2. Synthesis of OZIS nanosheets (O-doping)

For the synthesis of OZIS, $ZnCl_2$ (1.0 mmol; 0.136g), $InCl_3$ (2.0 mmol; 0.442g) and excessive thioacetamide (TAA) (8.0 mmol; 0.601g) and 0.2 g PVP were mixed in 30 ml water-ethanol (1:1) with vigorous stirring for 10 min. Then, the solution was poured into 50 mL Teflon-lined stainless-steel autoclave and kept in oven at 180 °C for 20 h. After 20 h, the autoclave was cooled down naturally. The pale-yellow product was obtained by centrifugation at 8000 rpm. The obtained precipitate was washed with absolute ethanol and distilled water several times to remove unreacted impurities. Finally, the precipitate was dried at 80 °C for 6 h in oven.

7.2.3. Synthesis of NZIS nanosheets (N-doping)

For synthesis of NZIS, $ZnCl_2$ (1.0 mmol; 0.136g), $InCl_3$ (2.0 mmol; 0.442g) and excessive thioacetamide (TAA) (8.0 mmol; 0.601g) were mixed in 30 ml DMF-water (3:1) with vigorous stirring for 10 min. Then, the solution was poured into 50 mL Teflon-lined stainless-steel autoclave and kept in oven at 180 °C for 20 h. After 20 h, the autoclave was cooled down naturally. The yellow product was obtained by centrifugation at 8000 rpm. The obtained precipitate was washed with absolute ethanol and distilled water several times to remove unreacted impurities. Finally, the precipitate was dried at 80 °C for 6h in oven.

7.2.4. Characterization

The powder-XRD measurements of the samples were acquired on the BRUKER D8 ADVANCE with Cu-Kα radiation (λ = 1.542 Å). The morphology of the samples was examined by using Transmission Electron Microscope (TEM, JEOL JEM 2100) operating at

an accelerating voltage of 200 kV. XPS measurements were carried out on an ESCALAB 250 photoelectron spectrometer (Thermo Fisher Scientific) at 2.4 x 10^{-10} mbar using a monochromatic Al Ka x-ray beam (1486.60 eV). The steady state absorption spectra were recorded with Shimadzu UV-2600 UV-vis spectrophotometer. Photoluminescence measurements were carried using Fluorolog 3-221 fluorimeter.

7.2.5. Evaluation of photocatalytic hydrogen evolution activity

Photocatalytic H$_2$ evolution was evaluated in a closed glass beaker under visible-light irradiation using 395 nm cut-off filter with 400-W Xe lamp as a light source for 5h. In typical process, 10 mg catalyst was suspended in 50 ml water-TEOA (9:1) solution. The solution was sonicated for 30 min and N$_2$ gas purged to remove the dissolved gas from solution. Again, at the time of photocatalytic process, the reaction mixture was continuously stirred by magnetic stirring. The evolved H$_2$ gas was analysed by gas chromatography at certain time intervals.

7.2.6. Femtosecond transient absorption spectroscopy

The transient setup includes a Ti: sapphire amplifier system (Astrella, Coherent, 800 nm, 3mJ/pulse energy, ~ 35 fs pulse width and 1 kHz repetition rate) and Helios Fire pump-probe spectrometer. The output laser pulses were cleaved into pump (95% of the output) and probe (remaining 5%) laser pulses using requisite beam splitters. Optical Parametric Amplifier (OPerA-SOLO) was used to produce different pump wavelengths. A delay stage is operating in path of probe beam to maintain a perfect delay between pump and probe throughout the experimental procedure. Monochromatic probe light was converted into UV-Visible probe pulses passing through CaF$_2$ crystal. This Probe pulse transmits through sample dispersion and falls upon fibre coupled CMOS detectors connected with the computer system. Surface explorer software was used to fit the collected data.

7.3. Results and discussion

7.3.1. Basic characterisation and steady state optical measurements ZIS nanosheets and its doped counterparts

Herein, ZIS nanosheets were synthesized using hydrothermal method, a simple, inexpensive, and mass production technique for the synthesis of photocatalysts. Subsequently, these pristine ZIS systems were doped with 'O' (OZIS) and 'N' (NZIS) to realize the effect of non-metal doping on the intrinsic properties of ZIS semiconductor.

XRD

Elemental doping modifies the crystal structure of any pristine material which will eventually reconstruct its electronic structure[11]. Thus, to study the phase and crystallographic features of these nanosheets, powder XRD was employed. **Figure 7.1a** compares the XRD patterns of ZIS nanosheets before and after non-metal doping. The diffraction peaks in ZIS XRD pattern confirms its hexagonal crystal structure (JCPDS 01-089-3963) with P-3ml space group. The diffraction peaks at 2θ values of 21.6°, 27.5°, 30.5°, 37.8°, 47.2°, 52.4°, and 55.6° could be assigned to (006), (102), (104), (108), (110), (112), and (022) planes of ZIS. No peaks corresponding to ZnS and In_2S_3 were observed, which confirms the purity of the prepared material. The XRD patterns of NZIS and OZIS suggest that doped ZIS still maintained its hexagonal crystal structure even after doping, confirming that the solvents; ethanol- water and DMF did not affect the crystal structure of ZIS[16]. The peak at 47.4 ° corresponding to (110) plane of ZIS is shifted to higher angles in NZIS and OZIS, indicating the successful incorporation of N and O dopant in ZIS. Here in smaller atomic size of N (0.71 Å) and O (0.64 Å) as compared to S (1.04 Å) might be playing a significant role.[16,27]
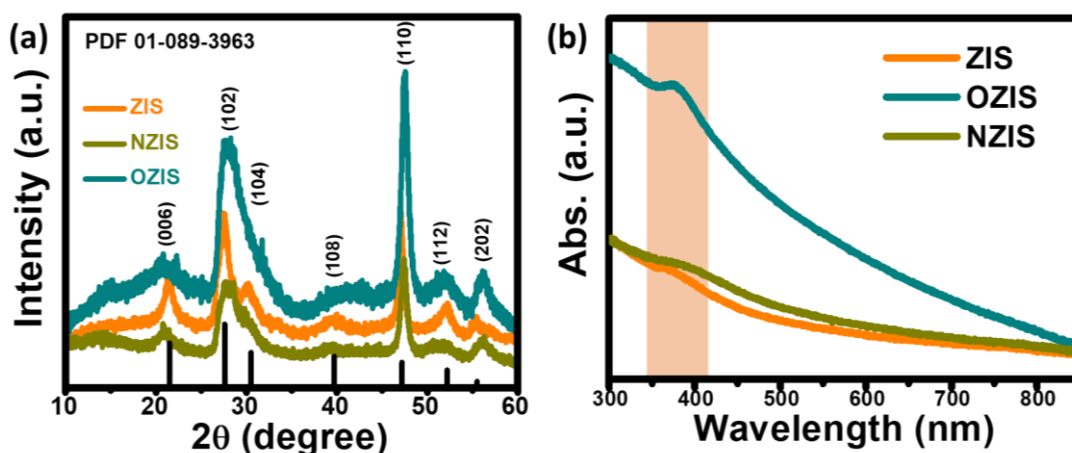
Figure 7.1: (a) Powder XRD patterns and **(b)** steady state optical absorption spectra of ZIS nanosheets, before and after N- and O-doping.

Steady state absorption spectroscopy

In **Figure 7.1b** we have presented steady state absorption spectra of ZIS, NZIS and OZIS. Interestingly, all these systems display a significant absorption peak around 400 nm, with an absorption tail extended up to 800 nm. The absorption spectrum of ZIS is in good accordance

bandgap of these systems as 2.65, 2.53 and 2.70 eV for ZIS, NZIS and OZIS respectively, from the Tauc plot (**Figure 7.2**). This means that the optical band edge must be lying in the 460-490 nm region of the electromagnetic spectra. Hence 400 nm hump must be originating from higher energy excitonics transitions triumphing over the lower energy transitions, which is already discussed in case of ZIS nanosheets.[29] Following O doping the absorption of ZIS is greatly enhanced, which indicates presence of larger number of defect states (active sites) in the system. This is also observable for N-doping case, though the intensity is not that high.
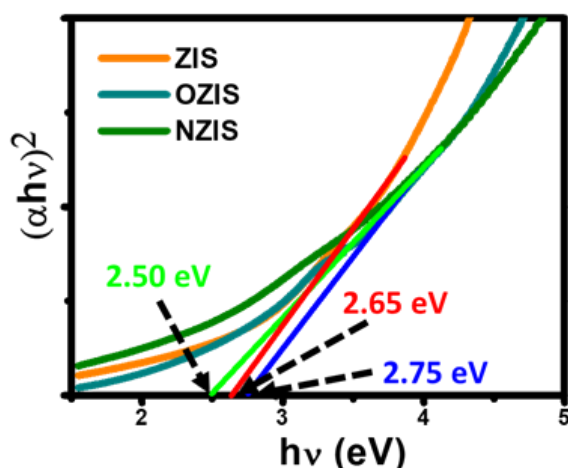
Figure 7.2: Tauc plot of ZIS, NZIS and OZIS for the calculation of optical band gap.

TEM and AFM study

Further to identify the morphology of the as prepared systems, TEM was employed. The TEM morphological features of ZIS, OZIS and NZIS are shown in **figure 7.3a, b, c** respectively. TEM images depict layered structure of ZIS and it retains nanosheet morphology in the doped samples as well. HRTEM images (**Figure 7.3d, e, f**) of all samples displayed the lattice fringes with a d-spacing of 0.32 nm corresponding to (102) plane of hexagonal ZIS. However, there is numerous structural defects were observed in the surface of doped ZIS nanosheets (indicated by red dashed circles in **figure 7.3e, f**). Furthermore, AFM studies were carried out to study the thickness of the nanosheets. The thickness of ZIS, OZIS and NZIS was found be *ca.* 5.9 nm, 4.4 nm, and 6.3 nm, respectively (**Figure 7.3g, h, i**). The thickness of a monolayer ZIS is reported to be *ca.*1.1-1.3 nm.[30] According to that, ZIS OZIS and NZIS systems exhibit 5-6 layers, 3-4 layers and 5-6 layers, respectively. Capping agent PVP, used for OZIS synthesis, might be playing a role in decreased thickness of these nanosheets, as it restricts the agglomeration of particles.[31]
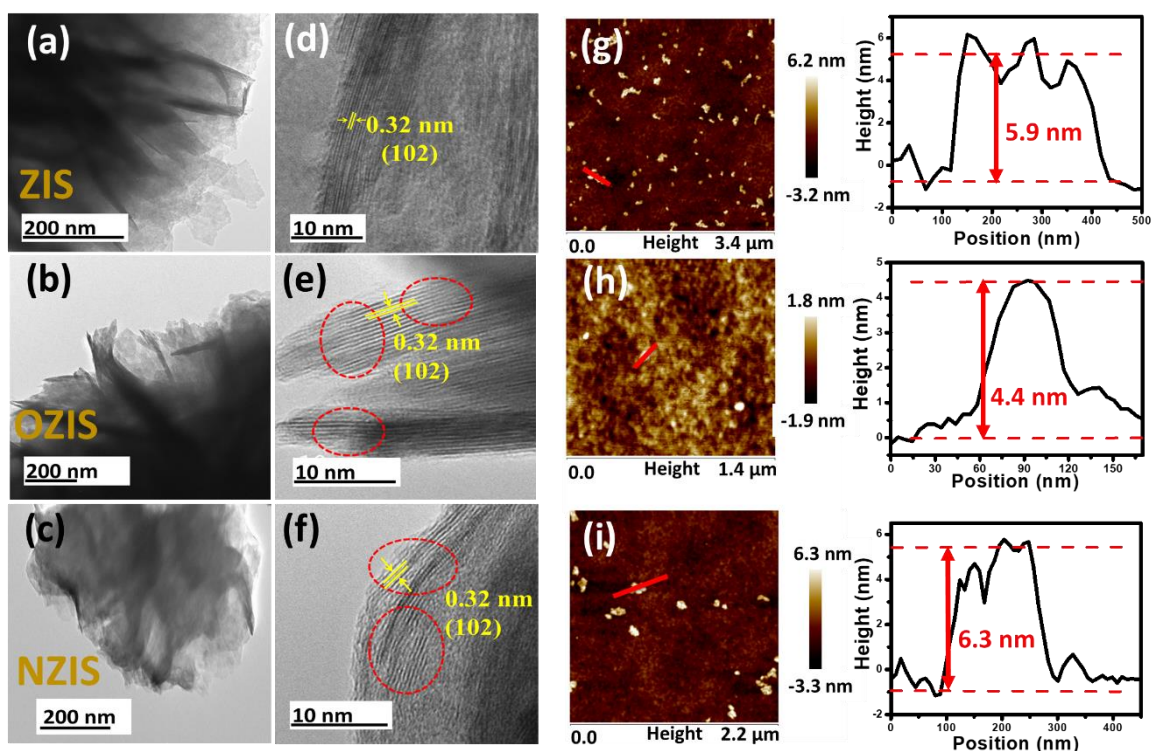
Figure 7.3: TEM images of **(a)** ZIS, **(b)** OZIS and **(c)** NZIS nanosheets. HRTEM images of **(d)** ZIS, **(e)** OZIS and **(f)** NZIS nanosheets representing (102) plane of ZIS. Red circles represent the discontinuity in the lattice fringes. AFM topographic images of **(g)** ZIS, **(h)** NZIS and **(i)** OZIS nanosheets on top of SiO₂/Si substrate, together with the cross-sectional height profiles along the red line in the AFM image. Three rows designate ZIS, OZIS and NZIS characterizations respectively from the top.

XPS measurements and H₂ evolution

Now, in pursuit of direct probing of O- and N-doping effect in ZIS crystals, XPS were carried out. In general, XPS is used to analyse elemental oxidation states and corresponding chemical compositions in any composite system. XPS analysis affirmed the presence of Zn, In and S in all three systems (**figure 7.4**). The high-resolution spectra of Zn present in ZIS nanosheet display two peaks at binding energy 1021.7 eV and 1044.8 eV which can be assigned to Zn $2p_{3/2}$ and Zn $2p_{1/2}$, respectively. The energy difference between these two peaks is affirmed the dominance of Zn^{2+} in the ZIS nanosheet. However, the binding energy of Zn 2p for NZIS nanosheet (1021.6 eV and 1044.7 eV) and OZIS nanosheet (1021.2 eV and 1044.2 eV) are slightly lower than the ZIS. Binding energies of In 3d in ZIS nanosheet show a pair of peaks at 444.9 eV and 452.4 eV which correspond to In $3d_{5/2}$ and In $3d_{3/2}$, respectively. The high-

resolution spectrum of S 2p in ZIS nanosheet clearly shows peaks at 161.7 eV and 162.7 eV, which can be assigned to S 2p $_{3/2}$ and S 2p$_{1/2}$, respectively and certified the (-2)-oxidation state of S. The small changes in the binding energies of peaks can be observed in the NZIS and OZIS samples after doping with high electronegative element N and O, which might be due to change in the coordination environment due to displacement of S from the lattice.

In **figure 7.4d** the positions of the VBM were calculated from the tangent drawn at the onset of the normalized XPS spectra. The VBM was found to be uplifted in case of non-metal doping with respect to that of pristine ZIS system.
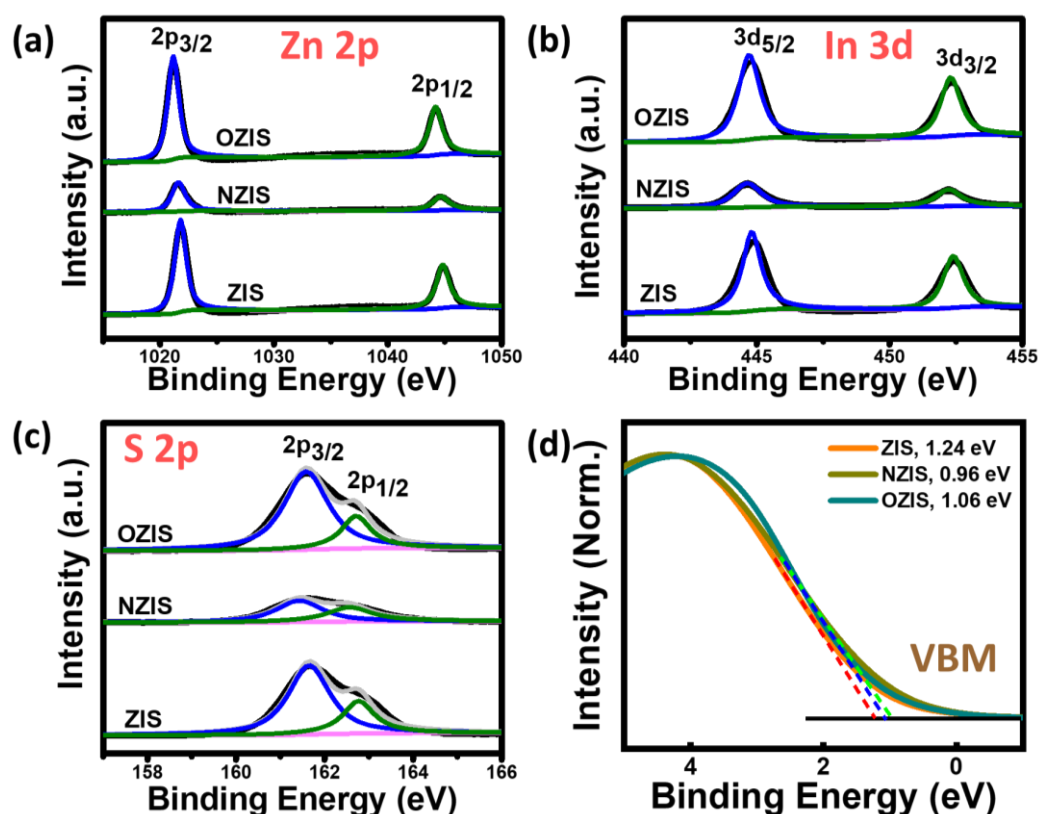
Figure 7.4: XPS spectra of (**a**) O 1S in pristine ZIS and OZIS, (**b**) N 1S in NZIS**,** along with (**c**) S 2P in ZIS, OZIS and NZIS. (**d**) Determination of valence band positions of ZIS, NZIS and OZIS from the normalized XPS spectra.

In **figure 7.5a** we plotted the XPS spectra corresponding to both ZIS and OZIS, which show two significant peaks at 531.6 eV and 532.4 eV, corresponding to the hydroxy oxygen and adsorbed water.[5] Along with these two peaks, a new peak emerges at 530.9 eV in case of OZIS, which can be attributed to the O^{2-} binding energy.[32,33] This illustrates the existence of lattice oxygen in the OZIS nanosheet and confirms effective doping of oxygen atoms in the ZIS structure. Similarly, in NZIS, there exist a doublet peak at 399.3 eV and 400.1 eV (**Figure**

7.5b), resulting from the Zn-N or In-N bonds and N species. The content of N and O are estimated to be approximately 7.3% and 5.3% in the NZIS and OZIS nanosheet from the XPS characterization.
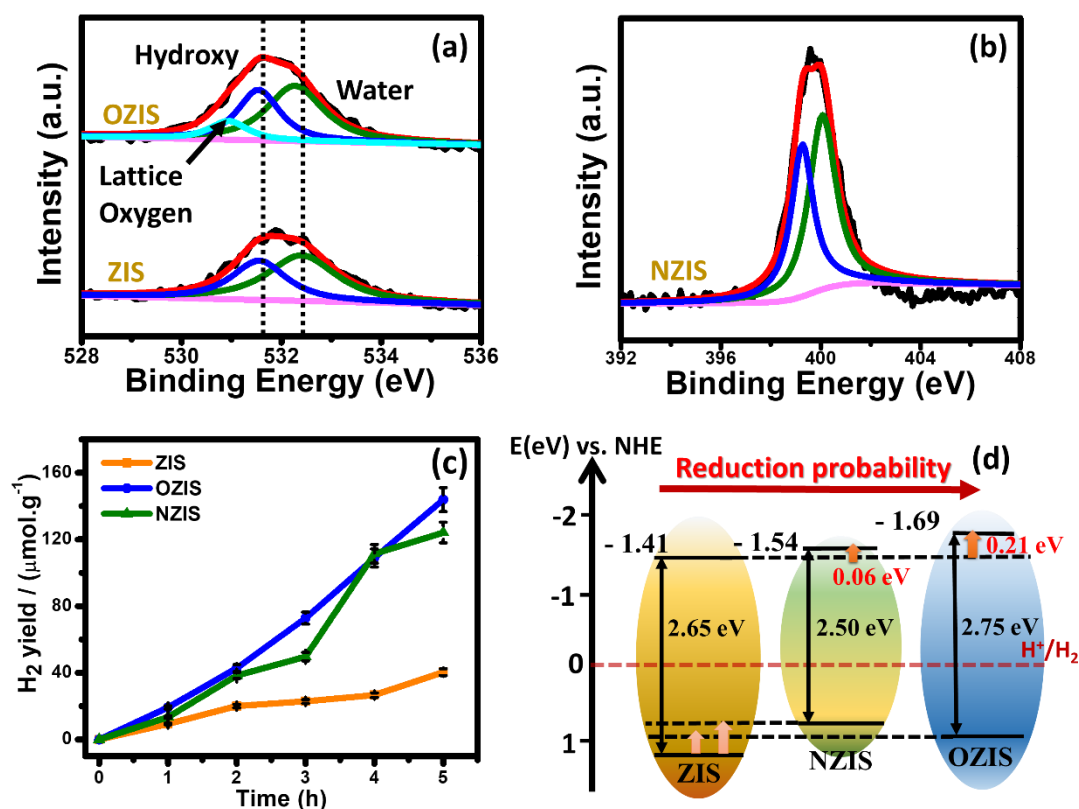
Figure 7.5: XPS spectra of **(a)** O 1S in pristine ZIS and OZIS, along with **(b)** N 1S in NZIS. **(c)** H_2 evolution yield of ZIS, NZIS and OZIS after visible light irradiation, with cut off filter at 395 nm. The figure includes error bar as well. **(d)** Respective energy level positions of ZIS, before and after doping, calculated from both XPS spectra and tauc plot.

The photocatalytic activity of these systems in terms of efficient evolution of H_2 was being monitored under the irradiation of visible light ($\lambda \geq 395$ nm). In **figure 7.5c** the pristine ZIS nanosheets demonstrated 40.5 µmol. g^{-1} H_2 generation over 5h illumination. This H_2 evolution activity is greatly enhanced following non-metal doping in the ZIS systems. OZIS and NZIS systems undergo almost 3-fold increment in the photocatalytic activity, quite well corroborating with the earlier reports.[5,16] We found O doped ZIS systems to be the best photocatalyst among all three. In **figure 7.5d** we presented the relative band structure positions of all the systems with the help of UV-Vis absorption and XPS spectra. The VBM position of the ZIS, NZIS and OZIS nanosheets were found to be 1.24 eV, 0.96 eV and 1.06 eV in earlier discussion (**Figure 7.4d**). The CBM of ZIS, NZIS and OZIS nanosheet was then calculated to

be -1.41 eV, -1.54 eV and -1.69 eV, respectively combining optical bandgap and VBM position. Therefore, N and O doping leads to the uplifting of the CBM of NZIS and OZIS approximately 0.06 eV and 0.21 eV, respectively as compared to pristine ZIS, which is schematically illustrated in **figure 7.5d**. This leads to the increment in the probability of photoreduction for H_2 evolution of ZIS system. Enhanced photoreduction potential might be playing an important role in effective formation of H_2 in the doped systems.

Photoluminescence (PL)

Now, we will try to understand the enhancement of photocatalytic activity with the help of steady state spectroscopy, where the interaction of light and matter can be directly visualized. PL spectra can be used to monitor the behaviour of photogenerated carriers, also it can introspect the effect of dopant in the crystal structure of a system. **Figure 7.6a** represents the PL spectra of ZIS, OZIS and NZIS following photoexcitation of 350 nm light. ZIS PL spectrum comprises of a strong peak around 420 nm, along with a broad luminescence extended beyond 700 nm. Correlating with the UV-Vis absorption data of ZIS, we can conclude that 420 nm peak must be originating from direct recombination of photogenerated electrons from the CBM of ZIS towards its VBM.
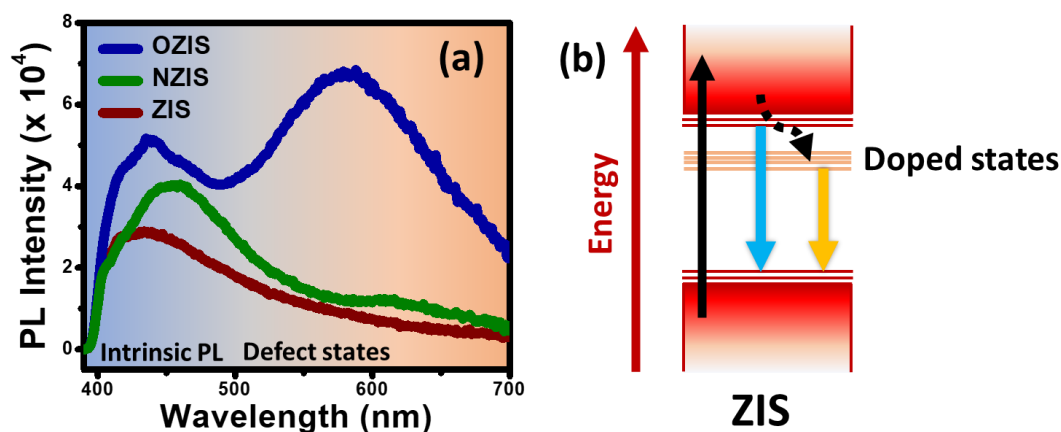
Figure 7.6: (a) Steady state PL spectra of ZIS, NZIS and OZIS after 350 nm excitation. Blue and red background of the spectra separates the luminescence of these systems into two parts: intrinsic ZIS PL and defect state induced PL. **(b)** The emergence of photoluminescence in ZIS band structure in doped condition. Blue and yellow arrow represent photoluminescence arising from CBM and defect states respectively.

This peak is very broad itself and can be deconvoluted into three peaks in 400-465 nm region (**figure 7.7**). These three peaks correspond to the intrinsic photoluminescence of ZIS, along

with two defect state mediated transitions. These bands correspond to the different transitions in ZIS electronic band structure[29]. Presence of broad PL spectrum in the red region indicates towards closely spaced defect states in the inter-bandgap region of ZIS. With O-doping, the PL spectrum undergoes almost 2-fold increment in the intensity, which is possibly the resultant of enhancement of charge carriers in the system.
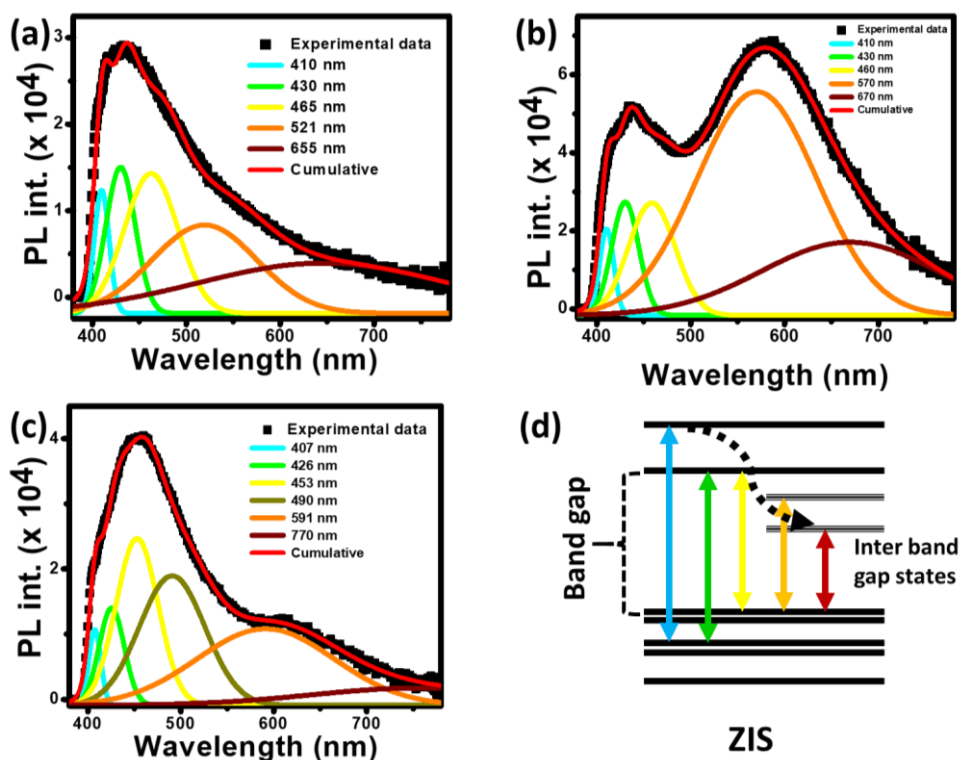
Figure 7.7: Deconvoluted PL spectra of **(a)** ZIS, **(b)** OZIS and **(c)** NZIS. **(d)** Simple energy band diagram of ZIS, representing probable transitions of pristine ZIS system for the emergence of broad PL spectrum.

Interestingly, the OZIS spectrum shows the emergence of another strong peak around 583 nm. This could be the direct evidence of O-doping induced defect states in the system. The photogenerated carriers are being trapped in these newly originated defect states and recombines with the valence band holes in order to generate this PL peak. Higher intensity of defect mediated PL signal as compared to the pristine PL of the system indicates towards the efficient trapping of photogenerated charge carriers in the O-doped systems. In NZIS, the PL signal intensity also increases as compared to that of pristine ZIS. However, both the intrinsic and defect induced PL signal show significant red shift in the NZIS PL spectrum. Hence in both the cases, doping induces defect states in the ZIS inter-bandgap region can modulate the

charge carrier population in the system, which can eventually influence photocatalytic activity of the material.

7.3.2. Transient study of pristine ZIS

Charge carrier population and the lifetime of photo-excited charge carriers are the key factors in evaluation of photocatalytic activity of any material. TA spectroscopy is known to be one of the most powerful technique for monitoring real time charge carrier characteristics in any condensed matter. In this work, ultrafast TA spectroscopy is utilized to study ultrafast charge carrier dynamics of ZIS nanosheets, before and after non-metal doping, to visualize possible mechanistic pathway involved for photocatalytic H$_2$ evolution in ZIS. In **figure 7.8a**, TA spectra of pristine ZIS systems are represented over a wide range of pump-probe delay time, after photo-excitation at 300 nm pump. The spectra include a strong photo-induced bleach signal peaking around 411 nm which is far from the optical bandgap of ZIS (2.65 eV, 468 nm). With the implication of non-resonant high energy pump photons (300 nm, 4.13eV), valence band electrons are excited to higher order energy in the conduction band of ZIS. Here in TA spectroscopy, the bleach signal corresponds to the phase space filling of energy band states and the maximum bleach intensity usually originates from the band edge states. However, in the present studies, the bleach peak signal originates from a higher energy band (411 nm, 3.02 eV). Previously, I. G. Stamov et al. reported several optical signatures in ZIS polytypes for direct transitions in Γ space of ZIS band structure.[29] They found that the band edge transition originating from VBM and CBM is not observable in room temperature. Rather, the 1st peak in the absorption spectra corresponds to the transitions occurring within higher energy valence band and CBM (**figure 7.1b**). This is also comparable to our bleach position (matches with steady state absorption and PL as well). Hence, it is safe to assume that the bleach maxima observed in our system does not correspond to the band edge excitons, rather originates from higher energy excitonic transitions. Along with this bleach maxima, a weak and broad bleach signal appear which extended up to 550 nm in the transient spectrum. This is possibly arising from closely spaced defect states near the valence band or conduction band, which was also visible as strong luminescence around 583 nm in PL spectra. We will further refer this signal as defect induced bleach (DIB) signal. In ZIS systems, TA bleach is dominated by electrons as effective mass of holes are much higher than electrons in the system.[34] So, the DIB signals must be originating from localized defect states near the conduction band (**figure 7.8b**). These

defect states are placed well above the H_2 reduction potential (according to **figure 7.5d**) and can easily take part in the H_2 evolution process.
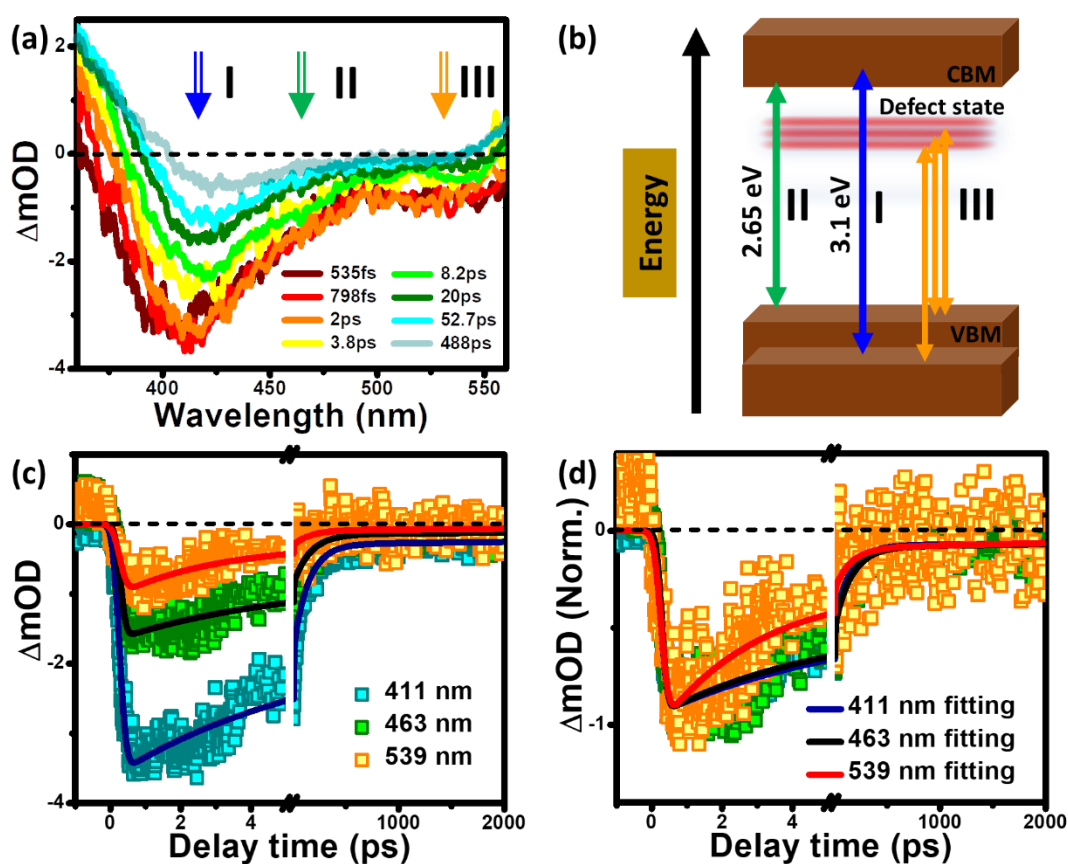
Figure 7.8: **(a)** Transient absorption spectra of pristine ZIS nanosheets, spreading over visible and near-UV region, plotted as a function of different pump probe delay time, upon photoexcitation at 300 nm laser pulses with 200 $\mu J/cm^2$ fluence. **(b)** Optical band structure of ZIS nanosheets. **(c)** Transient decay dynamic profiles of ZIS nanosheets in different probe wavelength: at 411 nm, 463 nm, and 539 nm. **(d)** Normalized decay dynamics of ZIS nanosheets at 411 nm, 463 nm, and 539 nm**.**

To further study the characteristics of the charge carriers in different regions the spectrum we choose three different wavelengths in the TA spectra, at 411 nm (bleach maxima), at 463 nm (optical band edge calculated from the Tauc plot) and at 539 nm (DIB). The dynamic profiles are fitted with multi-exponential functions and plotted in **figure 7.8c**. The fitting components are listed in **Table 7.1**. The kinetic profiles of 411 and 463 nm follow similar route (**figure 7.8d**), whereas the 539 nm kinetics is comparatively faster. This again confirms that the charge carriers involved with the DIB signal are very different from the charge carriers in the

maximum bleach region. Faster decay channel for this bleach indicates that the signal originates from charge carrier population in the native defect states of ZIS.

Table 7.1. Transient fitting components of ZIS for 300 nm pump excitation monitoring at different wavelength of the spectra.

Probe wavelength, nm	Growth		Decay	
	τ_1, ps	τ_2, ps	τ_3, ps	τ_4, ns
411	0.15	5.8 (49.1 %)	144 (42.9 %)	> 1 ns (8 %)
463	0.13	4.7 (46.6 %)	159 (44.6 %)	> 1 ns (8.8 %)
539	0.15	2.9 (69.6 %)	153 (21.5 %)	> 1 ns (8.9 %)

7.3.3. Transient study of OZIS and NZIS

Now, to find out the effect of non-metal doping on charge carrier behaviour of ZIS, TA spectroscopy is employed on both OZIS and NZIS. The TA spectra of OZIS and NZIS are presented in **figure 7.9a, b** following 300 nm pump excitation. In OZIS, the signal intensity has considerably increased (~ 2-fold increment) as compared pristine ZIS system. This indicates towards increment in charge carrier population in the ZIS CBM with O-doping, also observed from the steady state PL studies. Also, the ZIS bleach maxima undergoes a blue shift (411 nm to 384 nm), plausibly due to lower thickness OZIS sheets (which would provide stronger quantum confinement). In NZIS, the thickness is almost similar to pristine one and both the bleach maxima resides very close to each other. However, the maximum bleach signal intensity has been reasonably decreased in NZIS, without any alteration of DIB signal intensity at the red region of the spectra. It looks like defect mediated signal dominates over the characteristic bleach signal of ZIS in case of N-doping. In both OZIS and NZIS, the TA spectra is primarily dominated by the photo-induced bleach signals, similar to the pristine system. **Figure 7.9c** represents the comparative kinetic profiles of ZIS bleach signal before and after doping. The kinetic profiles reflect the corresponding change in the signal intensity for a particular wavelength. The transient signals are monitored at the bleach maxima as it

corresponds to the maximum population of the charge carriers (here electrons) in the respective band edge of the energy level being monitored. The kinetic profiles are fitted with multi-exponential functions and fitting parameters are listed in **Table 7.2 and 7.3**.

Table 7.2. Transient fitting components of OZIS for 300 nm pump excitation monitoring at different wavelength of the spectra.

Probe wavelength, nm	Growth		Decay	
	τ_1 , ps	τ_2 , ps	τ_3 , ps	τ_4
384	< 0.1	0.9 (23.5 %)	3.7 (50.9 %)	125 ps (125.6 %)
482	0.14	2.0 (39.5 %)	74.9 (27.5 %)	> 1 ns (33 %)
539	0.14	2.3 (46.1 %)	70.2 (31.4 %)	> 1 ns (22.5 %)

Table 7.3. Transient fitting components of NZIS for 300 nm pump excitation monitoring at different wavelength of the spectra.

Probe wavelength, nm	Growth		Decay	
	τ_1 , ps	τ_2 , ps	τ_3 , ps	τ_4 , ns
418	< 0.1	2.1 (77.8 %)	16 (22.2 %)	> 1 ns (100 %)
488	0.13	1.8 (26.3 %)	8.2 (51.9 %)	376 ps (21.8 %)
539	0.14	6.6 (72.6 %)	355 (20.6 %)	> 1 ns (6.8 %)
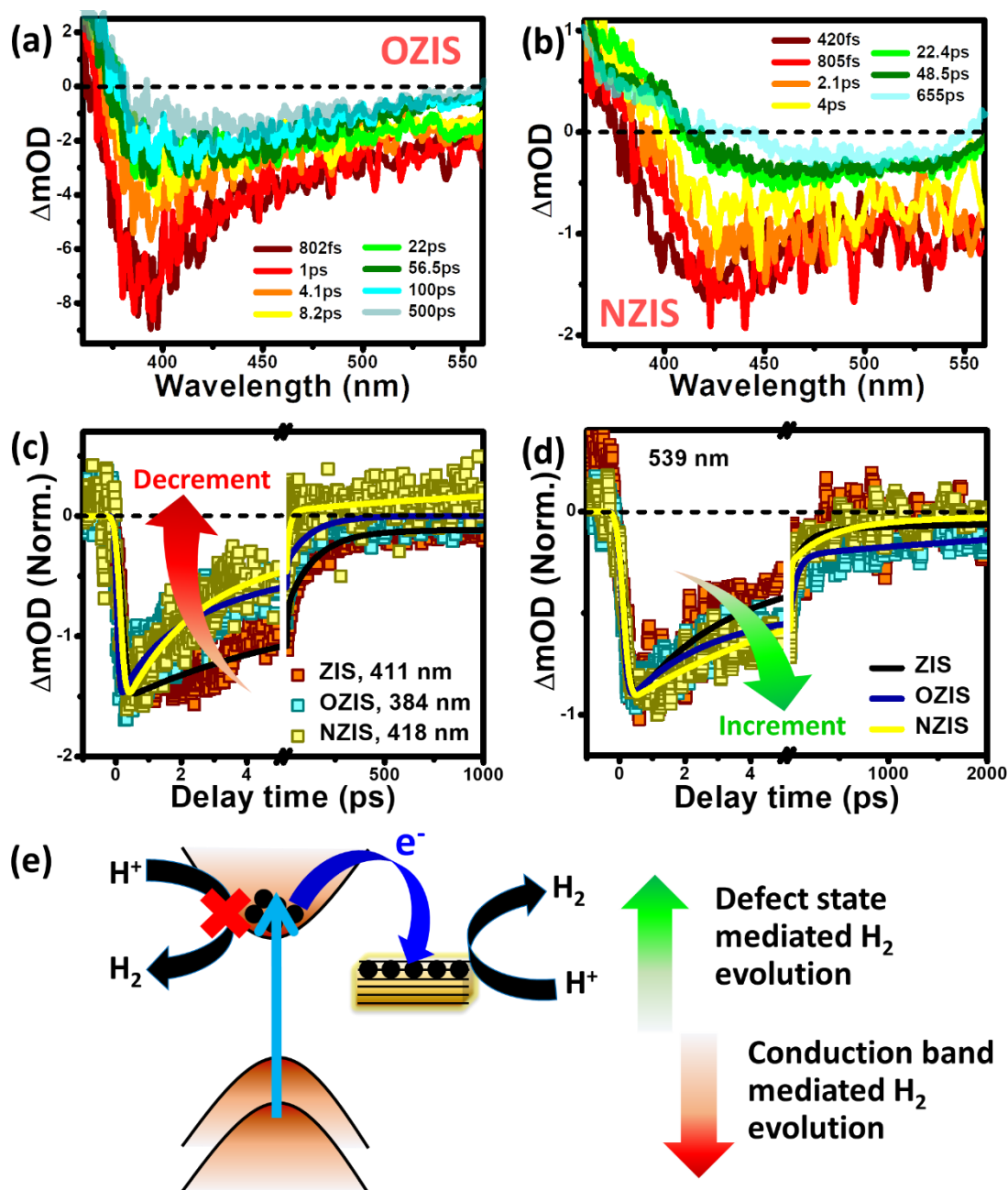
Figure 7.9: Transient absorption spectra of **(a)** OZIS and **(b)** NZIS probed in similar wavelength region as of pristine ZIS, plotted as a function of different pump probe delay time, upon photoexcitation at 300 nm laser pulses with 200 µJ/cm² fluence. **(c)** Normalized decay dynamic profiles of ZIS, OZIS and NZIS monitoring at corresponding bleach maxima (411, 384 and 418 nm respectively). **(d)** Kinetic profile of DIB signals at the red wing of the spectra (539 nm). **(e)** Graphical scheme representing the higher probability of defect state mediated H₂ evolution.

With the non-metal doping, the bleach signal recombines at a much faster rate as compared to that of pristine ZIS, irrespective of the fact that OZIS possess the most intense signal. This

indicates that, doping induces more defect states in the inter bandgap region of the ZIS system, which traps the charge carriers. The growth time of the ZIS bleach signal also decreases in doped samples (**figure 7.10**), pointing towards the instantaneous transfer of CBM electrons to the defect states. In **figure 7.9d**, we have compared the DIB signal kinetics for all the three systems probing at 539 nm. The signal intensity of NZIS system is almost comparable to the pure one, however OZIS signal intensity has been enhanced significantly. Interestingly, the decay profile is also slower in this case. This again indicates towards superior population of charge carriers in the inter bandgap states of OZIS, as compared to other two systems. NZIS also possess slower recovery kinetics than that of ZIS in shorter time scale. Hence, the charge carrier lifetimes of defect states are being enhanced with non-metal doping in ZIS system.
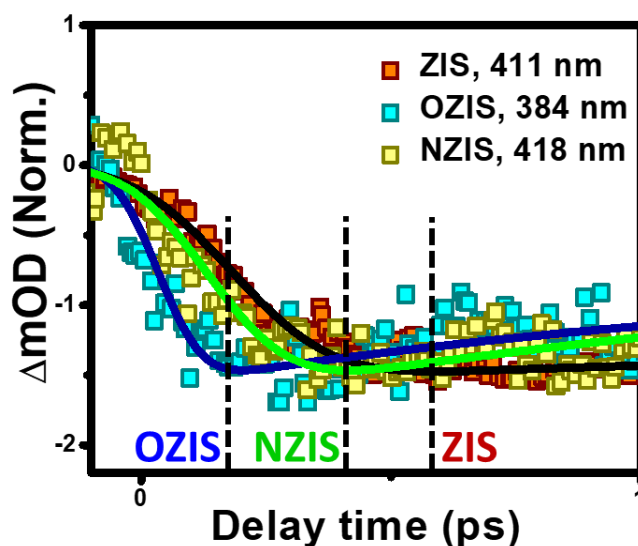
Figure 7.10: Normalized growth dynamic profiles of ZIS, OZIS and NZIS monitoring at the respective bleach maxima (411, 384 and 418 nm).

As photocatalytic activity of these systems also replicates the similar trend, one can conclude that the electrons involved in the H_2 evolution in case of ZIS, and might not directly mediated through conduction band of the system, rather use defect states in course of reduction of H^+. Here, defect states help in extended separation of charge carriers and efficient extraction of electrons from ZIS for H_2 evolution. Non-metal doping contributes towards the defect state density in the system. Enhanced charge carrier population and slower recombination both synergistically contribute towards their superior photocatalytic activity for non-metal doped ZIS.

7.4. Conclusions

In summary, the present work deals with comprehensive discussion on steady state photoluminescence and TA spectroscopy in ZIS nanosheets, to understand the optical mechanism behind the photocatalytic H$_2$ evolution process before and after non-metal (O and N) doping. The estimated band level positions indicate that the higher reduction probability of conduction band electrons in OZIS and NZIS could be one of the possible reasons for the enhanced H$_2$ production. PL study revealed the presence of broad defect induced spectra along with the intrinsic ZIS PL signatures. Moreover, enhanced photoluminescence in doped systems indicates towards superior charge carrier population in ZIS. TA studies show a strong photoinduced bleach signal at 411 nm in case of pristine ZIS, corresponding to the higher order transitions in ZIS optical band structure. A defect induced bleach signal is also observed along with the strong bleach, extended up to 550 nm, arising from the localized defect states close to conduction band. Ultrafast TA spectroscopy confirms that the electrons involved in the H$_2$ evolution, are not fed from the conduction band of the system, rather defect states are involved towards the reduction of H$^+$. The conduction band electrons are transferred to the inter bandgap defect states in sub ps time scale. The enhanced charge carrier lifetime as well as higher charge carrier population in doped ZIS results in 3-fold increase in the hydrogen evolution efficiency. This study would provide a better understanding on charge carrier dynamics in pristine as well as doped ZIS systems and will help in the advancement of 2D nanosheets-based photocatalytic devices for superior H$_2$ production.

7.5. References

(1)   Liu, B.; Abbas, A.; Zhou, C. Two-Dimensional Semiconductors: From Materials Preparation to Electronic Applications. *Adv. Electron. Mater.* **2017**, *3* (7), 1-17.

(2)   Henan, L.; Yumeng, S.; Ming-Hui, C.; Lain-Jong, L. Emerging Energy Applications of Two-Dimensional Layered Transition Metal Dichalcogenides. *Nano Energy* **2015**, *18*, 293-305.

(3)   Li, X.; Shan, J.; Zhang, W.; Su, S.; Yuwen, L.; Wang, L. Recent Advances in Synthesis and Biomedical Applications of Two-Dimensional Transition Metal Dichalcogenide Nanosheets. *Small* **2017**, *13* (5), 1-28.

(4)   Lin, M.; Kravchenko, I. I.; Fowlkes, J.; Li, X.; Puretzky, A. A.; Rouleau, C. M.; Geohegan, D. B.; Xiao, K. Thickness-Dependent Charge Transport in Few-Layer MoS$_2$ Field-Effect Transistors. *Nanotechnology* **2016**, *27* (16), 165203.

(5)   Das, S.; Chen, H.-Y.; Penumatcha, A. V; Appenzeller, J. High Performance Multilayer MoS2 Transistors with Scandium Contacts. *Phys. Rev. B* **1987**, *36* (2), 100-105.

(6)   Chang, H.; Yang, S.; Lee, J.; Tao, L.; Hwang, W.; Jena, D.; Lu, N.; Akinwande, D. High-Performance , Highly Bendable MoS$_2$ Transistors with High - K Dielectrics for Flexible Low-Power systems. *ACS Nano* **2013**, *7* (6), 5446-5452.

(7)   Radisavljevic, B.; Whitwick, M. B.; Kis, A. Integrated Circuits and Logic Operations Based on Single-Layer MoS$_2$. *ACS Nano* **2013**, *7* (4), 3729.

(8)   Dubey, M.; Li, L.-J.; Chin, M. L.; Kong, J.; Palacios, T.; Yu, L.; Lee, Y.-H.; Hsu, A.; Shi, Y.; Wang, H. Integrated Circuits Based on Bilayer MoS$_2$ Transistors. *Nano Lett.* **2012**, *12* (9), 4674-4680.

(9)   Friedman, A. L.; Jernigan, G. G.; Campbell, P. M.; Jonker, B. T.; Cobas, E.; Perkins, F. K. Chemical Vapor Sensing with Monolayer MoS$_2$. *Nano Lett.* **2013**, *13* (2), 668-673.

(10)   Yin, Z.; Zeng, Z.; Zhang, H.; Zheng, B.; Yang, H. Y.; Zhang, X.; Chen, J.; Cai, Y.; Wong, J. I.; Wu, J.; Zeng, Z.; Zhang, H.   Preparation of MoS$_2$-MoO$_3$ Hybrid Nanomaterials for Light-Emitting Diodes. *Angew. Chemie Int. Ed.* **2014**, *53* (46), 12560-12565.

(11)   Cho, J.; Hwang, H.; Kim, H. MoS$_2$ Nanoplates Consisting of Disordered Graphene-like Layers for High Rate Lithium Battery Anode Materials. *Nano Lett.* **2011**, 4826-4830.

(12)   Yue, G.; Lin, J. Y.; Tai, S. Y.; Xiao, Y.; Wu, J. A Catalytic Composite Film of MoS$_2$/Graphene Flake as a Counter Electrode for Pt-Free Dye-Sensitized Solar Cells. *Electrochim. Acta* **2012**, *85*, 162-168.

(13)   Su, S.-H.; Tsai, M.-L.; Chen, C.-H.; Tsai, D.-S.; Li, L.-J.; He, J.-H.; Chang, J.-K.; Chen, L.-J.; Wu, C.-I. Monolayer MoS$_2$ Heterojunction Solar Cells. *ACS Nano* **2014**, *8* (8), 8317-8322.

(14)   Wang, L.; Luo, S.; Xu, Y.; Tang, Y.; Zeng, Y.; Liu, C.; Zhang, S.; Liu, Y. Vertical Single or Few-Layer MoS$_2$ Nanosheets Rooting into TiO$_2$ Nanofibers for Highly Efficient Photocatalytic Hydrogen Evolution. *Appl. Catal. B Environ.* **2014**, *164*, 1-9.

(15)   Yang, Y.; Ng, D. H. L.; Zhang, N.; Wang, G.; Li, Q. High Efficiency Photocatalysis for Pollutant Degradation with MoS$_2$/C$_3$N$_4$ Heterostructures. *Langmuir* **2014**, *30* (29), 8965-

8972.

(16) Li, Z.; Xiao, Y.; Gong, Y.; Wang, Z.; Kang, Y.; Zu, S.; Ajayan, P. M.; Nordlander, P.; Fang, Z. Active Light Control of the MoS_2 Monolayer Exciton Binding Energy. *ACS Nano* **2015**, *9* (10), 10158-10164.

(17) Jariwala, D.; Sangwan, V. K.; Lauhon, L. J.; Marks, T. J.; Hersam, M. C. Emerging Device Applications for Semiconducting Two-Dimensional Transition Metal Dichalcogenides. *ACS Nano* **2014**, *2*, 1102-1120.

(18) Lee, Y. K.; Jung, C. H.; Park, J.; Seo, H.; Somorjai, G. A.; Park, J. Y. Surface Plasmon-Driven Hot Electron Flow Probed with Metal-Semiconductor Nanodiodes. *Nano Lett.* **2011**, 4251-4255.

(19) Chalabi, H.; Schoen, D.; Brongersma, M. L. Hot-Electron Photodetection with a Plasmonic Nanostripe Antenna. *Nano Lett.* **2014**, *14*, 1374-1380.

(20) Scheuschner, N.; Ochedowski, O.; Kaulitz, A.-M.; Gillen, R.; Schleberger, M.; Maultzsch, J. Photoluminescence of Freestanding Single- and Few-Layer MoS_2. *Phys. Rev. B* **2014**, *89* (12), 125406.

(21) Sie, E. J.; Frenzel, A. J.; Lee, Y.; Kong, J.; Gedik, N. Intervalley Biexcitons and Many-Body Effects in Monolayer MoS_2. *Phys. Rev. B* **2015**, *92*, 125417.

(22) Heinz, T. F.; Mak, K. F.; He, K.; Lee, C.; Shan, J.; Hone, J.; Lee, G. H. Tightly Bound Trions in Monolayer MoS_2. *Nat. Mater.* **2012**, *12* (3), 207-211.

(23) Kylänpää, I.; Komsa, H. P. Binding Energies of Exciton Complexes in Transition Metal Dichalcogenide Monolayers and Effect of Dielectric Environment. *Phys. Rev. B - Condens. Matter Mater. Phys.* **2015**, *92* (20), 1-6.

(24) Mak, K. F.; Lee, C.; Hone, J.; Shan, J.; Heinz, T. F. Atomically Thin MoS_2: A New Direct-Gap Semiconductor. *Phys. Rev. Lett.* **2010**, *105* (13), 136805.

(25) Kime, G.; Leontiadou, M. A.; Brent, J. R.; Savjani, N.; O'Brien, P.; Binks, D. Ultrafast Charge Dynamics in Dispersions of Monolayer MoS_2 Nanosheets. *J. Phys. Chem. C* **2017**, *121* (40), 22415-22421.

(26) Sim, S.; Park, J.; Song, J. G.; In, C.; Lee, Y. S.; Kim, H.; Choi, H. Exciton Dynamics in Atomically Thin MoS_2: Interexcitonic Interaction and Broadening Kinetics. *Phys. Rev.*

B - Condens. Matter Mater. Phys. **2013**, *88* (7), 1-5.

(27)   Voiry, D.; Fujita, T.; Chhowalla, M.; Eda, G.; Yamaguchi, H.; Chen, M. Photoluminescence from Chemically Exfoliated MoS₂ . *Nano Lett.* **2011**, *12* (1), 526-526.

(28)   Christopher, J. W.; Goldberg, B. B.; Swan, A. K. Long Tailed Trions in Monolayer MoS₂: Temperature Dependent Asymmetry and Resulting Red-Shift of Trion Photoluminescence Spectra. *Sci. Rep.* **2017**, *7* (1), 1-8.

(29)   Zhang, S.; Qin, Q.; Pei, J.; Lu, Y.; Wang, X.; Jiang, W.; Myint, Y. W.; Yang, J.; Zeng, Y.-H.; Xu, R.; et al. Exciton and Trion Dynamics in Bilayer MoS₂ . *Small* **2015**, *11* (48), 6384–6390.

(30)   Mouri, S.; Miyauchi, Y.; Matsuda, K. Tunable Photoluminescence of Monolayer MoS₂ via Chemical Doping. *Nano Lett.* **2013**, *13* (12), 5944-5948.

(31)   Lui, C. H.; Frenzel, A. J.; Pilon, D. V.; Lee, Y.-H.; Ling, X.; Akselrod, G. M.; Kong, J.; Gedik, N. Trion-Induced Negative Photoconductivity in Monolayer MoS₂. *Phys. Rev. Lett.* **2014**, *113* (16), 166801.

(32)   Li, H.; Zhang, Q.; Yap, C. C. R.; Tay, B. K.; Edwin, T. H. T.; Olivier, A.; Baillargeat, D. From Bulk to Monolayer MoS₂: Evolution of Raman Scattering. *Adv. Funct. Mater.* **2012**, *22* (7), 1385-1390.

(33)   Cheiwchanchamnangij, T.; Lambrecht, W. R. L. Quasiparticle Band Structure Calculation of Monolayer, Bilayer, and Bulk MoS₂. *Phys. Rev. B - Condens. Matter Mater. Phys.* **2012**, *85* (20), 1-4.

(34)   Berkelbach, T. C.; Hybertsen, M. S.; Reichman, D. R. Theory of Neutral and Charged Excitons in Monolayer Transition Metal Dichalcogenides. *Phys. Rev. B - Condens. Matter Mater. Phys.* **2013**, *88* (4), 1-6.

(35)   Radisavljevic, B.; Radenovic, A.; Brivio J.; Giacometti V.; Kis, A. Single-Layer MoS₂ Phototransistors. *Nature Nanotechnology* **2011,** *6*, 147-150.

(36)   Ross, J. S.; Wu, S.; Yu, H.; Ghimire, N. J.; Jones, A. M.; Aivazian, G.; Yan, J.; Mandrus, D. G.; Xiao, D.; Yao, W.; et al. Electrical control of neutral and charged excitons in a monolayer semiconductor. *Nature Comm.* **2013**, *4*, 1-6.

(37) Jones, A. M.; Yu, H.; Ghimire, N. J.; Wu, S.; Aivazian, G.; Ross, J. S.; Zhao, B.; Yan, J.; Mandrus, D. G.; Xiao, D.; et al. Optical Generation of Excitonic Valley Coherence in Monolayer WSe$_2$. *Nature Nanotechnology* **2013**, *8*, 634-638.

(38) Tsokkou, D.; Yu, X.; Sivula, K.; Banerji, N. The Role of Excitons and Free Charges in the Excited-State Dynamics of Solution-Processed Few-Layer MoS$_2$ Nanoflakes. *J. Phys. Chem. C* **2016**, *120* (40), 23286-23292.

(39) Pogna, E. A. A.; Marsili, M.; De Fazio, D.; Dal Conte, S.; Manzoni, C.; Sangalli, D.; Yoon, D.; Lombardo, A.; Ferrari, A. C.; Marini, A.; et al. Photo-Induced Bandgap Renormalization Governs the Ultrafast Response of Single-Layer MoS$_2$. *ACS Nano* **2016**, *10* (1), 1182-1188.

(40) Ceballos, F.; Cui, Q.; Bellus, M. Z.; Zhao, H. Exciton Formation in Monolayer Transition Metal Dichalcogenides. *Nanoscale* **2016**, *8* (22), 11681-11688.

(41) Nie, Z.; Long, R.; Sun, L.; Huang, C.; Zhang, J.; Xiong, Q. Ultrafast Carrier Thermalization and Cooling Dynamics in Few-Layer MoS$_2$. *ACS Nano* **2014**, *8* (10), 10931-10940.

(42) Shi, H.; Yan, R.; Bertolazzi, S.; Brivio, J.; Gao, B.; Kis, A.; Jena, D. Exciton Dynamics in Suspended Monolayer and Few-Layer MoS$_2$ 2D Crystals. *ACS Nano* **2013**, *7* (2), 1072-1080.

(43) Bhanu, U.; Islam, M. R.; Tetard, L.; Khondaker, S. I. Photoluminescence Quenching in Gold-MoS$_2$ Hybrid Nanoflakes. *Sci. Rep.* **2014**, *4*, 1-5.

(44) Lee, G.-H.; Lee, D.-Y.; Hone, J.; Hwan Lee, S.; Sup Choi, M.; Jong Yoo, W.; Yu, Y.-J.; Kim, P. Controlled Charge Trapping by Molybdenum Disulphide and Graphene in Ultrathin Heterostructured Memory Devices. *Nat. Commun.* **2013**, *4* (1), 1-7.

(45) Eastman, D. E. Photoelectric Work Functions of Transition, Rare-Earth, and Noble Metals. *Phys. Rev. B* **1970**, *2* (1).

Chapter 8

Summary and Future perspective

8.1. Summary

This thesis aimed to establish a thorough correlation between the optical behaviours of novel 2D chalcogenides and their inherent charge carrier dynamics in order to properly utilize these materials in the state-of-the-art photonic devices. We have used femtosecond transient absorption spectroscopy (FTAS) to explore the inherent photophysical processes in different chalcogenide based 2D materials, both in pristine and modified conditions. The first two chapters of my thesis consist of detailed discussion of the 'Introduction' of my work and the 'Synthesis and instrumentation' used throughout my thesis work, respectively. Starting from the third chapter, I have discussed my different projects where we have used FTAS to disentangle complex optical behaviours of unique 2D systems like, MoS_2, WS_2, Cu_2MoS_4, MoS_2/Au, CdS/MoS_2 and $ZnIn_2S_4$.

In my first project, we have investigated the formation and relaxation behaviours of both excitonic and trionic features in monolayer MoS_2 flakes, which were synthesized via CVD method. These flakes were comprised of both excitons (A, B) and trion (A^-) signatures in the room temperature, owing to strong coulombic interactions in these kinds of thin 2D layers. These quasiparticles were probed in the transient study and their formation time was calculated to be ~ 0.5 and ~ 1.2 ps for A exciton and A^- trion respectively. This trion formation time is associated with binding of 'A' excitons with abundant free electrons in the system, which was confirmed from the fluence dependent measurements. Further, we attached an Au NP interface to these monolayer flakes of MoS_2 to extract the free electrons from the system. In the MoS_2/Au heterojunction the monolayer PL signal was drastically quenched, indicating electron transfer from MoS_2 to Au. From the transient analysis, the electron transfer time was calculated to be ~ 0.6 ps. Both the exciton and trion signals were diminished in an ultrafast time scale in presence of Au. This study established the importance of free carriers for the formation of exciton and trions in a semiconducting system like MoS_2.

In the next project, we have applied broadband transient spectroscopy to simultaneously monitor all four excitonic features in few layer WS_2. Till now, the optical properties in these types of materials were considered to be solely dependent on the band edge (A, B) excitons, which are being extensively studied. The high energy (C, D) excitons were almost unexplored, despite their immense influence in the optical behaviours of these materials. Our study investigated the origin all these excitons and found a strong dependence among all these. We have seen that, all four excitonic features emerge in the system irrespective of the excitation

energy. This could be possible due the overlap of 'K' high energy states and the C excitonic states in the complex electronic band structure of these materials. Also, we found strong intervalley coupling in the system which induces a profound reliance of A, B exciton formation on the C, D charge carriers. In this few layer system, high energy excitons relax through Λ-Γ indirect recombination channel, unlike K-K direct recombination of A, B. This results in slower recovery in case of C, D excitons, which would be extremely beneficiary for a photonic device. Pauli blocking in K and Λ valley also take part in slowing down this recombination process. High oscillator strength and slower recombination of high energy excitons in WS_2 like TMDC materials would be highly preferable for device fabrications.

In the following chapter, we have studied both the steady state and time resolved optical properties of Cu_2MoS_4 (CMS) and explored the effect of electron-phonon (e-ph) coupling. This is the very first report of the complete optical analysis of this material. Raman spectroscopy shows the existence of multi-phonon peaks which stands for the strong e-ph coupling inside this material. The steady state PL signal is composed of band edge emission at ~ 600 nm and interband gap trap state mediated emission at the redder region. The FTAS spectra is mainly dominated by two contrasting features, exciton induced bleach at 573 nm and excited state absorption induced sharp positive signal at 543 nm, which decides most the optical properties of CMS. We found that the recombination of photoexcited charge carriers is influenced by charge trapping at low charge carrier concentration, while Auger process takes over at high fluence (above the saturation density of $5.3 \pm 0.7 \times 10^{14}$ photons/cm^2). When the lattice temperature of the system goes down towards 5K, the optical band gap goes up and the charge carrier recombination accelerates. This is due to the strong e-ph coupling of CMS at lower temperature, which is very important for the optical properties of this material.

In the next chapter, we have explored the hot charge carrier migration in an 1D/2D heterojunction, CdS/MoS_2. The heterocomposite system was fabricated using simple solvothermal synthesis route, where small flakes of MoS_2 covered the CdS nanorods. The PL signature of CdS was substantially quenched in the presence of MoS_2, indicating an instantaneous transfer of charge carriers from CdS to MoS_2. In transient study, CdS/MoS_2 showed the presence of both the individual characteristics of CdS and MoS_2. Though the intensity of the CdS signal was drastically decreased, which further substantiates the charge migration phenomenon. Transient analysis suggests the dominance of hot carrier transfer in the system, which occurs at much faster rate than that of the band edge one. The hot carrier transfer

time was calculated to be ~ 0.2 ps. Efficient extraction of hot charge carriers in a unique heterojunction like CdS/MoS_2 will be great news for the opto-electronic and photocatalytic devices.

In the last project, we investigated a real photocatalytic material and correlated its activity with the inherent charge carrier behaviours. We used hydrothermal method to synthesize pristine and elemental (O, N) doped $ZnIn_2S_4$ (ZIS) nanosheets. The doped systems showed 3-4 times higher photocatalytic efficiency than the pristine one. PL study indicates the enhancement of charge carrier population and defect density in the system after doping. In the transient study, two different kinds of signals appeared in ZIS, one was due to the conduction band population and the other one was due to the inter band gap trap state population. Following doping, the conduction band mediated signatures were found to be accelerated, indicating depopulation in the conduction band. Whereas, the trap signals were slowed down after doping. This is the direct evidence of the charge carrier migration from the conduction band to the trap states. As doping induces a greater number of trap states, the charge trapping process becomes more dominating. These trap states act as the active sites in this material and enhances the photocatalytic activity. Our study re-establishes the importance of trap states in the photocatalytic efficiency of a material.

8.2. Future perspective

Transient absorption spectroscopy has the capability of studying all different photophysical processes inside a material, which are crucial for the performance of the material in an optical device. Henceforth, this technique is now being widely used in case of many materials to realize their full potential and figure out the controlling mechanism deciding their behaviour in different devices. Our study explored many novel properties of few such 2D chalcogenide materials and opened a lot of opportunities in this field.

We have investigated the possibility of these materials in different photovoltaic and photocatalytic applications. Though these metal chalcogenide systems are extremely potent, there is still a big gap lies in between these laboratory-made prototypes and commercially usable products. Firstly, we must improve the synthesis routes of 2D chalcogenides. CVD made monolayer TMDC systems are being successfully implemented in many state-of-the-art opto-electronic devices in low scale for some time now. But this area has not yet reached its full potential because of the absence of any synthesis method which can produce defect-free large

area monolayer films in commercial scale. Secondly, we need to focus more on the modulation of pristine properties via doping or fabrication of heterojunctions. Unique heterojunctions like 2D/2D, 2D/0D, 2D/1D etc. are already showing lots of promise in the opto-electronics arena. Core-shell like heterostructures can also be very helpful, as this hetero-system not only improves the efficiency, it protects the chalcogenide system from the inevitable photo-corrosions. Doping and heterojunction fabrication will also induce new functionality in the 2D material which would broaden the prospect of the system in any photonic application.

Lastly, there are still very few instances where TAS is directly implemented to investigate a photocatalytic or photovoltaic process. It is very important to study the behaviour of the reaction mixture while doing a reaction or a hetero-interface after applying voltage, just like in the original device structure. Spectro-electrochemistry is one such technique, where TAS is blended with a live electrochemical reaction. Also, TAS study with lowering the lattice temperature would generate many interesting informations for a material. In summary, we need to use the TAS technique in wide range of materials to fabricate more able systems and eventually revolutionize the opto-electronic field.

List of publications

(Included in the thesis)

1. Ultrafast Carrier Dynamics of the Exciton and Trion in MoS_2 Monolayers Followed by Dissociation Dynamics in Au@MoS_2 2D Heterointerfaces: **Tanmay Goswami**, Renu Rani, Kiran Shankar Hazra, Hirendra N. Ghosh*, *J. Phys. Chem. Lett.,* **2019,** *10,* **3057-3063.**

2. Defect-Mediated Slow Carrier Recombination and Broad Photoluminescence in Non-Metal-Doped $ZnIn_2S_4$ Nanosheets for Enhanced Photocatalytic Activity: **Tanmay Goswami**, Dharmendra Kumar Yadav, Himanshu Bhatt, Gurpreet Kaur, Ayushi Shukla, K. Justice Babu, and Hirendra N. Ghosh*, *J. Phys. Chem. Lett.,* **2021,** *12,* **5000-5008**.

3. Ultrafast Insights into High Energy (C and D) Excitons in Few Layer WS_2: **Tanmay Goswami**, Himanshu Bhatt, K. Justice Babu, Gurpreet Kaur, Nandan Ghorai, and Hirendra N. Ghosh*, *J. Phys. Chem. Lett.,* **2021,** *12,* **6526-6534**.

4. Probing ultrafast hot charge carrier migration in MoS_2 embedded CdS nanorods: **Tanmay Goswami**, Himanshu Bhatt, Dharmendra Kumar Yadav, Ramchandra Saha, K. justice Babu and Hirendra N. Ghosh*, **J. Chem. Phys., 2022, 156, 034704.**

5. Temperature Dependent Charge Carrier Dynamics in 2D Ternary Cu_2MoS_4 Nanoflakes: **Tanmay Goswami**, Dharmendra Kumar Yadav, Himanshu Bhatt, Gurpreet Kaur and Hirendra N. Ghosh*, **Communicated.**

List of publications

(Not included in the thesis)

1. Interfacing g-C_3N_4 Nanosheets with CdS Nanorods for Enhanced Photocatalytic Hydrogen Evolution: An Ultrafast Investigation: **Tanmay Goswami**[†], Himanshu Bhatt[†], Dharmendra Kumar Yadav[†] and Hirendra N. Ghosh*; (†- Equal contribution) *J. Phys. Chem. B* **2022, 126, 2, 572-580**.

2. Gold–BODIPY Nanoparticles with Luminescence and Photosensitization Properties for Photodynamic Therapy and Cell Imaging: Atikur Rahman[†], Panangattukara Prabhakaran Praveen Kumar[†], Pranjali Yadav[†], **Tanmay Goswami**[†], Asifkhan Shanavas*, Hirendra N. Ghosh*, Prakash P. Neelakandan*; (†- Equal contribution) *ACS Appl. Nano Mater.* **2022, 5, 5, 6532-6542**.

3. Ultrafast Hot Electron Transfer and Trap-State Mediated Charge Carrier Separation toward Enhanced Photocatalytic Activity in g-C_3N_4/$ZnIn_2S_4$ Heterostructure. Himanshu Bhatt[†], **Tanmay Goswami**[†], Dharmendra Kumar Yadav, Nandan Ghorai, Ayushi Shukla, Gurpreet Kaur, Arshdeep Kaur, and Hirendra N. Ghosh*; (†- Equal contribution) *J. Phys. Chem. Lett.* **2021**, **12, 49, 11865-11872**.

4. Probing Ultrafast Charge Separation in CZTS/CdS Heterojunction through Femtosecond Transient Absorption Spectroscopy: Arshdeep Kaur[†], **Tanmay Goswami**[†], K. Justice Babu, Nandan Ghorai, Gurpreet Kaur, Ayushi Shukla, Sachin R. Rondiya, Hirendra N. Ghosh*; (†- Equal contribution) *J. Phys. Chem. C* **2020, 124, 36, 19476-19483**.

5. Polaron-Mediated Slow Carrier Cooling in a Type-1 3D/0D $CsPbBr_3$@Cs_4PbBr_6 Core–Shell Perovskite System. Gurpreet Kaur, K. Justice Babu, Nandan Ghorai, **Tanmay Goswami**, Sourav Maiti, and Hirendra N. Ghosh*; *The Journal of Physical Chemistry Letters* **2019, 10, 5302-5311**.

6. An Experimental and Theoretical Study into Interface Structure and Band Alignment of the $Cu_2Zn_{1-x}Cd_xSnS_4$ Heterointerface for Photovoltaic Applications: Sachin R. Rondiya, Yogesh Jadhav, Nelson Y. Dzade, Raihan Ahammed, **Tanmay Goswami**,

Abir De Sarkar, Sandesh Jadkar, Santosh K. Haram, Hirendra N. Ghosh*; *ACS Applied Energy Materials,* **2020, 3, 5153-5162**.

7. Effect of Confinement on the Exciton and Biexciton Dynamics in Perovskite 2D-Nanosheets and 3D-Nanocrystals. Gurpreet Kaur, Ayushi Shukla, K. Justice Babu, Nandan Ghorai, **Tanmay Goswami**, Arshdeep Kaur, and Hirendra N. Ghosh*; *J. Phys. Chem. Lett.* **2020, 11, 6344-6352**.

8. Temperature-Dependent Trap-Assisted Ultrafast Carrier Dynamics in Amorphous and Crystalline Thin Films. Palwinder Singh, Gurpreet Kaur, Nandan Ghorai, **Tanmay Goswami**, Anup Thakur, Hirendra N Ghosh*; *Phys. Rev. Applied* **2020, 14, 014087**.

9. Concurrent Energy- and Electron-Transfer Dynamics in Photoexcited Mn-Doped $CsPbBr_3$ Perovskite Nanoplatelet Architecture. Gurpreet Kaur, K. Justice Babu, Ayushi Shukla, Arshdeep Kaur, **Tanmay Goswami**, Nandan Ghorai, and Hirendra N. Ghosh*; *J. Phys. Chem. Lett.* **2021, 12, 302-309**

10. Fine-Tuning Plasmon-Molecule Interactions in Gold-BODIPY Nanocomposites: The Role of Chemical Structure and Noncovalent Interactions: P. P. Praveen Kumar, Atikur Rahman, **Tanmay Goswami**, Hirendra N. Ghosh*, Prakash P. Neelakandan*; *ChemPlusChem* **2021, 86, 87-94**.

11. Mechanistic Insights for Photoelectrochemical Ethanol Oxidation on Black Gold Decorated Monoclinic Zirconia: Ritika Wadhwa, Krishna K. Yadav, **Tanmay Goswami**, Ankush, Sujit Kumar Guchhait, Sunaina, S. T. Nishanthi, Hirendra N. Ghosh*, Menaka Jha*; *ACS Applied Materials & Interfaces* **2021, 13, 9942-9954**.

12. Enhanced Charge Carrier Separation and Improved Biexciton Yield at the p–n Junction of SnSe/CdSe Heterostructures: A Detailed Electrochemical and Ultrafast Spectroscopic Investigation: Arshdeep Kaur, **Tanmay Goswami**, Sachin R. Rondiya, Yogesh A. Jadhav, K. Justice Babu, Ayushi Shukla, Dharmendra Kumar Yadav, Hirendra N. Ghosh*; *J. Phys. Chem. Lett.* **2021, 12, 10958-10968**.

13. Atomically thin 2D photocatalysts for boosted H_2 production from the perspective of transient absorption spectroscopy: **Tanmay Goswami**, Himanshu Bhatt, Dharmendra

Kumar Yadav, Hirendra N. Ghosh*; *Phys. Chem. Chem. Phys.,* **2022, 24, 19121-19143**.

14. Hot electron migration from gold nanoparticle to an organic molecule enhances luminescence and photosensitization properties of a pH activatable plasmon-molecule coupled nanocomposite: Atikur Rahman, **Tanmay Goswami**, Nidhi Tyagi, Hirendra N. Ghosh*, Prakash P Neelakandan*; *Journal of Photochemistry and Photobiology A: Chemistry* **2022, 432, 114067**.

15. Defect-Mediated Charge Carrier Recombination of Zinc–Silver–Indium Sulfide QDs in the Presence of Naphthoquinone Derivatives: An Insight into the Interfacial Surface Dynamics: Naupada Preeyanka, **Tanmay Goswami**, Ramchandra Saha, Amit Akhuli, Asish K Dehury, Moloy Sarkar*; *J. Phys. Chem. C* **2022, 126, 15838-15848**.

16. Oligothiophene Ring Strapped Perylene Bisimides: A Functionalizable Co-axial Donor-Acceptor Macrocycle: Sairam Dnyaneshwar Veer, Vivek Chandrakant Wakchaure, Kiran Asokan, Ruchi Dixit, **Tanmay Goswami**, Ramchandra Saha, Rajesh Gonnade, Hirendra N. Ghosh*, Santhosh Sukumaran Babu*; *Angew. Chem* **2022**.

List of conferences attended

1. Presented a Poster entitled "*Room Temperature Exciton and Trion Formation in Monolayer MoS$_2$ followed by Dissociation in Presence of Au NPs*" in Ultrafast Sciences 2019 conference (UFS 2019) held at IIT Bombay, Powai, Mumbai (**7th– 9th November 2019**).

2. Actively participated and attended "*the Full Agenda of the DST & ACS Workshop*" held at Institute of Nano Science and Technology, Mohali (**20th November, 2019**).

3. Presented a Poster entitled "*Charge transfer driven water splitting in MoS$_2$-CdS heterostructure: A detail spectroscopic study*" in International Conference on Nano Science and Technology (ICONSAT 2020) held at Biswa Bangla Convention Centre, Kolkata (**5th– 7th March 2020**).

4. Presented a Poster entitled "*Transient absorption spectroscopy of few layer WS$_2$ in the perspective of high energy (C, D) excitons*" in Ultrafast Sciences conference (UFS 2021) in the Online Zoom Platform (**12th– 13th November 2021**).

5. Bagged the best Oral presentation award on "*Ultrafast spectroscopy of two-dimensional chalcogenide based semiconductors*", at 2nd Research Scholar Day, held at Institute of Nano Science and Technology, Mohali Punjab, India (**31st March– 1st April, 2022**).

6. Presented a Poster entitled "*Ultrafast Charge Carrier Dynamics of Two-Dimensional Cu$_2$MoS$_4$ Nanoflakes*" in Ultrafast Sciences conference (UFS 2022) held at Indian Institute of Science Education and Research, Thiruvananthapuram (**3rd– 5th November 2022**).

Ultrafast Carrier Dynamics of the Exciton and Trion in MoS₂ Monolayers Followed by Dissociation Dynamics in Au@MoS₂ 2D Heterointerfaces

Tanmay Goswami,[§] Renu Rani,[§] Kiran Shankar Hazra,[§] and Hirendra N. Ghosh*,[§,†]

[§]Institute of Nano Science and Technology, Mohali, Punjab 160062, India
[†]Radiation and Photochemistry Division, Bhabha Atomic Research Centre, Mumbai 400085, India

S *Supporting Information*

ABSTRACT: Many-body states like excitons, biexcitons, and trions play an important role in optoelectronic and photovoltaic applications in 2D materials. Herein, we studied carrier dynamics of excitons and trions in monolayer MoS₂ deposited on a SiO₂/Si substrate, before and after Au NP deposition, using femtosecond transient absorption spectroscopy. Luminescence measurements confirm the presence of both an exciton and trion in MoS₂, which are drastically quenched after deposition of Au NPs, indicating electron transfer from photoexcited MoS₂ to Au. Ultrafast study reveals that photogenerated free carriers form excitons with a time scale of ~500 fs and eventually turn into trions within ~1.2 ps. Dissociation of excitons and trions has been observed in the presence of Au, with time scales of ~600 fs and ~3.7 ps, respectively. Understanding the formation and dissociation dynamics of the exciton and trion in monolayer MoS₂ is going to help immensely to design and develop many new 2D devices.
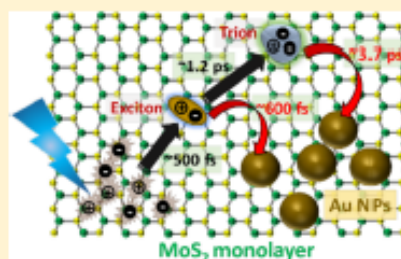
Research on two-dimensional (2D) transition metal dichalcogenides (TMDCs) has gained incredible interest and importance recently, attributable to their fascinating optical, electronic, and mechanical properties. They offer both fundamental and technological implications in various advanced electronic, optoelectronic, and gas-sensing devices, energy storage systems, photovoltaics, and photocatalysts.[1−3] Among TMDC materials, MoS₂, owing to its high stability and easy synthesis routes, finds promising applications in photo-transistors,[4,5] transistors with high current switching,[6] integrated circuits,[7,8] sensing,[9] light-emitting diodes (LEDs),[10] batteries,[11] solar cells,[12,13] and catalysis.[14,15] Presently, metal-2D heterostructure-based devices have gained significant limelight, where interaction between the plasmon and exciton in the metal−semiconductor (M−S) domain plays a crucial role.[16,17] Metal nanoparticles (NPs) are ideal light acceptors due to the presence of surface plasmons, which can restrain and manipulate light at the nanoscale.[18,19] In this context, it is very important to study intrinsic physical properties of semiconductor systems and charge transfer processes in M−S heterojunctions. A reduced dielectric constant in 2D monolayers results in strong interactions between quasiparticles, allowing formation of several many-body states like excitons,[20] biexcitons,[21] and trions.[22] Excitons and trions are stable even at room temperature, owing to their high Coulombic interaction and large binding energies in the range of a few hundred meV and tens of meV, respectively.[20,22,23] Photoluminescence (PL) and ultrafast pump–probe spectroscopic studies have been carried out to monitor excitonic population in 2D materials.[20,24−27] Unlike excitons, trions are not well explored for 2D materials, although they play a vital role in their intrinsic properties. There have been only a few luminescence experiments conducted where trions are reported at room temperature even in the absence of any electrical or chemical doping.[22,28−30] Mak et al. reported the formation of tightly bound trions in monolayer MoS₂ at room temperature.[22] Lui et al. demonstrated separate contributions of photoconductivity from the trion and electron, which provided direct evidence of trion transport.[31] Singh et al. reported trion formation dynamics in monolayer MoSe₂ using 2D spectroscopy, and they reported the trion binding energy and trion formation time to be 30 meV and ~2 ps, respectively.[32] Trions were found to be an important part of negative terahertz photoconductivity, as observed in the MoS₂ monolayer.[33] Trion studies have become very interesting for both scientific and technological pursuits due to their transport properties, density, and pseudospin, which can be easily controlled by electric fields and polarization.[28] In a metal-2D heterostructure, it is very important to understand both plasmon−exciton and plasmon−trion interaction, for better implications. To design and develop any efficient device out of these 2D materials, it is of utmost importance to understand the energy dissipation pathways, which include formation and relaxation of free carriers, excitons, as well as trions, where most of the

CCC
RightsLink

🏠 Home | ❓ Help ⌄ | ✉ Email Support | 👤 Sign in | 👤 Create Account

Ultrafast Carrier Dynamics of the Exciton and Trion in MoS2 Monolayers Followed by Dissociation Dynamics in Au@MoS2 2D Heterointerfaces

ACS Publications
Most Trusted. Most Cited. Most Read.

Author: Tanmay Goswami, Renu Rani, Kiran Shankar Hazra, et al

Publication: Journal of Physical Chemistry Letters

Publisher: American Chemical Society

Date: Jun 1, 2019

Copyright © 2019, American Chemical Society

PERMISSION/LICENSE IS GRANTED FOR YOUR ORDER AT NO CHARGE

This type of permission/license, instead of the standard Terms and Conditions, is sent to you because no fee is being charged for your order. Please note the following:

- Permission is granted for your request in both print and electronic formats, and translations.
- If figures and/or tables were requested, they may be adapted or used in part.
- Please print this page for your records and send a copy of it to your publisher/graduate school.
- Appropriate credit for the requested material should be given as follows: "Reprinted (adapted) with permission from {COMPLETE REFERENCE CITATION}. Copyright {YEAR} American Chemical Society." Insert appropriate information in place of the capitalized words.
- One-time permission is granted only for the use specified in your RightsLink request. No additional uses are granted (such as derivative works or other editions). For any uses, please submit a new request.

If credit is given to another source for the material you requested from RightsLink, permission must be obtained from that source.

BACK   CLOSE WINDOW

Letter

Ultrafast Insights into High Energy (C and D) Excitons in Few Layer WS₂

Tanmay Goswami, Himanshu Bhatt, K. Justice Babu, Gurpreet Kaur, Nandan Ghorai, and Hirendra N. Ghosh*

Cite This: *J. Phys. Chem. Lett.* 2021, 12, 6526–6534

Read Online

ACCESS | Metrics & More | Article Recommendations | Supporting Information

ABSTRACT: High energy (C and D) excitons possess extraordinary influence over the optical properties of atomically thin transition metal dichalcogenides (TMDCs), and the comprehensive understanding of these would play a pivotal role in advancing research on 2D optoelectronics. Herein, we employed transient absorption spectroscopy to monitor the underlying photophysical processes involved with different excitonic features in few layer WS₂, modeled as a TMDC representative. We observed a strong intervalley coupling across the momentum space and proposed the most plausible relaxation pathway for different excitons in few layer scenario. C and D exciton dynamics were significantly slower as compared to canonical A and B excitons, as a consequence of the indirect Λ–Γ relaxation in C and D and direct K–K combination in A and B. Most importantly, all four excitons emerge in the system and influence each other irrespective of the incident photon energy, which would be extremely impactful in fabricating wide range photonic devices.
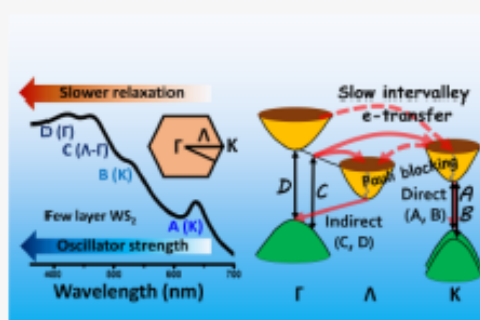
The optoelectronic response of any material has a profound reliance on the efficient absorption of electromagnetic radiation and subsequent relaxation of the photogenerated hot carriers in the system.[1,2] The efficacy of an quantum system in various optoelectronic applications like light-emitting diodes,[3] photodetectors,[4,5] opto-valleytronics,[6,7] or energy harvesting devices[8] could possibly be improved by slowing down the relaxation of hot carriers or by exploiting a broader absorption range.[5] Detailed understanding of the excitonic features generated in an extended range of the radiation would be crucial for developing advanced photonic devices out of any material.

Nowadays, layered transition metal dichalcogenides (TMDCs) are being projected as the semiconducting equivalent of graphene[9,10] and they confer great potential toward ultrathin and flexible optoelectronic devices.[11–13] As the 2D structure of TMDC approaches the monolayer limit, diverse electronic and optical properties emerge in the system, like exceptionally strong Coulombic interactions,[14] an increment in the electronic band gap,[15,16] strong spin–orbit coupling,[17–19] efficient light–matter interactions, fascinating spin-valley physics,[20,21] etc. The optical absorption spectrum of monolayer and few layer TMDC materials are generally comprised of four excitonic signals usually labeled as A, B, C, and D in energetic order,[22,23] where the spectrum is dominated by the C and D, suggested to be formed in a parallel band structure arrangement in their density of states and largely affected by band nesting phenomena.[24,25] The oscillator strengths of these excitons are surprisingly higher than those

low energy ones, even greater than monolayer graphene,[26] yet the PL quantum efficiency was found to be very low.[24] This indicates that the relaxation processes associated with these high energy excitons must be very different from those of fundamental excitons (A and B), which are well reported in the literature.[27–31] The dominance of phonon-mediated hot carrier relaxation could be one of the key reasons behind this poor quantum efficiency. Kozawa et al. reported that the photogenerated carriers (electron/hole) in the band-nesting region exhibit fast intraband relaxation toward nearest excited states (Λ valley/Γ hill), followed by a relatively slow nonradiative decay to reach the K/K' state in monolayer MoS₂.[24] They attributed this fast relaxation to the spontaneous charge separation in the momentum space (band nesting effect), which eventually restricts the quantum efficiency of the C excitonic state. Moreover, as 2D systems undergo a bulk to monolayer transition, the relaxation processes are modified accordingly, attributed to the increased carrier interactions in the reduced Coulombic environment, bandgap renormalization, and an indirect to direct band gap transition. Hence, it is very important to study these excitonic species in different

CCC
RightsLink

Home · Help ∨ · Email Support · Sign in · Create Account

Ultrafast Insights into High Energy (C and D) Excitons in Few Layer WS2

Author: Tanmay Goswami, Himanshu Bhatt, K. Justice Babu, et al

Publication: Journal of Physical Chemistry Letters

Publisher: American Chemical Society

Date: Jul 1, 2021

Copyright © 2021, American Chemical Society

BACK   CLOSE WINDOW

The Journal of Chemical Physics

ARTICLE

scitation.org/journal/jcp

Probing ultrafast hot charge carrier migration in MoS₂ embedded CdS nanorods

View Online   Export Citation   CrossMark

Tanmay Goswami,[1] Himanshu Bhatt,[1] Dharmendra Kumar Yadav,[1] Ramchandra Saha,[1] K. Justice Babu,[1] and Hirendra N. Ghosh[1,2,a]

AFFILIATIONS

[1] Institute of Nano Science and Technology, Knowledge City, Sector 81, SAS Nagar, Mohali, Punjab 140306, India
[2] Radiation and Photochemistry Division, Bhabha Atomic Research Centre, Mumbai 400085, India

Note: This paper is part of the JCP Special Topic on Transport of Charge and Energy in Low-Dimensional Materials.
[a]Author to whom correspondence should be addressed: hnghosh@inst.ac.in and hnghosh@gmail.com

ABSTRACT

Efficient utilization of hot charge carriers is of utmost benefit for a semiconductor-based optoelectronic device. Herein, a one-dimensional (1D)/two-dimensional (2D) heterojunction was fabricated in the form of CdS/MoS₂ nanorod/nanosheet composite and migration of hot charge carriers was being investigated with the help of transient absorption (TA) spectroscopy. The band alignment was such that both the electrons and holes in the CdS region tend to migrate into the MoS₂ region following photoexcitation. The composite system is composed of optical signatures of both CdS and MoS₂, with the dominance of CdS nanorods. In addition, the TA signal of MoS₂ is substantially enhanced in the heterosystem at the cost of the diminished CdS signal, confirming the migration of charge carrier population from CdS to MoS₂. This migration phenomenon was dominated by the hot carrier transfer. The hot carriers in the high energy states of CdS are preferentially migrated into the MoS₂ states rather than being cooled to the band edge. The hot carrier transfer time for a 400 nm pump excitation was calculated to be 0.21 ps. This is much faster than the band edge electron transfer process, occurring at 2.0 ps time scale. We found that these migration processes are very much dependent on the applied pump photon energy. Higher energy pump photons are more efficient in the hot carrier transfer process and place these hot carriers in the higher energy states of MoS₂, further extending charge carrier separation. This detailed spectroscopic investigation would help in the fabrication of better 1D/2D heterojunctions and advance the optoelectronic field.

Published under an exclusive license by AIP Publishing. https://doi.org/10.1063/5.0074155

I. INTRODUCTION

Phonon bottleneck mediated slow relaxation of hot charge carriers provides extra boost toward the device efficiency of a semiconducting material owing to the longer time range for the extraction of those carriers. It is expected that efficient utilization of hot carriers would enhance the efficiency of solar cells up to 66% under 1 sun illumination.[1] Among many other techniques, a heterojunction formation is one of the best-known methods for the extraction of hot carriers in a system.[2,3] In recent times, numerous heterojunctions have been fabricated and designed to form the state-of-the-art optoelectronic devices.[4–9] The efficiency of these heterosystems can possibly be improved with the detailed knowledge of the excited state behavior of hot carriers[2,10] and the formation of important quasiparticles, such as exciton, bi-exciton, and trion,[11] at the interface of those quantum materials. Hence, it is of utmost importance to explore the charge carrier dynamics of all possible

heterosystems suggested to have potential in advancing optoelectronic research.

Cadmium sulfide (CdS) is a versatile II–VI semiconductor[12] and a widely known photocatalyst[13] owing to its easy synthetic routes and outstanding optical and catalytic properties. Some of its properties important for catalytic applications are a suitable direct bandgap (~2.4 eV) for visible light harvesting, good chemical and thermal stability, appropriate redox potential, etc.[14–16] Along with these fascinating properties, low-dimensional CdS nanostructures endow some fundamental properties such as high charge carrier mobilities, relatively low work function, and large exciton binding energy.[17,18] CdS-based nanostructures hold great promise as a host material in high technology optoelectronic applications, such as photovoltaics, transistors, light emitting diodes, photochemical devices, and photodetectors.[18–20] Amid all nanostructures of CdS, 1D nanorods (NRs) are the hottest field of nanotechnology in recent times due to their unique optoelectronic properties.[18,21] Now,

AIP PUBLISHING LICENSE
TERMS AND CONDITIONS

Oct 21, 2022

This Agreement between Mr. Tanmay Goswami ("You") and AIP Publishing ("AIP Publishing") consists of your license details and the terms and conditions provided by AIP Publishing and Copyright Clearance Center.

License Number	5413561159014
License date	Oct 21, 2022
Licensed Content Publisher	AIP Publishing
Licensed Content Publication	Journal of Chemical Physics
Licensed Content Title	Probing ultrafast hot charge carrier migration in MoS2 embedded CdS nanorods
Licensed Content Author	Tanmay Goswami, Himanshu Bhatt, Dharmendra Kumar Yadav, et al
Licensed Content Date	Jan 21, 2022
Licensed Content Volume	156
Licensed Content Issue	3
Type of Use	Thesis/Dissertation
Requestor type	Author (original article)
Format	Print and electronic

Portion	Excerpt (> 800 words)
Will you be translating?	No
Title	Spectroscopic Investigation of Ultrafast Photo-physical Processes in Chalcogenide Based Two-Dimensional (2D) Materials
Institution name	Institute of Nano Science and Technology (INST) Mohali
Expected presentation date	Nov 2022
Portions	Full article
Requestor Location	Mr. Tanmay Goswami Institute of Nano Science and Technology Mohali, PUNJAB 140306 India Attn: Mr. Tanmay Goswami
Total	0.00 USD

Terms and Conditions

AIP Publishing -- Terms and Conditions: Permissions Uses

AIP Publishing hereby grants to you the non-exclusive right and license to use and/or distribute the Material according to the use specified in your order, on a one-time basis, for the specified term, with a maximum distribution equal to the number that you have ordered. Any links or other content accompanying the Material are not the subject of this license.

1. You agree to include the following copyright and permission notice with the reproduction of the Material:"Reprinted from [FULL CITATION], with the permission of AIP Publishing." For an article, the credit line and permission notice must be printed on the first page of the article or book chapter. For photographs, covers, or tables, the notice may appear with the Material, in a footnote, or in the reference list.

2. If you have licensed reuse of a figure, photograph, cover, or table, it is your responsibility to ensure that the material is original to AIP Publishing and does not contain the copyright of another entity, and that the copyright notice of the figure, photograph, cover, or table does not indicate that it was reprinted by AIP Publishing, with permission, from another source. Under no circumstances does AIP Publishing purport or intend to grant permission to reuse material to which it does not hold appropriate rights.
   You may not alter or modify the Material in any manner. You may translate the Material into another language only if you have licensed translation rights. You may not use the Material for promotional purposes.

3. The foregoing license shall not take effect unless and until AIP Publishing or its agent, Copyright Clearance Center, receives the Payment in accordance with Copyright Clearance Center Billing and Payment Terms and Conditions, which are incorporated herein by reference.

4. AIP Publishing or Copyright Clearance Center may, within two business days of granting this license, revoke the license for any reason whatsoever, with a full refund payable to you. Should you violate the terms of this license at any time, AIP Publishing, or Copyright Clearance Center may revoke the license with no refund to you. Notice of such revocation will be made using the contact information provided by you. Failure to receive such notice will not nullify the revocation.

5. AIP Publishing makes no representations or warranties with respect to the Material. You agree to indemnify and hold harmless AIP Publishing, and their officers, directors, employees or agents from and against any and all claims arising out of your use of the Material other than as specifically authorized herein.

6. The permission granted herein is personal to you and is not transferable or assignable without the prior written permission of AIP Publishing. This license may not be amended except in a writing signed by the party to be charged.

7. If purchase orders, acknowledgments or check endorsements are issued on any forms containing terms and conditions which are inconsistent with these provisions, such inconsistent terms and conditions shall be of no force and effect. This document, including the CCC Billing and Payment Terms and Conditions, shall be the entire agreement between the parties relating to the subject matter hereof.

This Agreement shall be governed by and construed in accordance with the laws of the State of New York. Both parties hereby submit to the jurisdiction of the courts of New York County for purposes of resolving any disputes that may arise hereunder.

V1.2

Questions? customercare@copyright.com or +1-855-239-3415 (toll free in the US) or +1-978-646-2777.

THE JOURNAL OF PHYSICAL CHEMISTRY LETTERS
A JOURNAL OF THE AMERICAN CHEMICAL SOCIETY

Letter

Defect-Mediated Slow Carrier Recombination and Broad Photoluminescence in Non-Metal-Doped ZnIn$_2$S$_4$ Nanosheets for Enhanced Photocatalytic Activity

Tanmay Goswami,[§] Dharmendra Kumar Yadav,[§] Himanshu Bhatt, Gurpreet Kaur, Ayushi Shukla, K. Justice Babu, and Hirendra N. Ghosh*

Read Online

ACCESS | Metrics & More | Article Recommendations | Supporting Information

ABSTRACT: Elemental doping has already been established to be one of the most effective approaches for band-gap engineering and controlled material response for improved photocatalytic activity. Herein atomically thin ZnIn$_2$S$_4$ (ZIS) nanosheets were doped with O and N separately, and the effects of doping were spectroscopically investigated for photocatalytic H$_2$ evolution. Steady-state photoluminescence studies revealed an enhanced charge-carrier population in the doped systems along with a defect-state-induced broad peak in the red region of the spectra. Transient absorption (TA) spectroscopy demonstrated that the conduction-band-edge electrons are transferred on an ultrafast time scale to the inter-band-gap defect states. TA analysis suggests that O and N doping contributes to the defect state concentration and ensures an enhanced photocatalytic activity of the system. This detailed spectroscopic analysis uncovers the role of inter-band-gap defect states in the photocatalytic activity of ZIS and will open new avenues for the construction of nanosheet-based optical devices.
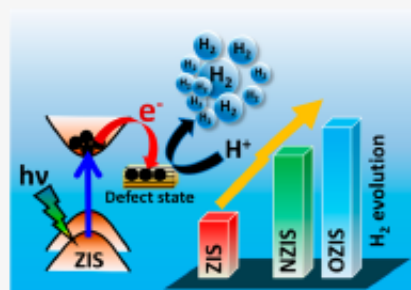
Photocatalytic H$_2$ evolution stands out as the next possible alternative source of energy ahead of the scientific community in the course of replacing nonrenewable and toxic energy sources like coal, petroleum, and so on.[1] Numerous semiconducting and metallic systems[2,3] are being used to convert earth-abundant waters into the chemical fuel H$_2$ using solar energy. Although these materials show immense potential, we are far from the stage where we can commercialize this energy. At this instant, proper knowledge of the photophysical processes, like the photoinduced behavior of charge carriers and the subsequent relaxation processes involved in the phenomena of H$_2$ evolution, would be extremely helpful in designing efficient and cost-effective photocatalytic materials.
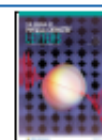
Currently, ZnIn$_2$S$_4$ (ZIS) is considered to be one of the best photocatalysts due to its low cost, high stability, low toxicity, and tunable band gap (2.06 to 2.85 eV).[4−6] It offers a wide range of applications in charge storage, solar cells, photodetectors, photoelectrochemistry, and photocatalysis.[7−12] ZIS nanosheets are usually exhibited in two crystal phases, cubic and hexagonal, where the hexagonal phase happens to show better photocatalytic performance compared with its cubic counterpart.[13] In bulk ZIS systems, the photocatalytic activity is hampered due to both the surface and bulk recombination of photoexcited charge carriers.[14] While in the atomically thin system, these bulk recombinations are diminished, riding upon the emerging quantum confinement phenomena.[15,14] Partic-

ularly, in the few-layer ZIS nanosheets, a large fraction of surface sulfur atoms are exposed in the sunlight and offer more active sites. The reduced diffusion length of charge carriers helps in the rapid transport toward the surface-active sites before recombination. As a result, few-layer ZIS shows much better photocatalytic activity than bulk;[16,17] however, it is often observed that the fast recombination of charge carriers limits the photocatalytic performance, even in few-layer ZIS nanosheets.[4] In this scenario, elemental doping has emerged to be an effective strategy to improve the photocatalytic activity by surface modification and tuning the electronic structure.[18] Various metallic cations like Cu^{2+}, Ni^{2+}, and so on[19−21] are being doped to enhance the light absorption range, which helps in the improvement of photocatalytic activity. However, there is a probability of trapping the photoinduced charge carriers in the metal centers as well, which can diminish the photocatalytic yield.[22] Contrary to that, elemental (O, N, P, etc.) doping is preferable for better photocatalytic performance.[16] Recently, O- and N-doped ZIS systems have

CCC
RightsLink

Home   Help ⌄   Email Support   Sign in   Create Account

Defect-Mediated Slow Carrier Recombination and Broad Photoluminescence in Non-Metal-Doped ZnIn2S4 Nanosheets for Enhanced Photocatalytic Activity

ACS Publications
Most Trusted. Most Cited. Most Read.

Author: Tanmay Goswami, Dharmendra Kumar Yadav, Himanshu Bhatt, et al

Publication: Journal of Physical Chemistry Letters

Publisher: American Chemical Society

Date: May 1, 2021

Copyright © 2021, American Chemical Society

PERMISSION/LICENSE IS GRANTED FOR YOUR ORDER AT NO CHARGE

BACK   CLOSE WINDOW

UFS 2019
IIT Bombay

Ultrafast Sciences - 2019

7 – 9th November, 2019
Indian Institute of Technology Bombay

CERTIFICATE OF PARTICIPATION

This is to certify that Mr. Tanmay Goswami from Institute of Nano Science & Technology Mohali presented a poster / attended the Ultrafast Sciences 2019 conference organized by IIT Bombay, Powai, Mumbai, Maharashtra – 400076.

Mumbai
7th November, 2019

Convener
Anindya Datta
UFS - (Convener)
IIT Bombay, India

Gopal Dixit
Secretary
(Secretary)
UFS - 2019
IIT Bombay, India

DST & ACS
WORKSHOP

Department of Science & Technology, Government of India · ACS Chemistry for Life

Certificate of Participation

VERIFYING THAT

TANMAY GOSWAMI

ATTENDED THE FULL AGENDA OF THE DST & ACS WORKSHOP:
INST MOHALI
NOVEMBER 20, 2019

DR. JAMES MILNE
Acting President, Publications Division
American Chemical Society

Conference certificates

7ᵀᴴ THEME MEETING ON ULTRAFAST SCIENCES - 2021 *(UFS-2021)*
Dates: November 12 - 13, 2021: Venue: On-line Zoom Platform
Organized by: UM-DAE Centre for Excellence in Basic Sciences,
Mumbai University, Kalina Campus, Santacruz (E), Mumbai-400098

CERTIFICATE OF PARTICIPATION & POSTER PRESENTATION

This certifies that
MR. TANMAY GOSWAMI,

Institute of Nano Science and Technology, Mohali, Punjab-140306, has participated and presented a poster on *"Transient absorption spectroscopy of few layer WS$_2$ in the perspective of high energy (C, D) excitons"* at the 7ᵗʰ Theme Meeting on Ultrafast Sciences 2021 (UFS-2021).

Dipak K. Palit
Convener, UFS-2021

Vimal K. Jain
Chairman, UFS-2021 & Director, CEBS

2nd Research Scholars' Day
31st March - 1st April, 2022

CERTIFICATE
OF PARTICIPATION

This is to certify that

Tanmay Goswami

has given an oral presentation on the topic entitled

Ultrafast spectroscopy of Two-Dimensional Chalcogenide based Semiconductors

Prof. Amitava Patra
Director, INST

Best Award

2nd Research Scholars' Day

31st March - 1st April, 2022

Best Oral Presentation Award
presented to

Tanmay Goswami (EEU)

for the topic entitled

" *Ultrafast Spectroscopy of 2D Chalcogenide based Semiconductors* "

Amitava Patra
Prof. Amitava Patra
Director, INST

UFS 2022

9ᵀᴴ Theme Meeting on Ultrafast Sciences

ORGANIZED BY

Indian Institute of Science Education and Research Thiruvananthapuram

CERTIFICATE

This is to certify that

Tanmay Goswami

Institute of Nano Science and Technology (INST), Mohali

has presented a poster in the UFS 2022 meeting held at

Indian Institute of Science Education and Research,Thiruvananthapuram

during 3-5 November 2022.

Convener
Dr. Rajeev N. Kini

Co-Convener
Prof. Mahesh Hariharan

Secretary
Dr. Adithya Lakshmanna